Physics of Intense Light Ion Beams, Production of High Energy Density in Matter, and Pulsed Power Applications

Annual Report 1996/97

H.-J. Bluhm (Editor)

Institut für Neutronenphysik und Reaktortechnik

Forschungszentrum Karlsruhe

Technik und Umwelt
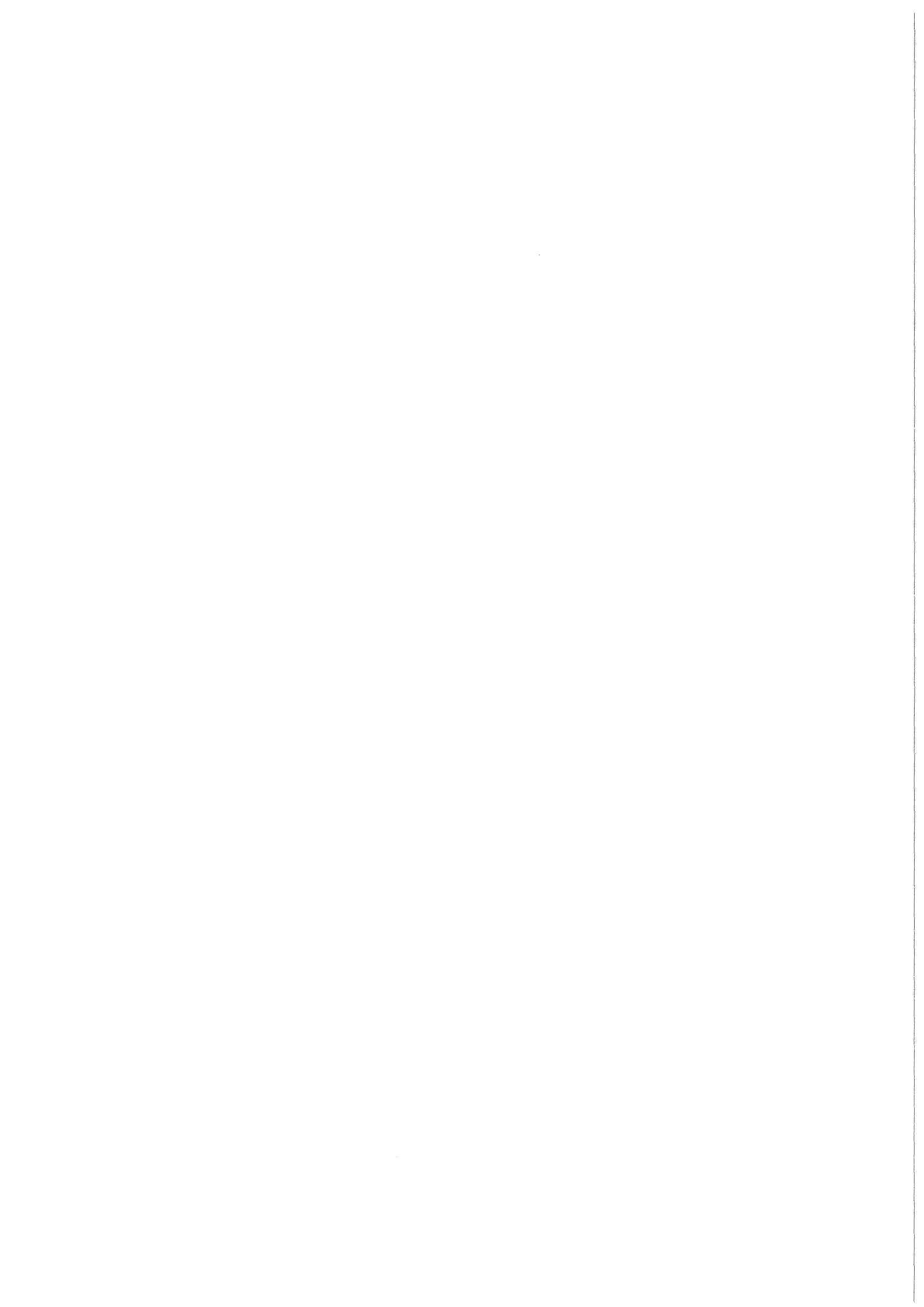
Wissenschaftliche Berichte

FZKA 6205

Physics of Intense Light Ion Beams, Production of High Energy Density in Matter, and Pulsed Power Applications

Annual Report 1996/97

H.-J. Bluhm
(Editor)

Institut für Neutronenphysik und Reaktortechnik

Abstract

This report presents research and development work carried out in 1996/97 in the INR under the general heading of scientific and industrial applications of pulsed power. In the two years covered by this report the main emphasis of the work has been further shifted to three areas with a large potential for industrial applications, namely electrodynamic fragmentation, pulsed electron and ion beam surface modification, and electrodynamic production of nanocrystalline materials.

Nevertheless, large progress has also been achieved in the field of intense light ion beam production and in beam matter interaction experiments. A rather consistent image of the operation of high power ion diodes has been obtained through new diagnostic developments and the world-wide first ion beam driven Rayleigh-Taylor instability experiments have been carried out.

Physik intensiver Strahlen leichter Ionen, Erzeugung hoher Energiedichten in Materie und Anwendungen der Pulsed Power Technik

Zusammenfassung

In dem Bericht werden die Forschungs- und Entwicklungsarbeiten zu wissenschaftlichen und industriellen Anwendungen der Pulsed Power Technik dargestellt, die im INR in den Jahren 1996/97 durchgeführt wurden. In den beiden durch diesen Bericht abgedeckten Jahren hat sich das Gewicht der Arbeiten noch stärker auf drei Gebiete mit großem industriellen Anwendungspotential verlagert, nämlich auf die elektrodynamische Fragmentierung, die Oberflächenmodifikation mit gepulsten Elektronen- und Ionenstrahlen und die elektrodynamische Erzeugung nanokristalliner Materialien.

Trotzdem konnten auch große Fortschritte bei der Erzeugung intensiver Strahlen leichter Ionen und bei der Strahl-Materie-Wechselwirkung erreicht werden. Insbesondere wurde durch die Entwicklung neuer Diagnostiken ein weitgehend konsistentes Bild der Betriebsweise von Hochleistungsionendioden gewonnen und die weltweit ersten ionenstrahlgetriebenen Experimente zur Untersuchung der Rayleigh-Taylor Instabilität durchgeführt.

Contents

4. TARGET PHYSICS

5. APPLICATIONS

1 Program goals and summary of results

Program goals and summary of results

H. Bluhm, G. Keßler, INR

In the two years covered by this report the main emphasis of the pulsed power research and development work in the INR has been further shifted to industrial applications and cooperations with industrial partners have been established. Judged by the numerous inquiries electrodynamic fragmentation of solid materials finds the strongest industrial interest. This results mainly from the fact, that unlike breaking and milling with mechanical devices, electrodynamic fragmentation has the capability to separate compound materials at the intercomponent boundaries. Thus a new quality in recycling of compound materials (like concrete) or material compounds (like electrical appliances) can be achieved. Another important feature of the process is that it creates only slight contaminations. So far little is known on synergetic effects that can result from fragmentation in combination with chemical compounds created in the plasma of the spark channel.

Surface modification with pulsed electron beams has also found appreciable industrial interest. Compared to conventional methods the pulse melting of surface layers leads to extremely high cooling rates ($10^6 - 10^8$ K/s). Another advantage is that a single pulse contains enough energy to melt on area of more than 100 cm^2. More than 1000 cm^2 seem possible with a larger generator.

We have conducted pulsed electron beam treatments of MCrAlY oxidation protection layers on high temperature gas turbine blades and created amorphous or nanocrystalin layers, on which homogeneous strongly adhering Al$_2$O$_3$ layers grew, improving the lifetime of the protection layers and establishing a bonding layer for thermal barrier coatings, envisaged for the next generation of turbine blades. Alloying thin layers into the surface of a bulk structural material offers new possibilities to improve the corrosion resistance of materials without sacrificing their thermal, mechanical or neutronic properties. Possible applications in the development of accelerator driven nuclear reactors are discussed on page ...

Nanopowder production by pulsed discharges through thin wires is an universally applicable method which is mainly limited by the availability of suitable wire materials. Potentially large amounts of nanopowder can be produced by this technique at relatively low specific costs. In the period reported we have produced oxides, nitrides and metallic nanopowders. The yield is still unsatisfactory since large amounts of small particles adhere to larger particles and are sorted out as waste in the cyclones used for separation. To break-up the agglomerated particles a new cyclone, designed at the Fachhochschule Flensburg, has been taken into operation. First trials showed that no particles > 200 nm were in the fraction, but the yield was still too low. Nevertheless several 100 g of different kinds of nanopowders could be produced both for industrial costumers and research institutes.

Intense ion beam research was continuing on the pulse generator KALIF. A two-wavelength dispersion interferometer system of hitherto unreached sensitivity has been completed and applied to the measurement of electron densities in the acceleration gap of high power ion diodes. These worldwide first measurements have appreciably improved our understanding about the physics developing in these diodes and led to a quite consistent picture of diode operation. One must conclude now that

the diamagnetic effect resulting from the drifting electron cloud should be kept small. This can be achieved by reducing the ion current densities, i.e. enlarging the ion emission area.

Rayleigh-Taylor instabilities belong to the most destructive hydrodynamic instabilities in target physics. We have used the KALIF proton beam to accelerate corrugated planar targets and to investigate for the first time ion beam driven Rayleigh-Taylor instabilities. Applying the line-imaging laser Doppler velocitmeter in these measurements a unique new method was introduced that allows a much more direct evaluation of the instability growth than in previous laser experiment. We observed an exponential growth which on the average amounted to only 40 – 65 % of the classical growth rate. The reduction is mainly attributed to heat transport driven mass convection through the plasma solid boundary at the ablation front.

The 6 MV, 400 kA accelerator KALIF-HELIA presently under construction will go into operation early in 1999 and offer new capabilities both in diode physics and for exploratory investigations of future industrial applications.

2 Machines and pulsed power technique

THE KALIF-HELIA ACCELERATOR: DESCRIPTION, PROGRAM AND STATUS

P. Hoppé[a], W. Bauer[a], H. Bluhm[a], V. Carboni[b], J. Fockler[b], G. Keßler[a], K. Leber[a],
K. Nielsen[c], K. Prestwich[b], W. Ratajczak[a], D. Rusch[a], J. Singer[a], I. Smith[b], P. Spence[b]

[a] *Forschungszentrum Karlsruhe, INR, P.O. Box 3640, D-76021 Karlsruhe, Germany*
[b] *Pulse Sciences Inc., 600 McCormick St., San Leandro, CA 94577, USA*
[c] *Physics International, 2700 Merced Street, San Leandro, CA 94577, USA*

Abstract

The accelerator KALIF-HELIA - presently under construction at the Forschungszentrum Karlsruhe - should produce a 60ns pulse of up to 6MV and 400kA. It is based on a design that couples a self-magnetically insulated transmission line with the linac induction principle. The accelerator can be used in either polarity for the generation of an ion- or an electron beam respectively. In positive polarity improvement of the quality of intense light ion beams will be the most important research area. Beam divergence scaling laws with voltage and mass will be investigated experimentally. In negative polarity the extracted electron beam will be used for potential future applications where a high dose, high dose rate and a large exposure area might be advantageous.

I. Introduction

Since the first induction linac built in 1964 [1], these accelerators were used mainly for the production of high quality electron beams with currents up to 10kA, energies up to 50MeV and kHz repetition rates. With their electric fields below the self emission threshold (~20MV/m) the achievable power density in linacs is limited to 0.5TW/m². Much higher power densities were achieved when the electron beam accelerated on axis of the linac cavities was replaced by a solid inner conductor that formed a coaxial transmission line with the inner bore of the cavities. This coaxial line was operated as magnetically insulated transmission line (MITL) with electric fields well above the emission threshold. Related to its high power density, the size and costs of accelerators based on this magnetically insulated voltage adder (MIVA) principle could be reduced and they therefore were considered as drivers for ICF related applications. However, the MIVA inherent problems and their influence on the beam properties remain to be solved. These are mainly: a) a fraction of the beam energy is carried as electron vacuum current, b) the beam must be generated and focused in one or two stages (the 'diode') and c) the ion- or electron source must deliver much higher currents compared to a linac source.

II. Description of KALIF-HELIA

KALIF-HELIA is the first accelerator in Europe based on this MIVA design that was already used for the construction of the accelerators HELIA, HERMES III and SABRE at Sandia National Labs. (SNL) and for the COBRA machine at Cornell.
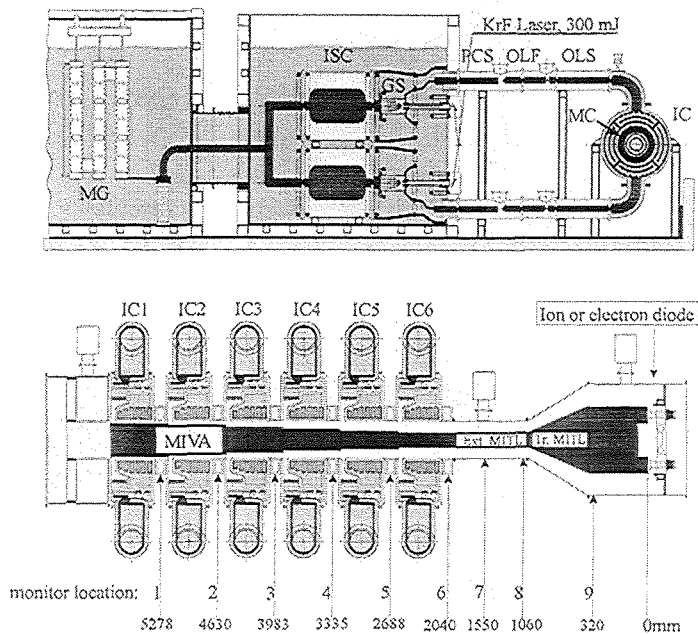
Fig. 1: Schematic of the KALIF-HELIA accelerator

The KALIF-HELIA Marx generator[1] (see MG in Fig. 1) consists of a total of 36 capacitors with 2.2µF each, chargeable to a maximum voltage of 100kV. Thus the maximum energy stored is 400kJ. This energy is transferred to 4 intermediate store capacitors (ISC). The capacitance of each of these coaxial water filled cylinders is 9nF; 12.5nF capacitors are optional. Their discharge is made by 4 gas switches (GS) triggered by a 300mJ KrF laser. The energy from the 4 ISC is transferred to a total of 12 water insulated pulse forming lines (PFL's), arranged in 2 horizontal rows on 2 different levels. Each PFL consists of 3 sections: the pulse charge section PCS is connected by the output switch to the first output line OLF which discharges by a prepulse switch to the second output line OLS. This switch/transmission line sequence produces the required pulse shape and minimizes the prepulse. The pulses delivered by the PFL's enter the induction cells (IC) at diametrically opposite points, are mixed by azimuthal distribution lines and fed homogeneously to the insulator stack and the radial feed section. The 6 insulating magnetic cores (MC) are tape wrap-ups of plastic for insulation between the amorphous metal layers. They experience a voltage which peaks at 1.3MV and integrates to 63mVs over the pulse. The core cross sections are chosen such that this delivers a flux swing of 3T to the magnetic material[2]. The MIVA impedance is strongly influenced by the electron vacuum flow. It is due to the high electric fields launching electrons into the vacuum gaps formed by the 'radial feed' sections and the 6 coaxial sections formed by the bore diameter of the cavities and the 6 different outer diameters of the inner stalk. The MIVA should deliver a fast rising 6MV pulse to the load with a minimum electron vacuum flow. The results from different approaches used for the determination of the MIVA gap sequence g_1 to g_6 (Fig. 2) are in rather good agreement but differed considerably from a non-emission design ($I_{vac}=0$). Finally, the gap width of the 6 coaxial sections was chosen according to the results from calculations of the vacuum impedance for each section (8.25, 14.1, 18.9, 23.0, 26.7, and 30.0Ω), that allows the highest value of the flow impedance

Fig. 2: Calculated gap width of the MIVA

4

for each section without adding any unnecessary inductance slowing down the rise time of the pulse [5].
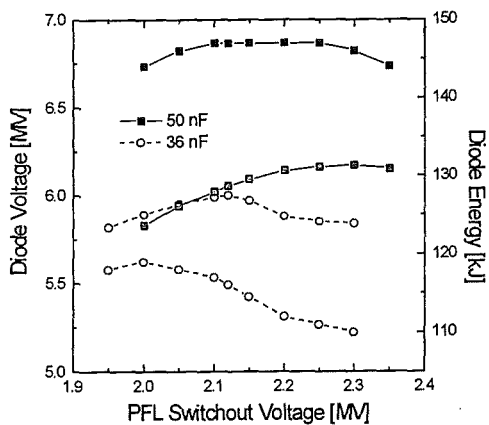
Fig. 3: Predicted peak-diode voltage and energy
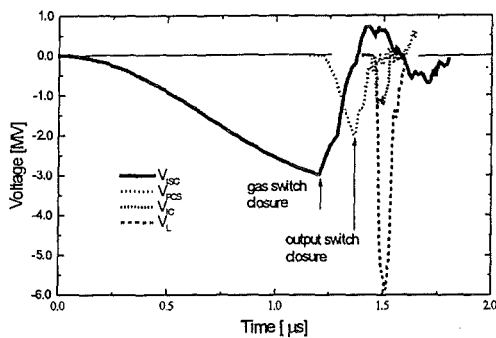
Fig. 4: Predicted voltage time histories
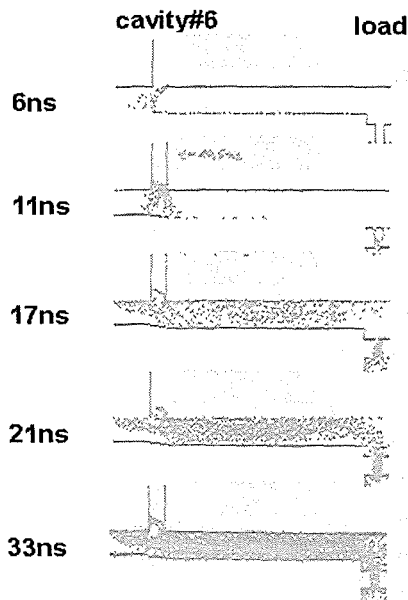
Fig.5: Results from PIC simulations [6]

The diode voltage and the total energy delivered to the assumed 15Ω load depend on the switch-out time of the PFL's. For the 36nF intermediate store capacitor, the maximum diode voltage V_d of 6MV will be achieved if the PFL's are allowed to charge up to 2.12MV, the energy E_d will be 116kJ (Fig. 3). If the PFLs are switched-out at about 2MV, the maximum energy of 120kJ is supplied at a somewhat lower diode voltage of 5.9MV. If considered useful, the energy delivered to the diode can be further increased by about 25% if the intermediate store capacitors are modified from 36nF (as built) to 50nF (Fig. 3). The predicted time histories of the voltages at the intermediate store capacitor V_{ISC}, at the middle of the pulse charge section V_{PCS}, close to the oil/vacuum interface of the induction cell V_{IC} and at the diode load V_L are shown in Fig. 4. The electron vacuum current -to be considered as a loss for an ion diode- is not taken into account in these transmission line calculations. According to 1D-laminar flow models and time dependent 2D PIC calculations (Fig. 5), the vacuum current may reach up to 30% of the total current of 440kA, assuming 5.4MV at the load [6]. The last cavity connects either to a 30Ω extension MITL with a length of 1.1m or to a 30Ω transition MITL which supports the anode or cathode of the diode. With possible outer diameters up to 50cm, large area diodes with correspondingly low current densities (<1kA/cm^2) can be used.

Compared to other MIVA type accelerators (Tab. 1) KALIF-HELIA offers the following improvements: a) the radial feeds of the induction cavities were covered with an anti-emission coating raising the emission threshold to 40MV/m, i.e. a reduced electron vacuum current is expected, b) a new magnetic material (called 'Vitrovac') was used for the fabrication of the induction cores. This new material was extensively tested and qualified, c) flexible joints on both sides of the PFL's allow variations in the axial extension of the adder which might be caused by spools for diagnostics or retrapping rings for the vacuum electron current and d) compared to its pulse length of 60ns the adder is electrically short, i.e. undermatching of the

5

diode to the adder should reduce the vacuum electron current. A more detailed description is given in [7]. In Tab. 2 the expected performance of the KALIF-HELIA accelerator is compiled.

Tab. 1: Comparison of KALIF-HELIA to other MIVA type induction accelerators

name of the accelerator	Ref.	site	no. of induct. cavity	peak power [TW]	peak voltage [MV]	peak current [kA]	pulse duration fwhm [ns]	max. energy [kJ]
HELIA	[10]	SNL	4	1	4	250	30	
HERMES III	[11]	SNL	20	16	22	730	40	400
SABRE	[12]	SNL	10	1.8	6	250	40	
COBRA	[13]	Cornell	4	0.5	4...5	100...250	46	
KALIF-HELIA		FZK	6	2.4...2.9	6	400...500	60	120

Tab. 2: Expected performance of the KALIF-HELIA accelerator

Load voltage:	from 1MV....6MV....(9MV)
Load currents:	200kA, up to 550kA
Pulsewidth:	60ns fwhm
Energy to load:	up to 150kJ
Jitter (rms):	< 20ns related to Marx
	< 2ns related to gas switch
Shot rate:	depends on experimental conditions, limited by HV charge supply to about 1/min
Beam type:	electrons
	ions (protons, light ions (Li, B, C))
shot reproducibility:	much better when compared to KALIF

III. Program for KALIF-HELIA

The main purpose of this accelerator is related to the following topics:

1. the investigation of the physics of matter under extremely high temperatures and pressures.
2. the study of future possible technological applications up to extreme conditions.
3. the gain of experience with the novel high voltage pulsed power components of KALIF-HELIA as well as the development and testing of future components.

Depending on the polarity of the output pulse, these applications are summarized in the following.

In positive polarity operation, the main fields of interest are related to either beam matter interaction experiments (a) or to proof of principle type experiments for technological applications (b).
(a) The maximum power density achievable in the focus of an extractor type ion diode is proportional to the beam brightness B which is proportional to $1/\Theta^2$ with the divergence Θ as half angle of the emission cone of a beamlet. Reliable scaling laws for the beam divergence are needed. The presently known sources of beam divergence can be subdivided in those

which favourably scale with the acceleration voltage V and/or ion mass M and those which are independent of V and/or M [8]. In particular, all effects resulting from anode plasma inhomogeneities are independent of V. If they dominate the contributions to beam divergence no improvement is to be expected from raising V and/or M. Therefore it is crucial to first supply a sufficiently homogeneous and smooth ion source from which a space charge limited ion beam can be extracted. Presently no high-power experiments are available that have been conducted both at low and high accelerating voltages with comparable high quality ion sources. The radial ion diode on PBFAII has produced a 9MeV Li$^+$ beam with 24mrad and a 5MeV proton beam with a divergence of 16mrad [9]. Similarly low divergence has been obtained for a proton beam at the 1.4MV accelerator PBFAI. This seems to indicate that in these cases the divergence was determined by the properties of the anode plasma. Therefore, in a first step it is foreseen to use the successful sliding discharge proton sources of the KALIF B$_{appl}$ diodes, adapt this source and diode to the needs of KALIF-HELIA and to operate this proton diode up to 6 MV. This would allow to test the voltage dependence in the divergence equations. In a second step, assuming a high quality lithium ion source becomes available, the mass dependence in the scaling laws will be checked. With 2-stage diodes a further divergence reduction will probably be achieved because ideally the second stage should add just longitudinal velocity to the beam. However, the operation of 2-stage diodes under high power conditions is rather complex and a verification of the predicted results on high power machines is necessary. KALIF-HELIA is -related to the axial flexibility in the positioning of the induction cells-ideally suited for this purpose.

(b) Technological applications require in general energy densities from 0.1 to at most several 10J/cm^2 and repetition rates up to 100Hz. With the energy available and the single shot operation mode of KALIF-HELIA only proof of principle type experiments up to extremes seem to be feasible. With the energies available of several 10kJ this accelerator would be useful for the ion treatment of large (m^2) areas with very high densities in one single shot. Possible applications are related to corrosion protection and modification of metallic surfaces.

In negative polarity, experiments are feasible in fundamental research related areas as well as for technological purposes. Examples for the first group are: the interaction between pencil-type e-beams and matter or the biological effect on micro-organisms depending on high dose rates and doses. If e-beams with sufficiently small energy distributions could be achieved, pumping of excimer- and FEL lasers or the production of pulsed high power microwaves could be considered. They might be related to areas like chemistry (polymerisation, production of fibers and foils...), material processing (all kinds of surface treatment of metals...), environment (treatment of biologically hazardous materials..) and food processing (sterilization).

The experience gained from the 'classical' pulsed power generators POLLUX and KALIF (developed around 1980) had strong influence on the pulsed power devices for technological applications presently under construction (like e.g. FRANKA-STEIN). KALIF-HELIA technology will have a strong influence on future pulsed power devices, namely on the design of:
- fast and compact triggered Marx generators with low jitter,
- laser triggered gas switches for voltages up to 4MV,
- voltage and current addition in induction cells with and without magnetic insulation,
- the theory and design of vacuum transmission lines with very high power densities.

Due to its flexibility with respect to its arrangement and polarity and its extensive instrumentation this accelerator is also very well suited to serve as a test-bed for novel high voltage pulsed power components.

IV. Status

The assembly of the accelerator started end of 1997 in building 423 which had to be adapted to the accelerator and the requirements of the licensing authorities. Actually, all of the components were put in place. The oil-, water-, gas- and energy supply systems are in progress as well as the safety- and control circuits.

The beginning of the start-up program -assuming that all the supply-, vacuum- and auxiliary systems were successfully tested and are available- is foreseen for November 1998For early 1999 the following test sequence is planned:

1. Test of the Marx generator and its safety- and dump circuits.
2. Operation of the trigger laser for the gas switches and synchronisation to the Marx trigger chain.
3. Adjustment of the switches in the PFL lines.
4. Calibration of the monitors using a short load.
5. Start of tests using an electrode diode with a variable gap width and a calorimeter for the measurement of the energy delivered at the end of the MITL

During this start up sequence the measurements will be accompanied and verified by transmission line calculations.

V. Summary

KALIF-HELIA is the first accelerator in Europe which couples the principle of an induction linac with that of the magnetically insulated transmission line. Comparatively low in costs and size it will deliver as much as 150kJ to a target either as an electron or an ion beam. However, it is of prime importance to improve the beam quality and reproducibility. With KALIF-HELIA in positive polarity we first intend to verify the voltage dependence of existing scaling laws for the beam divergence by operating the same type of proton diode already used successfully at KALIF. If a suitable Li^+ source becomes available the mass dependence of the beam divergence will be verified in a second step. In this case a specific power deposition of up to 5000TW/g might be achieved leading to radiation dominated high density plasma regimes so far not achieved. In negative polarity operation, proof-of -principle type experiments up to extremes or on large area samples are feasible. Finally the experience gained with this novel technology accelerator will stimulate the development of modern pulsed power devices for technological applications.

Acknowledgements

[1] N.C. Christofilos et al., Rev. Sci. Instr. **35**, 886 (1964)
[2] I. Smith, PSI, unpublished (1991)
[3] W. Bauer et al., Wiss. Berichte FZKA 5590, Forschungszentrum Karlsruhe, 5 (1995)
[4] A. Gordeev, unpublished (1994)

[5]   C.W. Mendel, S.E. Rosenthal, Phys. Plasmas 2, 1332 (1995)
[6]   S. Illy et al., Phys. Plasmas 1, 2748 (1994)
[7]   J. Fockler et al., Proc. 9th IEEE Int. Pulsed Power Conf., Vol.1, Albuquerque, NM, 431 (1993)
[8]   P. Hoppé et al., to be published in: Nucl. Instr. and Meth. in Phys. Res., A
[9]   T. A. Mehlhorn et al., Proc. 10th Int. Conf. High Power Part. Beams, Vol.1, San Diego, 53 (1994)
[10] J.J. Ramirez et al.: Proc. 5th IEEE Int. Pulsed Power Conf, Arlington, VA, 143 (1985) and
       J.P. Corley et al.: Proc. 7th IEEE Int. Pulsed Power Conf., Monterey, Cal., 571 (1989)
[11] J.J. Ramirez et al.: Proc. 6th IEEE Int. Pulsed Power Conf., Arlington, VA, 294 (1987) and
       D. L. Johnson et al.: Proc. 7th IEEE Int. Pulsed Power Conf., Monterey, Cal., 32 (1989)
[12] M. E. Cuneo et al., Proc. 9th IEEE Int. Pulsed Power Conf., Vol.2, Albuquerque, NM, 423 (1993)
[13] D. L. Smith et al., Proc. 10th IEEE Int. Pulsed Power Conf., Vol.2, Albuquerque, NM, 1449 (1995)

SWITCHING CHARACTERISTICS OF VITROVAC-CORES

S. Koenig
Institute of Electric Energy Systems and High-Voltage Technology, University of Karlsruhe.

This report deals with the switching characteristics of small amorphous softmagnetic strip-wound cores made of VITROVAC 7600Z[1]. The cores are used as a pulseline switch in a water-insulated coaxial pulseforming line replacing the typical gas-insulated spark-gap switch. Capacitive voltage sensors and Rogowski coils are used to measure the electric and magnetic fields. Characteristic output waveforms are presented.

In order to investigate the switching characteristics of amorphous strip-wound cores the water-insulated coaxial generator [KOE-97a], [KOE-97b] was modified. The spark-gap pulseline switch with low-inductive switching properties was replaced by a magnetic switch consisting of a stack of three strip-wound cores, Figure 1.
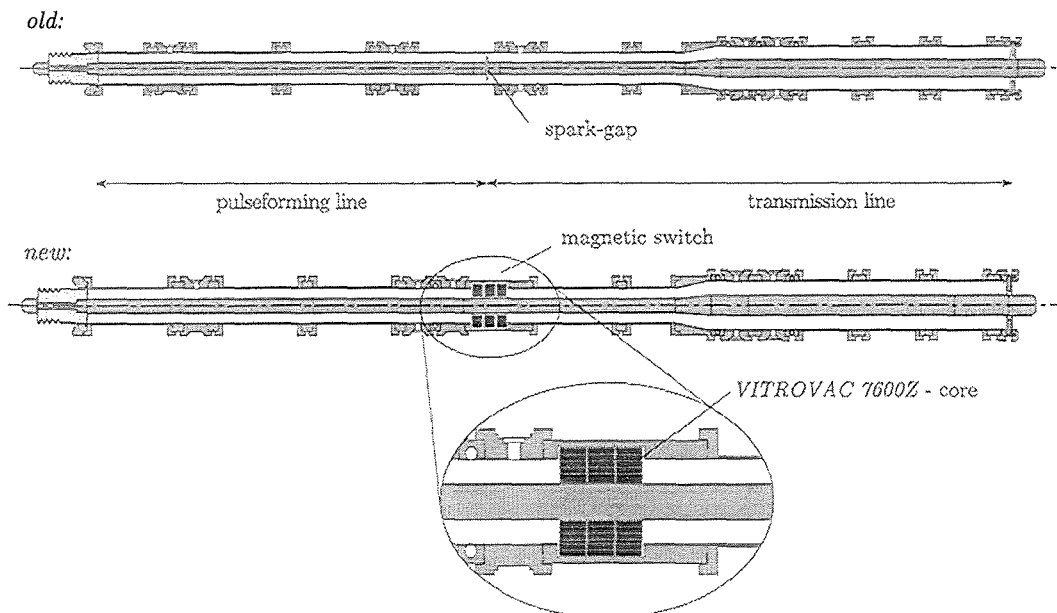
Figure 1 Water-insulated coaxial generator with a spark-gap switch (top) and three VITROVAC cores as a magnetic switch (bottom).

The main difference of the new switching method is its self-triggering mode with dependence on the time-voltage product applied to the cores. The total time-voltage product is $\Delta \Phi = 4,5\,\mathrm{mVs}$.

The comparison of the output waveforms of the two switching methods shows the most significant disadvantage of the magnetic switch. The pulse-shape of the spark-gap switched generator is nearly rectangular without any prepulse opposite to the magnetic switch, Figure 2.

---

[1] *VITROVAC 7600Z*: $(Fe,Co)_{83}(Si,B)_{17}$, Z-hysteresis loop, Vakuumschmelze Hanau, Germany.
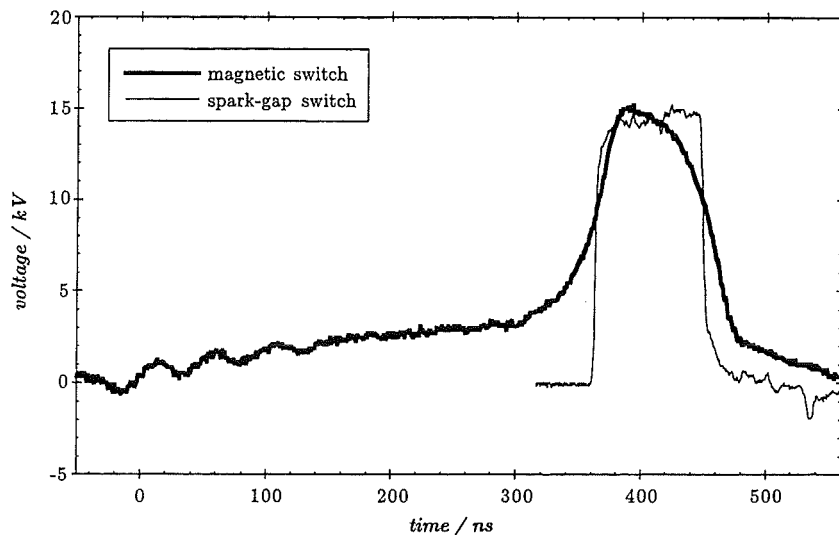
Figure 2   Comparison of the output waveform,
spark-gap switched generator versus magnetic switched generator.

Accepting the worse pulse-shape of the output waveform there is a great advantage using the magnetic switch. No additional supply of the switch is needed to operate. Furthermore, using a special operating point there is no external reset circuit needed. Driving the generator with higher (compared with the optimal energy transfer ratio) input-voltage the surplus of energy is used for automatic resetting the magnetic switch and a high repetition-rate generator can be built.
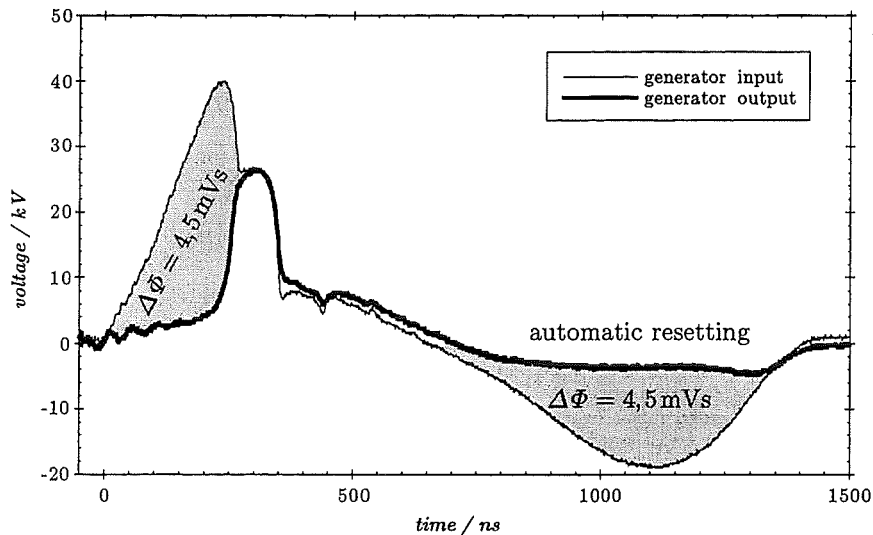
Figure 3   Input- and output waveform of the magnetic switch with the resulting time-voltage product during the switching and the resetting process.

References

[KOE-97a]   KOENIG, S.; Schwab, A.J.:
Rapid Magnetic Flux Change in Amorphous Strip-Wound Cores
11th IEEE Pulsed Power Conference, Baltimore, MD, U.S.A., 1997.

[KOE-97b]   KOENIG, S.:
IEH - Pulsed Power XI
Statusreport of the cooperation between *IEH*, University of Karlsruhe and *INR*, Forschungszentrum Karlsruhe, 1997.

12

Investigation of semiconductor opening switches (SOS) for the construction of compact repetitive high-voltage pulse generators

A. Enguelko, H. Bluhm

Forschungszentrum Karlsruhe
Institut für Neutronenphysik und Reaktortechnik, Postfach 3640, D-76021 Karlsruhe

Abstract

Different types of semiconductor diodes have been examined theoretically for use as an opening switch in high-voltage generators with inductive energy storage. The physics of current interruption in power semiconductor diodes with p^+-s-n^+ structures have been analyzed and a simulation code to model the opening process in these structures has been developed. Existing schemes of high voltage generator design based on semiconductor opening switches as well as their advantages and disadvantages are discussed and possible ways for improvement are pointed out.

Motivation

To develop qualitatively novel high-power pulse generators meeting the requirements for technological applications, the search is continued for new principles of accumulating and switching energy at high-densities.

To generate high-power nanosecond pulses, two major approaches are most commonly used, which differ in the way energy is stored. One of the techniques is based on storing electrical field energy in fast low-inductance capacitors and liquid-dielectric pulse forming lines and subsequently transmitting the energy to a load via closing switch devices. In the second method the energy is stored in the magnetic field of an inductive circuit and opening switches are used to transmit it to the load (Fig. 1).
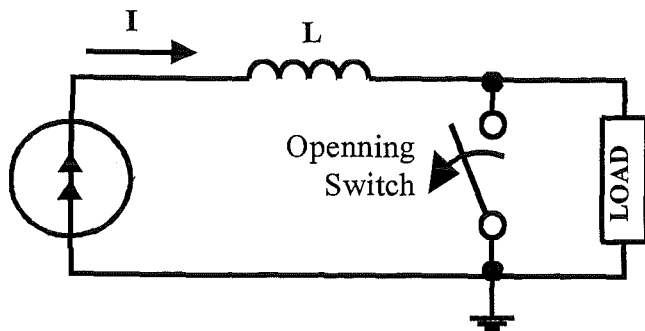
Fig. 1. Principle of inductive generator

The latter method is most promising for the development of high-power pulsed equipment for the following reasons:

- The energy density in an inductor is up to two orders of magnitude higher than in a capacitor. This allows in principle to construct much more compact generators.
- There is no need to use an intermediate store pulse forming element.
- The voltage inside the generator can be much lower then its output voltage. This reduces the electric stress and allows either a smaller setup or in some cases the use of air insulation.

- Parasitic inductance which limits the pulse rise time of capacitive devices can become a generator element. If at some point in the generator an intermediate capacitive store is used cheaper high inductance capacitors can be applied.

The most important component of any inductive generator is the opening switch (OS) which, essentially determines the characteristics of the output pulse. Different types of high power opening switches are presently under investigation. Some of the most promising opening switches are based on solid state technology. In comparison to other types they show the following advantages:

- Long life time (10^{11} pulses were reported /1/)
- Very short opening time.
- High repetition rate capability
- Relative simplicity of use.
- Several devices can be connected in series and/or in parallel to increase the switched current and/or the output voltage. The devices have an internal mechanism which allows the synchronization of their switching action.

There are of course also some disadvantages:

- Switch triggering is impossible
- A special circuit design and parameter calculations are needed to optimize their usage.
- The conduction current of a single device is smaller than that of other systems like plasma opening switches.

This contribution describes the main features of current interruption in solid state opening switches as well as their use in pulse power generators.

Physics of current interruption

There are several types of semiconductor diodes which can be used as opening switches in the generator circuit. All of them occur to have a p^+-s-n^+ structure (low doped n- or p-base in contact with two oppositely doped regions of high dopant concentration). Their most important characteristics are shown in Fig. 2. It is clearly seen that to achieve high densities of interrupted current one has to accept a longer opening time. For the aim of high voltage generation (several hundred kV) the best results reported so far were obtained with the so called Semiconductor Opening Switch (SOS) diodes /2/.

The differences in the achieved operating parameters result from the different mechanism of current interruption and the regimes of operation. All diodes considered here need to be pumped with an electron-hole plasma which will then be removed in the interruption phase. The pumping is normally realized with a short pulse in the

Fig. 2. Maximum current density vs. interruption time for different kinds of power diodes

forward direction. In this case most of the plasma is collected at the boundaries of the base so that it can then be removed fast during the opening process. The plasma concentration in the bulk of the base exceeds the equilibrium concentration by no more then two orders of magnitude.

The process of current interruption in the p-s-n diode can be divided into three parts: a high reverse conductivity stage, a space charge formation stage, and a high resistance stage /3/.

The dynamics of the electron-hole plasma in the stage of high reverse conductivity is schematically shown in Fig. 3. At this stage there is no significant electric field in the diode and the current through the diode is determined by the external circuit. The current flow inside the diode occurs by diffusion. As the diffusion coefficient of electrons is several times larger than that of holes the plasma concentration gradient at the p^+ side of the base (here at the left) must be larger by the same amount to provide an equal current. This means that the plasma always approaches the substrate dopant concentration first at the p^+-s contact. After reaching the dopant concentration the formation of space charge begins.
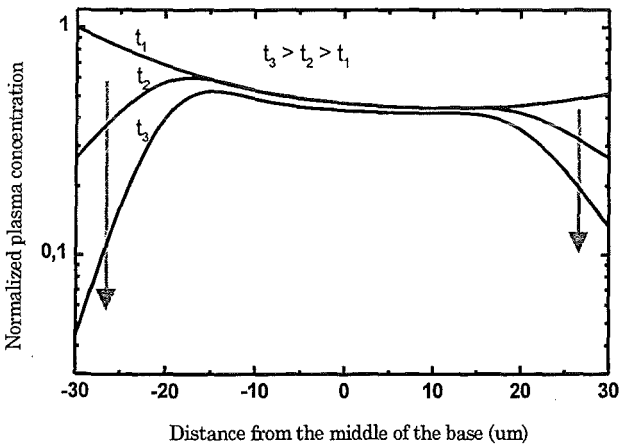
Fig. 3. Dynamics of the plasma concentration at the stage of high reverse conductivity

Fig. 4. Formation of space charge regions in the diode.

At this stage the whole diode can in general be divided into three parts: the base filled with an electron-hole plasma and two space charge regions near the highly doped parts of the structure. These two space charge regions are principally different because one of them (here the left p^+-p -boundary) is partially built by movable charge carriers. The effective voltage growth occurs at the other end of the structure where the space charge consist essentially of the stationary ionized dopants.

With time the interior space charge borders move into the bulk of the base and finally the electron-hole plasma disappears. At this moment no more current can flow through the diode (besides parasitic currents which are neglected), and the diode has reached a stage of high resistance.

Therefore, for complete current interruption the electron-hole plasma has to be removed completely from the base. But for the purpose of pulse generation complete current interruption is not necessary. It can be shown, that at the time, when the load voltage reaches its maximum value, the current density through the diode can be of the order of hundreds of

A/cm^2. The most important features are the maximum current density j flowing during the conduction phase and its time derivative dj/dt, which should be as high as possible. To obtain a high value of the interrupted current density the diode base must be filled with a plasma at the beginning of the interruption process, as it is in the case of SOS diodes.

One has to mention that in the space charge regions the high electric fields lead to efficient impact ionization, which serves as a synchronization mechanism in the case of series-connected diodes /2/.

A theoretical examination provides the following recommendations for the construction of the diodes:

- The recombination time must be long to avoid losses in the pumping direction.
- The doping profile must be smooth (diffusion profile) to provide a wide space charge region and a fast penetration of the electric field into the diode.
- It is theoretically more efficient to use p-type silicon as a substrate, because in this case the shape of switch impedance rise appears to be more favourable for voltage pulse generation /3/.

It should be mentioned here that currently n-type substrates are used for SOS diode construction. This is connected with some technological advantages and with better properties of the n-type silicon with respect to parasitic currents.

Circuit design

As was mentioned above the best results so far were obtained with SOS diodes. Therefore the usage of semiconductor opening switches will be discussed here in a configuration suggested by Mesyats et al /7/.
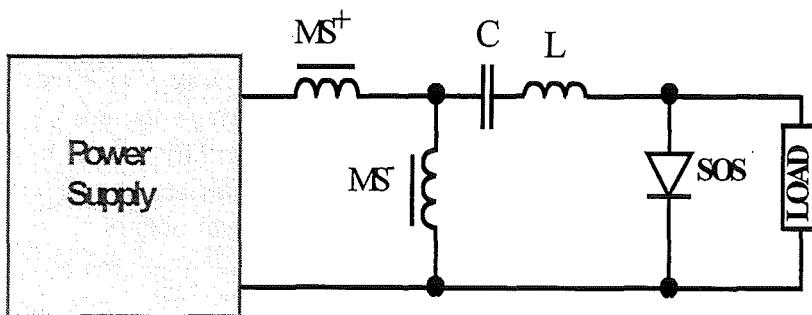
Fig. 5. General scheme of a generator taking advantage from a combination of SOS and magnetic switches

In their design a combination of magnetic closing and SOS opening switches as shown in Fig. 5 has been applied. This scheme operates in the following way: after closing of magnetic switch MS⁺ the current flows through the SOS in the forward direction charging the capacitor C. As the voltage at the capacitor reaches its maximum value the switch MS⁻ closes and the capacitor discharges through the diode in the reverse direction. At the end of the conduction period the SOS opens and a voltage pulse occurs at the load.

In this approach the SOS performs simultaneously the functions of a nanosecond pulse compressor and a voltage multiplier. For this reason, all other things being equal, SOS-based devices are simpler, more reliable and cheaper than traditional nanosecond pulse generators, involving magnetic switches alone, even in the scheme described below which uses capacitors as intermediate energy stores.

As an example of the application of this approach a schematic diagram of the SIBERIA accelerator /2/ is shown in Fig. 6.
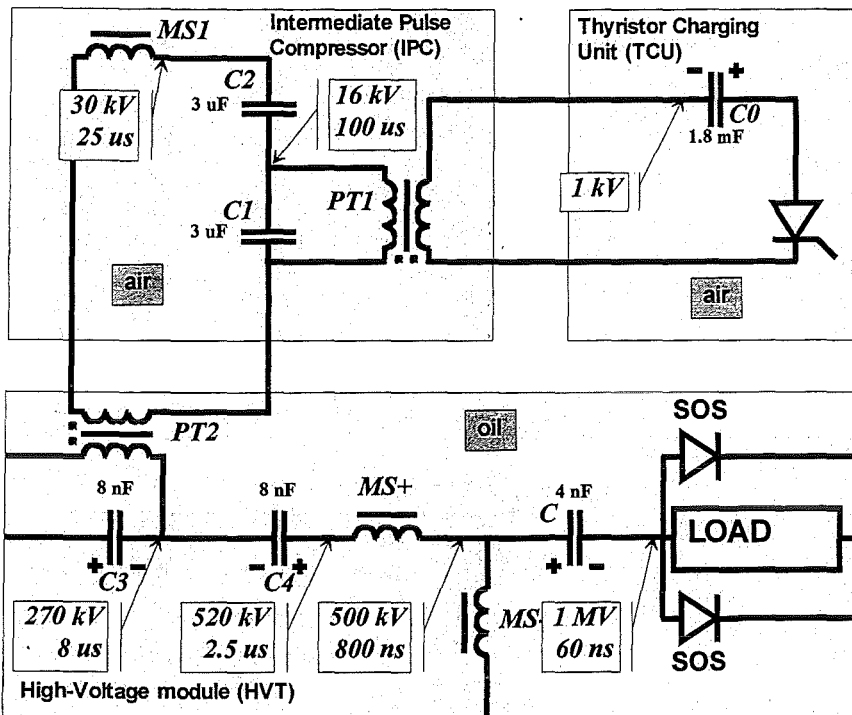
Fig. 6. Diagram of the SIBERIA HV-accelerator with an all solid state switching system

The accelerator consist of three parts: a thyristor charging unit TCU, an intermediate transformation and pulse compression stage IPC, and a high-voltage transformation and compression module HVT. Only the HVT is using oil for high voltage insulation.

At first the capacitor C_0 is charged to 1kV. Discharging the capacitor C_0 through the pulse transformer PT1 the capacitors C_1 and C_2 are charged to 16 kV within 100 μs. The current charging the upper capacitor C_2 begins to reverse the magnetization of MS1 and PT2. When the voltage at C_2 reaches its maximum the magnetic core of transformer PT1 becomes saturated and the capacitor C_1 recharges with inverse voltage. This leads to a voltage rise of 30 kV at MS1 and drives it rapidly into saturation. C_1 and C_2 are then discharged through PT2 and transfer their energy to C_3 and C_4. The charging current of C_4 flows through MS^+ and MS^- and reverses the magnetization of their cores. After saturation of the core of PT2 C_3 discharges to the inverse voltage and the voltage at MS^+ rises to 520 kV within 2.5μs. After closing of MS^+ the SOS diodes are activated, i.e. current flows in the forward direction and the capacitor C is charged. The maximum forward current becomes 3 kA and the activation time is 0.7 μs. After saturation of MS^- the current is reversed and at the end of the SOS conduction period a voltage pulse is generated across the load.

The value of the current flowing through the diodes at this time is 8 kA and the diodes reach impedances of 100 to150 Ohm.

The SOS is composed of 12 parallel columns. Each column consists of 1088 series-connected p^+-n-n^+ diode elements with an area of 0.2 cm^2 and with a base thickness of 0.3 mm each.

A number of less powerful generators based on the same scheme have demonstrated reliable operation.

The main advantages of the described generator scheme with the oscillatory LC pumping circuit are its simplicity and ease of use. This is at the same time an important disadvantage of

the approach because to realize such a solution one needs to store the energy temporarily in a capacitor and the main attraction of inductive generators - high energy density - is not exploited.

Current work

For the better understanding of the processes in the semiconductor opening switch and for the elaboration of the generator circuits one needs a simulation code. Such a code was created and named POSEOSS-I (POwer SEmiconductor Opening Switch Simulator). The code doesn't make any a priori assumptions on the particle concentration distributions in the diode and takes into account all main processes influencing the current interruption such as impact ionization, Auger and Shockley-Read-Hall recombination. The dependence of the electron and hole mobilities on the different scattering mechanisms is taken into account too.

For the proper description of the processes in the semiconductor diode the solution of the following system of equations is necessary:

$$div(\varepsilon \cdot grad(\phi)) = q \cdot (n - p - N_d) \qquad \textit{Poisson equation}$$

$$div(\vec{J}_n) - q \cdot \frac{\partial n}{\partial t} = q \cdot R \qquad \textit{Continuity equation for electrons}$$

$$div(\vec{J}_p) + q \cdot \frac{\partial p}{\partial t} = -q \cdot R \qquad \textit{Continuity equation for holes}$$

$$\vec{J}_n = -q \cdot (\mu_n \cdot n \cdot grad(\phi) - D_n \cdot grad(n)) \qquad \textit{Electron current density}$$

$$\vec{J}_p = -q \cdot (\mu_p \cdot p \cdot grad(\phi) + D_p \cdot grad(p)) \qquad \textit{Hole current density}$$

where

$$R = R(grad(\phi), n, p, N_d) = R^{SRH} + R^{AU} + R^I \qquad \textit{Recombination-generation part}$$

$$\mu_{n,p} = \mu_{n,p}(grad(\phi), n, p, N_d) \qquad \textit{Mobility of electrons and holes}$$

$$D_{n,p} = D_{n,p}(grad(\phi), n, p, N_d) \qquad \textit{Diffusion coefficients}$$

Classical numerical approaches do not provide acceptable solutions of this system of differential equations because of the exponential dependencies of particle concentrations on the potential. Specific methods (such as the one described in /6/) must be involved.

Future work

The future work in this field will be concentrated on the creation of a purely inductive generator and on improvements of the switch properties.

The creation of a purely inductive generator means the development of a scheme with separate pumping and main circuits. Here the investigations on the optimal pumping technology and current amplification in the main circuit will be needed.
The improvement of the switch characteristics such as opening time and current density occurs to be possible also, for example by a suitable deep impurity profile which will lead to the decrease of the recombination time in certain parts of the structure or by combination of materials with different band gaps to trap the plasma near the base boundaries.

References

1. R. G. Focia, E. Schamiloglu, C. B. Feddermann
    "Simple techniques for the generation of high peak power pulses with nanosecond and subnanosecond rise times"
    Rev. Sci. Instrum. 67 (7), p. 2626, (1996).

2. S. N. Rukin, Yu. A. Kotov, G. A. Mesyats
    "Pulsed power accelerator technology based solid statte semiconductor opening switches (SOS)"
    Proc. 10th Intern. Conf. On High Power Particle Beams, 1994, Vol. I, p. 33

3. H. J. Benda, E. Spenke
    "Reverse Recovery Processes in Silicon Power Rectifiers"
    Proceedings of the IEEE, Vol. 55, N 8, p. 1331, (1967)

4. M. J. Chudobiak
    "New Approaches For Designing High Voltage, High Current Silicon Step Recovery Diodes for Pulse Sharpening Applications"
    Thesis, Ottawa-Carleton Institute for Electrical Engineering Department of Electronics Carleton University, 1996

5. V. M. Tuchkevich, I. V. Grehov
    "New principles of switching high-power by semiconductor devices"
    Leningrad: Nauka, 1988

6. Siegfried Selberherr
    "Analysis and Simulation of Semiconductor Devices"
    Springer Verlag, New-York, 1984

7. S. K. Lyubutin, G. A. Mesyats, S. N. Rukin, B. G. Slovikovskii, A. M. Turov
    "New Solid State Opening Switches for Repetitive Pulsed Power Technology"
    Proc. 11th Intern. Conf. On High Power Particle Beams, 1996, Vol. I, p. 135

Conceptional Design of the Pulsed Electron Beam Facility GESA II

G. Mueller, D. Strauss, F. Zimmermann, Forschungszentrum Karlsruhe (INR), (Germany)
V. Engelko, A. Andreev, Efremov Institute of Electrophysical Apparatus, St. Petersburg (Russia)

Abstract

This paper describes the conceptional design of the new pulsed electron beam facility GESA II, which was developed for surface treatment of materials. The outstanding feature of the new facility, in comparison to the existing GESA I facility is the possibility to realize larger melting depths (> 100μm), which are required in many applications. This is achieved by the increase of the electron kinetic energy from 150 keV (GESA I) up to 400 keV (GESA II). The most important parts of the facility like, the high voltage generator and the magnetic system are presented in this article.

Introduction

The application of pulsed high energy electron beams, like those produced by GESA I have shown strong improvements of surface properties like wear resistance, corrosion resistance and hardness of the treated materials. However the melting depth that can be attained with this device is restricted to < 40 μm. For many applications it is necessary to melt thicker surface layers especially in the case when surface grinding and polishing is required after treatment. Sliding machine parts need surface finishing to keep the high abrasion during the initial phase of operation within a tolerable margin. For this purpose it would be necessary to melt the material up to a depth of about 100 μm. Melting depth of up to 100 μm can not be realized with GESA I because its available electron energy is limited to values below 150 keV. The relation between power density and melting depth for different electron energies is given in Fig. 1. The upper field with melting depths >100 μm can only be reached by increasing the electron energy to above 300 keV. Increasing the pulse duration with constant electron energy will shift the curves upwards to higher melting depth. However this would also increase the surface roughness due to boiling. To avoid boiling one could use a low power density, like that applied with DC - electron beams, with very long pulse durations, but in this case the cooling rates would drop down to values for which the desired material modifications can not be realized. The only way out is to increase the electron kinetic energy. Therefore it was decided to build the GESA II facility which is cabable to deliver the required electron energy. This paper describes the new facility.
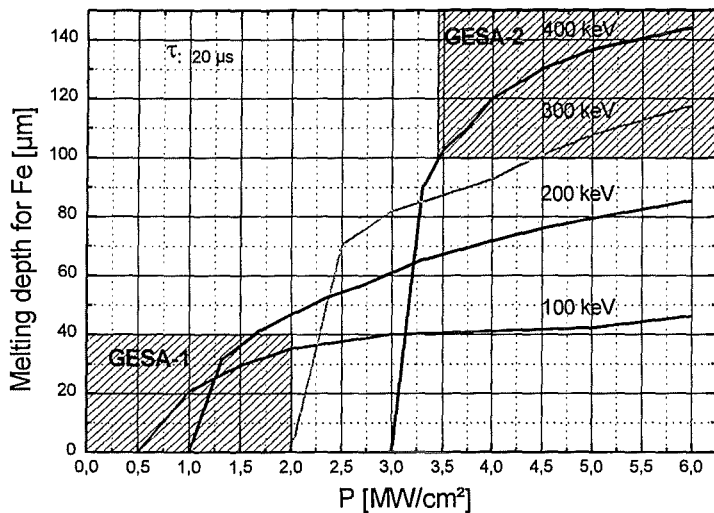
Fig. 1:   Dependence of melting depth for Fe on power density for different electron energies at a pulse duration of 20 μs.

1. Design of the facility

The required parameters of the GESA II facility are listed below:

	GESA II	*existing GESA I*
• accelerating voltage	**300 - 400 kV**	*50 - 150 kV*
• power density	**up to 6 MW/cm^2**	*up to 2 MW/cm^2*
• beam diameter at target	**4 cm**	*5 - 10 cm*
• pulse duration	**20 μs**	*4 - 40 μs*

The facility comprises the following main parts:
electron injector of triode type with a multipoint explosive emission cathode, transport channel, treatment chamber, magnetic system, high-voltage generator, vacuum system, control rack, radiation protection and mechanical support.

The general view of the facility is shown in Fig. 2. The description of the most important parts is presented below.
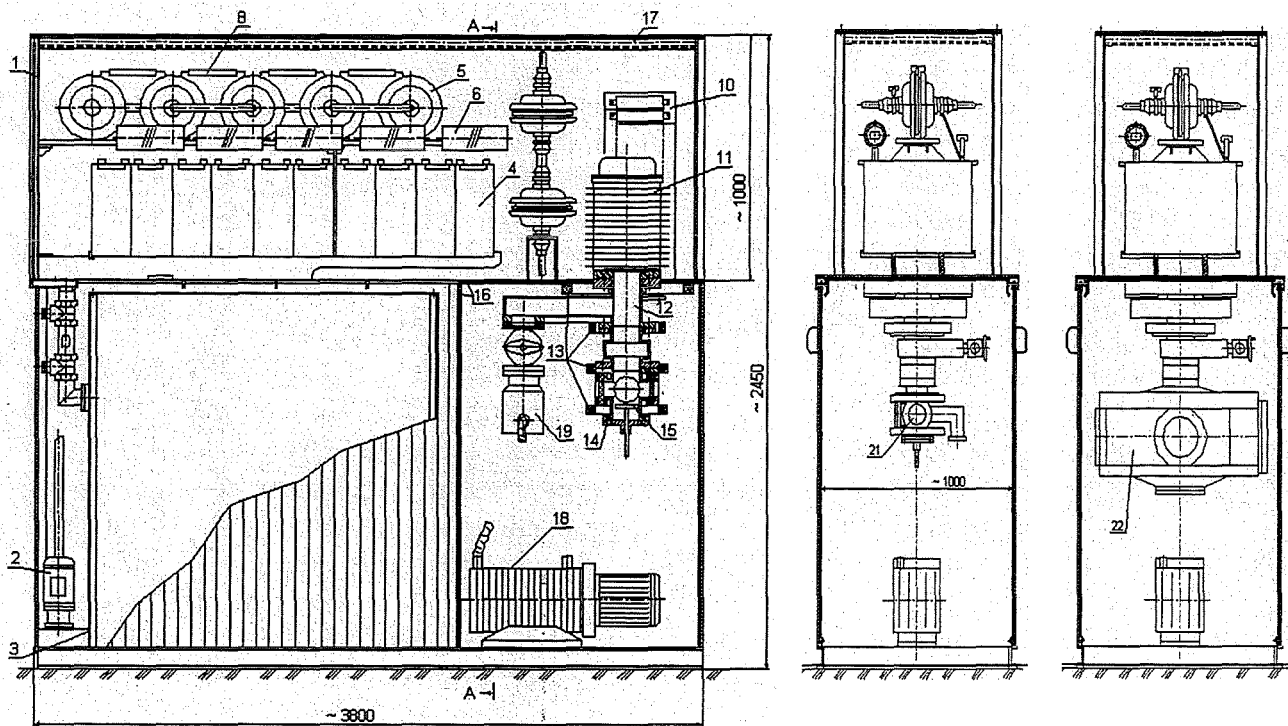
1	Oil tank (MARX)	12	Vacuum valve
2	Oil pump	13	Magnetic coils
3	Oil catching tank	14	Vacuum chamber
4	HV Capacitor	15	Target
5	Spark gap	16	Radiation shield
6	Inductance	17	Oil
7	Cor. resistor	18	Vacuum pump
8	Triggering resistor	19	High-vacuum pump
9	Charging resistor	20	Valve
10	Divider	21	Treatment chamber of GESA II
11	Electron gun and acceleration tube	22	Treatment chamber of GESA I

Fig.2: General view of the GESA II facility

The high voltage generator and the electron injector are positioned in a metallic tank, filled with transformer oil (2.5 m³). The tank dimensions are: length - 3648 mm, height - 1050 mm, width - 904 mm. An additional tank (2004x1410x1004 mm³) is used for removal of the oil from the first one. Both tanks, injector, transport channel, treatment chamber and vacuum system are positioned on a metallic support structure with the dimensions: 3800x1130x1500 mm³. The injector has a height of - 548 mm and an outer diameter of 420 mm. The length of the transport channel is 352 mm and its inner diameter is 150 mm. The over-all dimensions of the GESA II facility are 3800x2180x1500 mm³.

The radiation protection is performed with the help of a rectangular box consisting of one wall (1315x1000 mm²) and six doors (700x1300 mm² - 2 items; 487x1300 mm² - 2 items; 388x1300 mm² - 2 items) filled with lead of 25 mm thickness. Inside the radiation protection the transport channel, the treatment chamber and the vacuum system are placed. The electron injector is shielded by lead plates, positioned inside the oil tank.

To obtain a possibility for treatment of large specimens, the design of the transport channel allows to use the large treatment chamber (⌀=50cm) of the existing GESA I facility.

2. High-voltage generator

The high-voltage generator was built as a Marx configuration consisting of six stages. Each stage contains two capacitors (100 kV, 0.4 μF) and a correcting RL network (24 Ω, 200 μH). Gas filled (nitrogen or air under pressure of 1-2 atm.) three-electrode spark gaps are used as commutators.
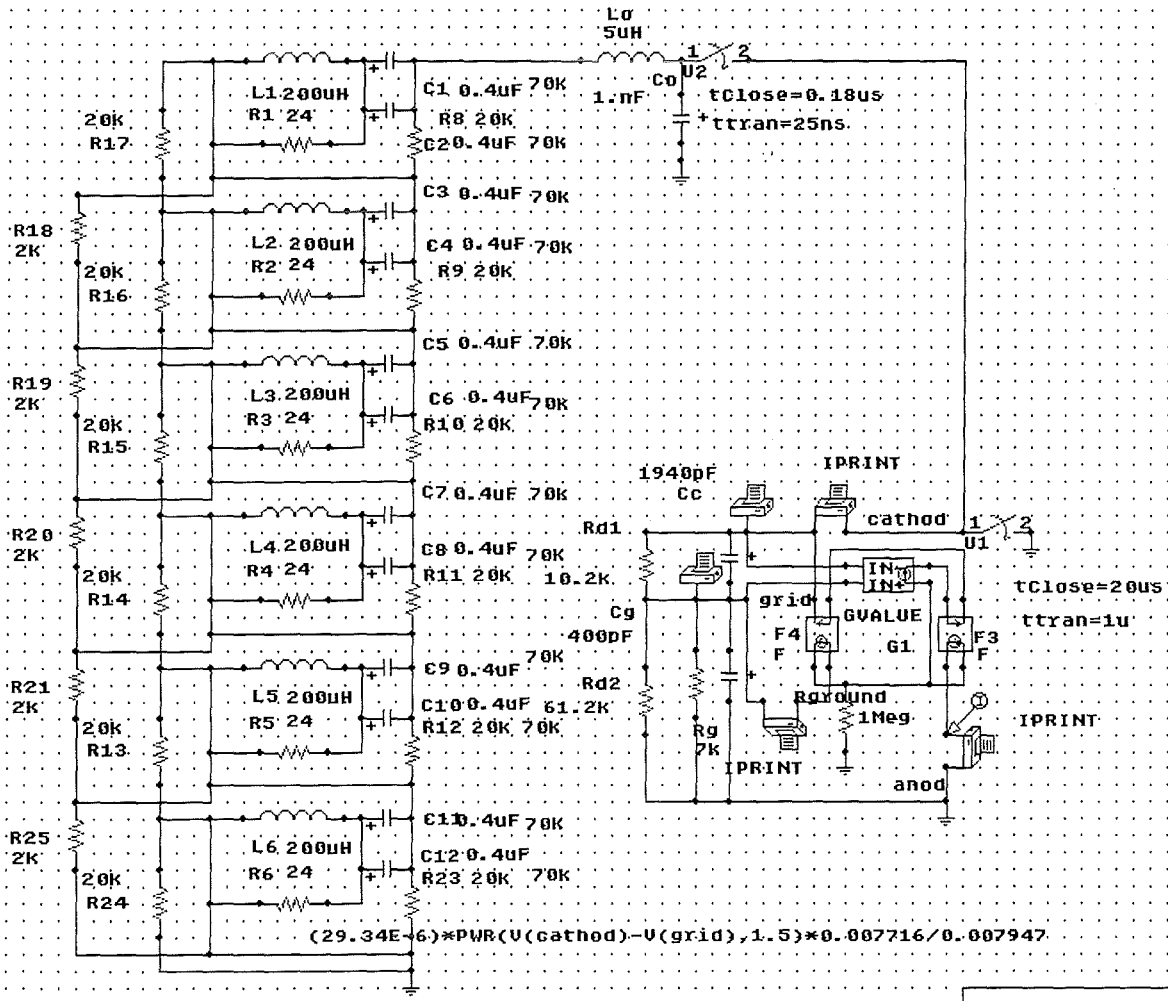
Fig.3: Equivalent electrical scheme of the GESA II facility

The parameters of the high-voltage generator were chosen on the base of numerical simulations, performed with the network analysis program PSpice. The equivalent electrical scheme is shown in Fig.3.

Here L_0=5 μH is the equivalent inductance of the high voltage generator mounting. Capacitor C_0=1 nF decreases the voltage rise time and eliminates the voltage drop after ignition of the electron emission.

The electron injector is presented as a triode. Its current I_0 is determined by the cathode-grid gap in accordance with the Child-Langmuir formulae. Part of this current αI_0 flows to the anode, where α is the grid transparency. The rest flows through the grid and grid resistor R_g. The potential drop of the cathode-grid gap is calculated as U_c-$I_0(1-\alpha)R_g$. Therefore one can change the current by changing the magnitude of R_g.

The resistive divider R_{d1}, R_{d2} and capacitors C_c, and C_g provide the optimal voltage distribution along the insulator of the injector. In Figs.4 and 5 the calculated pulses of the cathode voltage, the grid voltage, the cathode-grid potential drop and the anode and grid currents for R_g=7 kΩ, C_c=1940 pF, C_g=400 pF, α=0.9 are shown. The cathode-grid gap is 5 cm. Charging voltage - 70 kV.
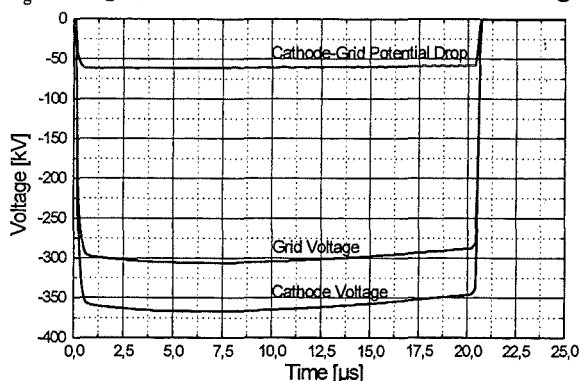
Figure 4:   Time variation of voltage on the cathode and grid of the GESA II facility.
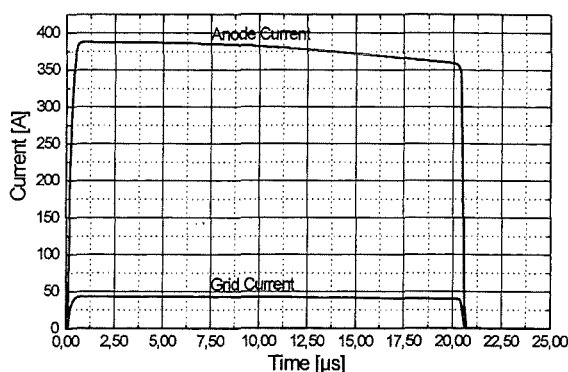
Figure 5:   Time variation of the anode and grid currents of the GESA II facility.

One can see that the cathode potential drops by 4% during 20 μs. The cathode current magnitude is 395-380 A. In this case the current density at the target has the required value when the facility is operating with the treatment chamber of GESA I. If the GESA II chamber is used the needed current density can be obtained with the cathode current of ~ 250 A. To get such a current the grid resistor magnitude should be equivalent to 12 kΩ and C_g=275 pF. Results of calculations are shown in Figs.6 and 7.
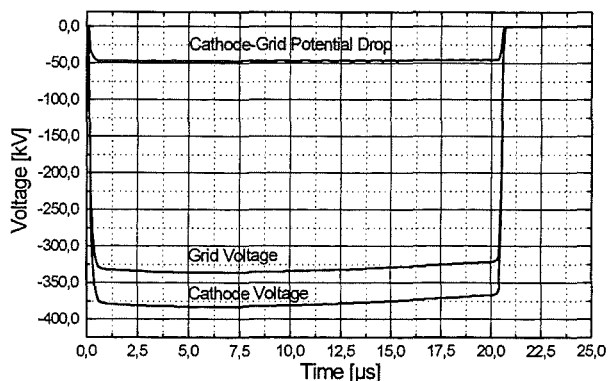
Figure 6:   Time variation of cathode and grid voltage of the GESA II facility with the own chamber.
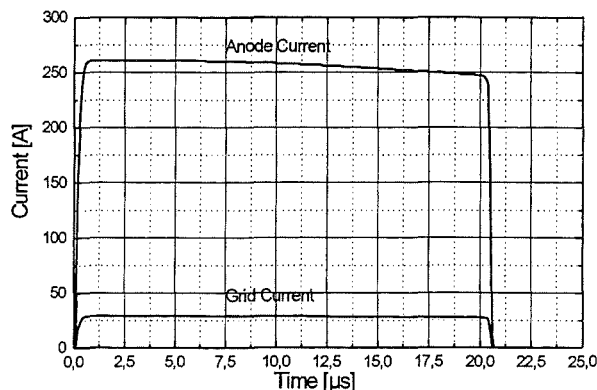
Figure 7:   Time variation of anode and grid currents of GESA II facility with the own chamber

The electric field strength in the cathode-grid gap is 11 kV/cm. This is sufficient for homogeneous excitation of an electron emission on the multipoint explosive emission cathode.

3. Numerical simulation of electron beam formation

Numerical simulations of the electron beam formation were carried out to optimise the design of the electron injector and the distribution of the electric and magnetic fields. Simulations were done with the help of the code "POISSON-2". Two versions of the treatment chamber were considered: the own chamber of the GESA II facility and the treatment chamber of the GESA I facility. Simulations show that the required electron beam parameters can be achieved under the following conditions described in table 1:

Table 1

Parameters	Treatment chamber of GESA II	Treatment chamber of GESA I
diameter of the cathode	21 cm	21 cm
cathode area	350 cm^2	350 cm^2
radius of the cathode curvature	60 cm	60 cm
radius of the grid curvature	55 cm	55 cm
voltage on the cathode - grid gap	48 kV	60 kV
cathode - anode gap	5 cm	5 cm
grid resistor	12 kΩ	7 kΩ
grid capacity	275 pF	400 pF
grid transparency	90%	90%
magnetic field at the cathode	10,7 mT	10,3 mT
magnetic field at the target	280,0 mT	160,0 mT
diameter of the transport channel	15 cm	15 cm
beam diameter	4 cm	5.4 cm
current density at the target	18 A/cm^2	15 A/cm^2
beam current	250 A	380 A

In Fig. 8 and 9 the electron beam trajectories for the parameter set of table 1 and for both versions of the treatment chamber are given. The simulations show that the current density at the target increases with radius and increases faster when the treatment chamber of GESA I is used (Fig. 10).
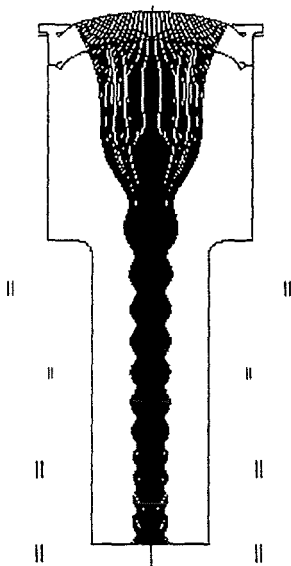
Fig.8: Electron trajectories in the GESA II facility with its own treatment chamber
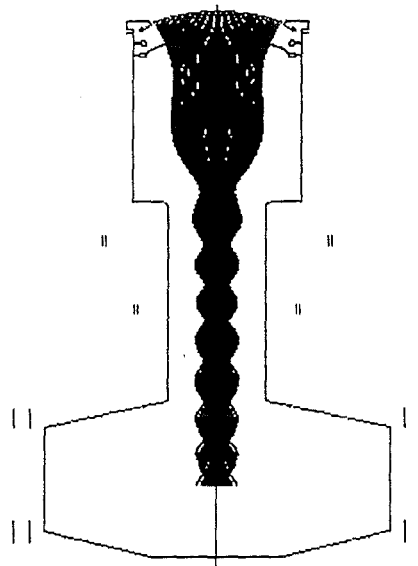
Fig.9: Electron trajectories in the GESA II facility using the treatment chamber of GESA I facility
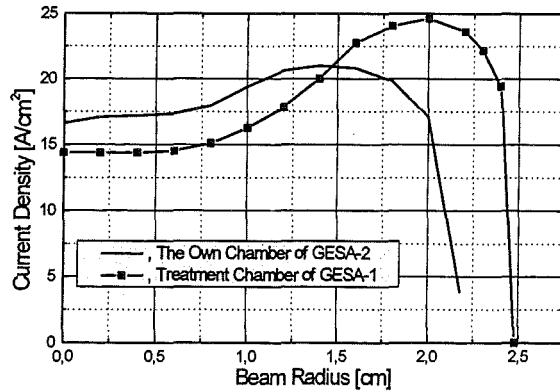
Fig. 10: Current density distributions at a target in the treatment chamber
of the GESA II facility for two versions of the treatment chamber design.

4. Magnetic system

The magnetic system should meet the following requirements:

1. The magnetic field induction at the cathode has to have the minimum value, which is sufficient to provide electron beam formation (usually 5-10 mT).

2. The magnetic field distribution has to support the formation of an electron beam with a sufficiently small angular spread of the electrons and the beam transport without loss of electrons at the anode and in the transport channel.

3. The magnetic field distribution has to provide the compression of the electron beam without reflection of electrons (virtual cathode).

4. The magnetic system has to be variable to provide the possibility to change the beam diameter at the target.

The magnetic system of the GESA II facility was made, of four coils, the parameters of which are given in Table 2. The coil pairs A, B and C, D are powered from separate capacitor banks. The parameters of the banks depend on the treatment chamber used.

Table 2

Parameters of magnetic coils	The first magnetic subsystem		Treatment chamber of GESA I		Treatment chamber of GESA II	
	A	B	C	D	C	D
Inner radius, cm	18.0	13.0	14.0	14.0	30.0	30.0
External radius, cm	19.3	13.7	15.3	15.3	34.0	34.0
Half-width of a coil, cm	1.2	0.9	1.5	1.5	1.65	2.20
Layout of a coil along an axis, cm	47.0	62.0	79.0	94.0	86.0	111.0
Number of wings	40	15	50	50	30	40
Type of a wire	PSD 7.5 mm^2	PSD 7.5 mm^2	PSD 7.5 mm^2	PSD 7.5 mm^2	PSD 35.0 mm^2	PSD 35.0 mm^2
Way of winding, N_ZxN_R	4x10	3x5	5x10	5x10		
Resistance, Ω	0.1116	0.0299	0.1095	0.1095	0.0296	0.0394
Inductance, mH	1.0807	0.1097	1.2200	1.2200	1.0222	1.7607
Inductance with tacking into account of mutual induction, mH	1.1965	0.2050	1.4830	1.4269	1.3645	2.0564

26

4.1 Treatment chamber of GESA II.

When the treatment chamber of the GESA II facility is used, the parameters of the banks are the following.

Table 3

	Type of capacitors	Number of capacitors in the bank	Maximum charge voltage, V	Capacity of the battery, mF
First magnetic sub-system	1000 μF, 300 V	60	600.0	15.0
Second magnetic subsystem	1000 μF, 300 V	60	600.0	15.0

In order to operate with a charging voltage at 600 V two capacitors are connected in series. The discharge currents through the first and second magnetic sub-systems are shown in Fig.11 for charging voltages of 500 V. The distribution of the magnetic field induction and the variation of the beam radius along the facility axis are shown in Fig.12. The beam radius was calculated on the basis of magnetic flux conservation within the beam cross-section.
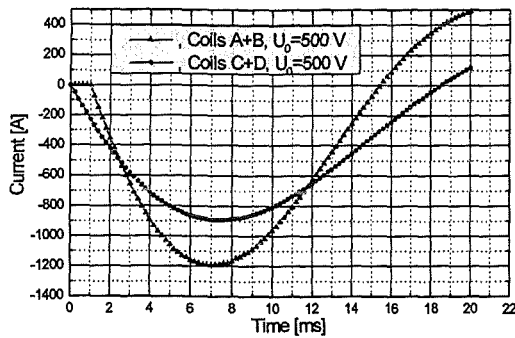
Fig.11:Discharge currents in the magnetic coils of the GESA II facility with its own treatment chamber.
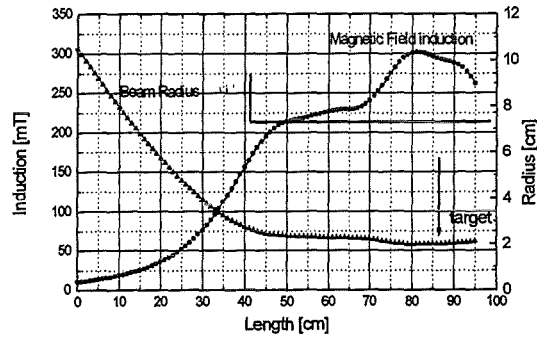
Fig.12: Distribution of magnetic field induction and beam radius along the facility axis when I_{A+B}=1200 A and I_{C+D}=900 A (7 us of capacitor banks discharge).

In this case, the magnetic field induction at the cathode and at the target are 10,7 mT and 280 mT respectively. The diameter of the beam at the target is 4 cm, the compression coefficient is 26. It is the maximum possible compression coefficient with this configuration of the magnetic system.

There is a possibility to change the compression coefficient by changing the charging voltage of the capacitor bank which supplies the second magnetic sub-system. The distributions of the magnetic field induction and the appropriate beam radii for different charging voltage of the second bank capacitors and hence for different discharge currents in the magnetic coils are shown in Figs.13 and 14.
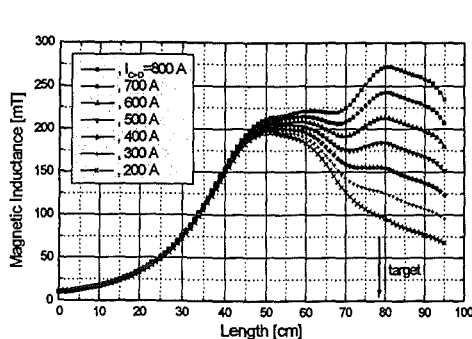
Fig.13:Magnetic field distribution for different discharge currents in the magnetic coils along the GESA II facility axis.
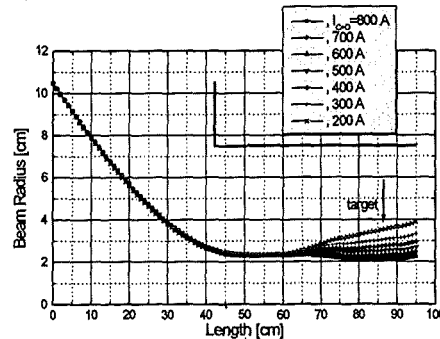
Fig.14: Beam radius variance along the facility axis for different magnetic field distributions shown in Figure 13.

27

4.2 Treatment chamber of GESA I.

When the treatment chamber of the GESA I facility is used, the parameters of the banks are the following.

Table 4

	Type of capacitors	Number of capacitors in the bank	Maximum charge voltage, V	Capacity of the bank, mF
First magnetic subsystem	1000 μF, 300 V	6	600.0	3.0
Second magnetic subsystem	1000 μF, 300 V	114	600.0	27.0

The discharge currents through magnetic coils A+B and C+D are shown in Fig.15 and the distribution of the magnetic field induction and the beam radius are shown in Fig.16.
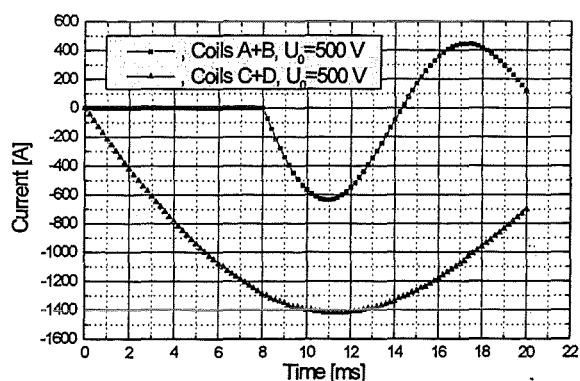
Fig.15: Discharge currents in the magnetic coils of the GESA II facility using the treatment chamber of GESA I. Charging voltage is 500 V.
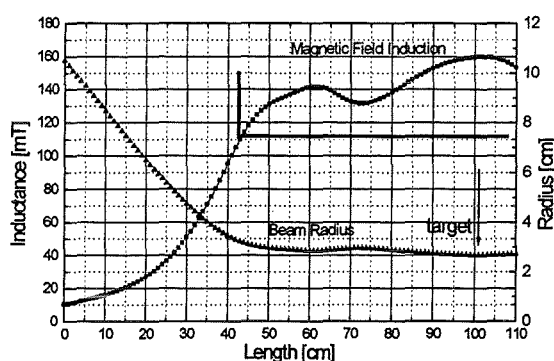
Fig.16: Distribution of magnetic field induction and beam radius 1ms after activation of the magnetic coils..

In this case, the magnetic field induction at the cathode and at the target are 10,3 mT and 160 mT respectively. The diameter of the beam at the target is 5.4 cm, the compression coefficient is 16.

5. Outlook

The GESA II facility is under construction and will go into operation at the end of 1998.

28

3 Production and focussing of high power light ion beams (diode physics)

TIME DEPENDENT FIELD AND PARTICLE DENSITY MEASUREMENTS IN THE ACCELERATION GAP OF A HIGH POWER ION DIODE

V. Licht, H. Bluhm, P. Hoppé, S.J. Yoo

Forschungszentrum Karlsruhe

Institut für Neutronenphysik und Reaktortechnik, Postfach 3640, D-76021 Karlsruhe

Abstract

Using a newly developed two-wavelength dispersion interferometer system of exceptionally high sensitivity we have been able to measure for the first time the electron density distribution inside a high power ion diode. The assumption of a flat electron density distribution across the gap -often made in theoretical models- is compatible with the present observations up to peak diode power. Afterwards a rapid increase of the electron density is seen. Combining these results with spectroscopic measurements in the anode plasma we conclude that the diamagnetic field penetration into the anode plasma can lead to its fast acceleration after peak power, affect the electron density increase in the gap, and the diode impedance collapse associated with it.

Introduction

Until today intense light ion beam production by single or two-stage acceleration in high power magnetically insulated diodes suffers from large beam divergence, ion energy spread, and the inability to adequately control the diode impedance. The latter until now prevents the possibility to take advantage from beam bunching by ramping the driving voltage pulse. Both, the light ion beam quality and the diode impedance history are mainly affected by the properties and the evolution of the anode plasma and of the electron cloud filling the diode gap.

Detailed measurements of particle densities, temperatures, composition, and field distributions inside the anode plasma as well as close to its surface have been carried out in recent years by a number of groups /1-4 / and improved our knowledge of the physical processes governing the operation of these devices. However, it seems difficult to generalise these results because some have been obtained with special types of passive ion sources, while others were achieved with rather low power diodes. In addition, a direct measurement of the electron density inside the diode gap was lacking until today.

Here we report on results obtained for the magnetically insulated high power ion diode used on the 1.7 MV, 1.5 TW pulse generator KALIF. In this diode the ion source is produced actively by initiating a sliding discharge in a hydrogen gas layer that is desorbed from a Ti-reservoir. Details of the ion diode and of the ion source can be found elsewhere / 5,6 /.

Using spectroscopic measurements we have determined the particle densities and temperatures as well as the magnetic field penetration into the plasma. The electron density inside the diode gap was determined with the help of a newly developed two-wavelength dispersion interferometer of exceptionally high sensitivity.

Diagnostic tools

Since the set-up of the spectroscopic diagnostic has been described in a previous annual report we refer to that publication for any details /7/. The line of sight of the spectrometer was aiming parallel to the anode. Using a lens with a large focal length (800 mm) a spatial resolution of up to 0.2mm could be realised. Depending on the requirements the spectral resolution was adjusted between 0.2 and 0.5 Å. The temporal resolution of 5-10 ns was mainly limited by the necessity to reduce the statistical error.

Since the interferometer was redesigned after the 1995 annual report we shall outline its main characteristics here. We have chosen a two-wavelength dispersion interferometer because it is a relatively simple and robust system well suited for the hostile environment of a high power
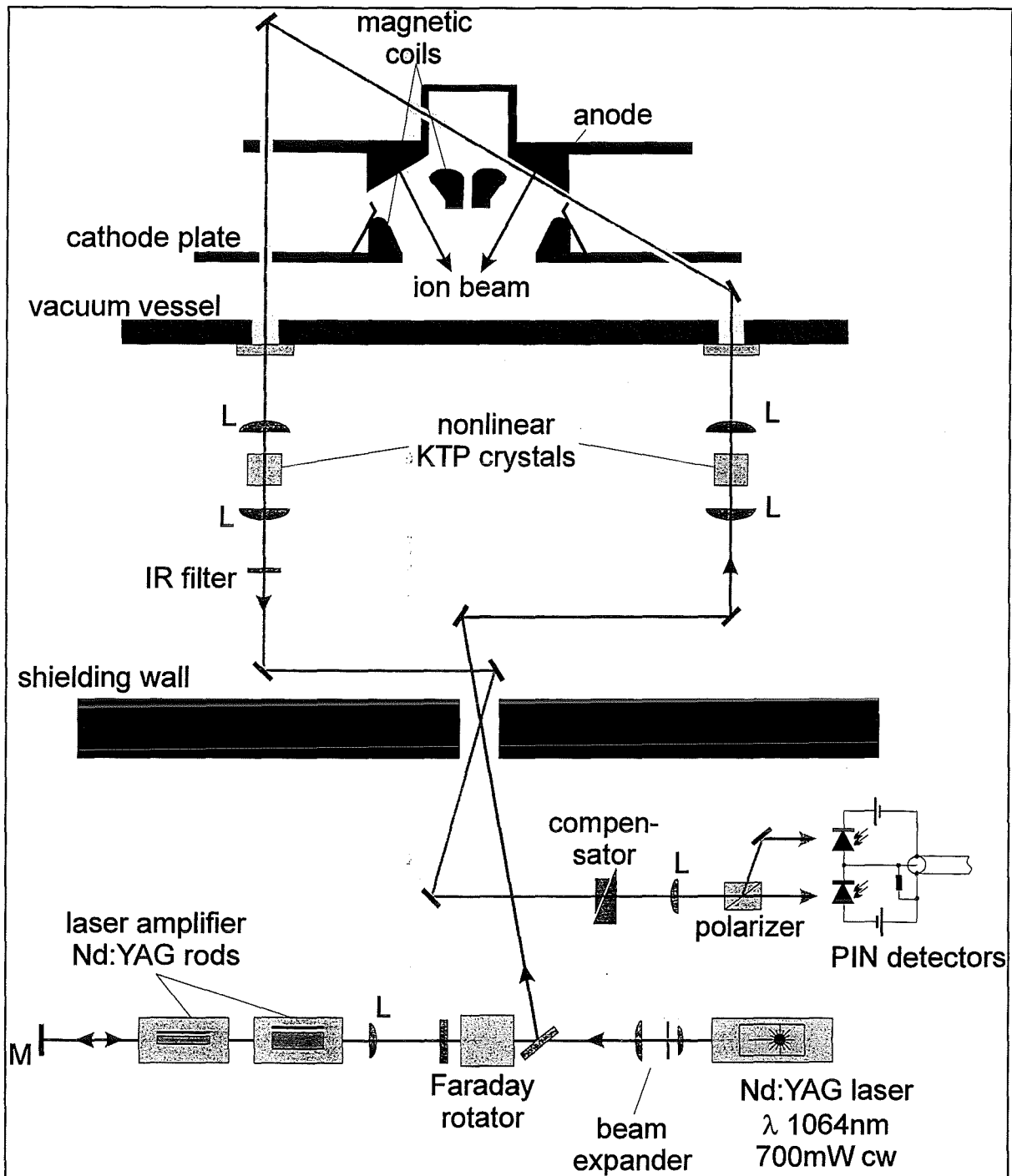
Fig. 1 Set-up of two-wavelength dispersion interferometer on KALIF

generator and diode. The arrangement of the interferometer is presented in Fig. 1. It starts with a single mode, single frequency 700 mW cw Nd:YAG ring laser oscillating at the fundamental wavelength of 1064 nm. To increase its intensity the laser beam is send twice through two flashlamp-pumped Nd:YAG amplifier rods and then focused into a KTP crystal for frequency doubling. Both, the nontransformed fundamental wave and its second harmonic are transmitted through the electron cloud in the diode gap. After exiting from the diode vacuum chamber a fraction of the remaining fundamental wave is frequency doubled too and its residual part is eliminated with an infrared filter. Due to the wavelength dependence of the refraction index in the electron fluid both beams have experienced different phase shifts which are conserved during frequency doubling. The KTP crystals are arranged such that the
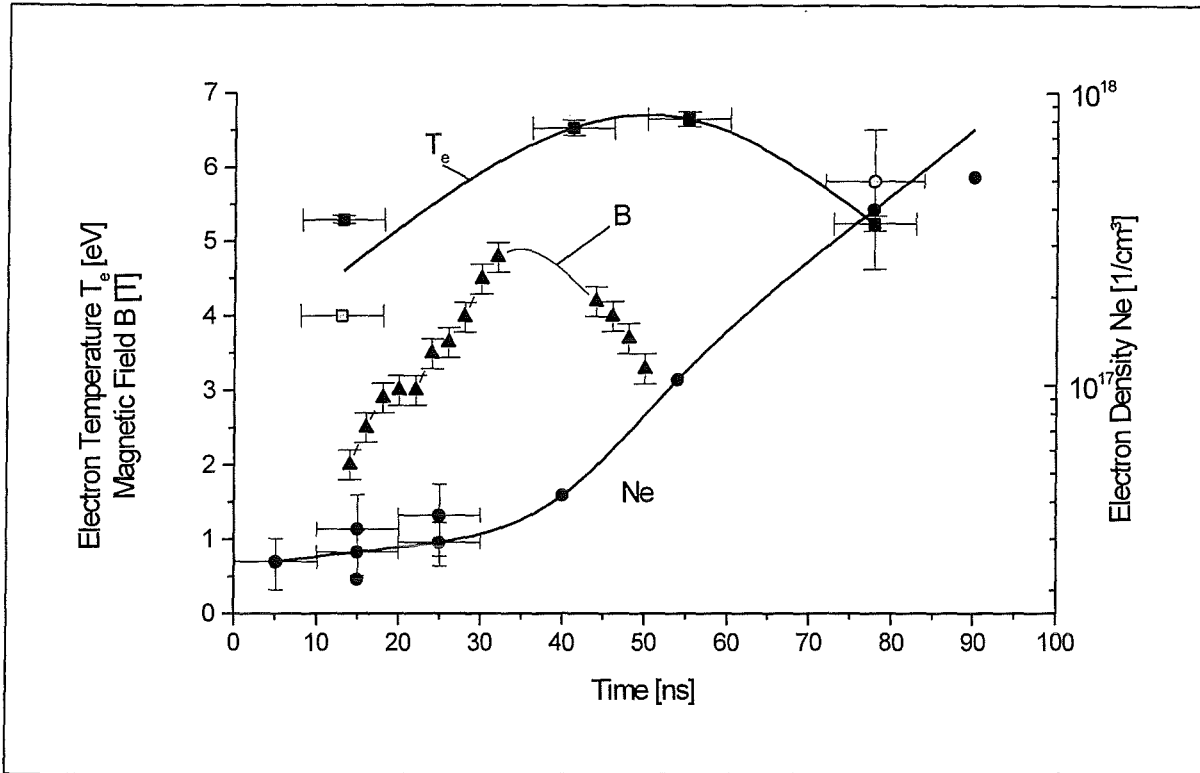
Fig. 2 Electron temperature (squares), electron density (circles), and B-field (triangles) in the anode plasma

green beams are produced with polarisation vectors perpendicular to each other. Using a beam splitting polarizer the beams are divided into two components with parallel polarisation vectors and two components with antiparallel polarisation vectors. Each of these beam pairs can interfere and their interference pattern are imaged onto two PIN photodiodes arranged in a compensating bridge circuit. With the help of a Babinet compensator the initial phase shift is adjusted to 90° such that the difference signal of the photodiodes becomes zero prior to the experiment. At this adjustment the system has its highest sensitivity and is largely independent of laser intensity fluctuations. Before the beams are brought to interference they have passed through the same optical media. Slow changes in the optical path between the first and the second KTP-crystal do not effect the results because they can be recorded immediately before the experiment.

To check the stability and the sensitivity of the interferometer we have measured the phase shift by transmitting the beams through a vacuum chamber in which the air pressure was varied between 0 and 10^5 Pa. These measurements showed excellent stability and linearity. During the period of data collecting, which lasted 45 minutes, a drifting of the interferometer was not observed. With the present set-up we are able to measure electron line densities below 10^{13} cm^{-2} corresponding to a fringe shift of 8* 10^{-5}.

Results

In order not to affect the normal operation of the diode only spectral lines from components naturally occurring in the anode plasma were used to infer the anode plasma properties.

During the first 30 ns after beginning of the diode voltage the Stark broadened H_α and C II (6578 Å) lines were exploited to derive the electron density as a function of time. Later in the pulse the refractive index gradient diagnostic described in Ref. /8/ was applied and supplemented by evaluating the Stark-broadening of the C IV (5801.3 Å) line. The electron density obtained at a distance of 0.25 mm from the anode surface is shown in Fig. 2. After a period of

about 30-40 ns, during which the electron density stagnates, it starts to rise by one order of magnitude before the end of the pulse.

The electron temperature was derived by evaluating the ratio of the C IV (5801.3 Å) and the C III (5696 Å) lines with the help of the stationary collisional-radiative-code NLTERT /9/. The use of a stationary code for this evaluation is justified by the short relaxation times for the carbon levels and by the fact that the carbon density in the plasma does not change during the pulse because it originates mainly from adsorbates at the Pd surface layer which covers the Ti hydrogen reservoir. These adsorbates are released at the beginning of the pulse. As shown in Fig. 2 the electron temperature starts between 4 and 5 eV, reaches a maximum at 50 ns into the pulse and than drops below 5 eV again.

The magnetic field inside the anode plasma was deduced from the Zeeman splitting of C III (4647.4 Å) and C IV (5801.3 Å) lines. Since the Doppler broadening affects the line shapes different trials for the ion temperature were used to reproduce the measured line shape. Fortunately the width of the lines is mainly determined by the magnetic field strength and not much influenced by the Doppler effect. However the depth of the valley in the centre of the split line strongly depends on the ion temperature and therefore can be used to determine it. It was found that the C IV ion temperature was around 50 eV and thus much larger than the electron temperature, a phenomenon that had also been found by other groups for passive flashover ion sources /10/. In Fig. 2 we also display the development of the magnetic field inside the anode plasma layer as a function of time. Initially the measured field is smaller than
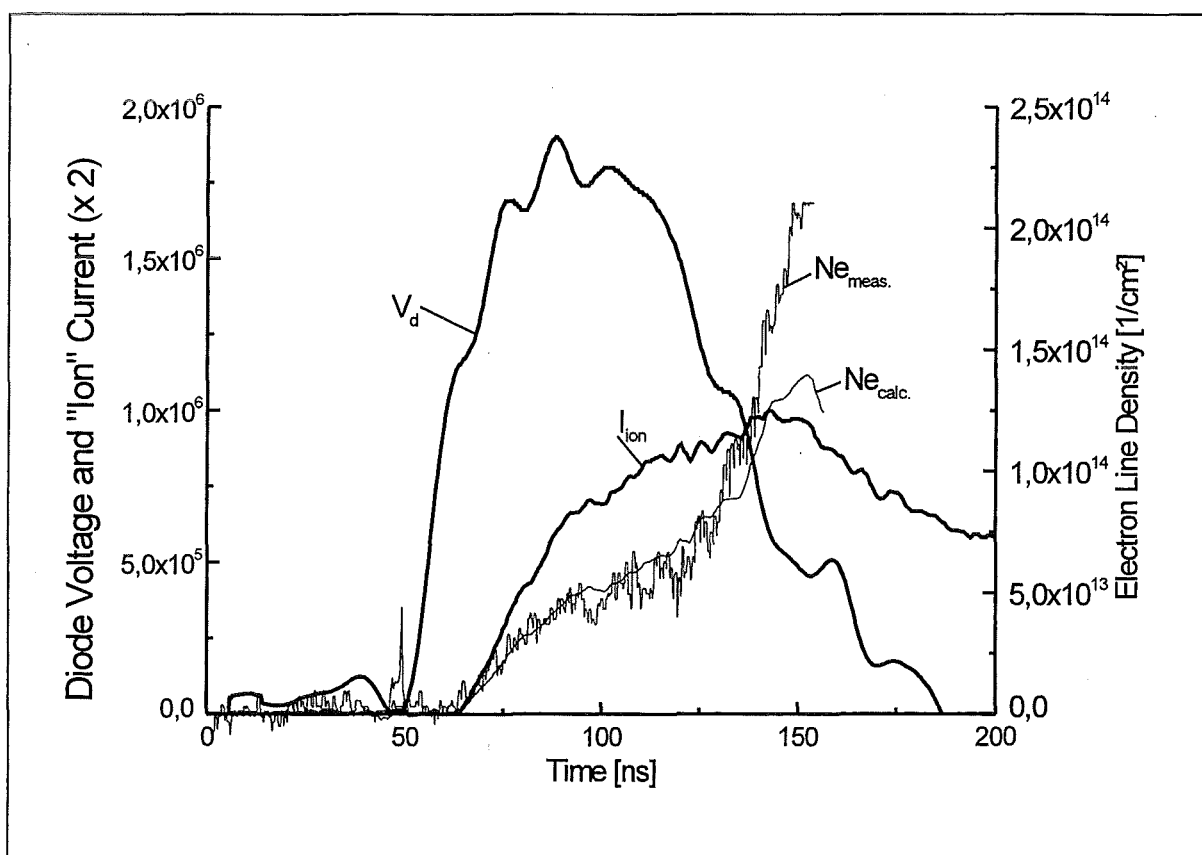
Fig. 3 Measured and calculated electron densities 3 mm from the anode, diode voltage, and ion current

the applied field of 3 T. This can be explained by the early expansion of the high density plasma with frozen-in magnetic field lines. As the plasma expansion stops the field rediffuses and because of the rising diamagnetic field in the diode gap surmounts the applied field. For

the KALIF-diode the maximum observed field was around 5 T. The consequences of this diffusion of the diamagnetic field into the plasma will be discussed below.

The electron line density measured at a distance of 3 mm from the anode surface is plotted in Fig. 3 together with the diode voltage and the "ion" current. The electron density starts to rise simultaneously with the ion current and reaches a plateau at $4 \cdot 10^{13}$ cm^{-2} which lasts for 20-30 ns and then - as the diode voltage begins to drop - continues to rise to much higher values. This general behaviour is found for all distances from the anode. Within our temporal resolution of 1ns the electron density increases simultaneously at all locations in the gap and achieves everywhere the same plateau value. At distances less than 2 mm from the anode surface the electron density exceeds the plateau value at first but after 10-20 ns decays to the same level.

Summarising the results we can say that 1.) significant ion current does not flow before an electron cloud occurs in the diode gap, 2.) the electron cloud occurs simultaneously at all positions in the gap, 3.) for a period of 40-50 ns the electron density distribution is flat, and 4.) at the time when the diode voltage decreases the electron density rises at all positions in the gap, although stronger at locations close to the anode and cathode surfaces (Fig. 4)
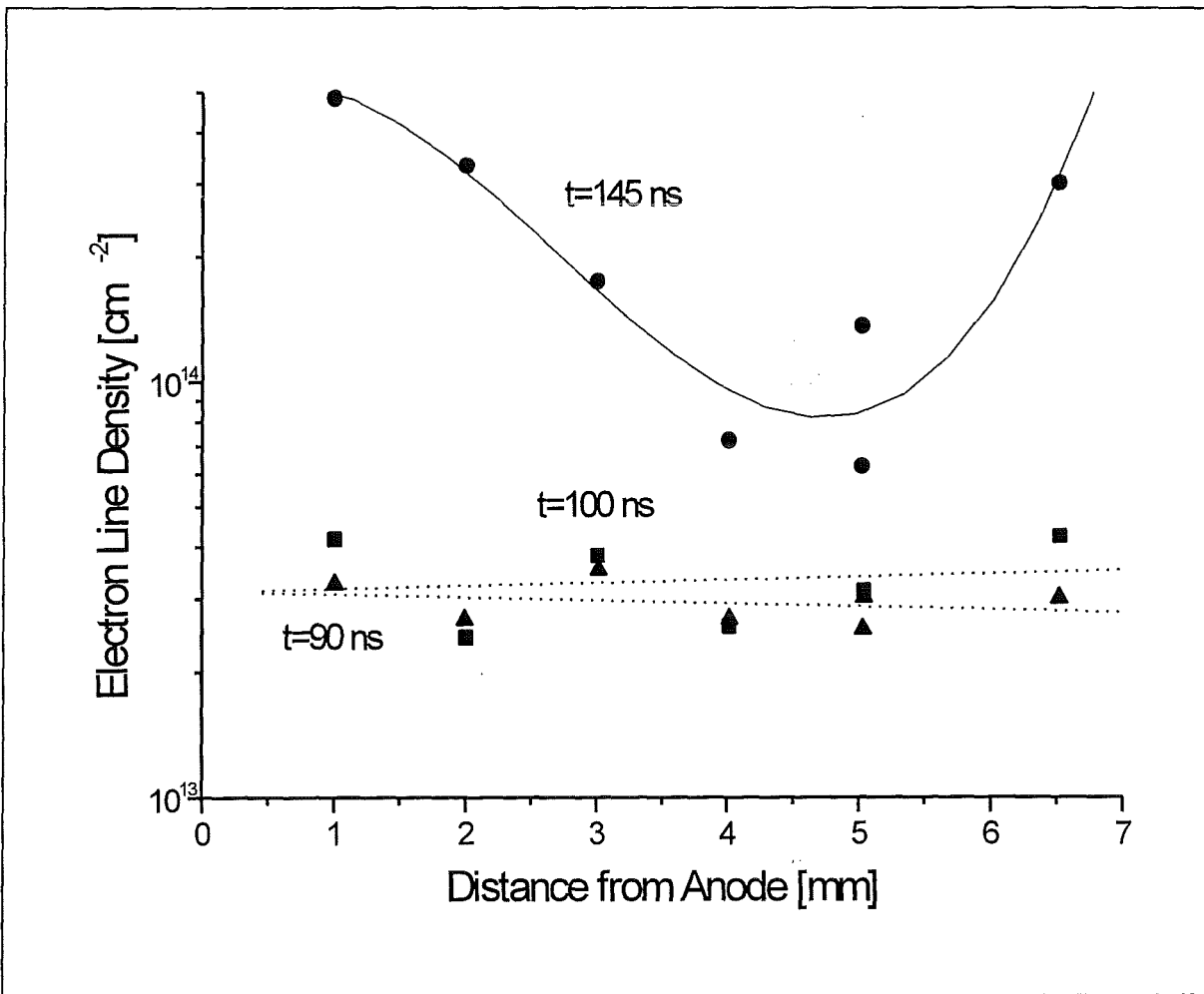
Fig. 4 Electron density distribution in the diode gap at different times into the pulse

Conclusions

It has been discussed previously /11/ that the diffusion of the diamagnetic field into the anode plasma can create strong heating, the magnitude of the electron temperature rise depending on the value of the plasma conductivity. It has been argued that, due to the high electron drift velocity, instabilities occur that increase the collision frequency and therefore reduce the plasma conductivity by up to a factor of 10 below the Spitzer value. Taking this value and assuming a mean plasma density of $5 \cdot 10^{16}$ cm^{-3} in a 0.5 mm thick plasma layer we obtain that about 225 eV of energy have been deposited per particle during the rising part of the diamagnetic field. Obviously there must be a heat loss mechanism to the substrate because we observe a much smaller electron temperature rise but a strong increase of particle density in the plasma, which, at the end of the pulse, reaches a value of $5 \cdot 10^{17}$ cm^{-3}. Taking this value and accounting for the ionisation energy of 13.6 eV the observed electron temperature of 5 eV at that time becomes comparable with the available energy. The observed large flux of hydrogen from the reservoir is supposedly also responsible for the ion energy spread reported previously/7/.

Perhaps an even more important effect of the diamagnetic field penetration into the plasma is the fact that it leads to a fast acceleration of the plasma as soon as the diamagnetic field drops due to a simultaneous decrease of ion current density and diode voltage. In this case the plasma is no longer magnetically confined but instead accelerated by both the thermodynamic and the magnetic pressure which act in the same direction. This can be seen from the magnetohydrodynamic equation of motion:

$$nM\frac{du}{dt} = -grad\frac{B^2}{2\mu_0} - grad(p_i + p_e)$$

For the densities and temperatures observed the magnetic field pressure is more important than the particle pressure. Assuming that the magnetic pressure gradient is constant in the plasma front layer we can also expect that the lower density zones will be accelerated fastest. It is presumably this mechanism that is responsible for the rapid impedance collaps generally observed with high power diodes after peak power. Since similar mechanism of acceleration can also occur in the cathode plasma the diode gap closes fastest at the cathode edge.

The described general picture is supported by the electron density measurements where a sudden rise of the electron density coinciding with the diode voltage and ion current density decay (inferred from Faraday-cup measurements not shown here) was observed. Also late in the pulse the measured electron density distribution resembles the expected profile of increasing densities towards the electrodes. A surprising result was the flat electron density distribution in the gap at least until the maximum diode voltage. This observation enables us to use the diode theory described by M. Desjarlais /12/ for the saturated case to derive further conclusions on the diode operation. To improve our confidence we can use the functional dependence of the electron density on the ion current density derived in /12/ to calculate the electron density from the electrical signals and compare it with the directly measured electron density. As shown in Fig.3 this leads to excellent agreement at least until the final increase of the density occurs. Now exploiting other predictions of the model we can determine the effective gap width and the entrapped magnetic flux using the measured electron density as a function of time. The results (Fig. 5) confirm that very rapidly about half of the initial flux is lost leading to a much weaker magnetic insulation than expected.

Summarising we can conclude that stable diode operation requires a small diamagnetic effect on the plasma. This can either be achieved by producing highly conductive electrode plasmas or by reducing the diamagnetic field. The latter means a lower ion current density but unfortunately it also favours a small ion mass and a small accelerating voltage.
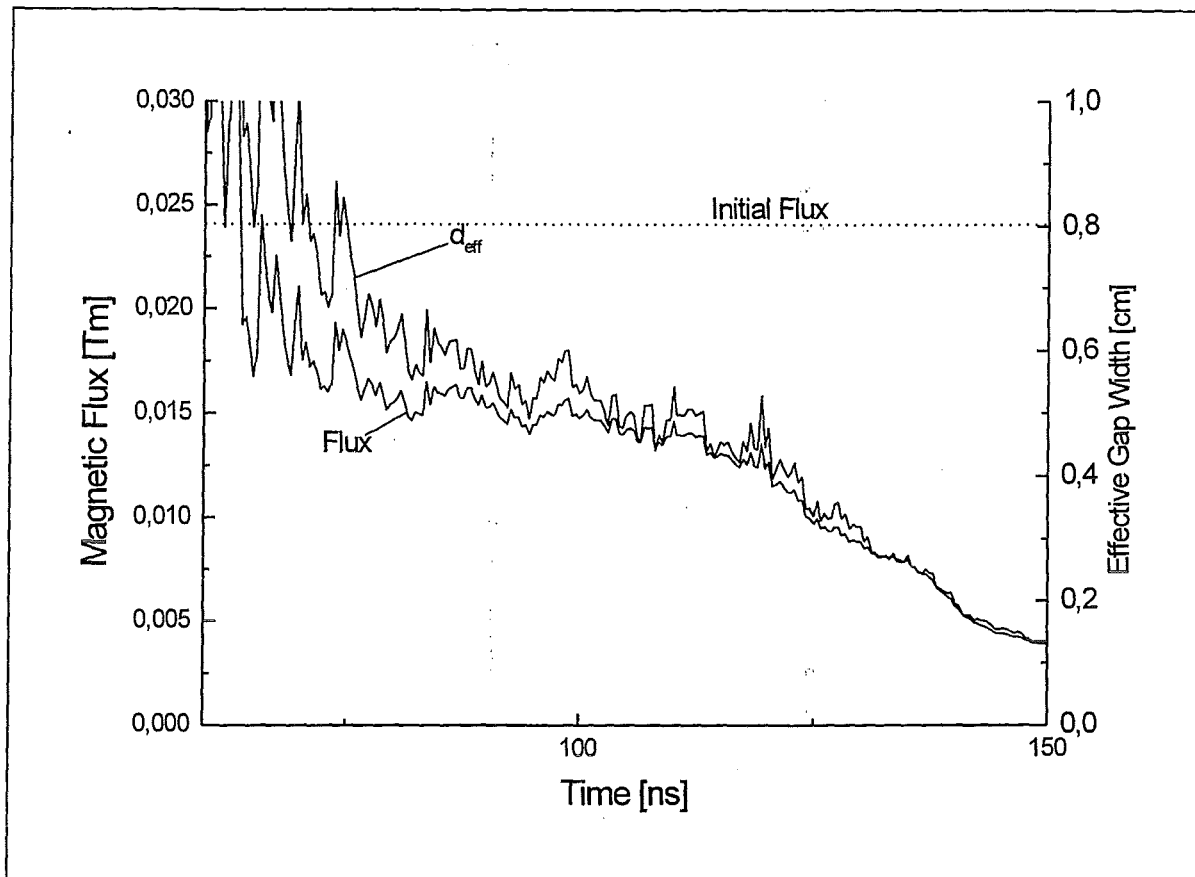
Fig. 5 Effective diode gap and entrapped magnetic flux as a function of time

References

[1] Y. Maron, E. Sarid, O. Zahavi, L. Perelmutter, M. Sarfaty, Phys. Rev. A, 5842, (1989)

[2]] Y. Maron, M. Sarfaty, L. Perelmutter, O. Zahavi, M.E. Foord, E. Sarid, Phys. Rev. A, 3240, (1989)

[3] A.B. Filuk, et al., Proc. 11th Int. Conf. on High Power Particle Beams, Vol. I, 48, (1996)

[4] J.B. Greenly, R.K. Appartaim, J.C.Olson, Proc. 11th Int. Conf. on High Power Particle Beams, Vol. I, 111, (1996)

[5] H. Bluhm, P. Hoppé, H. Laqua, D. Rusch, Proc. IEEE, Vol. 80, No. 6, 995, (1992)

[6] H. Laqua, H. Bluhm, L. Buth, P. Hoppé, J. Appl. Phys. 77, 5545, (1995)

[7] H. Bluhm (Editor), Physics of Intense Light Ion Beams, Production of High Energy Density in Matter, and Pulsed Power Applications, Annual Report 1995, FZKA 5840, (1996)

[8] M. E. Cuneo, T. R. Lockner, G. C. Tisone, IEEE Trans. On Plasma Sci. 19, 800, (1991)

[9] J. J. MacFarlane, P. Wang, NLTERT- A code for computing the radiative properties of non-LTE plasmas, FPA-93-6, Univ. of Wisconsin, (1993)

[10] L. Perelmutter, G. Davara, Y. Maron, Phys. Rev. E, 3984, (1994)

[11] C. L. Olson, Laser and Part. Beams, 2, 255, (1984)

[12] M. P. Desjarlais, Phys. Fluids B 1, 1709, (1989)

Influence of the Applied Magnetic Field on the Divergence and Focusing Properties of the Extracted Beam

P. Hoppé[a], M. P. Desjarlais[b], H. Bluhm[a], L. Buth[a], D. Rusch[a], O. Stoltz[a], W. Väth[a]

[a] *Forschungszentrum Karlsruhe, Institut für Neutronenphysik und Reaktortechnik*
P. O. Box 3640, D-76021 Karlsruhe, Germany
[b] *Sandia National Laboratories, P. O. Box 5800, Albuquerque, New Mexico 87185, USA*

Abstract

Ion beam divergence is influenced by the emission profile of the beam; inhomogeneities can stimulate the transition from the stabilizing diocrotron mode to the detrimental high divergence ion mode. Applied fields for homogeneous beam emission profiles, which differed in strength and tilt, were designed for the KALIF B_{appl} diode. Experiments were performed on KALIF with these fields. They resulted in the lowest divergences ever measured with this diode. This proves, that the beam emission profile is a controllable key variable to improve the focusing properties of the beam.

Introduction

One of the primary limitations for the maximum power density P_{max} achievable in the focus of light ion diodes continues to be unacceptably high beam divergence Θ, defined as the half angle of the emission cone of a beamlet accelerated in the diode. For extractor type ion diodes P_{max} is related to the beam brightness $B = JV/(\pi\Theta^2)$. In this equation V is the acceleration voltage and J the current density. Simulations have shown that the beam divergence can be reduced by improving the uniformity of the ion current density [1]. This diode type supports two large amplitude instabilities: the diocroton mode (high frequency, low divergence) and the ion mode or transit-time instability (low frequency, high divergence). Extraction diodes, with their 1/r dependence of the externally applied magnetic field for electron insulation, are especially susceptible to a radial skewing of the ion current density, which can stimulate the transition from the benign and stabilizing diocrotron mode to the detrimental high divergence ion mode under conditions that would otherwise favor lower divergence [2]. Experiments were performed with the B_{appl} proton diode on the KALIF accelerator [3] with the main goal to investigate the influence of various applied magnetic field configurations on the emission profile of the beam, on beam divergence and on the focusing properties of the diode.

Field calculations

The ion beam current density J_i of an extractor type diode (r,z geometry) is $J_i = \chi(r)J_{cl}d^2(r)/g^2(r)$ with the enhancement χ depending on the electron distribution in the acceleration gap with the geometrical gap width d_0 and the Child-Langmuir current density J_{cl}. The ratio $d(r)/g(r)$ describing the diamagnetic compression goes to infinity as the diode voltage V approaches the saturation voltage $V^* \sim 1/r$. Hence the current density peaks for larger radii. 'Tilting' the applied magnetic field may compensate for these radial variations in current density. However, the amount of tilt required for uniform emission depends on V and the unknown

Fig.1: Calculated stream lines $\Psi(r,z)$ for an applied field by a single feed (solid) and a double feed (dotted) coil. The position of the Faraday cups for the measurement of the beam emission profile is shown schematically. They measure positive charge only due to the applied field.

electron distribution in the gap and must therefore be investigated experimentally. This diode model was added to the magnetic diffusion code ATHETA [4] used for the calculation of the fields of the KALIF B_{appl} diode under emission conditions, i.e. the magnetic fields in the diode are due to the externally supplied currents through the inner and outer field coils (the 'applied' field) and the self-fields due to the non-neutralized beam in the acceleration gap (Fig. 1). Recent measurements of the electron distribution in the diode gap [5] might help to reduce the number of experiments.

In standard type single feed coils (SF), the inner and outer coil are connected in series to a common supply, i.e. the same current runs through both coils, hence the profile of the magnetic field is fixed. Applied fields which differed in tilt and strength were achieved by separating the inner from the outer coil and connecting them to independent power supplies (double feed design, DF) (Fig. 2). For the DF coils, the diffusion of the 'fast' insulating field into the aluminum anode due to currents I_{FIC} and I_{FOC} is compensated by the diffusion of a 'slow' field with opposite polarity due to currents I_{SIC} and I_{SOC}. The timing sequence of the required 4 capacitor banks is made such that the fast field components peak at the same time, namely when the KALIF pulse is fired. For the SF arrangement, the calculated stream lines Ψ show a strong radial dependence in contrast to the DF case (Fig. 1). With the currents selected for the DF case IZ (see Tab.1) the

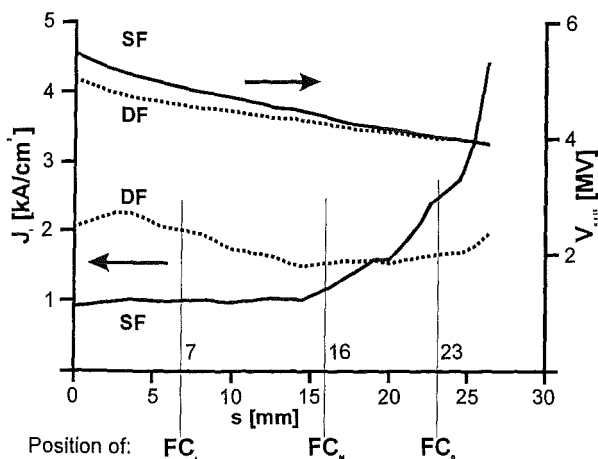Fig. 2: Double feed coil arrangement with pin-hole camera diagnostics (times are given in µs, dimensions in mm.)

38

Fig. 3: Calculated radial emission profile for a standard single feed case (SF) and for the double feed (DF) shot #4202

calculated current density (always using ATHETA) is much more uniform (see Fig. 3).

Diagnostics, data evaluation and measurements

The main beam diagnostics consisted of either a total of 6 magnetically insulated Faraday cups (FC) for the measurement of the radial beam profile or a filtered pin hole camera for the measurement of the beam divergence.

The maximum tolerable pinhole diameter in the front plate of the FC's (Tungsten, 0.2mm thick) was just 0.2mm due to the high expected current densities of up to 6kA/cm^2. In each experiment a set of 6 FC's was placed on 3 radial (inner, middle, out) and 2 azimuthal positions. The signals of the cups were routinely recorded with a bandwidth of 500MHz; additionally, 2 channels with a bandwidth of 4.5GHz were available. The upper frequency limit for the cups itself was estimated to be at least 2GHz.

The recordings made with 4.5GHz bandwidth should allow the measurement of the expected high frequency fluctuations related to the diocrotron instability (around 1GHz) and even might allow the verification of its theoretically predicted azimuthal velocity (around c/20) from the signals of two FC's placed on the same radius but on different azimuthal positions. However, as the 2 fast digitizers (SCD5000) cannot be operated by a common time base, the sampling rate of the digitizers had to be 'post-synchronized'. The trigger position for the recording frame of each digitizer was exactly determined and the sampling rate of the two recorded time series had to be matched. Both were checked by recording a 200MHz-sine-wave simultaneously on both digitizers. This delivered the total transit time difference - including all cabling to the FC's and trigger delays- and showed a small difference of about 0.5% between the sampling rates of the two recorders. Although small, this difference becomes important when looking into phase shifts for transit time determination. Modifying correspondingly the sampling rate of one recorder delivered the 'same' sine wave, but now the two time series were not sampled at the same instants. In order to achieve this, one time series was 're-digitized' to the sampling instants of the other recorder using a linear interpolation between adjacent data values. The recorded signals adjusted by this procedure were high-pass filtered before applying standard Fast Fourier Transform techniques. Actually this filtering process was realized by subtracting the Gaussian low-pass filtered contribution from the signal. The Gauss-filter was truncated at 2σ and had an effective cut-off frequency of 250MHz.

The time integrated beam focusing properties were constructed from track patterns on a CR39 film covered by a 10μm thick Al-foil and placed in a pin hole camera, (Fig. 2). Beamlets (6 or 12) were cut out of the main ion beam by 0.7mm diameter holes in a stainless steel aperture plate, placed 5mm downstream of the 1.5μm thick Mylar foil closing the drift space. The interaction of the beamlets with a 2.5μm thick Ni foil produced Rutherford scattered protons which in turn impact on the CR39 film. The impact patterns on the film from the higher energy ions (filtered with a 10μm thick Al-foil) were determined with an automatic track counting system [6].

The following table gives the shot numbers of the experiments performed on KALIF using double feed coils, the measured peak values of the currents generating the applied magnetic fields and the main diagnostics used. The experimental program foreseen could not be finished due to problems with the mechanical integrity of the coils related to the unusual high currents of up to 55kA through the inner coil. For comparison several shots were performed with the same diagnostics but using the standard single feed coil with a 'slow' current peaking at -9.2kA and a 'fast' current peaking at 49kA after 67μs. These shot numbers are from 4192 to 4200 and 4214, 4215, 4220, 4223, 4225.

Tab.1: Overview of the (successfully) performed experiments with DF coils.
(FC: Faraday-cup diagnostic, CR39: pin hole camera image on a CR39 film)

shot#	case	I_{SIC} (kA)	I_{SOC} (kA)	I_{FIC} (kA)	I_{FOC} (kA)	diagnostic
4201	IZ	0	-9.0	50.6	39.2	FC
4202	IZ	0	-9.1	50.5	39.1	CR39
4203	IZ	0	-8.7	49.8	38.8	FC
4204	IZ	0	-9.2	50.2	38.8	CR39
4205	IA	-3.8	-8.8	45.0	33.3	FC
4206	IA	-3.6	-8.9	45.4	33.2	CR39
4207	IA	-4.2	-9.5	45.3	33.1	FC
4208	IA	-4.1	-9.4	44.9	33.2	CR39
4209	IIZ	-9.4	-9.2	48.4	40.5	FC
4210	IIZ	-9.6	-9.5	48.5	40.5	FC
4211	IIZ	-9.0	-9.0	47.8	40.5	CR39
4212	IIZ	-9.4	-7.8	47.4	40.6	CR39
4217	IC	0	-8.9	51.2	42.3	CR39
4219	IC	0	-8.8	51.4	42.1	FC

Results

The time histories of the Faraday cups shown in Fig. 4 were achieved by averaging over a total of 16 signals (SF case) or 4 signals (DF, case IZ), respectively, measured in experiments performed under similar conditions and synchronized in time to the onset of the total ion current measured as IIS (see Fig. 2) They show, that the beam emission in SF and these (and all other) DF experiments started independently from the radius at the same time and with the same slope. In SF experiments the emission from the inner radii starts to saturate about 25ns after current onset while the middle and outer areas continue rising up to about $3.5kA/cm^2$. In contrast to the inner and middle areas, emission from outside starts increasing again and reaches up to $4.5kA/cm^2$. The rise characteristics for DF were similar corresponding signals measured in DF experiments showed an improved beam homogeneity: they are slightly extended over a longer time period but with reduced current densities; they showed less fluctuations and less radial differences. This emission structure for both, SF and DF experiments, corresponds well to the calculated stream lines (Fig. 1) and the calculated current densities (Fig. 3).

The comparison of the high frequency fluctuations of Faraday cup signals from SF to DF experiments proved, that all DF configurations showed strongly reduced amplitudes. This is demonstrated e.g. by the signals of the outer FC's for the DF case IZ compared to a SF standard shot (Fig. 5).

40
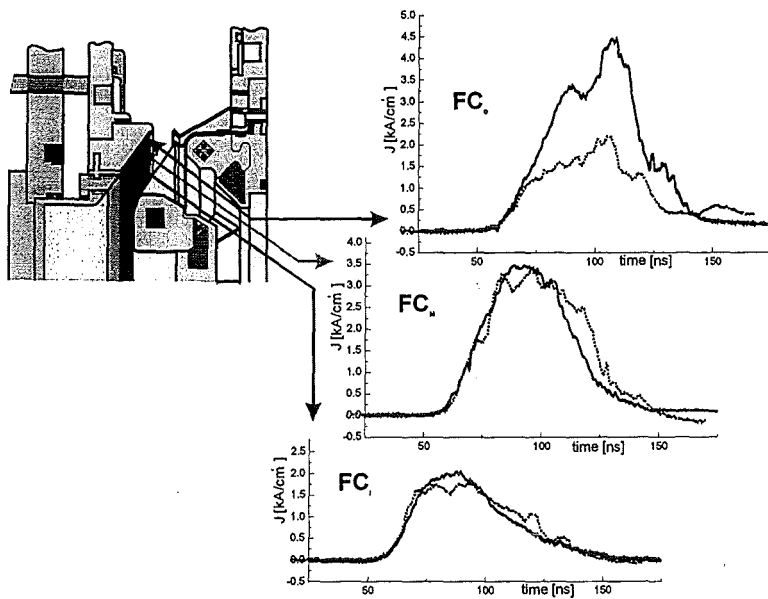
Fig. 4: Average of the FC signals measured in SF (solid) and DF (dotted) experiments at different radial positions
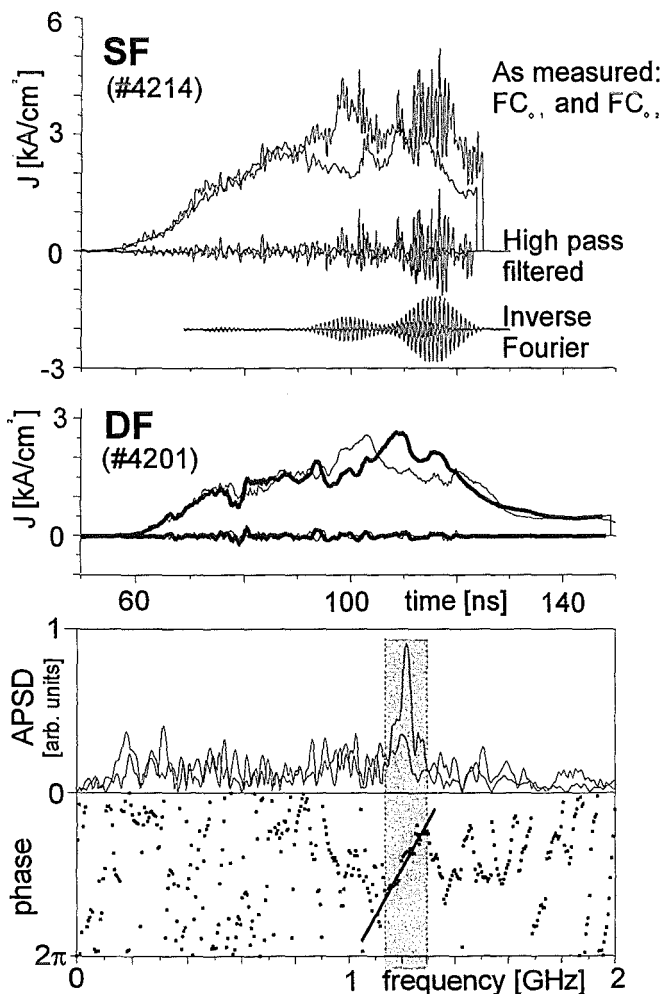
Fig. 5: Frequency analysis of two outer FC signals for the SF and DF configuration

The frequency analysis of these fluctuations (Fig. 5) showed strong contributions in the range around 1.2GHz which were not observed in DF experiments. Phase shift relations between FC signals, which might be caused by azimuthally propagating current fluctuations due to instabilities, were identified for SF experiments only. In the frequency region of the well pronounced resonance -less visible in the 2nd signal- the phase values indicate a transit time, i.e. they are proportional to the frequency.

The shaded frequency range in Fig. 5 indicate the frequency region used for the inverse Fourier transformations as well as for the calculation of the transit time. The first deliver band-pass filtered signals designated in Fig. 5 as 'inverse Fourier'. If these correlated signal fluctuations from about 1.1 to 1.3GHz are due to the ion mode instability the inverse Fourier transforms give the time of the occurrence of this instability. It starts first at about current maximum, then decreases and reaches a second maximum at late times. The transit time of the signal fluctuations in this frequency range is around 3ns for a distance of 28mm between the 2 outer FC's. This corresponds to an azimuthal velocity of c/30, which again is rather close to the predictions. However, the statistical basis for these numbers must be considered as rather limited.

The CR39 impact patterns consisting of up to 8 spots in Fig. 6 give an overview of the focusing characteristics for the 'best' SF shot (#4193) compared to the 'best' DF shot (#4202). The count density (i.e. the number of ion impacts per unit area) within each spot was individually normalized to its peak
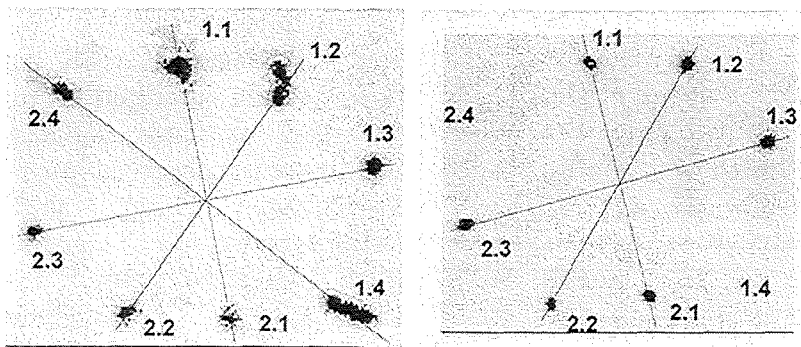
Fig. 6: Impact patterns on the CR39 films of a SF (left) and a DF (right) experiment. The transition from dark gray to light gray marks the half max. density of each spot

value. The transition from 'dark gray' to 'light gray' in Fig. 6 gives the half maximum density level for each spot. These impact patterns were achieved by counting the total CR39 film in one single step. A considerably better spatial resolution was possible by individually counting each spot in a separate step. The density distribution for each spot in Fig. 7 is shown in black for densities 90 to 100%, in dark gray for 50 to 90%, and in light gray for 20 to 50%. The solid line represents the 50% density.
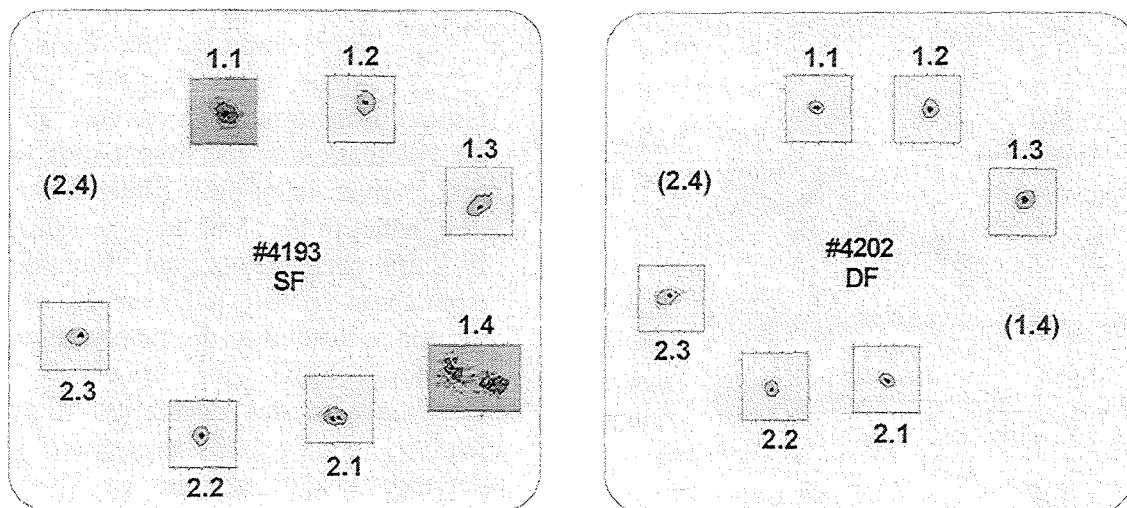
Fig. 7: Impact patterns on the CR39 films with enhanced resolution. The analyzed area around each spot is 5 by 5mm, except for the spot 1.4 with 5 by 7mm. The solid black line is at half maximum

In general, the analysis of the CR39 images so far a reduction of the spot size and hence less (#4204) was a divergence of 17mrad (half spots in one experiment) compared to 26mrad divergence numbers published earlier, these pinhole correction factor, since its influence contribution of about 9mrad from proton 1.5μm thick Mylar foil closing the gas showed for all DF experiments performed beam divergence. The best result (#4202 and width at half maximum averaged over all achieved in SF-experiments. In contrast to results were achieved without using any proved to be negligible. However, the scattering due to the 5mbar drift gas and the volume were taken into account.

The CR39 patterns were also used to investigate the focusing properties of the beam, assuming that a pure ballistic approach is valid for the reconstruction of the beamlets: Centering the spots (only 50% densities shown) of a SF and a DF shot on the same axis - defined by the intersection point of the connection lines between corresponding 100% levels-
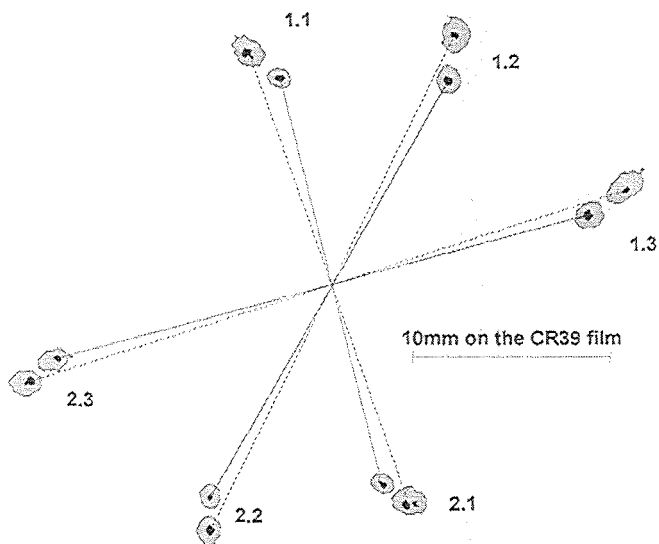
Fig. 8: Impact patterns on the CR39 films for the SF- (outer) and the DF-case (inner radii)

demonstrates, that the DF patterns are moved radially towards the center and are slightly shifted clockwise with respect to the SF patterns (Fig. 8).

The reconstruction of the focus position on the axis of symmetry of the diode (i.e. the z-axis) proved, that for the SF case the focus was at 28mm with reference to the edge of the coil support plate, which is in good agreement with the 'nominal' focus position of 27mm measured earlier. The intersection range of the beamlets with the z-axis has a length of 5.5mm, the 'focus diameter' is 5mm. The comparison of these values to those achieved for the DF case showed, that the focus position moved closer to the coil edge (by 8.7mm), i.e. the focal length was reduced, the intersection range was just 3.1mm long and the focus diameter was reduced to 3.6mm. These results are all in favor of an increased power density in the focal spot of the DF case.
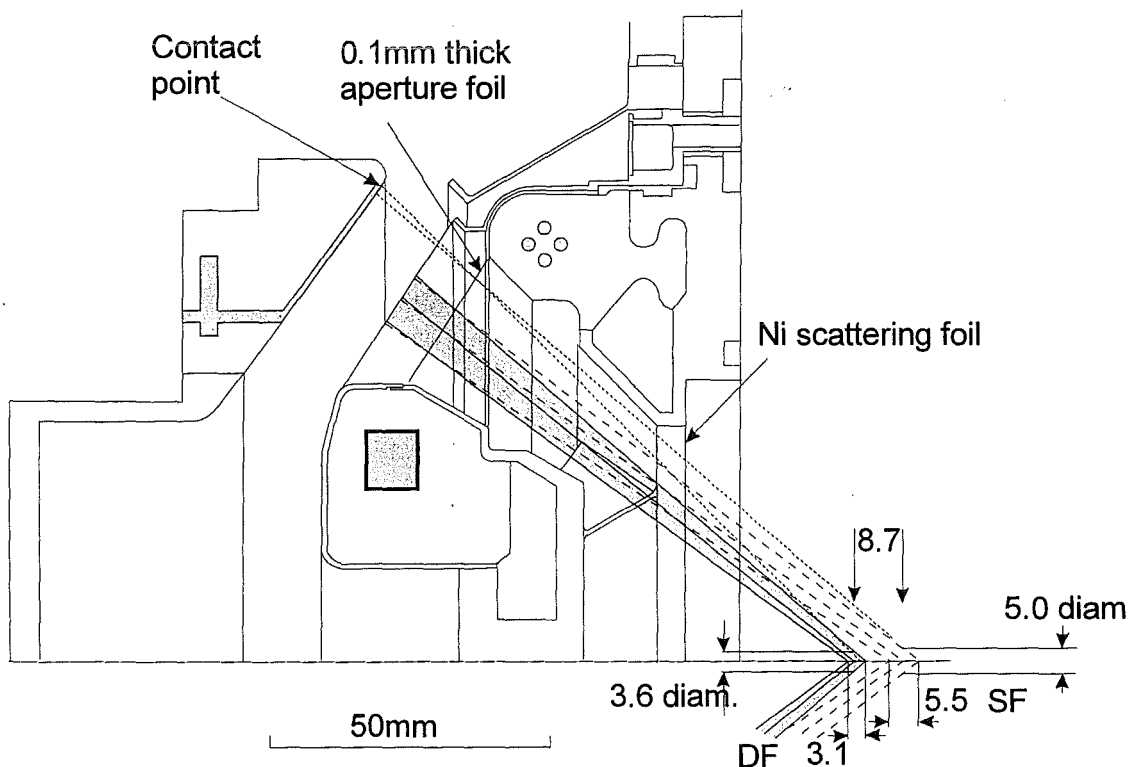
Fig. 9: Reconstruction of the beam focus based on the CR39 impact patterns shown in Fig. 8

The CR39 film spots named 1.4 and 2.4 (see Figs. 6 and 7) were different from all other impacts. They either showed a very low count density or were not detectable at all. If visible, they were radially rather extended. Both observations might be explained by the point on the anode surface were these beams come from (Fig. 9). Around this point, the hydrogen bearing PdTi layer is covered by an additional Al layer which should improve the electrical contact

between the PdTi layer and the bulk aluminum. Furthermore, this area might get heated additionally by ohmic contact losses leading to enhanced plasma expansion. Therefore these points were not taken into account.

Conclusion

The experimental results achieved so far are in excellent agreement with the theoretical predictions:

1. the magnetic field profiles designed for uniform current substantially improved the radial homogeneity of the ion current,
2. the amplitudes of the fluctuations attributed to the ion mode instability were dramatically reduced,
3. the divergence of the beam was reduced. This resulted in the lowest beam divergences ever measured on KALIF (17mrad vs. 26mrad) and
4. less damage on the diode hardware was observed. This demonstrates, that -unlike using limiters or additional wires on axis- the divergence improvement was not achieved on expense of the efficiency in ion beam generation.

In addition to the reduced divergence, the focusing properties of the beam were improved: the diameter of the focal spot was smaller by about 25%. Together with the slightly shortened focal length of the diode this should result in an increased power density.

The results achieved so far showed, that the ion beam current density profile is one controllable key variable in ion diode performance. The 'optimum' field profile was probably yet not achieved because -due to problems with the field coils- only a part of the considered parameter settings could be investigated. Therefore these experiments should be continued. Despite the problems with the poor reproducibility of KALIF shots, these results were generally confirmed by all shots performed under the same experimental conditions. Due to the better reproducibility expected for shots with the KALIF-HELIA accelerator this type of experiments can be performed much more effectively.

References

[1] S. A. Slutz, Phys. Fluids B **4** (8) August 1992
[2] M. P. Desjarlais et al., in Proc. of the 11th Int. Conf. on High-Power Particle Beams, Prague, Czech Rep., June 1996, p.101-110
[3] H. Bluhm et al., in Proc. of the 10th Int. Conf. on High-Power Particle Beams, San Diego, USA, June 1994, p.77-82
[4] J. P. Quintenz et al., Laser Part. Beams **12**, 283 (1994)
[5] V. Licht et al., to be published in Proc. of the 12th Int. Conf. on High-Power Particle Beams, Haifa, Israel, June 1998
[6] H. Guth et al., FZKA Bericht 5523, Forschungszentrum Karlsruhe (1995)

Production of intense Li-atomic beams for ion diode diagnostics

W. An, H. Bluhm, L. Buth, G.Meisel, B.A. Knyazev*,

Forschungszentrum Karlsruhe, Postfach 3640, D-76021 Karlsruhe, Germany
*Novosibirsk State University, Novosibirsk, 630090, Russia

Abstract
Conditions for the production of an intense atomic Li-beam for field diagnostics in high power ion diodes have been investigated. A frequency doubled Q-switched Nd:YAG laser with 2 J pulse energy and 5ns pulse duration has been used to vaporise a thin double layer of Al and LiF deposited on a glass substrate.
The atomic density found was much below that expected. It is speculated that the fraction of Li-atoms in the vapour is small and that the vapour is dominated by other species like LiF-molecules or Li-ions. Also two groups of Li-atoms were observed which may result from different processes of heat transfer to the films occurring early and late in time.
The measured density profiles have been fitted with a shifted Maxwellian, giving a centre of mass velocity of about 1.4 cm/μs and a temperature of 2.5 eV. It is assumed that most of the expansion occurs collision dominated.

Introduction
Pulsed atomic and molecular beams are widely used as diagnostic tools in plasma physics experiments. A very successful application is the use of atomic beams to determine the plasma parameters in Tokamak facilities/2-3/. For that purpose different techniques of atomic beam production have been developed. Especially laser induced vaporisation of thin metallic films has been applied to create the atomic source/4-6/.
Recently particle beam diagnostics have also been employed to investigate short living transient phenomena. Besides in Tokamaks the first measurements were done in high voltage electron diodes with μs pulse duration/7,8/. Later, electric and magnetic field strength measurements have been carried out in high power ion diodes operating in the ns regime/9/.
Increasingly higher temporal resolutions require higher densities of the atomic beams. E.g. to get an acceptable fluorescence signal to background ratio at ns time resolution an atomic density around 10^{12} cm^{-3} is needed. At these densities the fluorescence signal can be disturbed by self-absorption. Therefore it is necessary to limit the dimensions of the atomic beam parallel to the direction of observation, which at the same time improves the spatial resolution.
Different geometries for vaporisation have been developed. Früchtenicht/1/ was the first who used a film deposited on a transparent substrate that was illuminated with a laser beam from the backside. It has been found that in this case the efficiency of vapour production is larger than for front illumination.
It is this kind of atomic beam production that has been investigated in this work.

Theoretical model
The basis of the theoretical model considered here is the laser induced evaporation of a thin metallic film on a transparent substrate. In this case only a half range vapour expansion is possible. Depending on the initial gas density two developments of the expansion are possible/10-12/:
a) If the atomic density is sufficiently low (<10^{15} cm^{-3}) a collision free expansion can occur.
b) If the initial atomic density is high one has to consider gas dynamic effects.

In the case of a collision free expansion the velocity distribution of the atoms can be described by a half-range Maxwellian:

$$f_1(v_x, v_y, v_z) \propto \exp\left\{-\frac{m}{2kT_k}\left[v_x^2 + v_y^2 + v_z^2\right]\right\} \qquad (1)$$

$v_x > 0$, $-\infty < v_{x,y} < \infty$

Here T_s is the temperature at the target surface, m is the atomic mass and x is the direction parallel to the target normal (x=0 is the target surface).

In this case the angular distribution is proportional to $\cos\theta$, where θ is the ejection polar angle.

If the emission is sufficiently intense, such that the atomic mean free path becomes smaller than the lateral dimensions of the emission area a Knudsen layer (KL) forms in which the independently emitted particles come to equilibrium with each other and their velocity distribution becomes a shifted Maxwellian, i.e. beyond the KL a full-range Maxwellian has developed in a centre-of-mass coordinate system:

$$f_2(v_x, v_y, v_z) \propto \exp\left\{-\frac{m}{2kT_k}\left[(v_x - u_k)^2 + v_y^2 + v_z^2\right]\right\} \qquad (2)$$

$-\infty < v_i < \infty$, i={x,y,z }
where

$$u_k = \left(\frac{\gamma kT_k}{m}\right)^{1/2} \qquad (3)$$

u_k, the centre of mass velocity is close to the sound velocity and T_K is smaller than the surface temperature T_S ($T_K \approx 0.7\, T_S$). $\gamma = c_p/c_v$, k= Boltzmann constant. The angular distribution shows strong forward peaking $\sim \cos^4\theta$ /16/.

It has been shown /13/ that the equilibrium distribution function is already established after 3 collisions (happening within 1.5 mean free path). If after formation of the Knudsen layer the atomic density is still high the outflow continues as an unsteady adiabatic expansion, i.e. an adiabatic expansion that is time dependent /15/, until the collision free state is reached.

If the existence of the emission source is short compared to the target-detector-flight time, equation 2 can be transformed into a time of flight (TOF) signal for a density sensitive detector, such as laser-induced fluorescence /15/. To achieve this we must express the volume element $dv_x dv_y dv_z$ in velocity space by the volume element dtdydz. Assuming that the collision free flight time is much larger than the time for KL formation we can set the atomic velocity constant:

$v_i = i/t$, i=(x,y,z)

The Jacobian determinant of the velocity-time-space transformation becomes

$$\frac{\partial(v_x, v_y, v_z)}{\partial(t, y, z)} = \frac{x}{t^4}, \qquad (4)$$

if the detector is located on the x-axis and if the dimensions of its sensitive area are small compared to the target-detector distance ($\Delta y, \Delta z \to 0$).

For a density sensitive detector we therefore have the following TOF-signal:

$$dN = f_2 v_x dv_x dv_y dv_z = f_2 \frac{x}{t^4} v_x dt dy dz = f_2 \frac{x}{t^4} dV \qquad (5)$$

$$n = \frac{dN}{dV} = f_2 \frac{x}{t^4} \propto x \cdot t^{-4} \exp\left[-\frac{m}{2kT_k} t^{-2}\left\{(x - u_k \cdot t)^2\right\}\right] \qquad (6)$$

Here we have assumed y=z=0.
For a flux-sensitive detector such as a bolometer or a Faraday cup detecting ions the signal is

$$\varphi \propto x^2 \cdot t^{-5} \exp\left[-\frac{m}{2kT_k} t^{-2}\left\{\left(x - u_k \cdot t\right)^2\right\}\right]$$ (7)

Experimental set-up

The target used consisted of an Al-LiF double layer deposited on a glass substrate. The laser light was absorbed in the Al layer illuminated through the backside of the substrate. The 100 nm thick Al layer was chosen to be equal to the absorption length of the laser light and was not changed in the experiments while the LiF layer thickness was varied between 330 nm and 500 nm. The frequency doubled beam from a Q-switched Nd:YAG laser (6 ns pulse duration) was focused onto the Al-film from the target backside. Positioning the 30 cm focusing lens at different distances from the target it was possible to vary the energy density on target while the total laser energy of 1.9 Joule was kept constant (Fig.1).

The construction of the target holder allowed an axial movement in the vacuum chamber, enabling several laser shots without breaking the vacuum. 67 cm distant from the atomic source a laser induced fluorescence diagnostic was set-up. The 2s-2p transition in the Li-atom
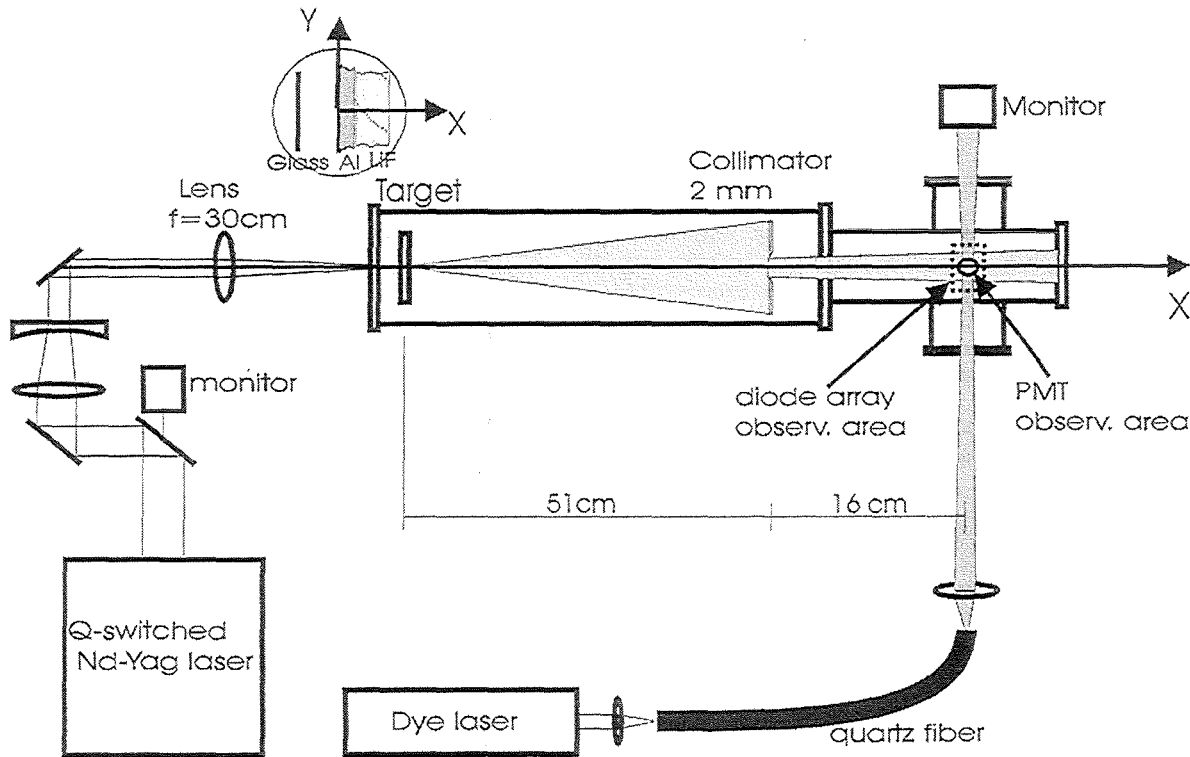
Fig.1 *Schematic diagram of the experimental setup.*

was pumped into saturation with the help of a dye laser. It was possible to record the fluorescence light simultaneously with two detector systems: a photo-multiplier system was used to measure the temporal evolution of the fluorescence and a diode array consisting of 700 elements was used to determine the spatial distribution of the light. The diode array which had been absolutely calibrated with a tungsten band lamp (RS-10A from EG&G) was looking perpendicularly to the x-axis such that the recorded signals became proportional to the Li density. Both detector systems were placed on the same axis opposite to each other.

Experimental results

Fig. 2 shows the signal recorded with the help of a Faraday cup. The ion collector was operated with a bias of -100 V in the saturation regime. A peculiarity of the signal is the existence of two components shifted in time. Similar signal distributions have been observed by other authors /17,18/, without giving any explanation. A comparison with the time of flight spectrum of Li atoms, presented in Fig. 3, indicates that this structure cannot be explained by species of different mass. It should be pointed out that the fluorescence light measurements discriminate all other species except Li atoms. We must therefore conclude that the source emits two groups of Li-atoms. A possible explanation can be found, if one assumes, that the evolution of the vapour is mainly determined by hydrodynamic expansion:

The vapour cloud created during the laser beam material interaction is initially peaking at the target surface and has a strong gradient. The temperature distribution is very similar/19/. This causes an even stronger pressure gradient accelerating the first group of particles. Later, more gas is produced from the substrate by thermal conduction. This gas may be created at a lower surface temperature and therefore expand more slowly. The difference in the group-velocities depends on the laser pulse duration, on the heat conduction, on the specific heat of the target material and on the characteristic hydrodynamic time constants (especially on the sound speed).

The TOF spectrum of the Li-atoms shown in Fig. 3 has been constructed from photo-multiplier signals and was

Fig.2 *Typical signals from biased ion collector, normalized to unity at the peak current. The collector was 67 cm from the target and was located along the normal to the target surface. The lasers energy density was 10.8 Joul/cm²*

obtained in different shots. The reproducibility was within 3-5% for the arrival time and within 7-10% for the amplitude, being better for thick than for thin LiF-films. In Fig.3 we also plot the theoretical curve calculated from equation 6. While using equation 6 we took into account that the vapour consisted of three components: Al, Li, and F. Their relative contribution was chosen according to the initial layer thickness. For all three cases the parameter γ is close to 1.2 and the TOF signal shape depends only weekly on γ. Therefore a determination of γ by fitting the theoretical curve to the experimental data leads to relatively large errors. Nevertheless we can say that the centre of mass velocity is close to the thermal
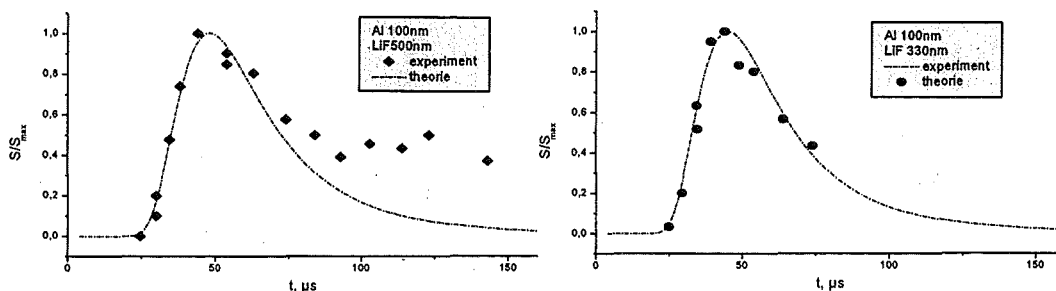
Fig.3 *The time of flight spektra of Li-atoms. The experimental conditions are same as Fig.2. The Maxwellians corresponds to a temprature of 23800 K and 27100 K for 500 nm and 330 nm LiF-films respectively.*

expansion velocity. Deviations of the theoretical curve from the experimental points at later times mainly result from the assumption that the source lifetime is small compared to the flight time, which is not true for the experiment. If this is not the case, the faster atoms started later will catch up with the slower atoms started earlier /20/. Fig. 3 also shows that thinner target layers lead to higher velocities. This has also been observed by other investigators /9,17/ and is consistent with the particle energy increasing with the energy density of the laser , as shown in Fig. 4. In these experiments the energy density of the Nd:YAG-laser was varied by changing the voltage of the amplifier flash lamps, thus keeping the irradiated area and the laser pulse duration constant.

Using the diode array calibration factor it was possible to determine the Li-atom density from the measured fluorescence signal, depending on the duration of the dye-laser excitation pulse (5 ns) and on the lifetime of the 2p-level, which is 27 ns. The detector integration time was 30 ns (Fig. 5).
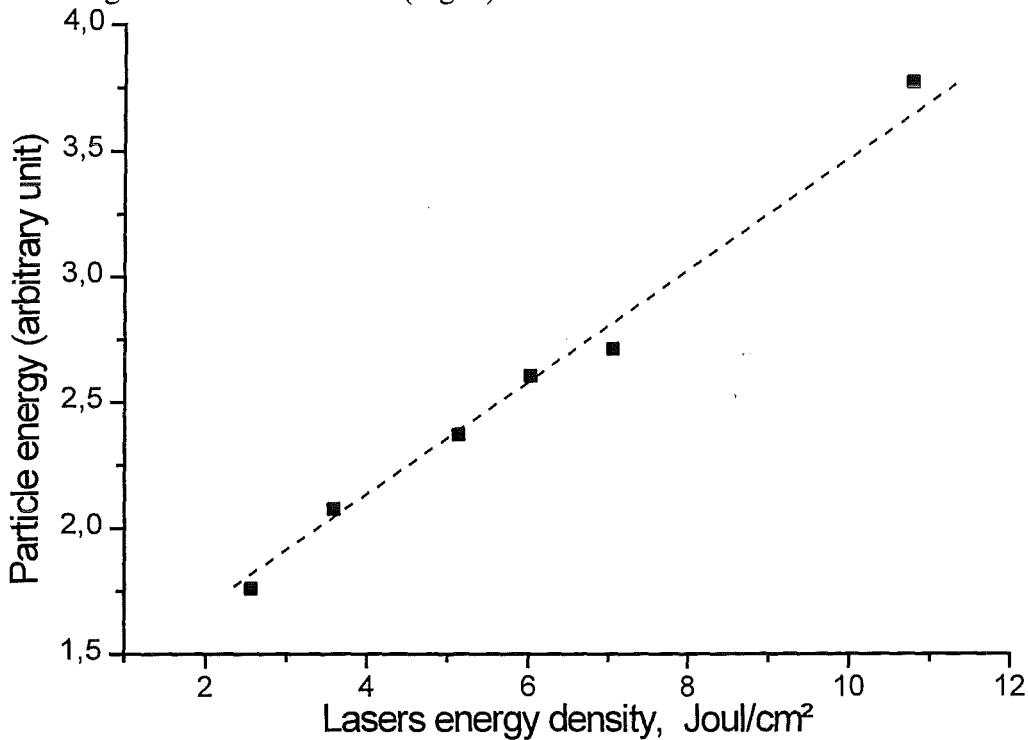
Fig. 4 *The particle energy versus lasers energy density.*
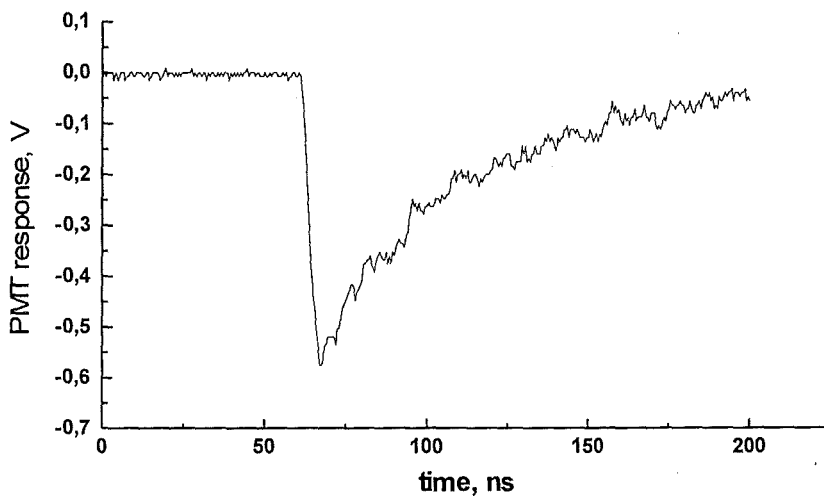
Fig.5 *Time dependence of fluorescence intensity.*

A collection of Li-beam profiles is presented in Fig. 6. The diameter of the dye-laser beam was 2 mm at the position of measurement. This translates to a velocity uncertainty of 10^3 cm/s for particles with an average velocity of $1.5 \cdot 10^6$ cm/s. Therefore the particles recorded in each frame can be considered as monoenergetic as long as bunching does not occur. Based on Fig. 6 we can conclude that the smaller the particle velocity the broader is the spatial profile of the Li-beam. Also the foot width of the profile increases stronger than the plateau. From simple geometric considerations we have for the plateau a and the foot b of the beam profile (see Fig.7): $a=d+(d- q) \cdot l/L$, $b=d+(d+q) \cdot l/L$. In our case the width d of the aperture was 2 mm. q is the effective diameter of the source from which particles are emitted. To explain the beam profile evolution shown in Fig.6 we must therefore assume a source moving axially and spreading radial, reducing the particle density. Since the fastest atoms leave the source first their profile is smaller.
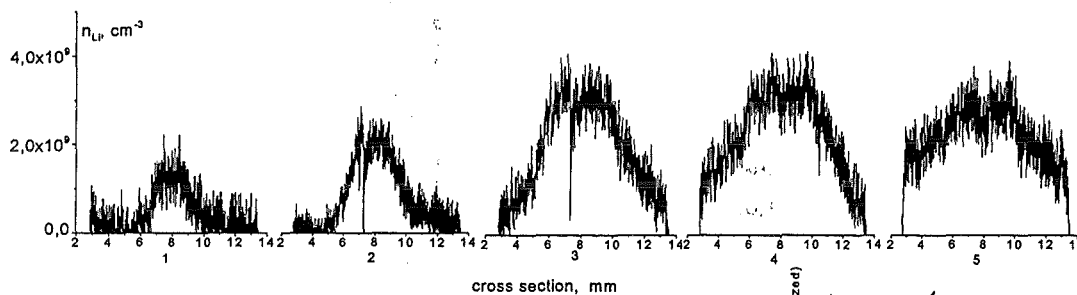
Fig.6 *The time dependence of Li-beams profile. The number of the picture (top) corresponds to a trigger position of dye-laser (right). The target consist of : Al-100 nm, LiF-330 nm.*

So far unexplained is the relatively small Li-atom density observed at the detector. A simple estimate based on the evaporated area $(0.2 \cdot 0.2$ cm$^2)$, the layer thickness $(5 \cdot 10^{-5}$ cm$)$, and the Li-density in the target film $(6 \cdot 10^{22}$ cm$^{-3})$ and on the pessimistic assumption of uniform expansion into the half space shows that the density at the detector position $(r=67$ cm$)$ should reach $2 \cdot 10^{11}$ cm^{-3}. This is 100 times larger than measured. A possible explanation may be that only a small fraction of the particles in the vapour were Li-atoms, the rest being either ions or LiF-molecules.
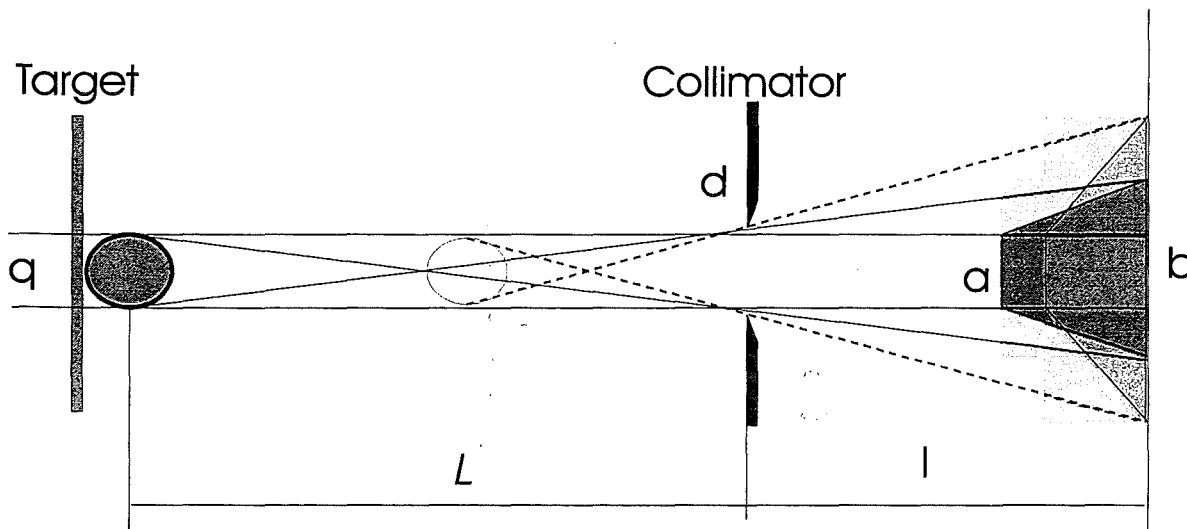
Fig. 7 Geometric arrangement of target, collimator, and detector.

50

Summary

An active particle diagnostic with high temporal and spatial resolution requires a high atomic density. We found that the creation of an atomic beam meeting both requirements has some inherent limitations. On the one hand the creation of a beam with high intensity requires a large amount of vapour which on the other hand leads to rapid hydrodynamic expansion deteriorating the geometric parameters. A rather low Li-atom density has been obtained which is in contradiction to simple particle balances. To get a more complete picture of the vapour expansion more investigations of the vapour evolution in the vicinity of the target are necessary.

References

1   J.F. Friichtenicht, Rev.Sci.Instrum. **45**, (1974), 51.

2   K.Kagota,H.Matsuoka, H.J.Ramos, S.Miyake, K.Tsuchida, J.Fujita, T.Usui, and T.Oda, J. Nucl. Mater. **128-129**, (1984), 960.

3   A.Pospieszczyk, F.Aumyr, H.L.Bay, E.Hintz, PlLeismann, Y.T.Lie, G.G.Ross, D.Rusbült, R.P.Shorn, B.Schweer, and H.Winter, J.Nucl.Mater. **128-129**, (1989), 574.

4   K.Kagota, K.Tsuchida, Y.Kawasumi, and J.Fujita, Plasma Phys., **20**, (1978), 1011.

5   E.S. Marmar, J.L.Cecchi, and S.A.Cohen, Rev. Sci. Inst. , **46**, (1975), 1149.

6   S.Sasaki, S.Takamura, Y.Uesugi, and Y.Ohkouchi, K.Kagota, Rev.Sci.Inst. **64**, (8), (1993), 2277.

7   B.A.Knyazev, S.V.Lebedev, and P.I.Melnikov, Proc. 12th Int. Conf.on Phenomena in Ionized Gases, **2**, (1985), 1004.

8   B.A.Knyazev, S.V.Lebedev, and P.I.Melnikov, Sov. Phys. Tech. Phys. **36**,(3), (1991)

9   C.H.Ching, J.E.Bailey, P.W.Lake, A.B.Filuk, R.G.Adams, and J.McKenney, Rev.Sci.Instrum. **68**(1), (1997).

10 T.Ytrehus, Rarefied Gas Dynamics, Editor J.L. Potter (AIAA, New York, 1977), 1197.

11 C. Cercignani, Rarefied Gas Dynamics, Editor S.S.Fisher (AIAA, New York, 1981),305.

12 A.Frezzotti, Rarefied Gas Dynamics, Editors V.Boffi and C.Cercignani (Teubner, Stuttgart, 1986), 313.

13 I. NoorBatcha, R.R. Lucchese and Y. Zeiri, J.Chem.Phys. **86**, (1987), 5816

14 R.Kelly, A. Miotello, Pulsed laser deposition of thin films, Editors D.Chrisey and G. Hubler , New York (1994)

15 R.Kelly, R.W.Dreyfus, Surf.Sci. **198**, (1988), 263.

16 K.Saenger, Pulsed laser Deposition of thin films, Editors D.Chrisey, G.Hubler, New York, (1994)

17 Y.T. Lie, A. Pospieszczyk, J.A. Tagle, Fusion tech. **6**, (1984), 447.

18 E.S. Marmar, J.L.Cecchi, S.A.Cohen, Rev. Sci. Instrum., **46**, 9, (1975), 1149.

19 A.Vertes, P.Juhasz, M.De Wolf, R. Gijbels, Scan. Microscopy, **2**, 4, (1988), 1853

20 C.Peugnet, J.Appl. Phys. **48**, 8, (1977), 3206.

21 N.Ramsey, Molecular beams, Oxford Univ. Press, London (1963).

The Finite-Volume Particle-in-Cell Simulation Program KADI –
Extentions and Applications

C.-D. Munz [1], P. Omnes, R. Schneider
E. Sonnendrücker [2], E. Stein, U. Voß [3], T. Westermann [4]

Forschungszentrum Karlsruhe — Technik und Umwelt,
Institut für Neutronenphysik und Reaktortechnik,
Postfach 3640, D-76021 Karlsruhe

1. INTRODUCTON

Computational simulations of technical devices whose electric behavior is substantially influenced by internal charged particle flow (non-neutral plasma) are starting to play an increasingly important role in applied science and technology. Typical representatives of those devices are pulsed-power diodes which have been developed at the Forschungszentrum Karlsruhe [5] and are the objects of extensive experimental [6] as well as numerical [24, 17] investigations. A detailed understanding of the fundamental time-dependent phenomena caused by this non-neutral plasma (e.g., the origin of instabilities) requires the solution of the Maxwell-Lorentz equations for realistic configurations.

An attractive numerical method to solve this non-linear problem is the particle-in-cell (PIC) approach based on ingenious particle-mesh techniques [12, 4]. Consequently, it is essential for the PIC method to have a computational mesh, covering in an appropriate manner the geometry of interest. Furthermore, in order to perform high quality simulations this grid should yield a very accurate replica of the border of the relevant device domain, where several kinds of boundary conditions are imposed.

Optionally, two different grid models are used for our purposes to discretize the computational domain: The first one based on boundary-fitted coordinates [21], resulting in a quadrilateral mesh zone arrangement with the decisive advantage of regular data structure. The second grid concept with the highest degree of freedom in mapping a geometry to a discrete image, rely on unstructured meshing techniques yielding a triangulization and tetrahedrization of the domain in the two and three-dimensional case, respectively.

The numerical solution of the Maxwell equations in the time domain is obtained by using a finite-volume (FV) approach formulated in the present paper for a non-rectangular quadrilateral (KADI2D) as well as for an unstructured triangle (KADI$_3^2$D) mesh in two space dimensions [18, 10]. A very favorable property

---

[1]IAG, Universität Stuttgart, Pfaffenwaldring 21, D-70550 Stuttgart
[2]Université Henri Poicaré Nancy I, IEC, B.P. 2339, F-54506 Vandoeuvre les Nancy Cedex
[3]Centre de Mathematiques Appliquées, Ecole Polytechnique, F-91128 Palaiseau
[4]Fachbereich Naturwissenschaften der FH Karlsruhe, Postfach 2440, D-76012 Karlsruhe

of these modern FV schemes consists in the fact that they combine inherent robustness at steep gradients with accurate resolution [13]. In the context of self-consistent charged particle simulation in electromagnetic fields the coupling of a high-resolution FV Maxwell solver with the PIC technique is a new approximation method [8, 17, 19].

2. NUMERICAL FRAMEWORK FOR THE MAXWELL-LORENTZ EQUATIONS

The PIC approach circumvents the direct force calculation between charged particles by introducing a grid-based and a mesh-free numerical model: On the computational mesh the spatial and temporal evolution of the electromagnetic field generated by all charges are determined, whereas the charged particles themselves are advanced in the continuous computational domain. The evolution of the electromagnetic fields is given by the vacuum Maxwell equations

$$\frac{\partial E}{\partial t} - c^2 \nabla \times B = -\frac{j}{\epsilon_0} \quad ; \quad \frac{\partial B}{\partial t} + \nabla \times E = 0 \, , \tag{2.1a}$$

$$\nabla \cdot E = \frac{\rho}{\epsilon_0} \quad ; \quad \nabla \cdot B = 0 \, , \tag{2.1b}$$

where E, B, ρ and j denote the electric field, the magnetic induction, the charge and current densities, respectively. The basic features applied for the numerical approximation of these equations are summarized in the subsequent sections.

The dynamics of the charged particle ensemble inside the computational domain is determined by solving the relativistic Lorentz equations

$$\frac{dx_k(t)}{dt} = v_k(t) \, , \quad \frac{dp_k(t)}{dt} = F(x_k, v_k, t) \, , \tag{2.2a}$$

numerically, where the index k runs over the total number N_p ($> 5 \cdot 10^5$) of charges. The Lorentz force

$$F(x_k, v_k, t) = Q_k[E(x_k(t), t) + v_k(t) \times B(x_k(t), t)] \tag{2.2b}$$

acting on the charge Q_k with mass M_k depends on the electromagnetic fields at the actual phase space coordinates (x_k, v_k) of the kth macro charge and is responsible for the redistribution of the particles inside the domain of interest. To obtain the numerical solution of (2.2a), we apply the second-order accurate, time-centered standard leapfrog-scheme introduced by Boris [7], taking explicitly the special structure of the electromagnetic force (2.2b) into account.

The link between the grid-based and mesh-free model is established by interpolating the fields onto the particle positions and by locating the charges with respect to the mesh zones of the computational grid. Both actions are carried out by applying the standard area-weighting interpolation scheme [16] extended to boundary-fitted, quadrilateral grid zones [23, 17] as well as unstructured mesh arrangements [14, 3, 10]. The charge and current density assignment to the nodes

of the computational mesh finally yields the sources

$$\rho(x, t) = \sum_{k=1}^{N_p} Q_k \, \delta[x - x_k(t)] \,, \tag{2.3a}$$

$$j(x, t) = \sum_{k=1}^{N_p} Q_k \, v_k \, \delta[x - x_k(t)] \tag{2.3b}$$

of the Maxwell equations for the subsequent iteration cycle. Together with the Maxwell (2.1) and Lorentz (2.2) equations, the latter equations form the non-linear Maxwell-Lorentz problem, the starting point for further numerical approximations.

3. Finite-Volume Approximation for the Maxwell Equations

The relevant formulation for the construction of FV schemes is the conservation form of the Maxwell equations [18]

$$\frac{\partial u}{\partial t} + \sum_{i=1}^{D} \frac{\partial f_i(u)}{\partial x_i} = q \,, \tag{3.4}$$

relying on the time-dependent equations (2.1a) only. In the present description we restrict ourselves to two space dimensions ($D{=}2$) and, hence, the vector of the electric field and magnetic induction $u(x, t) = (E_1, E_2, E_3, B_1, B_2, B_3)^T$ is independent of the coordinate x_3. However, when deriving FV schemes this is not a serious limitation since the extention of the methods to the three-dimensional case, for instance, on tetrahedral meshes is straightforward (see e.g., [10]). An interesting aspect of the form (3.4) is that the differential operator is now considered as the divergence applied component-by-component to the physical flux $f_i(u) = \mathcal{K}_i \, u(x, t)$, where the $\mathcal{K}_i$ are constant (6×6)-matrices (for details see e.g., [11, 22, 18]). The source term q in (3.4) does not depend on u and is, essentially, given by the current density. In order to solve (3.4) numerically, we apply a splitting ansatz in computing the following sequence of equations

$$\frac{\partial u^{(1)}}{\partial t} = q \,, \tag{3.5a}$$

$$\frac{\partial u^{(2)}}{\partial t} = -\sum_{i=1}^{D} \frac{\partial f_i(u^{(2)})}{\partial x_i} \tag{3.5b}$$

$$\frac{\partial u^{(3)}}{\partial t} = q \,, \tag{3.5c}$$

with the initial data $u_*^{(1)}(x, t^0) = u(x, t^0)$, $u_*^{(2)}(x, t^0) = u^{(1)}(x, t^0 + \Delta t/2)$ and $u_*^{(3)}(x, t^0 + \Delta t/2) = u^{(2)}(x, t^0 + \Delta t)$, respectively. The integration of the ordinary differential equations (3.5a) and (3.5c) can easily be performed (see e.g., [10]). More interesting is the numerical approximation of the homogeneous equation (3.5b), which will be discussed in the following.

As mentioned earlier, the computational domain Ω is discretized by a set of N non-overlapping quadrilateral or triangular mesh elements C_i ($\Omega = \bigcup_{i=1}^{N} C_i$) with the area V_i. Introducing the average u_i^n over the element C_i at time $t = t^n$ according to $u_i^n = \frac{1}{V_i} \int_{C_i} u(x, t^n) \, dV$, integrating each component of the homogenous equation (3.5b) over the space-time volume $C_i \times [t^n, t^{n+1}]$ and applying Gauß' theorem, we get the explicit FV scheme in conservation form

$$u_i^{n+1} = u_i^n - \frac{\Delta t}{V_i} \sum_{\alpha=1}^{\sigma_i} G_{i,\alpha}^{n+1/2} , \tag{3.6}$$

where the numerical flux $G_{i,\alpha}^{n+1/2} \approx \frac{1}{\Delta t} \int_{t^n}^{t^{n+1}} \int_{S_{i,\alpha}} \left[n_{i,\alpha}^{(1)} f_1(u) + n_{i,\alpha}^{(2)} f_2(u) \right] dS dt$ is an appropriate approximation of the physical flux normal to the side $S_{i,\alpha}$ of C_i. Furthermore, $\Delta t = t^{n+1} - t^n$, σ_i denotes the total number of faces of C_i and $n_{i,\alpha}^{(j)}$ abbreviates the jth component of the outwards directed unit normal at $S_{i,\alpha}$.

It is obvious that the explicit FV scheme (3.6) is completely declared if the numerical flux is specified as a function of u_i^n. To carry out this main task in the context of FV approximation, we compute the numerical flux with the aid of the solution of a Riemann problem (RP), which is an initial value problem with piecewise constant initial data [13, 18]. In the present case of the linear hyperbolic equations (3.4), the exact solution of the RP can be determined with the theory of characteristics. By the use of this solution, the local structure of wave propagation is directly incorporated into the numerical approximation, being the reason that the scheme is inherently very robust and able to resolve steep gradients without generating spurious oscillations.

A conclusive advantage of the RP based FV approach is the proper specification and implementation of boundary conditions. This is achieved by formulating an inverse RP whose solution yields the proper values which are prescribed at the border of the domain. A detailed description of these techniques including the numerical realization of physically occuring as well as computationally motivated boundary conditions is given in [22, 18, 10].

The outlined FV scheme is only first-order accurate in both space and time and introduces too much numerical dissipation for practical calculations. To remove this lack, well-established techniques can be applied and are reviewed, for instance, in [18, 10]. The resulting second-order accurate FV upwind-scheme is algorithmically realized as standard Maxwell solver in the KADI2D (quadrilateral grid zones) and KADI$_3^2$D (triangular or tetrahedron mesh elements) simulation program.

4. Diode Simulation using KADI2D

In this section we present two simulation results of the time-dependent behavior of the applied-B ion diode [6] obtained with the simulation program KADI2D. With these examples, we want to demonstrate the quality as well as the relevance and reliability of the applied approximation techniques for the complex numerical diode model.

In order to study the general features of the numerical model for the ion diode, we consider first a purely electromagnetic simulation, which means, that particle emission from the anode plasma and cathode tip is suppressed. For the calculation we prescribe perfect conducting wall conditions at the entire left and right border of the diode while the z-axis is the axis of rotational symmetry. At the upper boundary electromagnetic energy is irradiated into the ion diode by exciting the E_1 component of the electric field. Due to this special choice of irradiation only transverse electric waves will propagate in the device. To get an impression of the
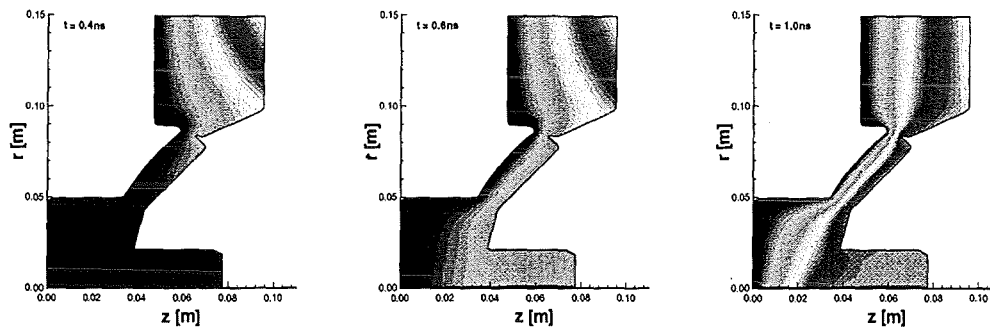
FIGURE 1. Sequence of spatial distribution plots of the electric potential monitoring the temporal evolution of the propagating wave in the ion diode.

temporal evolution of the fields inside the diode, three snapshots of the electric potential are seen in Figure 1 recorded at $t = 0.4$ ns, $t = 0.6$ ns and $t = 1.0$ ns, respectively. Obviously, the propagation of the transverse electric wave in the diode is clearly monitored by this sequence of plots. Furthermore, Figure 1 indicates that after $t = 1.0$ ns a smooth potential distribution has been formed in front of the anode surface. This is an important observation, especially, in view of ion acceleration in the anode-cathode gap which was also confirmed by stationary field calculations for this ion diode [25].

For the second numerical experiment the complexity of the numerical ion diode model is increased: We allow now that macro electrons can be emitted into the interior of the diode from several cells around the cathode tip. In each of these emission cells a macro electron with charge depending on the actual electric field strength and charge density is created and, afterwards, accelerated to the anode surface side. A typical simulation result for the self-consistent formation and development of the monopolar electron flow within the present diode model is depicted in Figure 2. Three snapshots of the electron distribution inside the diode and the corresponding charge density are presented at $t = 0.4$ ns, $t = 0.6$ ns and $t = 1.0$ ns, respectively. As can be seen from Figure 2, the electrons perform a complicated motion inside the anode-cathode gap. This motion is influenced by the magnetic fields induced by the movement of the particles themselves as well
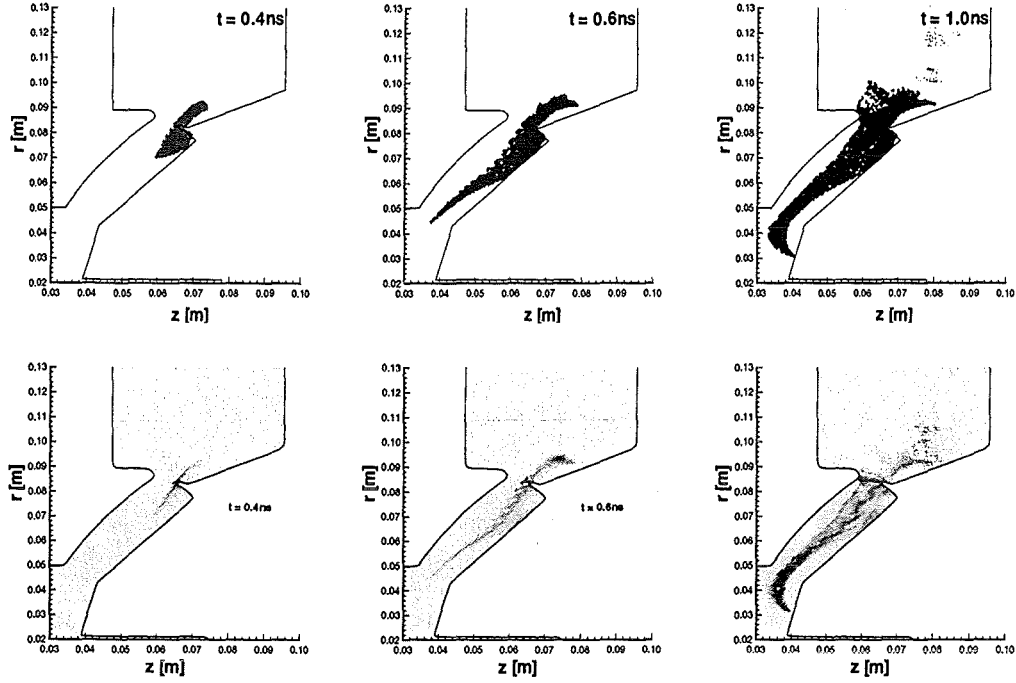
FIGURE 2. Time-dependence of the electron cloud formation (upper row) and the corresponding charge density (lower row of plots) inside the diode gap obtained from a self-consistent monopolar electron flow simulation with KADI2D.

as by the external magnetic field in the (z, r)-plane, resulting in an electron drift in the gap perpendicular to the electric and magnetic fields.

5. HYPERBOLIC CHARGE CORRECTION APPROACH

It is a well-known observation, that the different steps of particle treatment introduce numerical errors and, consequently, charge conservation is not guaranteed on this discrete level of approximation. To get rid of this numerically caused lack, sophisticated correction techniques to enforce Gauß' law have been proposed [9, 7, 15]. Here, we describe the correction of the electric field, as the discrepancy in charge conservation only affects this quantity. For that, we introduce the Lagrange multiplier Φ similar to Assous et al. [2], retain Faraday's law and replace Ampère's and Gauß' law by the strictly hyperbolic problem

$$\frac{\partial \boldsymbol{E}}{\partial t} - c^2 \nabla \times \boldsymbol{B} + c^2 \nabla \Phi = -\frac{\boldsymbol{j}}{\epsilon_0}, \tag{5.7a}$$

$$\frac{1}{\chi^2}\frac{\partial \Phi}{\partial t} + \nabla \cdot \boldsymbol{E} = \frac{\rho}{\epsilon_0}, \tag{5.7b}$$

where the magnitude of the parameter χ has to be estimated numerically. This system can be written as a hyperbolic evolution equation in the form (3.4) but now for the vector $\boldsymbol{U}(x,t) = (E_1, E_2, E_3, B_1, B_2, B_3, \Phi)^T$ [22, 18]. A detailed analysis of this system reveals that the information of correction does not spread out with infinite speed but with finite velocity χc, where χ is assumed to be larger than one. Empirically, we found that χ has to be chosen between two and four, leading to a severe restriction of the time step size given by the CFL-condition. Nevertheless, an efficient solution for large values of χ is possible by splitting up the system (5.7) (plus Faraday's law) into the evolutionary Maxwell equations and a correction system, containing all the terms involved by the Lagrange multiplier [22, 18]. Then, a sub-cycling procedure for the correction system can easily be
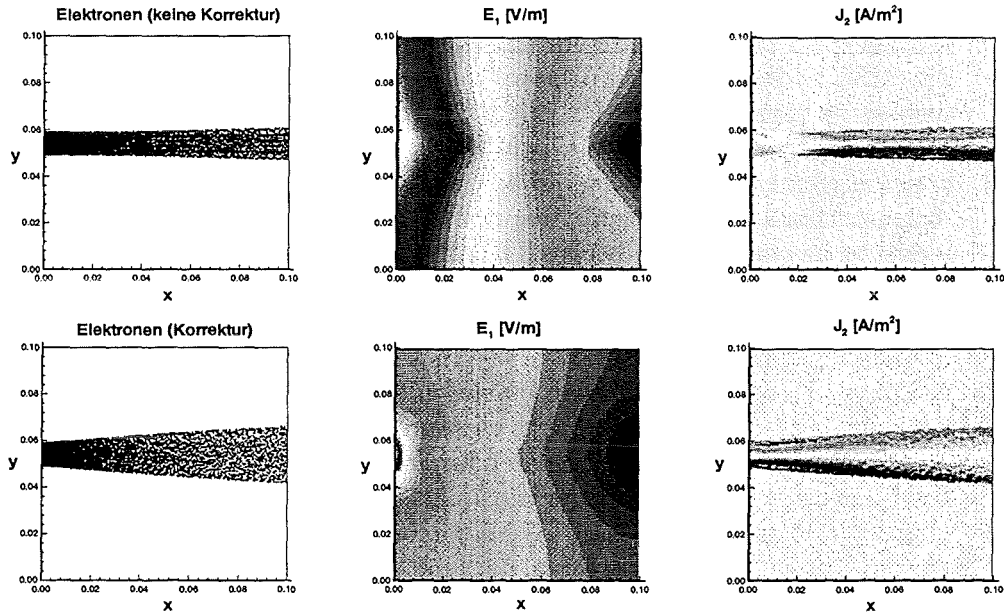
FIGURE 3. Self-consistent electron beam simulation in an external applied electric field without charge correction (upper row of plots). The results enforcing charge conservation by the hyperbolic correction technique ($\chi = 3$) are given in the lower sequence of pictures.

incorporated into the existing FV Maxwell solver resulting in an efficient hyperbolic correction scheme, being more the 20 % faster than the implicit charge correction approximation [7]. Furthermore, the hyperbolic correction approach is parallel in nature and, consequently, fitting in an excellent manner in our parallelization endeavor of KADI2D and KADI$_3^2$D .

The importance of electric field correction is explicitly seen in Figure 3, where an electron beam is emitted at the cathode ($x = 0$) and accelerated to the anode ($x = 0.1$ m) under the action of a constant external field E_1. The upper three plots show the simulation results where no charge correction is performed: the

electron distribution indicates constriction and filamentation of the beam while nonphysical gradients are observed in the electric field, both as a consequence of numerical errors in charge conservation. The situation is drastically improved towards physical reliance (lower row) performing the proposed strictly hyperbolic charge correction with $\chi = 3$.

6. Parallel Finite-Volume Maxwell Solver

Realistic numerical simulations of large and complicated-shaped technical systems - like ion diodes - with high precision require to exploit the full potential of modern supercomputers. In order to get in near future a very efficient diode simulation program being able to use the capacity of the parallel platforms available at the University and Forschungszentrum Karlsruhe (IBM RS/6000 SP with 256 RISC nodes and SNI vpp300 with 16 vector processors), we developed, in first instance, a highly portable FV Maxwell solver for the KADI2D code [20].

To transform the serial to a parallel Maxwell solver, we apply domain decomposition concepts (cf. [1]), subdividing the computational domain in equidistant stripes which are subsequently mapped onto the processor domains. This strategy seems to be very flexible because it can be applied, in principle, for an arbitrary number of processors and, apart from that, this decomposition leads to a natural load balancing. The explicit communications and synchronizations of the processors are organized with the aid of the message passing model and are realized by the software tool called Message Passing Interface (MPI). From the decomposition structure it is further obvious, that each processor needs only a small subset of the data of the entire computational domain, and information exchange only occur at the border of the processor domains. This high data locality suggest to use the single program multiple data (SPMD) model, where the same program runs on each processor with the individual data information provided by the pre-processing procedure.

The new parallel Maxwell solver was validated for standard test cases, yielding identical numerical results as the serial code and, hence, revealing that the interprocessor communications are well organized and correctly implemented. Furthermore, the parallel performance of the KADI2D Maxwell solver has been extensively investigated with the aid of usual criteria, like speedup and efficiency (for the definition of these quantities we refer to [20] and the references given therein). A series of measurements reveal that the performance of the parallel Maxwell solver depends significantly form the size of the computational grid (problem size) as well as from the computational effort [20]. A very impressive measurement result obtained with the second-order accurate parallel Maxwell solver is depicted in Figure 4 . There, we observe that the execution time for the 16 times larger problem on the SP (upper left) and the eight times larger problem on the vpp300 (lower left) is nearly the same as the corresponding single processor time. This result clearly indicates that the parallel Maxwell solver is scalable regarding to the computation time. Hence, the time required for the problem of size n executed on one processor is roughly the same as for the problem of size $n \cdot p$ on p processors.
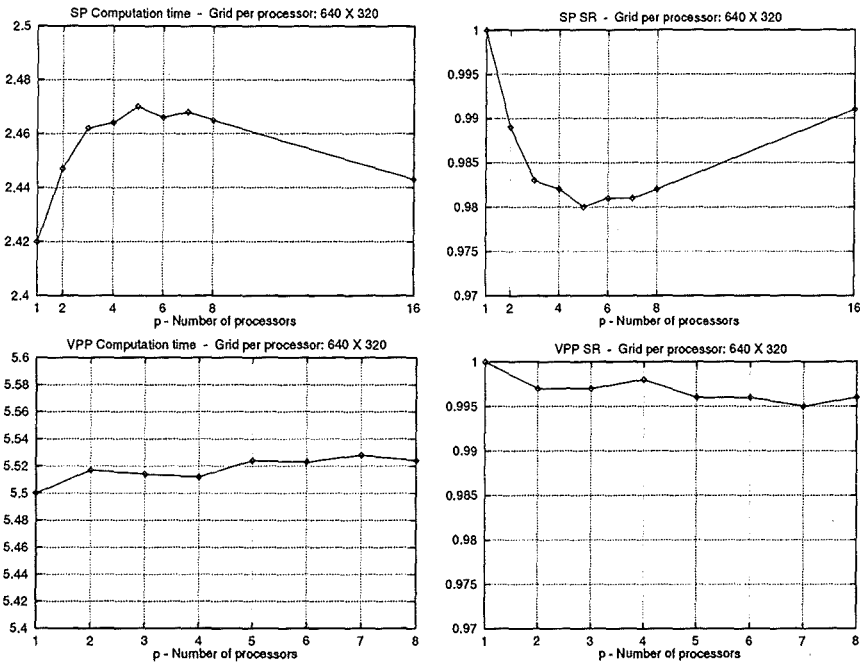
FIGURE 4. Computation time per time step and scalability of the computation time for the SP (upper plots) and VPP300 (lower pictures) for the 640 × 320 computational grid. The second-order accurate Maxwell solver is used for these calculations.

7. CONCULSIONAL REMARKS

Solving numerically the Maxwell-Lorentz equations, the coupling of a robust FV Maxwell solver with the PIC method is a new and powerful alternative to approximations commonly applied in the field of self-consistent charged particle simulations in electromagnetic fields. Simulation results of the time-dependent behavior of the ion diode presented in this paper demonstrate the properties and quality of the new FV-PIC approach. Furthermore, these calculations reveal the relevance of this new numerical tool for advanced simulations and investigations of technical devices. Further activities will concern the improvement of particle emission models and the extension of charge correction techniques as well as the assessment of the unstructured grid based $KADI_3^2D$ code to the last detail. Parallelized versions of the the entire KADI2D and $KADI_3^2D$ program systems are also under development.

References

[1] M. Alef, *Concepts for efficient implementation of multigrid methods on SUPRENUM-like architectures*, Kernforschungszentrum Karlsruhe GmbH, **KfK 4614**, (1989).

[2] F. Assous, P. Degond, E. Heintze, P. Raviart, and J. Segré, *On a finite-element method for solving the three-dimensional Maxwell equations*, J. Comput. Phys., 109 (1993), pp. 222–237.

[3] F. Assous, P. Degond, and J. Segré, *A particle-tracking method for 3D electromagnetic PIC codes on unstructured meshes*, Comput. Phys. Commun., 72 (1992), pp. 105–114.

[4] C. Birdsall and A. Langdon, *Plasma Physics via Computer Simulation*, McGraw-Hill, New York, 1985.

[5] H.-J. Bluhm, P. Hoppé, H. Bachmann, W. Bauer, K. Baumung, L. Buth, J. Greenly, H. Karow, D. Rusch, E. Stein, and O. Stoltz, *Progress in the development of a high power focusing B-applied extractor type ion diode for the 1.5 TW pulse generator KALIF*, in Proc. 8th Int. Conf. on High-Power Particle Beams, Novosibirsk, Singapore, 1990, World Scientific, pp. 451–456.

[6] H.-J. Bluhm, P. Hoppé, H. Laqua, and D. Rusch, *Production and investigation of TW proton beams for an annular diode using strong radial magnetic fields and a preformed anode plasma source*, IEEE Trans. Plasma Sci., 80 (1992), p. 995.

[7] J. Boris, *Relativistic plasma simulations – Optimization of a hybrid code*, in Proc. 4th Conf. on Num. Sim. of Plasmas, NRL Washington, Washington DC, 1970, pp. 3–67.

[8] J. Cioni, L. Fezoui, and D. Issautier, *High order upwind schemes for solving time-domain Maxwell equations*, La Recherche Aérospatiale, 5 (1994), pp. 319–328.

[9] J. Eastwood, *The virtual particle electromagnetic particle-mesh method*, Comp. Phys. Commun., 64 (1991), pp. 252–266.

[10] M. Fedoruk, C.-D. Munz, P. Omnes, and R. Schneider, *A Maxwell-Lorentz solver for self-consistent particle-field simulations on unstructured grids*, Forschungszentrum Karlsruhe – Technik und Umwelt, **FZKA 6115**, (1998).

[11] E. Halter, M. Krauss, C.-D. Munz, R. Schneider, E. Stein, U. Voss, and T. Westermann, *A concept for the numerical solution of the Maxwell-Vlasov system*, Forschungszentrum Karlsruhe – Technik und Umwelt, **FZKA 5654**, (1995).

[12] R. Hockney and J. Eastwood, *Computer Simulation using Particles*, McGraw-Hill, New York, 1981.

[13] R. LeVeque, *Numerical Methods for Conservation Laws*, Birkhäuser, Basel, 1990.

[14] R. Löhner and Ambrosiano, *A vectorized particle tracer for unstructured grids*, J. Comput. Phys., 91 (1990), pp. 22–31.

[15] B. Marder, *A method incorporating Gauß' law into electromagnetic PIC codes*, J. Comput. Phys., 68 (1987), pp. 48–55.

[16] R. Morse and C. Nielson, *Numerical simulation of the Weibel instability in one and two dimensions*, Phys. Fluids, 14 (1971), p. 830.

[17] C.-D. Munz, R. Schneider, E. Sonnendrücker, E. Stein, U. Voss, and T. Westermann, *A Finite-Volume Particle-in-Cell Method for the Numerical Treatment of the Maxwell-Lorentz Equations on Boundary-Fitted Meshes*, Int. J. Numer. Meth. Engng., accepted for Publication, (1998).

[18] C.-D. Munz, R. Schneider, and U. Voss, *A finite-volume method for Maxwell equations in time domain*, appears in SIAM J. Sci. Comput., (1997).

[19] ——, *A Finite-Volume Particle-in-Cell Method for the Numerical Simulation of Devices in Pulsed Power Technology*, Surveys in Mathematics for Industry; Special Issue: Scientific Computing in Electrical Engineering, accepted for publication, (1998).

[20] F. Rotzinger, *Parallelisierung eines expliziten Finite-Volumen-Verfahren zur Lösung der zeitabhängigen Maxwellgleichungen*, Diploma Thesis, Fakultät für Mathematik der Universität Karlsruhe, (1998).

[21] J. Thompson, Z. Warsi, and C. Mastin, *Boundary-fitted coordinate systems for numerical solution of partial differential equations - A review*, J. Comput. Phys., 47 (1982), p. 1.

[22] U. Voss, *Finite-Volumen-Verfahren für die instationären Maxwellgleichungen*, Forschungszentrum Karlsruhe – Technik und Umwelt, **FZKA 5884**, (1997).

[23] T. Westermann, *Localization schemes in 2D boundary-fitted grids*, J. Comput. Phys., 101 (1992), p. 307.

[24] ———, *Numerical modelling of the stationary Maxwell-Lorentz system in technical devices*, Int. J. Num. Mod., 7 (1994), pp. 43–67.

[25] ———, *Particle-in-cell simulations with moving boundaries – Adaptive mesh generation*, J. Comput. Phys., 114 (1994), pp. 161–175.

INFLUENCE OF ELECTRONS REFLECTED FROM A TARGET ON THE OPERATION OF DIODE AND TRIODE ELECTRON SOURCES

V.Engelko[2], V.Kuznetsov[2], G.Mueller[1], G.Viazmenova[2]

1- Forschungszentrum Karlsruhe, INR, Postfach 3640, D-76021 Karlsruhe, Germany
2- Efremov Institute of Electrophysical Apparatus, 189631, St. Petersburg, Russia

Abstract

When an electron source and a target are immersed in an external magnetic field electrons reflected from the target can not disappear but move back along the magnetic force lines and reenter the source region, where they are stopped by the electric field and rereflected to the target. The penetration of these electrons into the source can lead to a distortion of the electric field and through this to changes of the equilibrium current density emitted from the cathode. First results from calculations of the equilibrium current densities occurring in electron diodes and triodes under these conditions are presented. The space charge density distribution resulting from reflected electrons has been calculated taking into account their real energy spectrum obtained from Monte - Carlo simulations. It was found that the penetration of reflected electrons into a diode can significantly decrease the equilibrium current density. When the electrons are reflected back with their incident energy, the maximum reduction factor for the current density is between 3 and 2 for reflection coefficients of k=1 and k=0.5 respectively. For tungsten the current density depression is around 1.5 at more realistic energy spectra. The results of these calculations are in a good agreement with experimental data. The analysis performed shows that the consideration of reflected electrons is necessary if accurate calculations of the specific beam energy deposition in the target are desired .

Introduction

It is well known that the probability of reflection of fast electrons from an irradiated target depends on the charge number of the target material and for high-Z elements can be rather high. For example, for tungsten it is close to 50 % . If the irradiation of a target is performed without an external magnetic field, preventing the transverse motion of reflected electrons, electrons can leave the target and escape to the wall of the transport channel or of the vacuum chamber. In this case the reflection of electrons influences the energy transfer to the target only indirectly, because part of it is carried away by the reflected electrons. In the case of intense electron beams an external magnetic field is frequently used for transportation to the target. This field prevents the motion of reflected electrons in the transverse (relatively to the field) direction . Therefore, electrons moving along magnetic field lines can reach the electron source where they are rereflected by the source electric field. Penetration of reflected electrons into the source can lead to a distortion of the electric field and through this to changes of the equilibrium current density emitted from a cathode. The influence of electrons reflected from a target on the current of an electron beam produced by a coaxial magnetically insulated diode was considered in [1]. Taking into account the angular spread of the reflected electrons the authors

found from calculations that a 50% reflection of beam electrons leads to a decrease of the beam current by 40 %. Despite the fact that the experimentally observed decrease of the beam current is smaller than that theoretically predicted the results obtained in [1] confirm that the influence of reflected electrons on the operation of electron sources and on the energy delivered to a target can be significant. This is very important when an electron beam is used for the modification of material surfaces. Presently two types of electron sources are used for the production of intense pulsed electron beams for this purpose: diodes and triodes. A triode electron source is used, for example, at the GESA facility [2]. In order to quantity the influence of reflected electrons on the emitted current density for these schemes we performed calculations taking into account both the energy and the angular distributions of the reflected electrons. Results from these investigations are presented below.

Method of calculation

Diode. Let as consider a diode, consisting of two planar electrodes and containing a magnetic field perpendicular to the electrode surfaces. As usual to determine the equilibrium emission current density we will use the Poisson equation with zero boundary conditions at the cathode surface
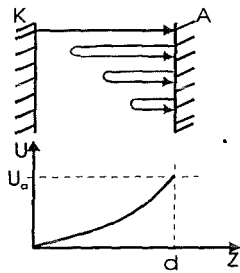
$$\frac{d^2U}{dz^2} = \frac{\rho_1}{\varepsilon_0} + 2\frac{\rho_2}{\varepsilon_0},$$ (1)

$$U(0) = U'(0) = 0,$$
$$U(d) = U_a ,$$

Fig. 1: Diode scheme

where ρ_1 and ρ_2 are the space charge densities of primary and reflected electrons respectively, U is the potential, d the interelectrode gap, ε_0 the dielectric constant. The space charge of the reflected electrons is counted for two times, because they move twice through each cross-section inside the diode.

As usual the density of the beam electrons is connected with their current density j_1 through the relation

$$\rho_1 = \frac{j_1}{\sqrt{\frac{2e}{m}U}} \cdot ,$$ (2)

where e and m are the electron charge and mass respectively.

Integrating equation (1) one can obtain the following expression for the equilibrium current density in the presence of reflected electrons

$$j_1 = \frac{1}{2}\varepsilon_0\sqrt{\frac{2e}{m}}M\frac{U_a^{3/2}}{d^2},$$ (3)

where the parameter M is determined by the energy distribution of the reflected electrons through the following relationships:

$$M = \left[\int_0^1 \frac{d\varphi}{\sqrt{F_1(\varphi)}}\right]^2 ; \qquad F_1 = 2\varphi^{1/2} + \frac{2k}{C_0}\int_0^{\varphi} F_{01}(\varphi)d\varphi ;$$

$$F_{01}(\varphi) = \int_{1-\varphi}^{1} \frac{\dfrac{dj_2}{d\varepsilon}d\varepsilon}{\sqrt{\varepsilon - (1-\varphi)}} ; \qquad C_0 = \int_0^1 \frac{dj_2}{d\varepsilon}d\varepsilon , \qquad (4)$$

where $\varepsilon = E_0/(E_0)_{max} = U_0/U_a$; E_0 is the initial energy of the reflected electrons; $\varphi = U/U_a$; $dj_2/d\varepsilon$ is the energy distribution of the reflected electrons.

Triode. In the case of a triode scheme the mathematical approach is the same but now Poisson's equation has to be solved separately for two gaps: the cathode-grid gap and grid-anode gap. We will consider here a special type of the triode in which the grid and the anode are connected through a resistor R_g. In this case the grid potential depends on the current to the grid and on the magnitude of R_g. Therefore one can control the grid potential (and through this the equilibrium current density) simply by changing the resistor magnitude.

It is known that in the general case the distribution of the potential in the grid-anode gap can have a minimum whose value U_m can be less then the grid potential U_g. It is clear that if the potential distribution has such a form, the space charge distribution of the reflected electrons in the cathode-grid gap will be sensitive to U_m (or φ_m) because the region with $\varphi < \varphi_m$ can be reached by reflected electrons whose initial energy ε is not less then $1-\varphi_g$, but the region with $\varphi_m < \varphi < \varphi_g$ is accessible for electrons with $\varepsilon \geq 1-\varphi_m$. Taking this into account we can write the following set of equations for the determination of the equilibrium current density in the triode.
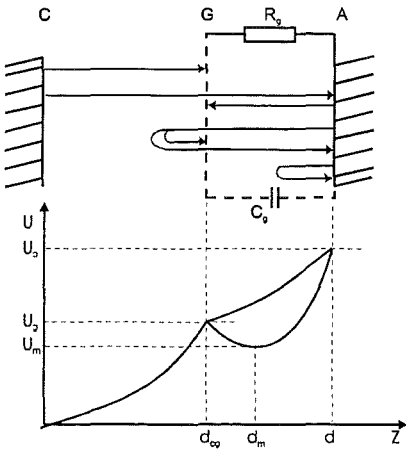
$$\frac{d^2\varphi}{dz^2} = \frac{1}{\varepsilon_0 \cdot U_a}(\rho_1 + 2\rho_2), \qquad (5)$$

$$1 - \varphi_g = v_R \cdot j_1(\varphi_g, \varphi_m) \cdot S_k \cdot R/U_a, \qquad (6)$$

$$\varphi(0) = \varphi'(0) = 0, \quad \varphi(d_{cg}) = \varphi_g, \qquad \varphi(d) = 1.$$
(7)

Fig.2: Triode scheme

Here: $v_R = (1 - \alpha + k\alpha \cdot k_m - k\alpha^3 \cdot k_m)$ - is the coefficient accounting for the current to the grid of both, primary and reflected electrons, S_k - is the cathode area, α - is the grid transparency, k_m - is the coefficient, determining that part of electrons which has passed through φ_m and penetrated into the cathode-grid gap.

After integration one can find the dependence of the equilibrium current density j_1 on φ_g and φ_m:

$$j_1 = \frac{1}{2}\varepsilon_0\sqrt{\frac{2e}{m}}M_1(\varphi_g,\varphi_m)\frac{U_a^{3/2}}{d_{cg}^2}, \quad \text{where} \quad M_1(\varphi_g,\varphi_m) = \left[\int_0^{\varphi_g}\frac{d\varphi}{\sqrt{F_{11}(\varphi,\varphi_m)}}\right]^2, \tag{8}$$

$$F_{11} = \begin{cases} 2\varphi^{1/2} + \dfrac{2k\alpha^2}{C_0}\displaystyle\int_0^{\varphi}F_{01}(\varphi)d\varphi, & \text{for } 0<\varphi<\varphi_m, & \text{9a)} \\[3mm] 2\varphi^{1/2} + \dfrac{2k\alpha^2}{C_0}\displaystyle\int_0^{\varphi_m}F_{01}d\varphi + \dfrac{2k\alpha^2}{C_0}\displaystyle\int_{\varphi_m}^{\varphi}F_{02}d\varphi, & \text{for } \varphi_m<\varphi<\varphi_g & \text{(9b)} \end{cases}$$

$$F_{02} = \int_{1-\varphi_m}^{1}\frac{\frac{dj_2}{d\varepsilon}d\varepsilon}{\sqrt{\varepsilon-(1-\varphi)}}, \quad M_2(\varphi_m) = \left[\int_{\varphi_m}^{\varphi_c(\varphi_m)}\frac{d\varphi}{\sqrt{F_{12}(\varphi,\varphi_m)}}\right]^2, \quad M_3(\varphi_m) = \left[\int_{\varphi_m}^{1}\frac{d\varphi}{\sqrt{F_{13}(\varphi,\varphi_m)}}\right]^2 \tag{10}$$

The magnitudes of j_1, φ_g and φ_m are determined from equations (6), (8) and (11)

$$d_{ga} = z_{ga}(\varphi_m) = \left[\frac{1}{2}\varepsilon_0\sqrt{\frac{2e}{m}}\frac{U_a^{3/2}}{j_1(\varphi_m)}\right]^{1/2}\cdot\left(M_3^{1/2}(\varphi_m) + M_2^{1/2}(\varphi_m)\right) \tag{11}$$

If φ_m is absent than F_{11} is determined by (9a), j_1 and φ_g can be obtained from (6) and (8).

Inclusion of angular distribution

The angular distribution of reflected electrons can be described accurately by the function $\cos\theta$ for various materials [3]. Taking this into account one can refine the expressions for F_{01}, F_{02}, F_{03}.

$$F_{01}(\varphi) = \frac{\pi}{2}\int_{1-\varphi}^{1}\frac{\frac{dj_2}{d\varepsilon}d\varepsilon}{\varepsilon^{1/2}}, \quad F_{02}(\varphi) = \int_{1-\varphi_m}^{1}\frac{\frac{dj_2}{d\varepsilon}\arcsin\left[\frac{\varepsilon-(1-\varphi_m)}{\varepsilon-(1-\varphi)}\right]^{1/2}d\varepsilon}{\varepsilon^{1/2}}, \quad F_{03}(\varphi) = \frac{\pi}{2}\int_{1-\varphi}^{1-\varphi_m}\frac{\frac{dj_2}{d\varepsilon}d\varepsilon}{\varepsilon^{1/2}} \tag{12}$$

The expressions for $F_1(\varphi)$, $F_{11}(\varphi,\varphi_m)$, $F_{12}(\varphi,\varphi_m)$, $F_{13}(\varphi,\varphi_m)$, M, M_1, M_2, M_3 and j_1 remain unchanged.

Results of calculations

Modeling functions for the energy distribution of reflected electrons

Calculations performed with special energy distributions (uniform, linear, and δ-function) showed that reflected electrons can appreciably decrease the equilibrium current density of an electron source. The results are shown in Fig. 3 - 4.
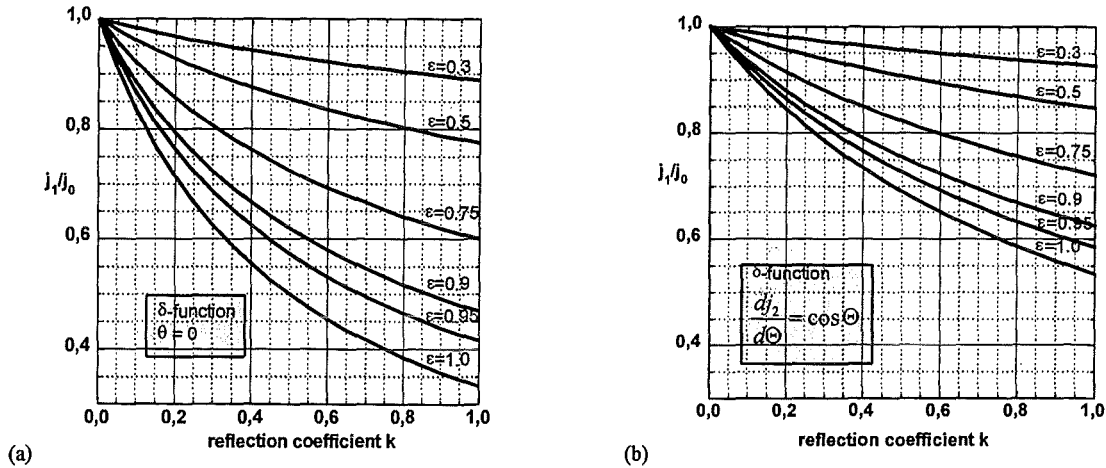

(a)   (b)

Fig. 3: Results of calculations for a δ-function energy distribution of the reflected electrons and for different reflection coefficients without taking into account the angular distribution (a) and with angular distribution (b).

(a)   (b)
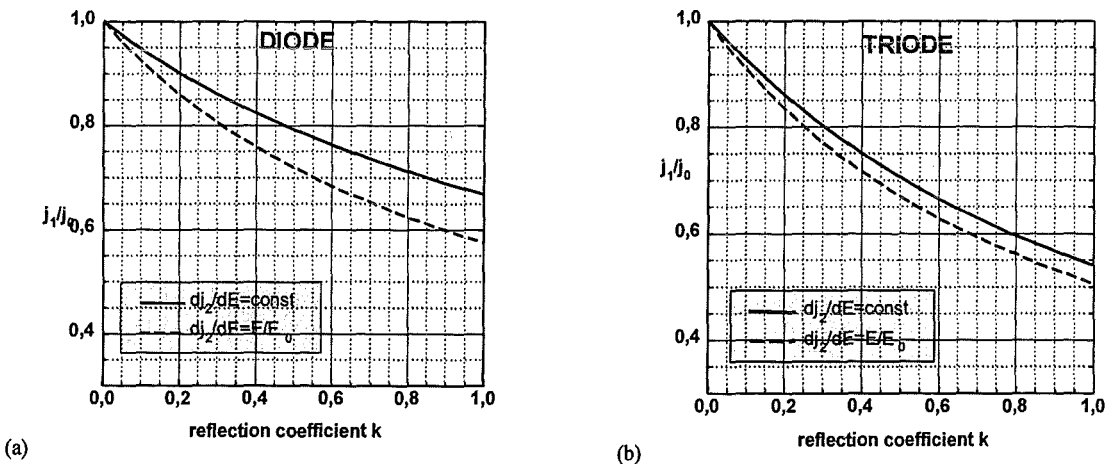
Fig. 4: Results of calculations for a uniform and a linear energy distribution of the reflected electrons for different reflection coefficients for diode (a) and triode (b) schemes.

The maximum theoretical reduction factor for the current density $(\varepsilon = k = 1)$ from a diode is as high as 3 (Fig. 3a). This result is obvious without any calculations. The angular spread of the reflected electrons leads to an increase of the emission current density (Fig. 3b), because the angular distribution reduces the number of reflected electrons which can reach the region close to the cathode.

Fig.4 shows the dependence of the relationship j_1/j_0 on k for uniform and linear energy distributions for diode and triode schemes. Results for the triode scheme were obtained under conditions corresponding to the GESA facility: $U_a = 120\ kV$, $d_{cg} = 6\ cm$, $d_{ga} = 12\ cm$, $\alpha = 0.8$. $R_g = 580\ \Omega$

One can see that for both, diodes and triodes, the influence of reflected electrons on j_1 in the case of a linear energy distribution is somewhat larger than in the case of a uniform one, because in the latter case a smaller fraction of the reflected electrons can reach the cathode region. In the

case of a triode the source current j_1 decreases faster than for a diode because, part of the reflected electrons is absorbed by the grid, and therefore the potential drop between the cathode and the grid is reduced.

Real energy distribution of reflected electrons
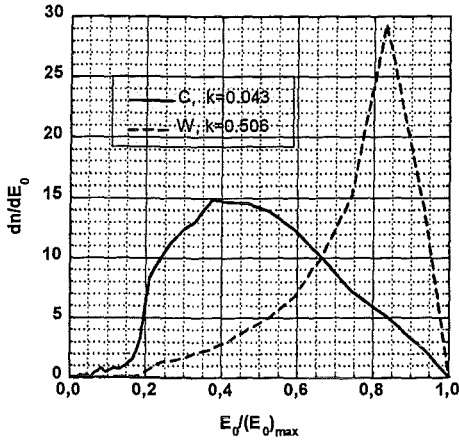
Fig. 5: Real energy distribution of reflected electrons for C, W as anode material (angle of incidence 0°)

Real energy distributions and reflection coefficients were obtained with the help of Monte-Carlo simulations. Fig.5 shows the energy distributions for carbon and tungsten targets. In table 1 results of calculations for a diode scheme are presented. One can see that in the case of reflected electrons from tungsten a large reduction*(~38%)* of the emitted current density occurs.

In the case of carbon the reduction of the emitted current density is not very significant *(~10%)*. The relationship between the emitted current densities for carbon and tungsten anodes is equal to $j_1^c / j_1^w = 1.45$

Calculations for the triode scheme of the source were performed for conditions corresponding to measurements at the GESA-facility, which were mentioned above. The numerical results are given in table 2. Besides the ratio j_1/j_0 the influence of the reflected electrons on the grid potential (U_g/U_a) is shown for both materials. For tungsten the grid potential decreases due to the larger reflection coefficient k.

| C		W	
k=0.04	j_1/j_0=0.90	k=0.51	j_1/j_0=0.62

Table 1: Results of calculations for C and W with real energy distributions of the reflected electrons for a diode scheme

The most important value from a practical point of view is the current density j_a at the anode. The ratio between the current density for graphite and tungsten at the anode is $j_1^c / j_1^w = 1.71$, which is somewhat higher than for the diode source.

C	W
U_g/U_a=0,44	U_g/U_a=0,36
j_1/j_0=0,96	j_1/j_0=0,68
j_a/j_0=0,76	j_a/j_0=0,44

Table 2: Results of calculations for C and W with real energy distribution of reflected electrons for triode scheme
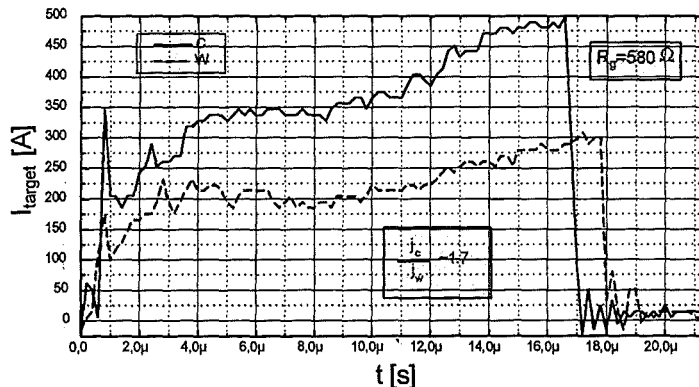

Fig. 6: Target (anode) current measured at the GESA facility for C and W as target material.

In Fig. 6 the results of experimental measurements performed at the GESA facility for two different target materials (C, W) are shown. From this measurement we have a factor of ≈ 1.7, which is in very good agreement with theoretical calculations.

Conclusions

The influence of electrons reflected from a target in the presence of an external magnetic field on the equilibrium emission current density in diode and triode electron sources has been analyzed taking into account the energy and angular distributions of the reflected electrons. It was found that reflected electrons can appreciably decrease the equilibrium current density of an electron source. When electrons are reflected with their incident energy [the energy distribution being a δ-function] the maximum reduction of the current density is as high as 3 and 2 for reflection coefficients of $k=1$ and $k=0.5$ respectively. The realistic reduction of the current density for a tungsten target is 1.5. This is in a good agreement with experimental observations. The results show that a consideration of the reflected electrons is necessary for a correct calculation of the beam energy deposition into a target and for a better understanding of the electron source operation.

References

[1]. N.I.Zaitsev et al. Sov. J. Plasma Phys. 8(5), Sept.-Oct. 1982, p.515.

[2]. G.Mueller et al. Proc.11-th Int. Conf. High Power Particle Beams, Prague, 1996, vol.1, p.267.

[3]. R.W.Dressel, Phys. Rev. **144**, 1962, p.332

A lens model for applied-B ion diodes[1]

I.S.Landman, H.Würz

1. Troitsk Institute for Innovation and Fusion Research, 142092 Troitsk, Russia
2. Forschungszentrum Karlsruhe, INR, Postfach 36 40, D-76021 Karlsruhe, Germany

Abstract

The sensitivity of a one-dimensional modeling of ion diodes with applied magnetic field is clarified with respect to principally 2 dim effects which could be of importance for diodes of the extraction type with their focus rather far from the electrodes. A perturbation analysis based on the relativistic Hamilton function for particles and the Vlasov-Maxwell model for the plasma was developed. The Desjarlais 1 dim model was used as initial approximation. First and second order corrections to the 1 dim solution are used for calculating the focal distance of an ion beam.

The gap between the anode and cathode is considered as a lens that distorts slightly the ion trajectories. The magnetic field generated by the electric current of the diode causes beam focusing. The effect is shown to be of the order of $(V_i/c)^2 \ll 1$ with V_i the velocity of accelerated ions and c the velocity of light. Distortion of the virtual cathode due to the diamagnetic current of the $\mathbf{E} \times \mathbf{B}$ electron drift causes an additional focusing of the order of $(\upsilon_D/c)^2 \ll 1$ with υ_D the characteristic drift velocity.

From the analysis it is concluded that the 1 dim approach is quite adequate for applied-B diodes as long as only the above mentioned focusing mechanisms are most important. Thus numerical simulation may focus mainly on the investigation of small scale turbulent perturbations caused by instabilities in the gap.

1. Introduction

Essentially two theories are available for describing the operation of a diode principally: the first one of M. Desjarlais [1] and the second one of A.V. Gordeev and A.V. Grechikha [2]. Numerical codes for detailed calculations based mainly on the Particle In Cell simulation (PIC method) of Vlasov-Maxwell equations are also available [3] – [5]. In order to demonstrate the current state of diode investigations a short revue of these publications is given below.

The principal scheme of the diode is shown in Fig. 1 in the Cartesian x- and z-coordinates. In the perpendicular y-direction translation symmetry is assumed. Such plane approximation is rather usual for analytical models of both 'extraction' and 'radial' diode. Magnetic lines of the external field B_{app} belong to the xz-plane. The anode is located at $x = 0$. The cathode of size L is located between the two tips at $z = \pm L/2$. If voltage between the anode and cathode is applied then an ion beam is produced at the anode and a virtual cathode arises between the sharp ends of the tips. The virtual cathode consists of electrons which are produced from the tips of height h by means of field emission at $x = l$.

In Ref. [1] an idealized 1 dim model of the diode is considered. Ions are produced at the anode and are accelerated by the electric field. The electron density in the gap is assumed to be constant. The model explains the behavior of the diode in the frame of a quasi-stationary approach. Current collapse was predicted after the diode voltage reaches the value $\varphi_a = (5/9)A_a$ with A_a the vector potential at the anode. Magnetic self focusing was not modeled. The diamagnetic shift of the virtual cathode towards the anode surface was taken into account. The crossed magnetic and electric fields cause an $E \times B$ electron drift. Thus an additional electric current arises along the y-axis. This current changes the applied magnetic field non-homogeneously resulting in a pressure gradient which pushes the virtual cathode to the anode. However distortion of the virtual cathode was not modeled. Therefore diamagnetic focusing of the ion beam was not obtained. The turbulent behavior of the electrons as well as effects of plasma pressure are not considered in this model. This theory claims to describe the diode behavior before the voltage peak.

In Ref. [2] a turbulent distribution of magnetized electrons in the anode-cathode gap is considered in order to explain the unstable behavior of the diode in experiments just after the peak phase. The turbulence is a consequence of the development of the diocotron instability. Using the drift approximation for electrons and assuming a small field emission rate at the virtual cathode it was concluded that for 1 dim geometry the only adiabatic invariant B/n_e should be important for the electron distribution function. Thus the main principal development compared to Ref. [1] is the calculation of the density behavior.

The numerical code KADI2D [3] at FZK is still rather preliminary. A direct simulation of turbulent processes is under development. One of already developed parts of this code is a computational grid generator allowing to map realistic 2 dim geometrical configuration of the gap onto some regular data structure. Another developed part is the solver of the Vlasov-Maxwell problem on the base of the PIC and the Finite Volume (FV) methods.

In Ref. [4] the plasma evolution in the diode with resistive anode plasma layer is considered using a 2 dim PIC code in order to demonstrate the electron sheath collapse. The ion beam was ignored and the anode plasma resistivity was assumed to be constant. According to first results it seems that the physics of the developing collapse is similar to the interchange instability in the magnetic field. The destabilizing force is caused by the electric field which tries to push rather dense anode plasma through the rare electron sheath.

In Ref. [5] the code QUICKSILVER is described. It was used recently [6] for the numerical simulation of the Particle Beam Fusion Accelerator II. With PBFA II for Li^{+1} beams, pulse duration 20 ns, voltage 10 MV, ion current 0.7 MA, focal power density 1.4 TW/cm^2 an intrinsic beam divergence $\Delta\theta \approx 20$ mrad was obtained. The main goal of these

simulation is to find out how to reduce $\Delta\theta$ because for purposes of Inertial Confinement Fusion (ICF) it is necessary to achieve $\Delta\theta \approx 6$ mrad at 30 MV. This code may be considered as most advanced tool available for diode simulations. It is fully vectorized and equipped with many additional programming tools including a pre-processor for grid generation or an output post-processor. Its field solver utilizes both explicit and implicit finite-difference algorithms in Cartesian, cylindrical or spherical coordinate systems. A particle handler advances multiple particle species with three-dimensional relativistic kinematics. At simulations with the computer Cray YMP a three dimensional (r, ϕ, z-coordinates) spatial grid fits to the realistic diode geometry. At this the whole number of 3 dim cells exceeds 10^5, the required number of particles is of $3\ 10^6$. During one simulation the code completes $\sim 6\ 10^4$ time steps taking ~ 350 CPU hour. For feed line of the diode a simulation wave guide model was used.

2. Results from numerical simulations

Earlier simulations of the diode demonstrated the development of two distinct instabilities: the high frequency diocotron instability and a low frequency ion mode. The diocotron instability is responsible for the fast broadening of the initially narrow electron sheath of the virtual cathode. It arises from wave-electron resonance at the electron drift velocity. It is valid $\omega\tau_i \gg 1$ with ω the instability frequency and τ_i the ion gap transit time. The diocotron instability saturates after trapping of electrons by the waves. Then the electrons occupy the whole gap. Ions don't take part in this fast process, i.e. the diocotron instability doesn't induce significant ion beam divergence. In the course of voltage increase the ion current density J_i increases drastically exceeding the Child-Langmuir current J_{CL}. After the ratio $J_i/J_{CL} \sim 4$ - 8, an abrupt transition to the ion mode instability at much lower frequency ($\omega\tau_i < 1$) occurs which induces significant ion beam divergence.

Calculations of Ref. [6] also detected the diocotron instability early in time followed by a transition to the ion mode later. The characteristic period of the diocotron instability is less than 1 ns, and that of the ion mode is of 2 - 3 ns at $\tau_i \approx 2.5$ ns. The amplitudes of electric field strength of harmonic modes is less than 1 MV/cm. If the ion flux from the anode increases slowly enough, it may cause a delay of the development of the ion mode thus reducing the ion beam divergence.

3. Justification for this analysis

Diode investigations are mainly done by application of large codes. The physics models of the codes are based on the simplest theoretical approach realizing direct numerical solution of most general equations for the fields and matter. Theoretical ideas which allow to clarify effects principally as well as accelerate calculations drastically for the specific considered problem are not included.

Many-fold gain of efficiency may be realized after recognizing parameters intrinsically inherent in the problem (such as the relation $\eta = \lambda/r_e$ of characteristic wave length λ of the

instability to the electron gyro-radius r_e). Quite often situations realize where the problem exceeds the technical possibilities of the best computers. Thus making prior theoretical analysis and adequate problem reduction unavoidable. For example, according to a theoretical analysis [7] based on the weak turbulence approach [8] of anomalous electron diffusion across magnetic field in a magneto-electrostatic trap, the parameter η becomes important at $\eta \sim 1$, thus an adequate 3 dim numerical grid must contain more than $(L/r_e)^3 \sim 10^9$ cells for 100 eV electrons which is impossible to be handled by present day machines.

One remarkable feature of the calculational results from Ref. [6] is the rather low level of the perturbation fields in comparison with the quasi-stationary ones (for the electric field strength it was calculated $\delta E/E < 1/5$). Such smallness could be a quite natural assumption for the whole problem because the goal of diode investigations is minimization of the ion beam divergence which may be possible only at low perturbation levels.

Hence for the analysis of applied-B ion diode it is quite reasonable to use methods of perturbation theory. As an initial approximation a quasi-stationary state is assumed. The particle distribution function f_0 and the self-consistent field ψ_0 are reflecting the initial symmetry of the unperturbed system (e.g. independence on the coordinates y and z). In this paper only those small perturbations δf and $\delta \psi$ are considered which are caused by voltage increase. The equations for $f_0 + \delta f$, $\varphi_0 + \delta \psi$ are derived from general Vlasov and Maxwell equations using the Hamilton function of particles.

In chapter 4 general mathematical expressions are given and in chapter 5 a 1 dim model of the diode is considered describing the initial approximation. Principally this 1 dim approach is similar to the Desjarlais model [1]. First and second order corrections are then calculated in order to get the focal distance F. Thus the gap between the anode and cathode is considered as a lens that distorts slightly the ion trajectories. In chapter 6 the influence of a first order additional magnetic field generated by the electric current through the diode is analyzed. This field causes focusing of the ion beam because it bends the ion trajectories. In chapter 7 the focusing effect of the distortion of the virtual cathode is analyzed. This distortion is due to a diamagnetic electron drift current which decreases the magnetic strength near the cathode causing a second order 2 dim change of electric field in the gap. Thus the acceleration of ions changes its direction resulting in focusing.

4. General equations

The formulas of this chapter are taken from Ref. [9,10]. The relativistic Hamilton function H_α of an electron (index $\alpha = 'e'$) or ion ($\alpha = 'i'$) is given as:

$$H_\alpha(t,\mathbf{r},\mathbf{p}) = q_\alpha \varphi(t,\mathbf{r}) + \left(m_\alpha^2 c^4 + c^2 \left(\mathbf{p} - (q_\alpha/c)\mathbf{A}(t,\mathbf{r})\right)^2\right)^{1/2} \tag{1}$$

with charges $q_e = -e$ and $q_i = e$, masses m_α , the elementary charge e and the velocity of light c. The electromagnetic field is described with the scalar electric potential φ and the vector magnetic potential $\mathbf{A}$. Time t, position $\mathbf{r}$, canonical momentum $\mathbf{p}$ are the coordinates of the

problem. The field strengths **E** and **B** are expressed as $\mathbf{E} = -\partial\mathbf{A}/c\partial t - \nabla\varphi$ and $\mathbf{B} = -\nabla\times\mathbf{A}$. The Maxwell equations for the potentials φ and **A** are given with the Lorenz gauge as

$$\frac{\partial^2\varphi}{c^2\partial t^2} - \Delta\varphi = 4\pi e(n_i - n_e), \qquad \frac{\partial^2\mathbf{A}}{c^2\partial t^2} - \Delta\mathbf{A} = \frac{4\pi e}{c}(\mathbf{j}_i - \mathbf{j}_e) \qquad (2)$$

Density $n_\alpha(t,\mathbf{r})$ and flux $\mathbf{j}_\alpha$ $(t,\mathbf{r})$ are expressed via the distribution function $f_\alpha(t,\mathbf{r},\mathbf{p})$ and the velocity $\mathbf{v}_\alpha$:

$$n_\alpha = \int f_\alpha d^3p, \qquad\qquad \mathbf{j}_\alpha = \int \mathbf{v}_\alpha f_\alpha d^3p \qquad (3)$$

The momentum **p** is expressed as $\mathbf{p} = \gamma m_\alpha\mathbf{v}_\alpha + q_\alpha\mathbf{A}/c$ with the relativistic factor $\gamma = (1-v^2/c^2)^{1/2}$, $v = |\mathbf{v}_\alpha|$. Expressing γ from Eq. (1) and then $\mathbf{v}_\alpha$ via **p** it is obtained for the flux:

$$\mathbf{j}_\alpha = c^2 \int (H_\alpha - q_\alpha\varphi)^{-1}(\mathbf{p} - (q_\alpha/c)\mathbf{A})f_\alpha d^3p$$

The Vlasov kinetic equation for the function $f_\alpha(t,\mathbf{r},\mathbf{p})$ is given as

$$\frac{\partial f_\alpha}{\partial t} + \{H_\alpha, f_\alpha\} = 0 \qquad (4)$$

with $\{,\}$ the Poisson brackets. Boundary conditions for Eqs. (2) and (4) are given in the course of the further considerations.

5. Initial quasi-stationary approach

5.1. Formulation of the one dimensional problem.

Initially it is assumed that the diode operation is quasi-stationary and with translational symmetry along the y- and z-axes. The position $x = l$ in Fig. 1 corresponds to the undisturbed surface of the virtual cathode. The applied magnetic field is directed along the z-axis and is described by the y-component only: $\mathbf{A}_0 = (0, A_{y0}(x), 0)$. Both electric $\varphi_0(x)$ and magnetic $A_{y0}(x)$ potentials are zero at the cathode and assigned with given values $\varphi_0(0) = \varphi_a > 0$, $A_{y0}(0) = A_a$ > 0 at the anode.

The Hamilton function of Eq. (1) is represented as $H_{\alpha 0} = H_\alpha(A_{y0},\varphi_0,\mathbf{p})$. Due to the independence of $H_{\alpha 0}$ on t, y and z the Poisson brackets $\{H_{\alpha 0},H_{\alpha 0}\}$, $\{H_{\alpha 0},p_y\}$, $\{H_{\alpha 0},p_z\}$ are equal to zero, thus $H_{\alpha 0}$ and the momentum components p_y, p_z keep constant along an unperturbed particle trajectory. Eq. (4) gets stationary: $\{H_{\alpha 0},f_{\alpha 0}\} = 0$ showing that the value of the function $f_{\alpha 0}$ is also a trajectory integral.

Ions appear with zero velocity at the anode, pass the gap and disappear at the cathode. Thus their distribution function is determined by the anode emission. The x-component of the ion flux at the anode j_{ix1} is introduced with the additional index 1 that shows first order approximation values.

Electrons gyrating in the applied magnetic field can be characterized by the momentum component p_y. For small gyration radius the x-coordinate of the leading center $x_c(p_y)$ is found from the equation $p_y + eA_{y0}(x_c)/c = 0$ that follows from the condition that $H_{\alpha 0}$ is constant at $eA_{y0}/\gamma m_e c \gg v_\alpha$. Electron trajectories are infinite spirals along the z-axis, thus there is no boundary condition determining the electron distribution. Therefore in order to find

the physical solution for f_{e0} turbulent collisions are assumed to occur resulting in a local Maxwellian distribution. Then the equilibrium distribution is characterized by functions of the electron density $n_{e0}(p_y)$ and electron temperature $T_{e0}(p_y)$ at $z = 0$. The Maxwell equations and those for the densities and the electron flux Eqs. (2) and (3) are also reduced to 1 dim expressions. The density n_{i0} is obtained as:

$$n_{i0} = j_{ix1}\left[2e(\varphi_a - \varphi_0)/m_i - (e/cm_i)^2(A_a - A_{y0})^2\right]^{-1/2} \tag{5}$$

The diamagnetic electron current is obtained as

$$-ej_{ey0} = -cen_{e0}(d\varphi_0/dx)/(dA_{y0}/dx) \tag{6}$$

5.2. Simplest one dimensional solution.

To demonstrate the characteristic features of the initial approximation the anode emission is assumed to be given by the Child-Langmuir space charge limited ion current ej_{ix} and the cathode is a virtual cathode which provides the electron population in the gap. The ion current limitation reduces the anode electric field drastically. Turbulence creates anomalous electron diffusion across the gap. It is sufficient to have a relatively small electric field strength $E_c = -d\varphi_0(l)/dx$ at the virtual cathode for driving the anomalous current. Thus at both electrodes zero value of electric field strength is assumed. These boundary conditions will be used in order to find the unknown values of the flux component j_{ix1} and the density n_{e0} which is assumed to be homogeneous.

The equation for the magnetic field strength $B_{z0} = dA_{y0}/dy$ is obtained as:

$$B_{z0}^2/8\pi = B_{z0}^2(0)/8\pi - e(\varphi_a - \varphi_0)n_{e0} \tag{7}$$

At small densities B_{z0} is minimal at the cathode and maximal at the anode (diamagnetic effect due to the electron drift). The density n_{e0} is assumed to be small enough to get a positive right hand side (RHS) in Eq. (7).

It is convenient to use the potential φ as new variable. Then the equations for flux j_{ix1} and density n_{e0} are obtained as:

$$\varphi_a n_{e0} = j_{ix1}\int_0^{\varphi_a} d\varphi/V_{ix}(\varphi), \qquad l = \int_0^{\varphi_a} d\varphi/E_{x0}(\varphi) \tag{8}$$

with V_{ix} the ion velocity.

To solve the 1 dim problem a set of dimensionless variables is used which are introduced by the following expressions:

$$\xi = x/l, \qquad u = \varphi_0/\varphi_a, \qquad w = A_{y0}/A_a, \qquad \eta = E_{x0}/\sqrt{8\pi en_{e0}\varphi_a} \tag{9}$$

and a set of dimensionless parameters is defined as:

$$\varepsilon_i = l/r_i, \qquad \varepsilon_D = \lambda_D/l, \qquad \varepsilon_a = \varphi_a/A_a \tag{10}$$

with $r_I = V_c/\omega_i$ the ion gyro-radius, $V_c = (2e\varphi_a/m_i)^{1/2}$ the x-component of the ion velocity at the cathode, $\omega_i = eA_a/m_ic$ the ion gyro-frequency and $\lambda_D = (\varphi_a/8\pi en_{e0})^{1/2}$ the Debye length. The flux j_{ix1} and the field strengths $E_{x0}(0)$, $B_{z0}(0)$ are made dimensionless according to:

$$\iota = j_{ix1}/n_{e0}V_c, \qquad \eta_0 = E_{x0}(0)/\sqrt{8\pi en_{e0}\varphi_a}, \qquad b = B_{z0}(0)/\sqrt{8\pi en_{e0}\varphi_a} \tag{11}$$

As a result the whole problem is transformed to a set of dimensionless equations for the unknown two functions $\eta(u)$, $w(u)$ and the three numbers ι, b, ε_D. Details of solving these equations are given in Ref. [11]. For a large applied magnetic field ($\varepsilon_a \ll 1$) the anode dimensionless magnetic field strength is obtained as $b \approx 1/\pi\varepsilon_a + (5/16)\pi\varepsilon_a$. Using an additional parameter q the behavior of the dimensionless electric and magnetic potentials u, w, of the spatial coordinate ξ and of η is given by the following expressions [11]:

$$u = 1 - q^4, \qquad \eta = q\left(2\iota - q^2\right)^{1/2} \qquad (12)$$

$$\xi = (2/\pi)\left(\arcsin q - q\sqrt{1 - q^2}\right), \quad w = 1 - \xi(q) - \tfrac{5}{12}\pi\varepsilon_a^2 q^3\left(1 + \tfrac{4}{5}q^2\right)\sqrt{1 - q^2} \quad (13)$$

For the case of small width of the gap compared to the ion gyro-radius (the limit $\varepsilon_i \rightarrow 0$) the value of the number ι for which η gets zero at the virtual cathode follows from Eq. (12) at $q = 1$: $\iota = 1/2$. The parameter ε_D is obtained as $\varepsilon_D = 1/\pi$ thus giving the electron density as $n_{e0} = \pi\varphi_a/8el^2$. Thus the Child-Langmuir ion current is obtained as $ej_{CL} = (\pi/8)(e/2m_i)^{1/2}(\varphi_a)^{3/2}/l^2$.

The dependencies $u(\xi)$, $w(\xi)$ and $\eta(\xi)$ are shown in Fig.2. For this demonstration the parameter $\varepsilon_a = 5/9$ is chosen that is used later in chapter 7.3. In the Desjarlais model the current collapse occurs after the voltage reaches the value $\varphi_a = (5/9)A_a$. The dotted diagonal on the plot shows the undisturbed magnetic potential at $\varepsilon_a = 0$. As the parameters ε_i and ε_a may have arbitrary values a numerical calculation was performed in order to demonstrate the dependence of the parameters b, ι and the relative Debye length ε_D on ε_a and ε_i. The results of the calculation are shown in Fig. 3. The dependence of the parameters ι and ε_D on ε_a and ε_i is rather weak in comparison with the dependence of the parameter b on ε_a.

6. Perturbation analysis for the magnetic self focusing

6.1. The equations for first order corrections.

The principal scheme for calculation of the focal distance F is shown in Fig. 4. The process of solution of the self consistent system of equations is indicated as a loop diagram in this Fig. Because of quasi-stationary operation the time derivatives in the Vlasov and Maxwell equations are omitted in the scheme. Solutions of the Vlasov equation $\{H, f\} = 0$ are determined by the Hamilton function H of particles using appropriate boundary conditions. H is a mathematical expression for the energy via spatial coordinates and canonical momentum of particles. The canonical momentum is contained explicitly in H. The coordinates are contained implicitly via the electric and the magnetic potential. The zeroth order solution of the Vlasov equation forms the distribution function f_0 with which the density and the particle flux are integrated. Using these results at the RHS of the Maxwell equations first approximation corrections to the potentials are obtained. The corrected potentials are substituted into the Hamilton function which determines finally the first order solution $f_0 + f_1$ of the Vlasov equation. In order to obtain next order correction this cycle is repeated.

If $j_{ix1} \neq 0$ then in accordance with Eq. (2) a x-component of the magnetic potential A_x does exist. After neglecting A_z at the first order approximation from the Lorenz gauge for the stationary problem follows that A_x is a function of z only. Thus from Eq. (1) p_z can't be derived as motion integral, hence ions are accelerated in z-direction. This acceleration of ions causes magnetic self-focusing. The scheme of the magnetic self focusing for an extraction

diode is shown in Fig. 5. Due to the current compensation outside of the gap the ions are propagating straightforward after passing the virtual cathode and then arrive at the focal point F. The small bend implies the introduction of a small parameter describing contributions from A_x. The value of this parameter is obtained at the end of this chapter. The perturbation source is the x-component of the ion flux j_{ix1}. Therefore in accordance with Eq. (2) the component A_x is the first order perturbation. The component A_z appears only as a second order perturbation because the equality $j_{iz1} = 0$ is valid. The slow change of the ion beam parameters along the z-direction allows to assume that the derivatives of the initial approximation functions on coordinate z are negligibly small compared to those on coordinate x.

The Vlasov equation of the first order approximation obtained from Eq. (4) is given as $\{H_{i0}, f_{i1}\} + \{H_{i1}, f_{i0}\} = 0$ and from Eq. (2) follows $A_{x1}(z) = -2\pi e j_{ix1} z^2/c$. The first order approximation H_{i1} to the ion Hamilton function is obtained from Eq. (1) as:

$$H_{i1} = -2\pi e^2 j_{ix1} z^2 p_{ix} (H - e\varphi_0)^{-1} \qquad (14)$$

6.2. The first order solution.

The Vlasov equation is becoming as

$$\frac{d}{dt}\left(f_{i1} - H_{i1}\frac{\partial f_{i0}}{\partial H}\right) = \frac{\partial f_{i0}}{\partial p_z}\frac{\partial H_{i1}}{\partial z} \qquad (15)$$

with the symbol d/dt designating the time derivative along unperturbed trajectory. From Eqs. (14) and (15) the expression for the function f_{i1} is obtained as:

$$f_{i1} = \frac{2\pi e^2 j_{ix1} z}{H - e\varphi_0}\left(z p_{ix}\frac{\partial f_{i0}}{\partial H} + 2m_i x\frac{\partial f_{i0}}{\partial p_z}\right) \qquad (16)$$

The z-component of the ion flux is obtained from Eq. (3) as $j_{iz2} = -4\pi(e/c)^2 x z n_{i0} j_{ix1}$. For estimation of the focal length F it is assumed that after reaching the cathode the ions which have initially some coordinate z are going further straightforward. In this case F is given by the expression $F = z \operatorname{ctg}\beta$ with β the angle under which the ions are crossing the plane $z = 0$. β is determined by the ratio of z- to the x-component of the ion flux at the cathode plane $x = l$: $\operatorname{tg}\beta = |j_{iz2}/j_{ix1}|_{x=l}$. With $l = 1/2$ and $\varepsilon_D = 1/\pi$ the following expression for F is obtained:

$$F = l(8/\pi^2)(c/V_i)^2 \qquad (17)$$

According to Eq. (17) the inequality $F \gg l$ is valid at non-relativistic ion velocities. Hence as long as the perturbation parameter $(V_i/c)^2$ is small the validity of the perturbation analysis for the effect of the magnetic self-focusing is confirmed.

7. Diamagnetic focusing

Another mechanism for ion focusing concerns the mobility of the virtual cathode. The electric and the magnetic potentials are assumed to be constant at the surface of the virtual cathode. It is assumed also that the surface is fixed at the points $(x,z) = (l,\pm L/2)$ of the tip ends. The real cathode is the surface of constant potentials, too. In chapter 5.2 it was shown that the magnetic field strength at the virtual cathode decreases. But there are no electric currents in

the region of constant electric potential $\varphi = 0$ between the virtual and the real cathode (this region is called the cathode region). Thus the virtual cathode surface gets distorted, because its middle part shifts to the anode in order to keep the momentum equilibrium but the ends are assumed to be fixed. The distortion of the surface results in perturbation of the electric field in the gap and consequently in bending of ion trajectories. The distorted surfaces A_y = constant inside of the gap are shown in Fig. 6.

To describe small perturbations a sinusoidal function is used in the surface equation $\sigma(x,z) = x - l - a_1\cos(\pi z/L) = 0$ with a_1 the amplitude of the first order perturbation. Interaction between the cathode region and the gap is represented as the momentum balance equation at the separating surface.

$$\left(B^2/8\pi\right)_{\sigma\to-0} = \left(B^2/8\pi\right)_{\sigma\to+0} \tag{18}$$

The magnetic strength at both sides of the surface $\sigma = 0$ is obtained below.

7.1. Magnetic field in the cathode region

At $\sigma > 0$ the magnetic field is described by the y-component of magnetic potential A_y only. According to Eq. (2) in the cathode region the Laplace equation $\Delta A_y = 0$ is valid. The boundary conditions at the surfaces of the real cathode and the virtual cathodes are given as $A_y|_{x=l+h} = -A_a h/l$ and $A_y = 0$. The function A_y is given as

$$A_y = -(A_a/l)(x - l - a(x)\cos(\pi z/L)) \tag{19}$$

Substituting Eq. (19) into the Laplace equation and neglecting small terms a boundary problem is obtained for the amplitude $a(x)$. Calculating finally $\mathbf{B} = (-\partial A_y/\partial z, 0, \partial A_y/\partial x)$ the magnetic pressure of the first order accuracy at the surface $\sigma = 0$ from the side of the cathode region is obtained as:

$$\left(B^2/8\pi\right)_{\sigma\to+0} = \left(A_a^2/8\pi l^2\right)\left(1 + 2\pi(a_1/L)\mathrm{cth}(\pi h/L)\cos(\pi z/L)\right) \tag{20}$$

7.2. Magnetic field in the gap

The source of perturbations is the electric potential φ_a applied to the gap. Therefore φ_a is considered as a small perturbation. In order to use the results of chapter 5.2 small values of the dimensionless parameters ε_i and ε_a are assumed which are defined by Eq. (10). For a small electric potential it is sufficient to use Eq. (12) independently on z. But for large magnetic potentials the initial solution Eq. (13) has to include the dependence on z thus requiring second order perturbation terms. The magnetic potential in the gap is given as

$$A_y = A_a\left(w|_{\varepsilon_a=0} + \left(w - w|_{\varepsilon_a=0} + l^{-1}a(x)\right)\cos(\pi z/L)\right) \tag{21}$$

Substitution of Eq. (21) into Eq. (2) gives an equation for the unknown function a. The magnetic pressure at $\sigma = 0$ calculated from the side of the gap is obtained as:

$$\left(B^2/8\pi\right)_{\sigma\to-0} = \left(A_a^2/8\pi l^2\right)\left(1 + \left(\tfrac{5}{6}\pi\varepsilon_a^2\chi|_{q\to1} - 2\pi(a_1/L)\mathrm{cth}(\pi l/L)\right)\cos(\pi z/L)\right) \tag{22}$$

7.3 Perturbed motion of ions and the focal distance F

In order to find the focal distance F the z-component of the ion flux j_{iz2} is calculated in a similar way as described in chapter 6.2. The first approximation correction H_{i1} for the ion Hamilton function Eq. (1) is obtained as $H_{i1} = -(p_y - m_i\omega_i a)\omega_i a\cos(\pi z/L) + e\varphi$. Estimating characteristic values of the functions a, φ and p_y as $a \sim a_1$, $\varphi \sim \varphi_a$ and $p_y \sim m_i V_c$ the magnetic term in H_{i1} is found to be negligibly small. Thus ions are influenced mainly by the electric

term $e\varphi$. Up to now in chapter 7 the electric potential φ was calculated as the first order perturbation function of the coordinate x but the focusing of ions is caused by the z-dependence of H_{i1}. Therefore the perturbation of φ has to be calculated up to the second order contribution.

Densities and electric potential are represented as

$$n_\alpha = n_{e0}\left(\rho_\alpha(\xi) + \rho_{\alpha 2}(\xi)\cos(\pi z/L)\right), \quad \varphi = \varphi_a\left(u(\xi) + u_2(\xi)\cos(\pi z/L)\right) \tag{23}$$

with the constant dimensionless electron density $\rho_e = 1$ and the functions u, ρ_i being the results of the one dimensional analysis of chapter 5.2. For small values of ε_i it is obtained $\rho_i = (1-u)^{-1/2}/2$. For more details see Ref. [11].

In order to calculate the electron density correction ρ_{e2} the Boltzmann distribution function f_e of the temperature T_{e0} along the magnetic surface $A_y = $ constant is assumed in the linear approximation for the exponent. Coordinate x_c at the plane $z = 0$ belongs to a magnetic surface crossing the point (x,z). For small a the difference between $a(x)$ and $a(x_c)$ is neglected. For small ε_a the function $w = 1 - x/l$ is used. Thus the expression for x_c is obtained as $x_c = x + a(x)\,[1 - \cos(\pi z/l)]$. As a result the correction ρ_{e2} is obtained as $\rho_{e2} = (u_2 - \eta a/l)/\varepsilon_T$ with the dimensionless parameter $\varepsilon_T = T_{e0}/e\varphi_a$.

Then f_{i1} is given as:

$$f_{i1} = e\varphi_a\left[\frac{\partial f_{i0}}{\partial H}u_2\cos(\pi z/L) - \frac{\pi}{L}\frac{\partial f_{i0}}{\partial p_z}\int u_2(\xi(t'))dt'\sin(\pi z/L)\right] \tag{24}$$

Since the second term in the RHS of Eq. (24) is an odd function of p_z there is no contribution to the density correction $n_{i1} = n_{e0}\rho_{i2}$. For small parameter ε_i the following expression is obtained for ρ_{i2}: $\rho_{i2} = u_2/4(1-u)^{3/2}$ and u_2 is given as:

$$\frac{d^2 u_2}{d\xi^2} - \varepsilon_z^2 u_2 = \tfrac{1}{2}\pi^2\left(\rho_{e2} - \rho_{i2}\right), \qquad u_2(0) = u_2(1) = 0 \tag{25}$$

with the dimensionless parameter $\varepsilon_z = \pi l/L$. In order to simplify the analysis it is assumed that ε_T is small (the case of relatively cold electrons in the gap when the inequality $T_{e0} \ll e\varphi_a$ is valid). The final expression for the function u_2 then is obtained as $u_2 = \eta a_1 \text{sh}(\varepsilon_z\xi)/l\text{sh}\varepsilon_z$. This solution is valid in the main volume of the gap except of the sheath regions at the anode and the virtual cathode. The sheaths there are formed to satisfy the boundary conditions. The thickness l_c of the sheaths is estimated as $l_c = l/G^{1/2} \ll 1$ with $G = \pi^2/2\varepsilon_T$. The influence of the sheaths is neglected below.

The z-component j_{iz2} of the ion flux is integrated taking into account only a contribution from the odd part of the function f_{i1} of Eq. (24) with respect to the momentum component p_z because the contributions from the even part of this function and from the even term containing the Hamilton function correction H_{i1} are equal to zero due to the factor p_z under the integral. Thus the relation of the z- to the x-components of the ion flux at the virtual cathode plane $x = l$ is obtained as

$$\left(j_{iz2}/j_{ix1}\right)_{x=l} = \frac{\pi^2 z a_1}{L^2}\int_0^1 \frac{\eta(\xi)\text{sh}(\varepsilon_z\xi)}{\text{sh}\varepsilon_z\sqrt{1-u(\xi)}}d\xi \tag{26}$$

The integral in Eq. (26) is calculated for the cases $\varepsilon_z \ll 1$ ('shallow gap'), $\varepsilon_z \gg 1$ ('deep gap') and $\varepsilon_z = 1$. At $\varepsilon_z \ll 1$ the integral is equal to $(2\pi)^{-1}$. At $\varepsilon_z \gg 1$ only a small interval of thickness $l_z = L/\pi$ near the virtual cathode is important for the calculation. Assuming that the parameter ε_T is small enough for neglecting of the above mentioned sheaths ($l_z \gg l_c$), the integral is calculated as $\pi/(2\varepsilon_z)^2$. For the intermediate case $\varepsilon_z = 1$ a numerical integration results in the approximate value $1/7$.

Finally the focal distance F is obtained as

$$F = \varepsilon_a^{-2} \tfrac{16}{3}\left(L/\pi^3\right)\left(\mathrm{cth}\,\varepsilon_z + \mathrm{cth}(\pi h/L)\right) \times \begin{bmatrix} 2\pi & \text{for } \varepsilon_z \ll 1 \\ 7 & \text{for } \varepsilon_z = 1 \\ 4\varepsilon_z^2/\pi & \text{for } \varepsilon_z \gg 1 \end{bmatrix} \qquad (27)$$

For example, the high voltage proton diode has the following parameters: $l = h = 1$ cm, $L = 3.14$ cm, the applied magnetic field A_a/l is 3 T, the voltage φ_a is 5 MV. Then the values of the dimensionless parameters are equal to $\varepsilon_z = 1$ and $\varepsilon_a = 5/9$. The focal distance is obtained as $F \approx 32.5$ cm. There is a minimum of the function $F(\varepsilon_z)$ at fixed values of the parameters ε_a and h/l. For $h = l = 1$ cm and $\varepsilon_a = 5/9$, F reaches the minimum value $F_{min} = 24$ cm at $\varepsilon_z = 1.3$ ($L = 2.4$ cm). A further increase of the potential moves the focal point towards the electrodes. The perturbation model can't be applied anymore.

The parameter ε_a can be expressed as $\varepsilon_a = \upsilon_D/c$ with $\upsilon_D = cE_x/B_z \approx \varphi_a/A_a$ the characteristic electron drift velocity in the gap. In the limit $\varepsilon_a \to 1$ the drift velocity in the diode should approach the velocity of light. In this case at small electron temperature T_0 the Buneman instability should develop increasing T_0 self consistently.

8. Conclusion

At non-relativistic ion velocities the effect of the magnetic self-focusing is of the order of $(V_i/c)^2$ with V_i the velocity of accelerated ions at the cathode. The effect of self focusing due to the curvature of the virtual cathode is of the order of $(\varphi_a/A_a)^2$. At $\varphi_a < A_a$ the focus distance F is significantly larger than the characteristic dimensions of the diode. To obtain the dependence of F on the higher voltage φ_a (at F comparable with the diode electrode sizes l, h and L) either a higher order perturbation analysis with the small parameter $(\varphi_a/A_a)^2$ or a direct numerical calculation are necessary. For available installations φ_a/A_a doesn't exceed the value of 0.5 . Therefore for the development of a comprehensive model for an analysis of turbulent processes it is sufficient to use a plane 1 dim approach (in the simplest case the solution of chapter 5.2) as an adequate initial approximation neglecting the effects of self focusing as long as the electric potential is not extremely high.

References

1. M. Desjarlais, Theory of applied-B ion diodes, Phys. Fluids B, **1**, 1709, 1989.
2. A.V. Gordeev, A.V. Grechikha, New model for electron screening in an ion diode in an external magnetic field, JETP Lett., **61**, 196, 1996.
3. M. Boger, E. Halter, M. Krauß, C.-D. Munz, R. Schneider, E. Stein, U. Voß, T. Westermann, The Karlsruhe Diode Simulation Program System KADI2D, FZK, Annual report FZKA 5840, 69, 1995.
4. A. Grechikha, Electron sheath collapse in an applied-B ion diode, FZK, Annual report FZKA 5840, 61, 1995.
5. J.P. Quintenz, D. B. Seidel, M.L. Kiefer, T.D. Pointon, R.S. Coats, S.E. Rosenthal, T.A. Mehlhorn, M.P. Desjarlais, N.A. Krall, Simulation codes for light-ion diode modeling, Laser and Particle Beams, **12**, 283, 1994.
6. T.D. Pointon, M.P. Desjarlais, Three-dimensional particle-in-cell simulations of applied-B ion diodes on the particle beam fusion accelerator II, J. Appl. Phys., **80**, 2079, 1996.
7. V.P. Pastukhov, Anomalous electron transport in the transition layer of an electrostatically plugged magnetic mirror, Sov. J. Plasma Phys. **6**, 549, 1980.
8. A.A. Galeev, R.Z. Sagdeev, In: Reviews of Plasma Physics, 7, Consultants Bureau, New York, 1974.
9. L.D.Landau, E.M.Lifshitz, Mechanics. Pergamon Press, 1959.
10. L.D.Landau, E.M.Lifshitz, The classical theory of fields. Pergamon Press, 1959.
11. I.S.Landman, H.Würz, FZK report to be published.
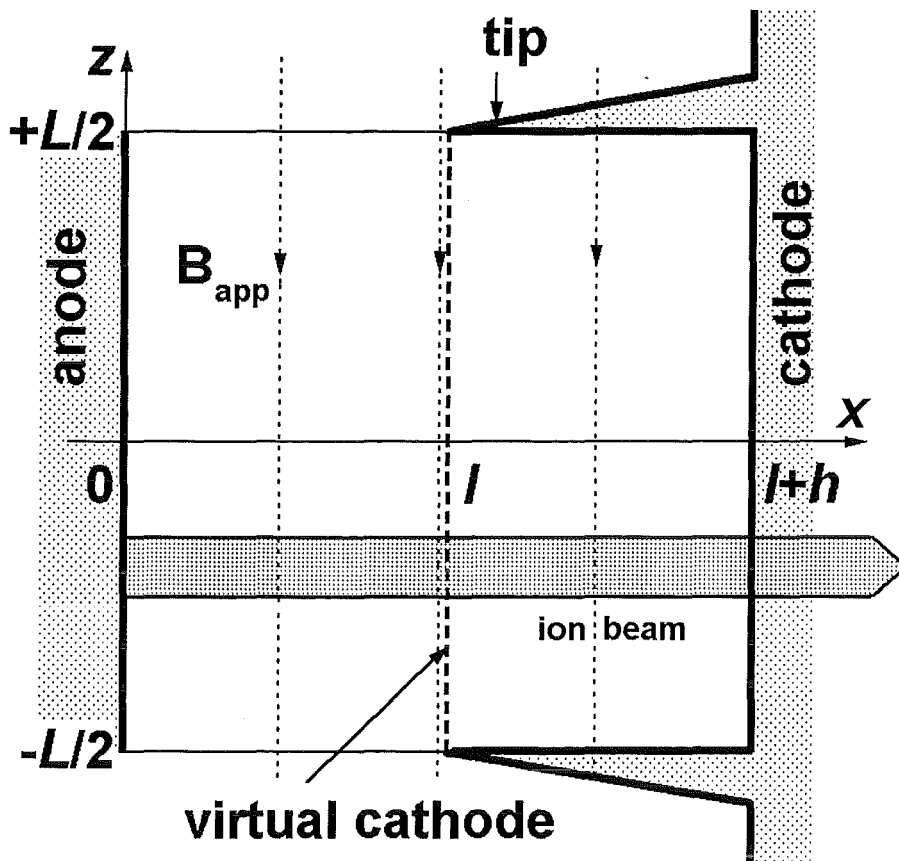
Fig. 1 Principal scheme of a diode
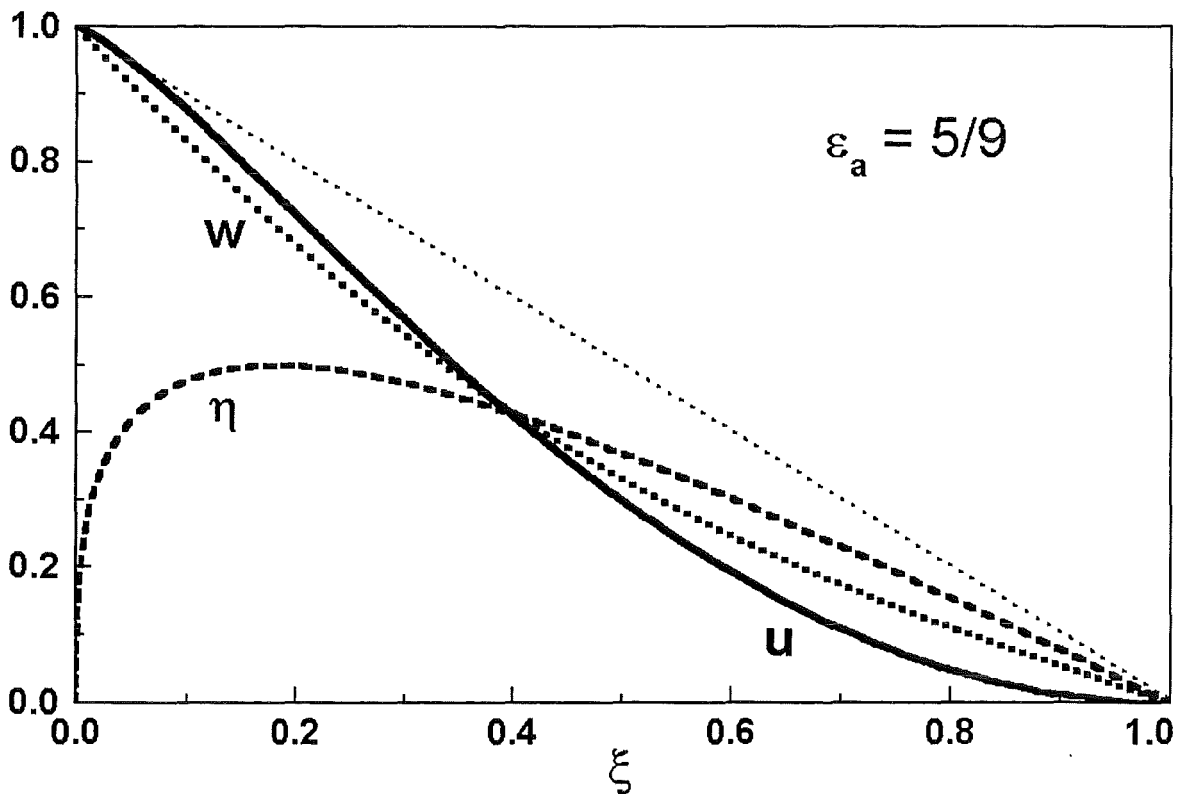
Fig. 2 Dependence of dimensionless functions electric (u) and magnetic (w) potentials as well as electric field strength η on dimensionless coordinate ξ
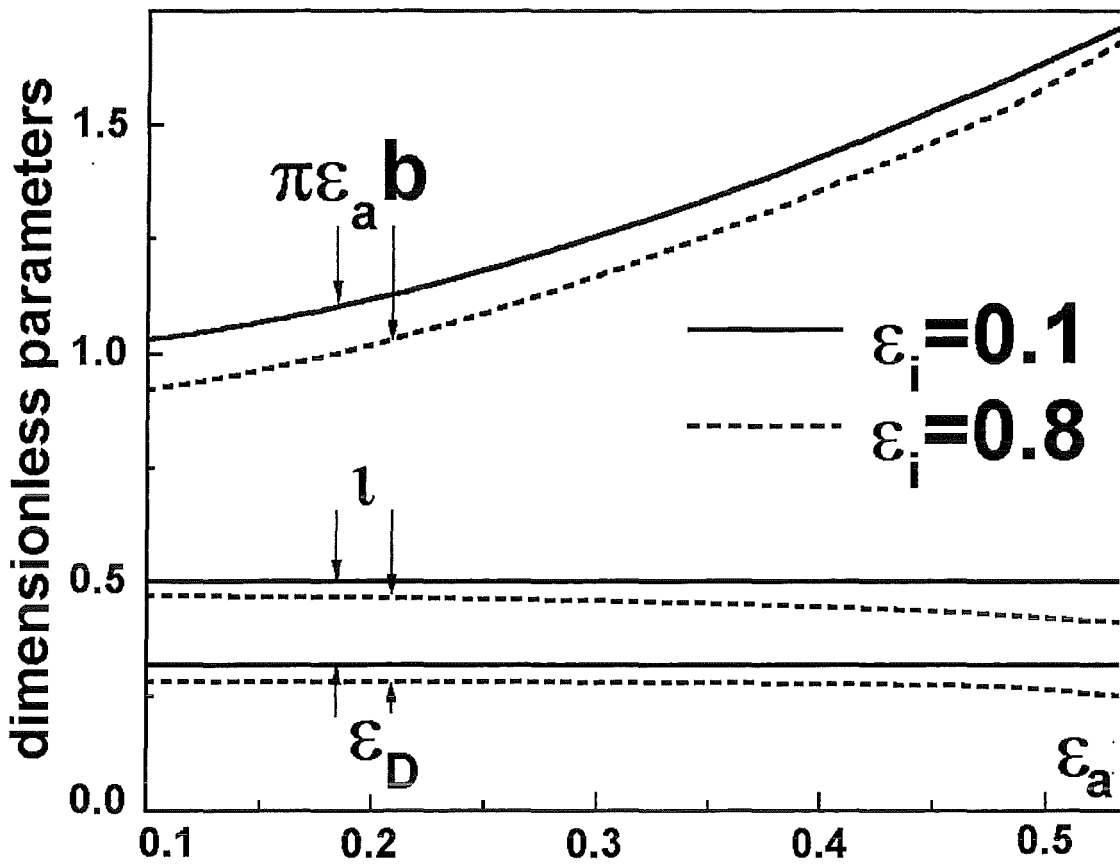
Fig. 3 Dependence of the dimensionless parameters anode magnetic field strength(b), ion flux(ι) and Debye length(ε_D) on dimensionless anode electric potential ε_a
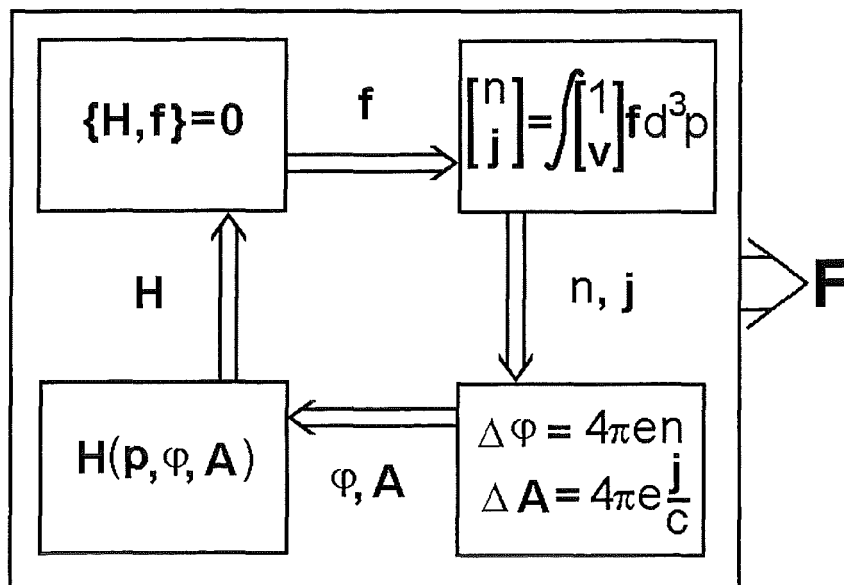

Fig. 4 Scheme of consistent calculation of the focal length
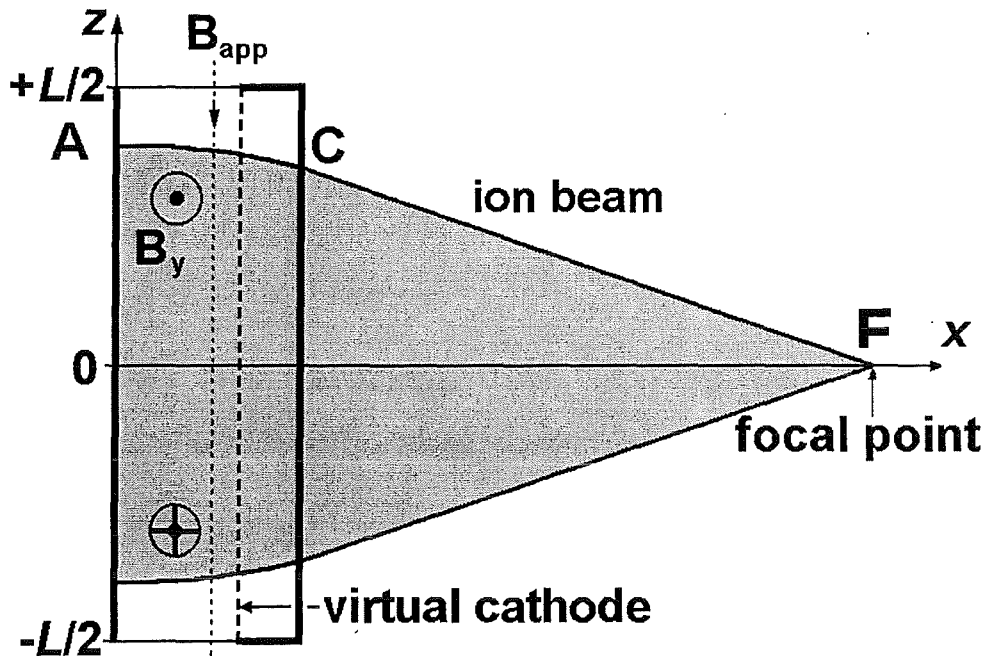
Fig. 5 Magnetic self - focusing schematically
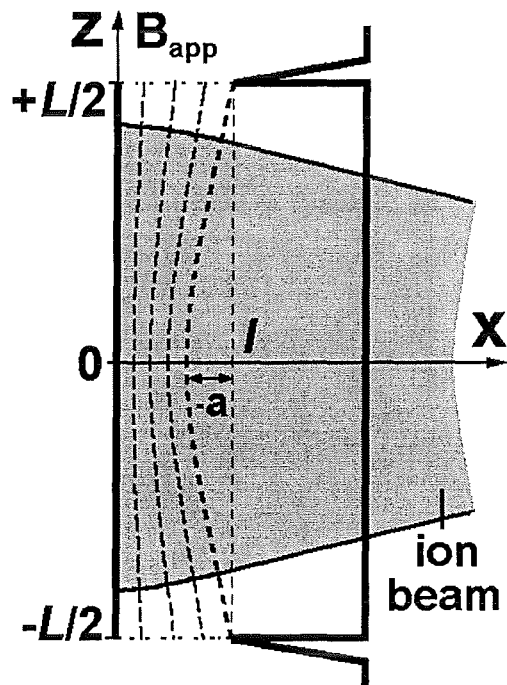
Fig. 6 Diamagnetic self
focusing schematically

4   Target physics

Experiments on the Rayleigh-Taylor instability of ion-beam driven targets

K. Baumung, L. Buth, H. Marten, A.V. Shutov*, J. Singer, O. Stoltz

Abstract–*We have used the pulsed high-power proton beam of the Karlsruhe Light Ion Facility KALIF to ablatively accelerate 20-50-µm-thick planar targets provided with a 2D periodic structure to velocities of ~10 km/s. Line-imaging laser Doppler velocimetry with high spatial (≥ 10 µm) and temporal (≥ 200 ps) resolution is employed to measure the velocity of the rear surface of targets provided with a small-scale corrugation. From the temporal evolution of the transverse velocity profiles we obtain the feed-through of the hydrodynamic instability developing at the boundary to the ablation plasma. We find stable acceleration during the first wave reverberation cycle. Afterwards, an exponential growth is observed at an average rate that amounts to 40% - 65% of the classical value. The reduction is mainly due to heat transport driven mass convection through the boundary between the condensed part of the target and the ablation plasma.*

1. Introduction

On the Karlsruhe Light Ion Facility KALIF we are performing shock-wave experiments driven by the direct action of the high power proton beam or by impacting 20-100 µm thick flyer plates ablatively launched to hypervelocities [1]. Occasionally, our ORVIS laser-Doppler velocimeter [2] showed early abnormal signal loss during the acceleration process. Burn-through of the target foils, hot-spots in the power density distribution due to beam filamentation, and hydrodynamic instability were supposed to be possible reasons. To clarify the issue we upgraded our velocimeter to provide 1D spatial resolution [3]. This paper presents first results of experiments on the development of hydrodynamic instabilities.

Ablatively accelerated projectiles are susceptible to the evolution of a hydrodynamic instability commonly referred to as Rayleigh-Taylor (RT) instability which develops when a layer of dense material (ρ_{hi}) is accelerated by a medium of low density (ρ_{lo}). The classical theory [4] considers the evolution in time of a small-scale 2D-corrugation of the interface (located at $y=0$) between the two media with an initial transverse (x direction) perturbation amplitude $\eta(x) = \eta_0 \cos kx$ and perturbation wavelength $\lambda = 2\pi/k$. At time t after acceleration onset, the displacement δ_y in y-direction (direction of acceleration g) of a mass element initially located at (x,y) is given by

$$\delta_y(x,y,t) = \eta_0 \cos(kx)\, e^{-ky} \cosh(\gamma t) \quad , \tag{1}$$

where $\gamma = \sqrt{Akg}$ is the growth rate with the Atwood number $A = (\rho_{hi} - \rho_{lo})/(\rho_{hi} + \rho_{lo})$. The displacement is proportional to the initial perturbation amplitude at position x and decreases with the distance y to the interface with the decay constant k. For $\gamma^2 < 0$, a stable oscillation

---

*) Permanent address: Institute for Chemical Physics Research, Chernogolovka 142432, Russia

establishes whereas for $\gamma^2 > 0$ the perturbation grows exponentially with a growth constant that approaches γ for times $t > 1/\gamma$. The growth rate depends on the acceleration and the difference of the fluid densities, and increases for small perturbation wavelengths.

Unlike the classical case, ablative acceleration involves density gradients between the two media instead of a step as well as heat and mass transport across the boundary. Taylor had found that accelerating a dense fluid of finite thickness $d \leq \lambda$ should reduce the growth rate [4]. The RT instability of ablatively accelerated layers is of particular interest in inertial confinement fusion because it could spoil the uniform implosion of the fuel capsule crucial to obtaining fusion conditions, and extensive work has been performed on this issue in the past decades. In 1974 already, it was found that with ablatively accelerated layers convective effects in the ablation zone should stabilize the growth and, for short wavelengths λ, even suppress the RT instability [5]. Mikaelian worked out the stabilizing effect of a smooth density gradient in the ablation zone [6]. These first results were substantiated in numerous theoretical investigations (survey in ref. 3) and in direct drive and indirect drive laser experiments where, depending on k, reductions of the growth rate γ to 20-60% of the classical values were found with planar targets [7–10].

Using the KALIF high-power proton beam ablative accelerations of thin target foils in the 10^{13}-10^{14} cm/s^2 range can be realized which is high enough to cause a measurable instability growth within 10-20 ns. Unlike in laser-driven experiments, where head-on x-radiography is used to measure the areal mass density change caused by the instability growth, we have measured the feed-through of the instability to the rear surface of the target foils. By means of a high-resolution line-imaging laser Doppler velocimeter we are able to record the transverse velocity distribution of the rear target surface. From the different velocity histories of peak and valley positions we deduce the growth rate of the perturbation at the target rear free surface which is caused by the feed-through of the instability developing in the ablation zone. Analytical correlations and 2D simulations using a wide-range equation of state and a detailed energy deposition has been used to compare the experimental data with the instability growth at the ablation plasma boundary.

2. Experimental technique and setup

The experiments reported here were performed using the B_Θ-diode providing peak power densities of 0.15±0.05 TW/cm^2 allowing 30 to 50 μm thick aluminum foils to be accelerated beyond 10 km/s within 10-30 ns.

The interaction of the proton beam delivered by the B_Θ-diode with a solid target is characterized by high bulk energy deposition right in the beginning [1]. High pressure builds up – 30 to 100 GPa in aluminum – that causes the hot, partially ionized material in the energy deposition zone to expand rapidly or "ablate", and a compression wave to progress into the adjacent cold material. Reverberations of compression waves starting from the boundary of the ablation plasma and rarefaction waves starting from the rear free surface, step by step, "ablatively" accelerate the residual condensed part of the target. This process is quite different from the assumptions made in the classical theory that supposes incompressibility and constant acceleration. To approximate the latter condition we decided to cut the beam front of 0.3-0.8 MeV ions by a filter foil which decreases the initial velocity jump (see Fig. 1). In return, we used thin targets. Reducing the target thickness not only increases the acceleration but, by shortening the reverberation period and by blurring the velocity steps, also gives a more uniform acceleration. In addition, thin targets should show a higher feed-through of the instability to the rear surface. Because it is difficult to machine aluminum foils
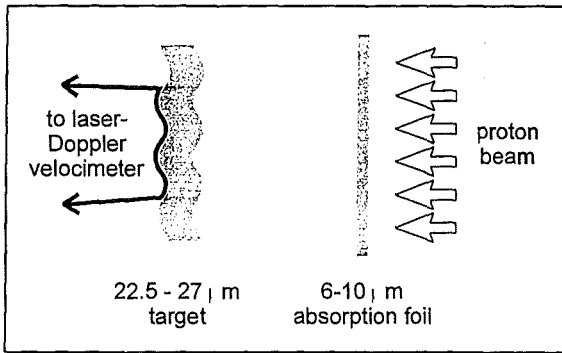
Fig.1: Schematic of the target arrangement. The filter 2 mm upstream of the corrugated target absorbs the bunched front of the beam in order to obtain a more uniform acceleration

of 20-30 μm thickness we decided to corrugate them by means of dies manufactured by cutting parallel shallow groves with a 155°, v-shaped diamond blade into the planar surface of a brass block. Dies with four different periods λ (50, 70, 100, and 150 μm) and peak-to-peak amplitudes of $2\eta_0 = 0.11$ λ were made by the micromachining group at the HVT-EA department of Forschungszentrum Karlsruhe. The mechanically polished aluminum target foils are corrugated by pressing them between matching dies. The resulting profiles show slightly v-shaped valleys and more rounded peaks with a modulation amplitude of 0.03-0.1λ, depending on the wavelength and the target thickness. With plastic pads inserted between the dies and the target foil nearly sinusoidal corrugations with modulations of 0.01-0.02 λ are obtained.

Fig. 2 depicts the line-imaging laser-Doppler velocimeter adjusted to meet the particular requirements of the present experiments. The instrument illuminates on the target a ~300 μm long by ~30 μm wide line transverse to the corrugation. Because the diffraction-limited focus diameter of the incoming laser beam is ~300 μm, a 1D beam expander is employed to increase the horizontal extent of the beam so that it can be focused down to ~30 μm in this direction. This was necessary in order to transmit a maximum of the available laser power of <1W through the input slit of the streak camera. The measuring line is imaged onto the mirror planes of a Michelson-type interferometer by a custom made 300 mm *f*/4 objective designed for optimum resolution through a thick plane-parallel plate (the window of the KALIF vacuum vessel). The angle between the two legs is kept as small as possible to reduce astigmatism caused by the oblique beam splitter. In a second stage - by means of the tele-
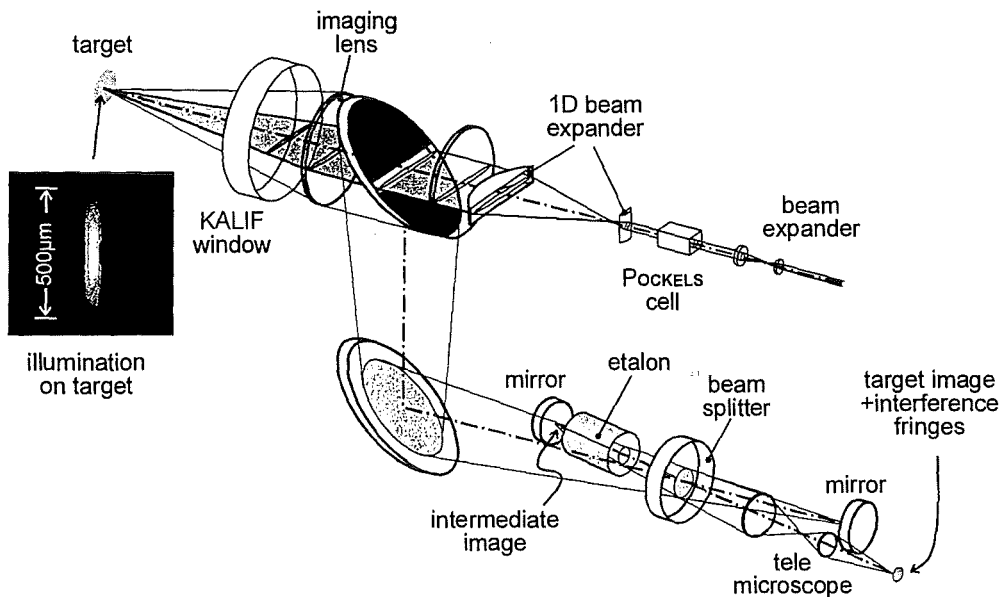

Fig. 2: Schematic of the line-imaging velocimeter. At the output of the interferometer, the image of the measuring line on the target is superimposed by interference fringes. Doppler shift of the reflected laser light causes a transverse displacement of the fringes which is proportional to the local target surface velocity

microscope - the measuring line is imaged to the input slit of a streak camera. The interferometer works as a high-resolution two-beam interference spectrometer with an optical path difference of the two legs of 10^4-10^6 laser wavelengths λ_0. The precision glass etalon not only increases the path length but, by correcting the spherical wave front mismatch in the two legs, also extends the acceptance angle of the interferometer needed for high spatial resolution. The interferometer is adjusted such that the interference fringes - successive high orders ($N \approx 10^4$-10^6) of the laser line - are oriented parallel to the image of the measuring line. When the target surface accelerates, the wavelength of the reflected laser light is Doppler shifted and the interference fringes sweep across the camera slit, modulating the intensity
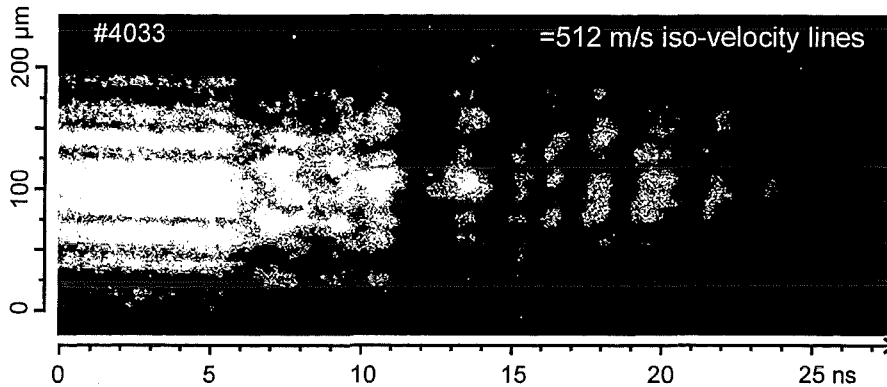
Fig 3: Velocimeter streak record. The white lines stress the change of the interference fringes which represent lines of equal velocity in this picture.

recorded. One full intensity cycle corresponds to a velocity increment called fringe constant v_0 that can be varied with our instrument in multiple steps between 170 m/s and 6 km/s.

3. Measurements and results

Fig. 3 displays a streak camera record of an experiment using a 22 μm thick target with a 50 μm period and initial peak-to-peak perturbation amplitudes of 1.5 μm on the side facing the ion beam and 0.5 μm on th rear side, and a 10 μm thick absorber 2 mm in front of the target. The vertical bright and dark bands represent lines of equal velocity. The fringe constant was 512 m/s in this experiment.

The spacing of the bands is not equidistant indicating that the acceleration was not quite constant. The bands are straight until ~15 ns. After that, a periodic deformation appears indicating that the velocity varies with the position on target. The velocity is maximum in the positions of the peaks facing the velocimeter and minimum in the valleys. Fig. 4. displays the velocity history of the rear target surface together with the path difference developing between peak and valley positions on their ~105 μm trajectory. The average acceleration is $g = 2.9 \times 10^{11}$ m/s^2. The phase shift of the intensities in peak and valley positions in Fig. 3 directly gives the velocity differences. Time integration of the differences provides the relative displacement of the rear target
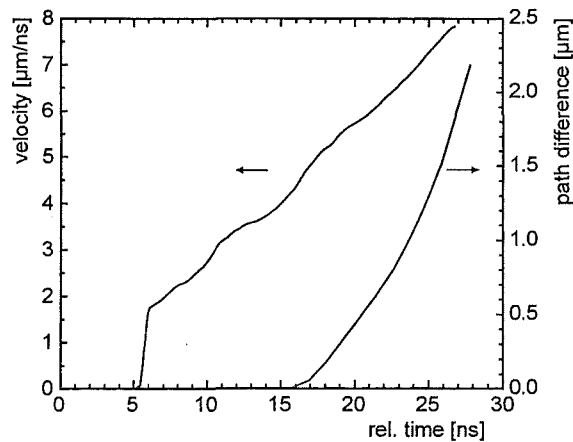

Fig 4: Velocity history of the rear surface of the target and path difference covered by peak and valley positions.

surface in these positions displayed in Fig. 4.

First, this result means that during the ablative acceleration of a corrugated target over ~5 times its initial thickness the rear side deformation increases to 1.5 times the initial peak-to peak perturbation of 1.5 μm on the plasma boundary. The deformation measured is the result of the attenuated feed-through of the instability growing on the plasma boundary [11]. The attenuation e^{-kd} decreases in time because the residual thickness d reduces during acceleration.

Usually, the R-T instability is characterized by the growth coefficient γ. In a first step, we tried to determine γ by fitting the instability feed-through to the experimental results. We supposed that equ (1). applies despite the finite thickness of the target and time-integrated the perturbation growth by taking into account the following boundary conditions:

(1) Finite average feed-through velocity of the perturbation of 6.5 μm/ns. This is the bulk sound velocity corresponding to the measured mass velocity.

(2) Time-dependent feed-through distance. Up to ~12-14 ns, the reduction of the residual thickness d is due to the increase of the proton range. We allowed for the interval displayed in Fig. 5 in order to take into account that protons accelerated by a defined voltage show an energy distribution. After peak voltage is reached (12-14 ns), the plasma boundary moves into the condensed matter due to material ablation caused by heat transfer. For the fit, we used ablation velocities of 0.1-0.2 μm/ns obtained from 1D simulations and wave reverberation experiments [12].

(3) Simulations show that instability conditions ($\nabla p \times \nabla \rho < 0$) in the ablation front arise after the arrival of the first rarefaction wave from the rear free surface only. This agrees with the arrival of the perturbation at the rear surface together with the second compression wave (8-11 ns in Fig. 4). For the fit, we varied the time interval for the instability onset in the ablation zone from 5-7 ns after the beginning of the irradiation.
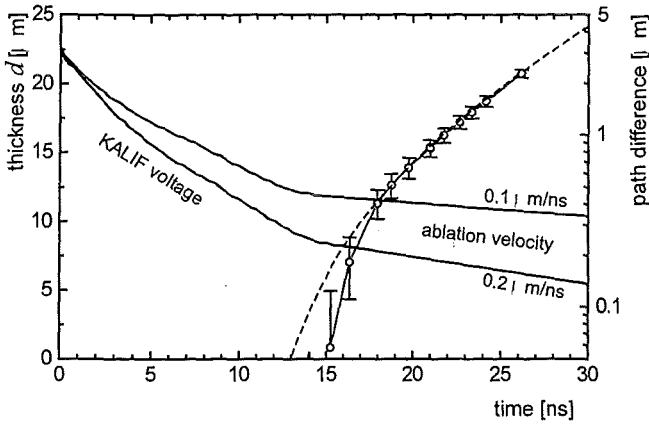

Fig. 5: The residual thickness of the target is first determined by the proton range increasing with KALIF voltage. After peak voltage it is further reduced by material ablation. The dashed line is the fit of the experimental data.

The best estimate for the growth coefficient obtained by this procedure is $\gamma=(1.2\pm0.09)\times10^8$ s^{-1} or ~65% of the classical value $\gamma_{class}=1.80\times10^8$ s^{-1} obtained with an Atwood number of $A=0.89$ taken from detailed 1D simulations including heat conduction and radiative heat transfer.

Using the analytical correlations given in refs. [11, 13, 14] the reduction of the growth rate could be explained as mainly due to convective heat and mass flow through ablation front and to a smaller extent to the presence of a smooth density gradient. Taking $L=3$ μm as density gradient scale length in the ablation region from 1D simulations gives a reduction of the growth constant by 6% only because $L \times \lambda$. The reduction due to the finite thickness of the dense layer is of the order of 1-2%. Both effects can be assigned to an effective Atwood number $A_{eff} = 0.77$. For laser driven experiments, the reduction of γ by convective effects is

described by the Takabe formula [13]

$$\gamma = \sqrt{A_{\mathrm{eff}} kg} - \beta k v_a$$

where v_a is the ablation velocity caused by the heat transport into the dense part and β is a factor ranging from 2 to 3 derived from simulations considering laser drive. Kilkenny et al. [7] give a plausible explanation why an average mass flow velocity v in the unstable region (where $\nabla p \times \nabla \rho < 0$) should be taken instead of v_a defined at the position of maximum density. 1D simulations of KALIF experiments show that, like in the example for laser
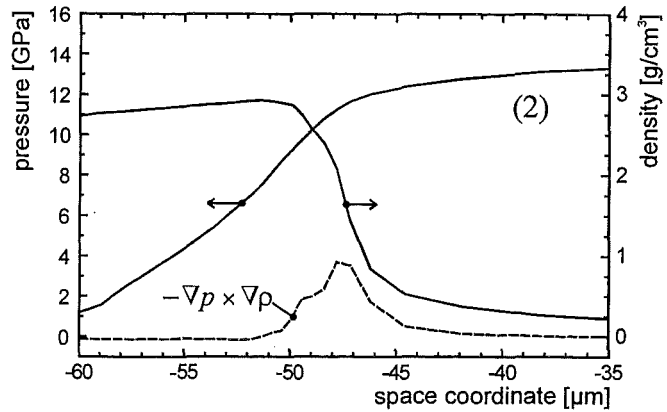
Fig. 6: Pressure and density profiles in the unstable region. $\nabla p \times \nabla \rho$ (rel. units) is minimum at intermediate densities (results from 1D simulations including heat transport).
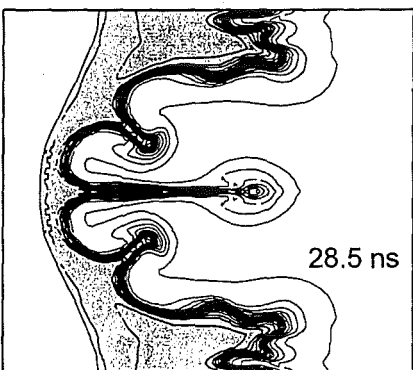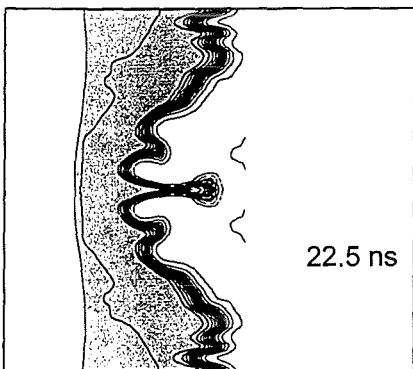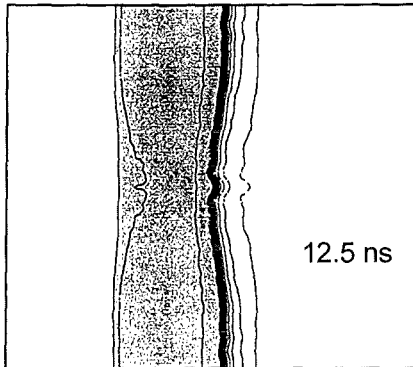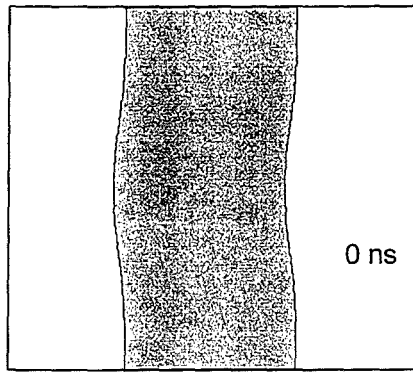
drive in ref. [7], $\nabla p \times \nabla \rho$ is minimum at intermediate densities where the mass flow velocity has increased to $v \approx 2 - 3\ v_a$ because of $\rho \times v = const$ (see Fig. 6). This is probably due to hydrodynamics rather than to the particular heat transport mechanism because simulations without heat transport give very similar density, pressure and flow profiles. Actually, we find good agreement between two experimental results available so far and the Takabe formula equ. (2) using $\beta = 3.2$ for $v_a = 0.1$ µm/ns, and $\beta = 2$ for $v_a = 0.2$ µm/ns with the corresponding growth constants which of course depend on v_a.

It is interesting to note that the fast progression of the ablation front due to the ion range increase during the KALIF voltage rise has no stabilizing effect. First 2D simulations using an adaptive grid hydrocode [15] with detailed modeling of the energy deposition and a wide-range multi-phase EOS but with heat transport option deactivated exactly reproduce the classical growth rate at the ablation front. This suggests that convective reduction is caused by transverse heat transfer. Figs 7 a-d show density contour plots of such simulations for the power history and target thickness of the experiment presented above but using the same sinusoidal 1.5 µm peak to peak corrugation on both surfaces.

Finally it should also be noticed that despite sufficient sensitivity we do not observe oscillations at the - stable - rear target surface predicted by analytical solutions [11] and obtained by the 2D simulations mentioned above. Whether this is due to strain rate dependent effects on the viscosity and yield strength not included in the available EOS has to be clarified.

4. Conclusions

We have performed first experiments on the growth of RT instabilities with planar 2D corrugated targets using a direct proton beam drive and measuring the feed-through to the rear target surface. After an acceleration over 5 times the initial thickness we find a perturbation amplitude that amounts to 1.5 times the initial corrugation amplitude at the unstable interface. We find reductions of the growth rates to 40-65% of the classical value which are mainly due to convective effects in the ablation zone.

Using absorption filters in front of the target results in an energy deposition that starts with

low-energy protons right on the surface. Without filters, the first protons to reach the target have energies of 0.5-0.8 MeV (due to bunching of the beam front) and ranges up to 10μm. Preliminary experiments and 2D simulations have shown that bulk energy deposition has a stabilizing effect because it induces convergent mass flows filling up the valleys on both the ablation front and the rear target surface in the very beginning of the acceleration. Also with regard to ion beam drive for inertial confinement fusion bulk energy deposition is the more realistic case. This is why we are planning to investigate this subject in future experiments and by simulations including heat transfer and appropriate treatment of mechanical properties.

Acknowledgments

Fig. 7a-d: Density contour plots of 2D simulation results for different times after irradiation onset. Initial thickness 22.5 μm, period λ=50 μm, peak-to-peak perturbation amplitude 1.5 μm. The shaded area indicates nominal or higher density.

References

[1] K. Baumung et al., Laser Part. Beams 14, 181(1996).

[2] D.D. Bloomquist and S.A. Sheffield, J. Appl. Phys. 54, 1717(1983).

[3] K. Baumung et al., Shock Compression of condensed matter - 1995, edited by S.C. Schmidt and W.C. Tao (AIP Press, Woodbury, NY, 1996) 1015.

[4] G. Taylor, Proc. R. Soc. Lond. A201, 192(1950).

[5] S. E. Bodner, Phys. Rev. Lett. 33, 761(1974).

[6] K.O. Mikaelian, Phys. Rev A 26, 2140(1982).

[7] J.D. Kilkenny et al., Phys. Plasmas 1, 1379(1994).

[8] J.D. Kilkenny, Phys. Fluids B 2, 1400(1990).

[9]   B.A. Remington *et al.*, *Phys. Plasmas* **2**, 241(1995).

[10] T. Endo *et al. Phys. Rev. Lett.* **74**, 3608(1995).

[11] K.O. Mikaelian, *Phys. Rev. A.* **28**, 1637(1983).

[12] V.E. Fortov *et al.*, *IEEE Trans. Plasma. Phys.* **25**, 729(1997).

[13] H. Takabe *et al.*, *Phys. Fluids* **26**, 2299(1983).

[14] H. Jacobs, *Nucl. Technol.* **71**, 131(1985).

[15] V.E. Fortov *et al.*, *Nucl. Sci. Eng.* **123**, 169(1996).

Measurement of the adhesive strength of 200 µm thick turbine blade coatings by a dynamic method

K. Baumung, L. Buth, R. Huber, G. Müller, J. Singer, O. Stoltz,
A.A. Bogatch*, G.I. Kanel*

Abstract–*The adhesive strength on the substrate is one likely criterion to judge the quality of coatings that may help optimizing the coating process parameters. We have employed a novel technique using the ablation pressure pulse of the high-power proton beam of the Karlsruhe Light Ion Facility KALIF and spatially resolving laser-Doppler velocimetry to measure the adhesive strength by a dynamic method.*

1. Introduction:

Natural gas turbines for electric power generation are gaining ground because of their flexibility and competitiveness. Single cycle 250 MW plants reach efficiencies of nearly 40% and increasing peak temperature by 50 K makes a difference of 3%. This is why considerable effort is made to go to higher and higher temperatures.

One current measure consists in coating the blades of the first turbine stage with single or multiple protective layers that improve the resistance to corrosion and high temperatures. In order to identify and optimize relevant parameters of the coating procedure like process temperature and annealing conditions, guidelines are required that allow the quality of the coating to be characterized avoiding long-term tests. Because the boundary layer between the substrate and the coating is a critical region the adhesion strength is a possible criterion. The small thickness of the coatings makes it difficult or impossible to apply usual direct methods. This is why we decided to employ a dynamic technique based on the spall phenomenon [1, 2] using the KALIF pulsed high-power proton beam to generate pressure pulses of suitable intensity and duration.

2. Experimental method and setup

2.1. Dynamic fracture

When a compression wave propagating in a solid reaches a free surface the compressed material may expand freely causing a jump in the surface velocity. The expansion propagates back into the material and is called a rarefaction wave. Formally, this process can be described as a "wave reflection at the open end" which inverts both the amplitude and the direction of propagation. The resulting pressure distribution is the outcome of the superposition of the incoming compression wave and the back-running release wave. In particular, tensile stresses may build up in case a wave of finite duration is reflected at a free surface as displayed in Fig. 1 for a triangular compression wave. An almost triangular shape establishes automatically

---

*) Permanent address: Institute for Chemical Physics Research, Chernogolovka 142432, Russia
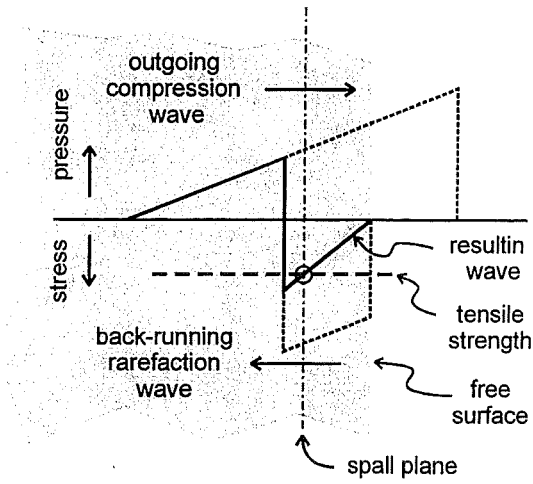
Fig. 1: The superposition of compression and reflected rarefaction waves generate tensile stresses which cause fracture in a plane near the surface if the tensile strength is exceeded.
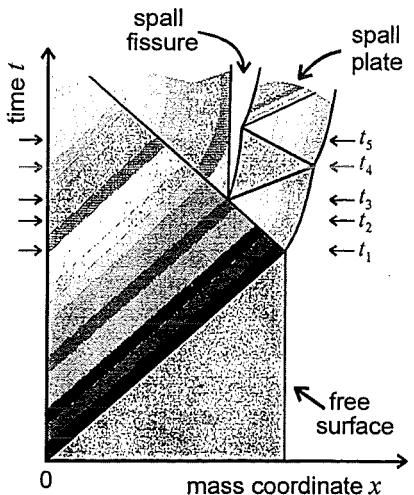

Fig. 2: x-t-diagram (x: Lagrangian coordinate) of the wave phenomena associated with spalling (cf. text and Fig. 3).
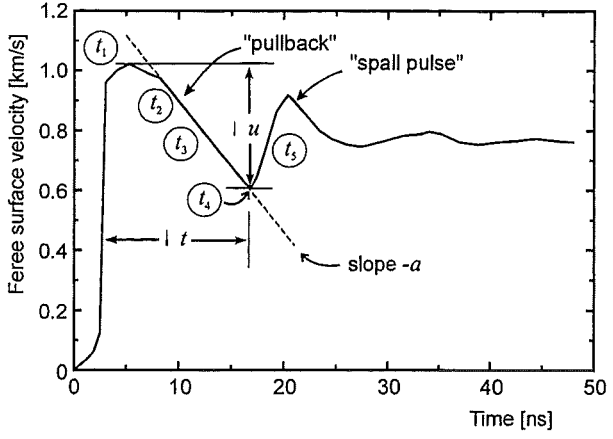

Fig. 3: Measured free surface velocity profile showing characteristics of spalling.

from any initial pressure wave of finite duration because the velocity of the unloading front exceeds the shock wave. That means after some distance covered, peak pressure has overtaken the wave face forming a shock front whereas the rear slope is spreading out forming a "rarefaction fan". In 1D geometry - planar wave front parallel to the surface plane - the peak stress increases with the distance from the surface. If it exceeds the tensile strength (R in Fig. 1) the material ruptures in the "spall plane" at a specific distance from the surface splitting off the so-called "spall plate". As can be taken from Fig. 1, this distance depends, apart from the tensile strength, on the gradient of the rear slope of the pressure pulse. The latter depends on both the peak amplitude and the duration of the pulse.

The advantage of the spall method is that all the information needed is obtained by the measurement of the "velocity profile", that is the evolution in time of the free surface velocity [3, 4]. This is explained in figures 2 and 3 displaying the wave phenomena connected with spalling in a x-t-diagram, and a typical velocity profile showing characteristics indicative of spalling. A short compression wave of triangular shape with a step front moves to the right. At t_1 it reaches the free surface where material expansion causes a velocity jump. At the same time, a rarefaction wave starts moving to the left. As it runs into the decaying tail of the compression wave (t_2) - tensile stresses build up decelerating the surface and eventually causing rupture of the material (t_3). The stressed material relaxes, the resulting collapse causes a compression wave to move to the right again. Its arrival, at t_4, at the surface breaks the deceleration, and may even re-increase the surface velocity again, giving rise to the so-called "spall pulse" (t_5). Whether a spall pulse appears or not depends on the residual stress in the spall plate. This is determined by the speed of the rupture process: brittle

materials fail rapidly by crack coalescence, leaving residual stress in the spall plate, whereas tough materials fail by coalescence of voids which needs some more time so that the stress relaxes during the rupture process. High residual stress in the spall plate causes reverberations of pressure and release waves showing up in Fig. 3 as velocity oscillations.

The appearance of a clear kink in the pullback pulse or even of a spall pulse is the unambiguous indication of dynamic failure in the material. Without rupture, the surface velocity would be slowed down to a small residual value caused by a hysteresis of elastic-plastic response. After multiple reflections of the load pulse within the sample plate, a final velocity is established which corresponds to the momentum transferred to the whole sample. The advantage of the method consists in the fact that, with the assumption of planar geometry, the dynamic tensile strength, the thickness of the spall plate, and the strain rate can be directly quantified from a single time-resolved velocity measurement. The dynamic tensile strength or "spall strength" σ^* is determined from the pullback Δu_{fs} of the free surface velocity and the - plastic - bulk sound velocity of the material c_b. The spall thickness δ is determined from the duration Δt of the pullback pulse taking into account that the release wave travels with the bulk sound velocity c_b whereas the spall signal, that is the compression wave running back from the spall plane, propagates at the - elastic - sound velocity c_0. The strain rate $\dot{\varepsilon}$ is calculated from the slope a of the pullback pulse. In the case a spall pulse appears, a correction should be made for different propagation velocities of the spall pulse front and the rarefaction wave in an elastic-plastic material [5].

$$\sigma^* = \tfrac{1}{2}\rho_0 c_b \Delta u_{fs} \qquad\qquad (1)$$

$$\delta = \tfrac{1}{2}(c_0 + c_b)\Delta t \qquad\qquad (2)$$

$$\dot{\varepsilon} = \tfrac{1}{2}a/c_b \qquad\qquad (3)$$

2.2. Spalling thin layers

The coatings to be investigated are typically 200 μm to 250 μm thick. Because the surface of the coating comes out from the coating process rough and nearly black it has to be ground and polished in order to obtain a smooth, optically reflecting surface needed for the operation of the laser velocimeter. In our case, this procedure reduced the coating thickness to 100-170 μm. To locate the spall plane at a distance of $\delta \approx 150$ μm from the surface a pulse duration of roughly $\tau = \delta/c_b$ is required where c_b is the - plastic - bulk sound velocity. For the coating material we calculated c_{b0} at zero pressure form the elastic modulus E, nominal density ρ_0, and POISSON's ratio ν

$$c_{b0} = \sqrt{\frac{E}{\rho_0}\frac{(1+\nu)}{3(1-\nu)}} = 4.42 \text{ km/s} \qquad\qquad (4)$$

The dependence of the sound velocity on the pressure was taken into account, as usual in shock wave physics, by the linear dependence on the particle velocity u_p

$$c_b = c_{b0} + 1.5\, u_p \qquad\qquad (5)$$

rather than on the pressure because u_p is directly determined by measuring the free surface velocity $u_{fs} = 2\, u_p$. The factor 1.5 is typical for medium density metals. With particle velocities

of several 100 m/s we obtain sound velocities of ~5 km/s and pressure pulse durations of ~30 ns. That is close to the 20-25 ns fwhm duration of the ablative pressure pulse generated by the direct interaction of the 0.15 TW/cm^2 pulsed proton beam of the B$_\Theta$-diode on KALIF with condensed matter which was already used for spall experiments [5, 6]. Choosing a sufficiently large sample thickness that increases the pulse duration therefore allows to realize spall thicknesses in the range of the coating thickness.

2.3. Placing the spall plane into the interface

Determining the adhesive strength of a coating requires the rupture to occur in the interface between coating and substrate. This can be achieved by choosing the decisive quantities appropriately. As shown in chapter 2.1 the distance of the fracture plane from the free surface depends on the pressure gradient in the rarefaction tail of the pulse. With peak pressure given, the gradient can be adjusted by the distance the pressure wave covers because the tail disperses during propagation. With the sample thickness given, the gradient depends on the pressure amplitude. So, varying the sample thickness or the pressure allows to place the fracture in the interface.

The task of "hitting" the interface is much simplified if a 1D spatially resolving velocimeter is employed which allows velocity profiles to be measured simultaneously at different positions. In this case it is sufficient that the spall plane and the interface intersect each other within the field of view of the velocimeter. How the intersection can be realized is illustrated in Fig. 4.

If the pressure amplitude is constant across the measuring line, the spall plane in a plane-parallel sample is oriented parallel to the surface. In this case, the direct approach to intersect the spall plane with the interface is cutting the test specimen such that the interface is lilted relative to the surface (Fig. 4a). With our specimens angles of 1-2 degrees would have been necessary which are not quite easy to manufacture by laboratory means, especially if a certain average thickness has to be met. Another approach is to use a wedge-shaped sample in which the distance covered by the pressure wave varies considerably along the measuring line. Because of the different spreading out of the rarefaction wave the pulse length increases with the thickness whereas the amplitude decreases. This results in a spall plane which is inclined relative to the surface (Fig. 4b). Making a virtue of necessity, for the experiments presented here we have utilized the fact that the power density distribution of the KALIF beam is bell-shaped with a 10 mm fwhm [7]. Placing the ~4 mm long measuring line in the gradient of the power density allows us to cover a pressure interval of typically ±25 % and a similar variation of the spall plate thickness. The resulting tilt of the spall plane relative to the surface of
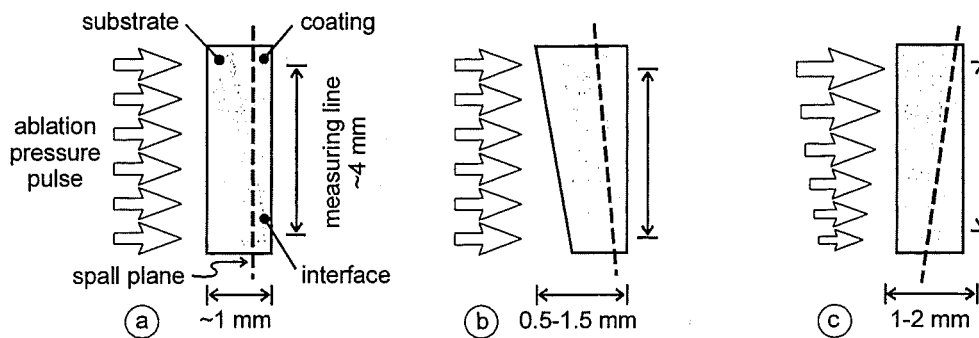

Fig. 4:   Possibilities to have the spall plane intersected with the interface. (a) Plane-parallel speci-
men, interface tilted. (b) Wedge shaped specimen: longer distance covered by the compres-
sion wave results in longer rarefaction tail and larger distance of the spall from the surface.
(c) Plane-parallel specimen and varying pressure. Higher pressure causes steeper pressure
gradients and rupture closer to surface.

~1 degree is small enough to approximately meet the assumption of planar geometry used in the derivation of eqs (1) to (3). The sample geometry is plane parallel, the spall plane is inclined with regard to the interface (Fig. 4c) because the pressure amplitude is varying whereas the pulse duration is approximately constant.

2.4. Line-imaging laser-Doppler velocimetry

We have upgraded our ORVIS-type [8] laser-Doppler velocimeter such that the velocity can be measured with high spatial and temporal resolution along a 0.3 mm to 8 mm long measuring line [6]. It combines an imaging system and a wide-angle Michelson-type interference spectrometer such that a picture of the measuring line is superimposed by contrasty interference fringes. Their deflection relative to the initial position with the target surface at rest is a direct measure for the local velocity on the target surface. Fig. 5 displays an ORVIS-type interferogram obtained by recording the fringe shift with a streak camera. The deflection of the interference fringes from the horizontal line (downwards shift means velocity increase in this illustration) gives a general impression of the velocity history: the surface starts moving at ~90 ns. Peak velocity is reached between 115-130 ns, depending on the pressure (which is highest at the top). The following deceleration is interrupted because
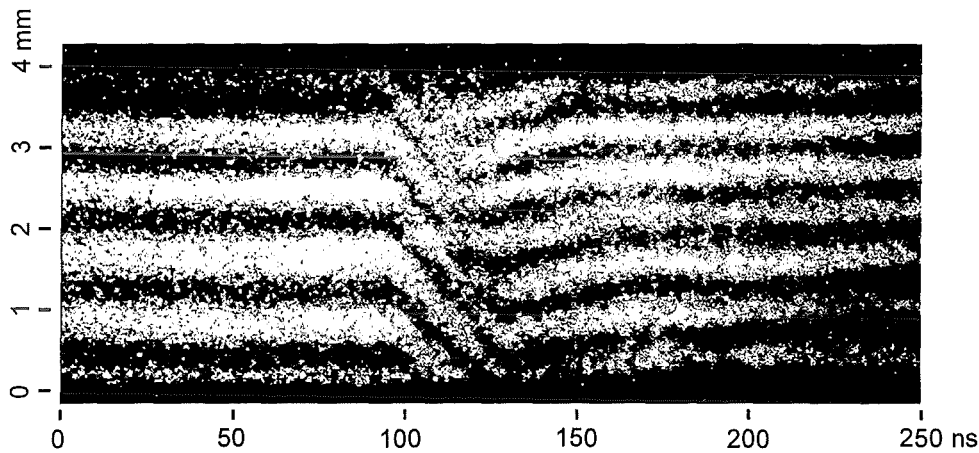

Fig. 5: Line-imaging laser-Doppler velocimeter streak record. The downward deflection from the horizontal line of the interference fringes starting at ~90 ns is proportional to the velocity. The corresponding velocity histories are displayed in Fig. 6 (solid curves).

spalling occurs. In order to obtain the exact local velocity history, however, the intensity variations along a horizontal line have to be analyzed because the ordinate, in reality, represents a space coordinate. Velocity histories evaluated from this interferogram are displayed in Fig. 6 by solid lines.

3. Measurements and results

Three different kinds of coatings (types A, B, and C) manufactured under special conditions were examined. The 30 mm diameter samples were 4 mm thick. The coating had the standard thickness of 200-250 μm. The specimens were divided into 6 segments of equal size from which 1 mm, 1.5 mm, and 2 mm thick slices were cut off. The coating was ground and polished to achieve optimum reflection of the laser beam of the velocimeter. This procedure
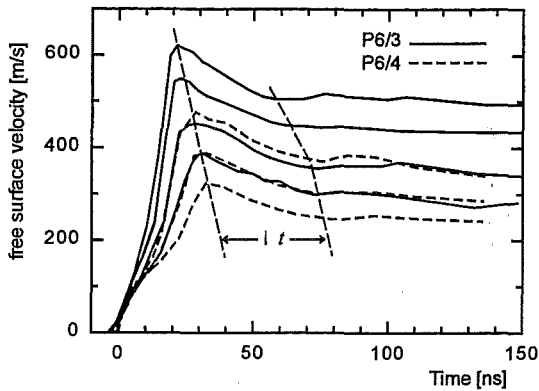
Fig. 6: Velocity profiles measured with two samples of coating type C. Δ*t* is a measure for the distance of the spall plane to the surface. At high velocities spalling occurs within the coating. With decreasing velocity it moves towards the interface and stops there.
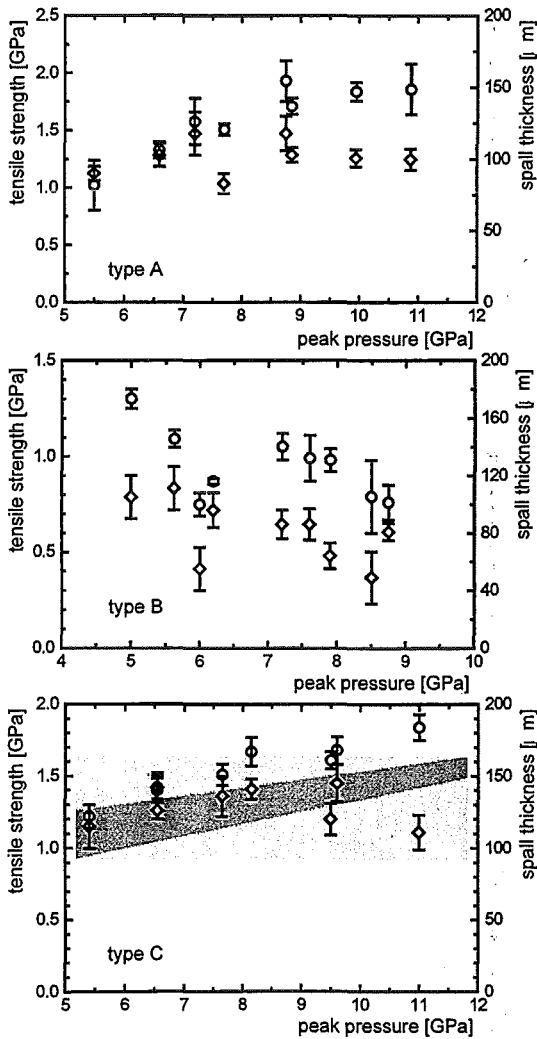

Fig.7 a-c: Measured tensile strength (circles) and spall thickness (diamonds) for the three types of samples. The shaded area in Fig c indicates the probable position of the interface.

reduced its thickness to 100-160 μm. At first, experiments with stainless steel specimens were performed. They showed that 1.5 mm thick samples and positioning the center of the measuring line 2-4 mm off the proton beam axis was suitable to achieve fracture in a range of distances from the surface including the coating thickness.

Figure 6 displays velocity profiles measured with two samples of type C in two positions relative to the proton beam axis. The different curves represent local velocities at different places along the measuring lines on the samples. The kink in the rising slope of the curves at about 150 m/s is due to the elastic-plastic transformation when the dynamic yielding point is exceeded. The peak velocities cover the interval from 325 m/s to 625 m/s. This corresponds to a pressure range of 5.4–11 GPa. The length Δ*t* of the pullback first increases with reducing peak velocity and pressure, respectively, and then stabilizes. This is interpreted as follows: at high pressure amplitudes the rupture occurs inside the coating. As the pressure decreases the spall plane goes away from the surface. Because the tensile strength of the substrate is by a factor of 3 higher than that one of the coating the rupture threshold, even at very low pressures, is always reached at the interface before sufficiently high stresses can build up inside the substrate. That means the spall plane is centered in the interface.

The tensile strengths and adhesive strengths, respectively, measured with the different types of coatings are displayed in Figs 7a-c (circles) together with the corresponding distances of the spall zone from the surface (diamonds). They are plotted as a function of peak pressure which makes results from different shots comparable despite KALIF power variations. Unfortunately, grinding and polishing was carried out on the individual segments instead on the whole disk-shaped samples. This resulted in different coating thicknesses which in many cases even considerably vary along the measuring line. Except for the samples of type C, it is therefore often difficult to assign data to the interface.

The results can be summarized as follows.

100

The samples of type A show the highest strength in the coating (1.88 GPa) and an average adhesive strength of 1.39 GPa. There is probably a tendency to fail at a depth of about 100 μm which, according to thickness measurements by means of a microscope at the polished side faces of the samples, should be located within the coating.

The samples of type B are the most heterogeneous and show the smallest strength with an average of 0.95 GPa. Rupture seems to occur mainly within the coating.

With an average value of 1.68 GPa the strength of the type C coating is about 12 % smaller than for type A samples, but the adhesive strength of 1.38 GPa is nearly the same. As expected, the rupture is located inside the coating at high pressure amplitudes, and centers in the interface as the pressure reduces. This indicates that, in comparison with samples of type A, the coating is quite homogeneous.

4. Conclusions

We have demonstrated a novel application of the spall technique for measuring the adhesive strength of 100-200 μm thick metallic coatings on a substrate. We have utilized the pulsed high-power proton beam of KALIF to generate short intense pressure pulses that cause dynamic failure or spalling inside samples at distances from the surface comparable to the thickness of the coatings. Taking profit of the power decrease at the edge of the bell-shaped beam profile we were able to cover a whole range of distances in each single experiment and to measure the corresponding free surface velocity histories by use of a spatially resolving laser-Doppler velocimeter. The experimental data obtained with turbine blade coatings provide a potentially important information for the optimization of the coating procedure and the performance of the layers.

References

[1] L. Davison and R.A. Graham, *Phys. Rep.* **55**, 255 (1979).
[2] D.R. Curran *et al.*, *Phys. Rep.* **146**, 253 (1987).
[3] S. Cochran and D. Banner, *J. Appl. Phys.* **48**, 2729 (1977).
[4] S.A. Novikov and A.V. Chernov, *J. Mech. Tech. Phys.* **23**, 703 (1982).

[5] G.I. Kanel *et al.*, *J. Appl. Phys.* **74**, 7162 (1993).

[6] K. Baumung *et al.*, *J. Phys. IV France* **7**, C3-927(1997).

[7] K. Baumung *et al.*, *Int. J. Impact Engng,* **20**, 101 (1997).

[8] D.D. Bloomquist and S.A. Sheffield, *J. Appl. Phys.* **54**, 1717 (1983).

[9] K. Baumung *et al.*, *Shock compression of Condensed Matter-1995*, 1015 (ed. by S.C. Schmidt and W.C. Tao), AIP Press, Woodbury, NY(1996).

SIMULATION OF KALIF BEAM-TARGET INTERACTION EXPERIMENTS

H. Marten[1], K. Baumung[1], P. Hoppé[1], G. Meisel[1]
and
J.J. MacFarlane[2], P. Wang[2]

[1] *Forschungszentrum Karlsruhe GmbH, INR, Postfach 3640, D-76021 Karlsruhe, FRG*
[2] *PRISM Computational Sciences, P.O. Box 260181, Madison, WI 53726-0181*

Abstract. Recently, Marten et al. [1] presented a parameter study of beam-target interaction experiments performed at KALIF. Foil acceleration experiments were simulated with different numerical codes, and the influence of homogeneous and time dependent proton beam angle and energy distributions as well as the influence of the maximum beam power density on the target dynamics were investigated on the basis of experimentally determined beam data. However, the discrepancy between simulated and measured target velocities could not be improved significantly by the studied effects. This lead to the conclusion that the time history of the beams had to be modified to simulate individual KALIF experiments. It was also shown in [1] that a modification of the beam history changes the plasma temperatures, and it was speculated that this could be observed by K_α spectroscopy.
The present report complements the work given in [1]. Measured target velocities are simulated with individual beam profiles and synthetic K_α spectra are compared with measured spectra in order to deduce details about the KALIF beam history at the targets.

1. Introduction

In foil acceleration experiments performed at KALIF Aluminum foils with initial thicknesses larger than the proton range are irradiated with intense proton beams. A dense plasma forms in the proton energy deposition zone and the corresponding ablation pressure accelerates the remaining solid and cold part. The rear surface velocity of these foils is recorded with a space and time resolving laser-Doppler velocimeter.

In a different experiment subrange targets are completely evaporated by the proton beam thus forming an almost homogeneously expanding plasma. In this plasma K-shell electrons are removed by direct impact of beam particles. As the K-shell vacancies are spontaneously filled by L-shell electrons, K_α lines are observed in emission, the satellite structure of which is related to the degree of collisional ionization and can be used for temperature estimates.

In the following we present a comparison of measured and calculated target velocities for the selfmagnetically insulated B_Θ diode (Section 2) and for the applied B diode (Section 3) currently used at KALIF. The computations are based on 1 D radiation hydrodynamic models with the code KATACO [2] taking into account realistic beam angle and energy distributions of the protons along the KALIF beam history [1]. The state of Aluminum is described by the wide range equation of state given in [3], and radiation transport is treated in the diffusion approximation with LTE opacities provided by the code EOSOPC [4] for 100 frequency groups. K_α spectra are computed in a postprocessing step to be described in Section 4.

2. Foil acceleration experiments with the B_Θ diode

Fig. 1 shows experimental results (symbols) and computational simulations (solid lines) of foil acceleration experiments with Al foils of 33, 50 and 75 μm initial thickness performed with the
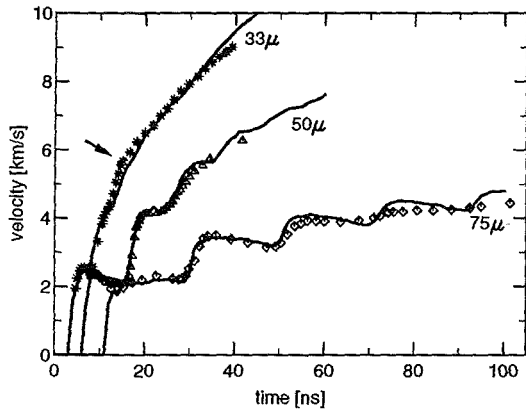
Figure 1: Measured (symbols) and computed (solid lines) rear surface velocities of Aluminum foils with 33, 50 and 75 μm initial thickness during irradiation with the B$_\Theta$ proton beam
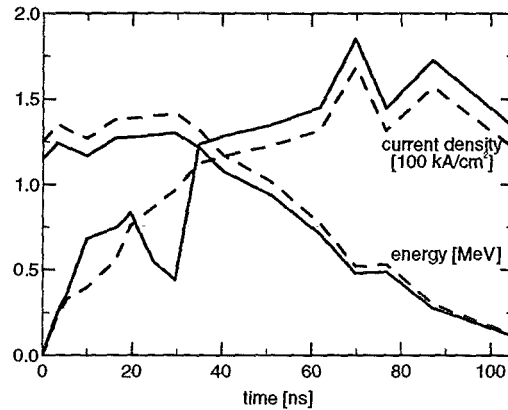
Figure 2: Dashed: Experimentally determined time history of the B$_\Theta$ proton beam at the target. Solid lines exemplarily show the beam parameters used for the simulation of the 50 μm foil in Fig. 1

B$_\Theta$ diode. Once the protons start to deposit their energy and heat the target, the corresponding plasma pressure drives a compression wave into the remaining solid part. At the rear surface of the foil the compression wave is reflected as a release wave running back into the target, the release wave is reflected at the ablation plasma bounday as a compression wave, and so on. These wave reverberations lead to a stepwise increase of the target velocity whenever the compression wave reaches the rear surface.

The average beam history of the B$_\Theta$ diode derived from electrical signals is shown by dashed lines in Fig. 2. Solid curves exemplarily demonstrate the modifications necessary to simulate the 50 μm foil of Fig. 1. The models take into account a distribution of proton impact angles between 20° and 40° with respect to the target normal due to the ballistic focusing of the diode as well as a Gaussian distribution of proton energies with a FWHM of 20 % of the average value. According to recent measurements with a magnetic energy analyzer the average proton energy has been reduced by 8 %. The proton current density has been increased by 10 % accordingly to keep the experimentally determined peak power density of 0.15 ($\pm$ 0.05) TW/cm^2. The ion current density was slightly increased additionally between 5 and 15 ns of the pulse in order to get a correct height of the first two velocity plateaus. Furthermore, we introduced a local current minimum at about 30 ns which leads to an early decoupling between the beam energy input and the accelerated foil. This decoupling is visible as a kink in all experimental velocity data, it is the more pronounced the smaller the accelerated mass is (see e.g. the arrow at $t = 14$ ns for the 33 μm foil in Fig. 1). Such a current minimum could be caused by a parasitic load similar to that found in the B$_{appl}$ diode (see next section). Qualitatively the same modifications of beam parameters had to be introduced in all three models of Fig. 1.

3. Foil acceleration experiments with the B$_{appl}$ diode

The beam parameters used in simulations for the B$_{appl}$ diode are given in Fig. 3. As for the B$_\Theta$ diode the models account for a distribution of proton impact angles (here between 30° and 42°) as well as for a Gaussian distribution of proton energies (FWHM = 20 % of the average value). The average kinetic energy of the protons in Fig. 3 is taken from the electrical diode
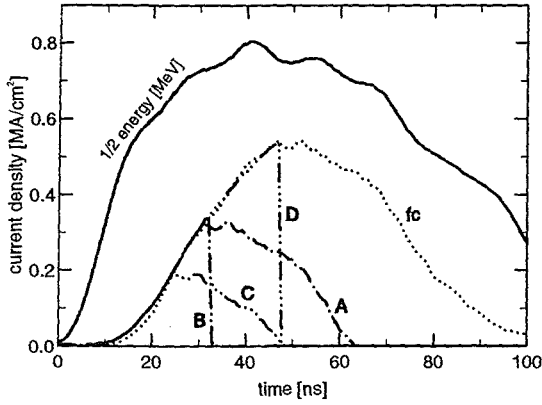
Figure 3: Average proton energies and proton current densities used to simulate different experiments with the B_{appl} diode (see text)
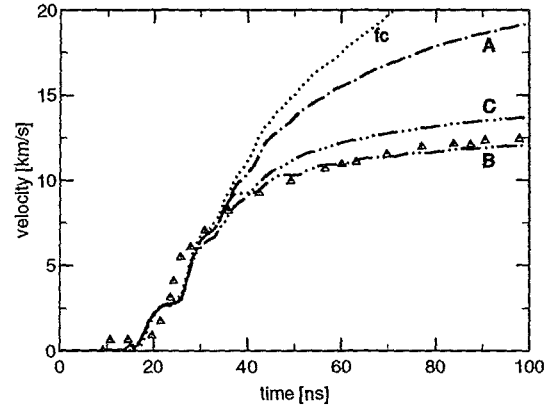
Figure 4: Computed rear surface velocities of a $50\,\mu m$ Al foil for the beam models of Fig. 3 The triangles are measured velocities for shot #3360

voltage without modifications. Curve fc is an average current density derived from Faraday cup measurements inside the diode. The current falloff is caused by the development of some "parasitic load". Curves A to D were given the same early current development as fc; they model different assumptions about the onset time of the parasitic load and its further development.

Fig. 4 compares measured (symbols) and computed (lines) rear surface velocities of a $50\,\mu m$ Al foil. The results of the calculations mainly differ at times later than 35 ns. The target velocities are found to depend on both, the peak proton flux (compare models A & C) and on the slope after peak current (A & B). Model B gives the best fit to the measurements, fc is far off the experimental results at late times. We also tried to model the target acceleration with the Faraday current density multiplied by a factor of 0.5. However, such beam models can completely be ruled out because they produce too small target velocities between 20 and 40 ns [1].

4. K_α satellite spectroscopy with the B_{appl} diode

For the computation of K_α spectra the target surface is devided into four concentric regions with radii of 2.4, 3.84, 5.76 and 9.6 mm (0.3, 0.48, 0.72 and 1.2 times the measured FWHM of the spacial beam profile). For each of these regions radiation hydrodynamic simulations of $6\,\mu m$ thick Al foils are performed with 88.4, 64.6, 36.3 and 8.6 % of the current densities shown in Fig. 3. The resultant temperature and density profiles at different times together with the respective proton fluxes are then fed into the Non-LTE radiation transport code NLTERT [5] to calculate time dependent emission spectra. Finally, the spectra of the four regions are space integrated over an observational slit of 1 mm width, time integrated over the whole KALIF pulse and broadened to account for an experimental resolution of 500.

The experimental spectra mostly show 3 components as in Fig. 5c). The intensity ratio of the two stronger components (Al IV to Al I-III) is about 0.3; it is well reproduced from shot to shot. The intensity ratio Al V to Al I-III varies widely between 0.05 and 0.2 in the same experiments. The Al VI satellite is very weak and only rarely observed.

Comparing the computed with the observed spectra in Fig. 5 it is again obvious that current fc is not consistent with the experiments since the satellites Al VI and Al VII were never observed with a relative intensity as given in Fig. 5b. The same is true for current curve D. B and
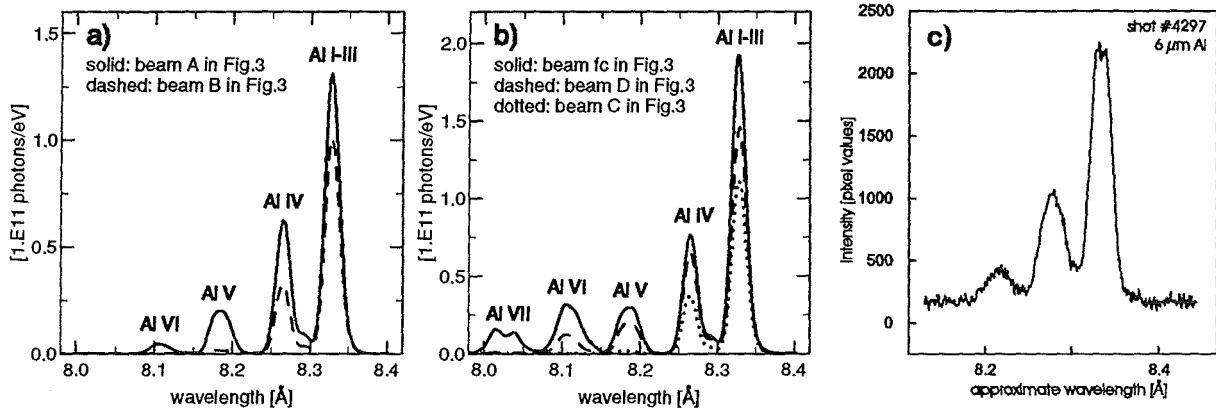
Figure 5: a) and b) are computed K_α spectra of a 6 μm Al foil with beam parameters given in Fig. 3. c) is a typical observed K_α spectrum

C result in almost the same spectra; they have a very weak but still observable Al V component. The spectrum calculated for current A is close to the "strongest" observed spectra. Altogether, the actually observed spectra all lie between the spectra calculated with models A and B (or C). The peak temperatures for models A and B (or C) are about 20 eV and 13 eV in the beam centers, respectively.

5. Conclusions

Two types of target experiments quite different in nature have been performed with the B_{appl} diode. A comparison of the experimental results and of the simulations nevertheless leads to similar conclusions for both types of experiments. Both experiments allow to exclude certain developments of the ion current density at the target such as, e.g., fc and D. The acceleration experiments can distinguish between curves C and B because the voltage and thus the proton range keeps increasing all time during the proton flux, the K_α spectra vary considerably between current curves B and A or C and A. Both types of experiments can serve as a sensitive means to determine the onset of the parasitic load and the following current decay. The calculations show that velocities in excess of 20 km/s and plasma temperatures above 30 eV were obtained if curve fc could be realized, which requires to delay the parasitic load by about 15 ns.

In the case of the B_Θ diode only small modifications of the beam parameters for each individual experiment lead to a satisfactory agreement between measured and computed target velocities. A comparison of individual experiments with simulations for average beam profiles or even of individual experiments among each other is limited by the shot to shot variation of the KALIF diodes. In this respect a simultaneous measurement of target velocities and K_α spectra together with beam parameters during individual KALIF shots would significantly improve the analysis of the experiments.

It should be emphasized once more, that the beam parameters in the focal plane used in the simulations were derived from measured electrical signals of, and Faraday cup signals in the diode. The fact that the beam parameters in the simulations had to be modified in order to match the experimental velocity and K_α data does *not* mean that the measured electrical or Faraday signals are incorrect. Instead, there seems to be a missing link between the ion current densities in the diodes and the ones at the target. For example, a loss of beam particles on their way to the target, e.g. by the beam interaction with the diode mounting or diode walls, would

not be observed by Faraday cups placed in the diode nor by any electrical diode signal. The current density at the target could especially be reduced by a "sudden" beam defocusing due to plasma instabilities inside the diode. Instabilities of the ion accelerating electron sheath are known to develop at a certain time, and it is planned to reinvestigate a possible beam defocusing with a PIN diode cross in the focal plane.

References

[1]   Marten H., Goel B., Höbel W., Hoppé P., Gryaznov V.K., Lomonosov I.V., Shutov A.V., Vorobiev O.Yu., A numerical parameter study of the beam-target interaction performed at KALIF, Report Forschungszentrum Karlsruhe GmbH, FZKA 6106, 1998

[2]   Goel B., Höbel W., Würz H., Numerical Simulation of Radiation Transport on Supercomputers. in: H. Küsters (ed.) Proc. of the Joint Internat. Conf. on Mathematical Methods and Supercomputing in Nuclear Applications, Karlsruhe, Germany, April 19-23, 1993 Vol. 2, p.63

[3]   Lomonosov I.V., Fortov V.E., Kishchenko K.V., Levashov P.R., Multi-Phase Wide-Range Equation of State for Metals. 8th International Workshop on Atomic Physics for Ion-Driven Fusion, Heidelberg, Germany, September 22-23, 1997

[4]   Wang P., 1993, EOSOPC – A code for computing the equations of state and opacities of plasma with detailed atomic model. Internal Report Forschungszentrum Karlsruhe, 1993

[5]   MacFarlane J.J., NLTERT – A code for computing radiative properties of Non-LTE plasmas. Fusion Power Associates Report, FPA-93-6, Madison, 1993

Studies of K_α Spectra from Targets at the KALIF Focus

G. Meisel, H. Bluhm, B. Goel, P. Hoppé, R. Hüttner, H. Marten, O. Stoltz, E. H. Saenger, T. Schön

Forschungszentrum Karlsruhe GmbH, INR, P. O. Box 3640, D-76021 Karlsruhe, Germany.

Abstract. A solid target at the KALIF ion beam focus is rapidly converted into a plasma with temperatures in the 15 to 25 eV range. Due to their satellite structure, K_α transitions give information on the plasma temperature and on the proton flux. Both, emission and absorption are considered. We present K_α emission spectra for subrange targets of Al, Si, and Mg. The Al spectra are discussed with respect to the incident proton current; it is found that the current is cut off considerably earlier than is observed in experiments with Faraday cup probes positioned upstream of the focal plane.

1. Introduction

The KALIF facility generates a 50 ns proton burst with proton energies up to 1.7 MeV. Its current reaches to several hundred kA. The proton flux is concentrated to an area of about 1 cm^2. If solid matter is exposed to this beam, it is rapidly heated up to temperatures with kT in the 20 eV range, forming a dense and fast expanding plasma. Its properties can be studied by observing the K_α soft x-ray spectra associated with the plasma atoms [1]. K_α transitions are made possible by collisions between beam protons and target atoms. If a collision results in a hole in the 1s shell of a target atom, K_α emission is induced. A 2p hole allows for K_α absorption.

Since the outer electrons of an atom contribute somewhat to the screening of the nuclear charge, their removal from its original shell and excitation to some higher shell or to the continuum slightly increases the effective nuclear charge which determines the 1s and 2p energy eigenvalues. The resulting 1s and 2p level shifts lead to an increase of the 1s ↔ 2p transition energy for every single removed outer shell electron. The ionization states of the plasma atoms in turn are strongly dependent on the plasma temperature. Therefore an observed K_α spectrum is composed of several components ("satellites") with intensities that correspond to the population of the different ionization states. By comparison with calculated model spectra [2] plasma temperatures can be determined. Since the x-ray spectra depend on the proton flux, the spectra also allow us to draw conclusions on the proton current time structure at the target position [3].

For the present experiments target foils with subrange thickness are used to obtain uniform energy deposition conditions. The K_α emission is dispersed by a Bragg crystal to record its satellite structure. For absorption experiments a laser induced plasma is explored to be used as source of backlighter radiation.

2. Experimental Details

A schematic diagram of the setup is given in Fig. 1. A target foil is placed at the nominal KALIF focus position. It was made of Al or Si which have approximate K_α energies of 1.5 and 1.7 keV, respectively ($\lambda \approx 8.3$ and 7.1 Å). The target foil thickness was chosen between 2 and 8.2 μm.

A slit of 0.5 or 1 mm width is the resolution defining spectrometer entrance. Since the slit jaws serve as proton beam dump, ablated material might close the slit already during the proton pulse which would falsify the observed spectra. To test this assumption, the distance between the slit and the focus was varied from 40 to 80 mm; in addition, the slit jaws were made of stainless steel, graphite or tungsten. All these variations had no observable effect on the K_α spectra, allowing us to reject the slit closure assumption.
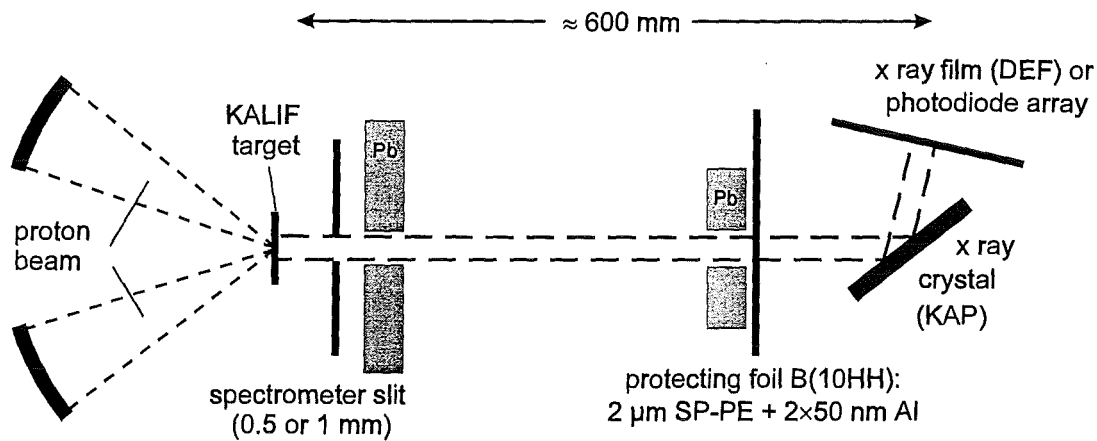
Figure 1: Schematic diagram of the experimental setup for K_α emission with the soft x-ray spectrometer.

A 2 μm polyethylene foil is used to protect the spectrometer crystal against debris from the target area. The foil is coated with 50 nm Al on each side to keep target light away from the x-ray detector.

The K_α dispersing element is a thin cleaved flat crystal of KAP (potassium hydrogen phthalate - $C_6H_4(COOH)(COOK)$; 2d = 26.632 Å [4]). It is used in first order; for the entrance slit widths given above the resolution for Al is 400 and 200, respectively.

As detectors we used either DEF soft x-ray film (by Kodak) or a linear photodiode array modified for soft x-ray detection (model RL1024SAU by EG&G Reticon).

Shielding is of particular importance since KALIF is a strong source of hard x-rays and of microwaves. As is shown schematically in Fig. 1, lead shielding was used to attenuate the hard x-rays. The remaining x-ray background intensity is the sensitivity limiting factor for the spectrometer since its background noise dominates the total noise for low level signals. The rf pollution by KALIF reaches to several GHz. To avoid failure of the photodiode array electronics, massive Al shielding was employed. The K_α radiation reaches the photodiode detector through a tapered waveguide of 230 mm length. Its calculated amplitude attenuation for H_{01} waves is 10^{-6} at 6 GHz; the cutoff frequency is 8 GHz. With this shielding all rf problems were completely eliminated.

For absorption experiments the target and spectrometer setup are unchanged. A backlighter target is added behind the KALIF target. A laser beam is focused with a lens of 500 mm focal length on the backlighter target. Care must be taken to avoid that material ablated by diffuse protons attenuates the laser beam. The laser system has a seeded Nd:YAG oscillator followed by 3 Nd:glass amplifier stages. The output beam is frequency doubled resulting in pulses of 5 ns duration with energies between 4 and 7 J. The laser system is synchronized with the KALIF discharge by triggering its Q switch by a signal derived from the intermediate store switch spark. The resulting rms jitter is 7 ns.

3. Measurements and Results

Most KALIF shots were performed with Al emission targets. Almost all spectra showed 3 components, a few had a very weak fourth line. Fig. 2 shows three representative examples including the extremes. The strongest component at about 8.32 Å is a superposition of satellites with none to all of the n=3 electrons removed from the $1s^2 2s^2 2p^6 3s^2 3p^1$ Al atomic configuration; the satellite shift for n=3 electrons is too small to be resolved in our set-up. The other lines at shorter wavelengths are emitted by atoms that have one or more of the eight n=2 electrons excited.

The sample spectra given in Fig. 2 differ essentially by the intensity of the weak higher energy component at about 8.21 Å. Qualitatively, the satellites with more outer shell electrons excited (i. e., with shorter wavelength) correspond to higher temperatures. The information contained in a spectrum essentially is the intensity ratio of its three components. Fig. 3 is a plot for all Al spectra obtained so far. It shows a wide variation of #3/#1 by about a factor 5 for seemingly constant shot conditions. In contrast, #2/#1 is comparatively constant over the range observed.
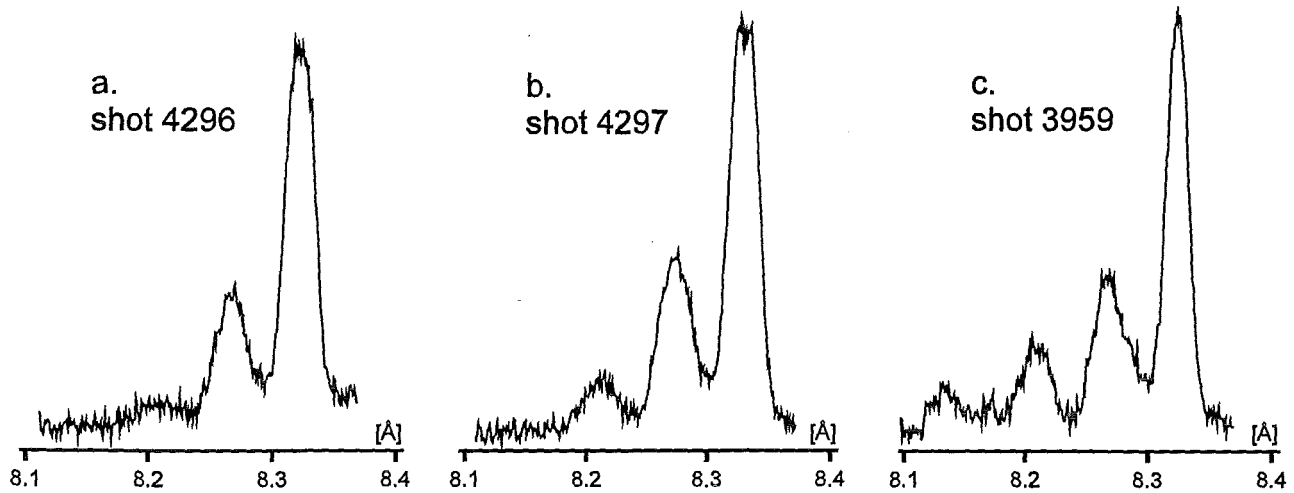

Figure 2: Three representative K_α emission spectra from 6 µm Al targets. For the spectra a. and b. the spectrometer slit was 1 mm wide, for spectrum c. the slit width was 0.5 mm. The wavelength scale is approximate only.
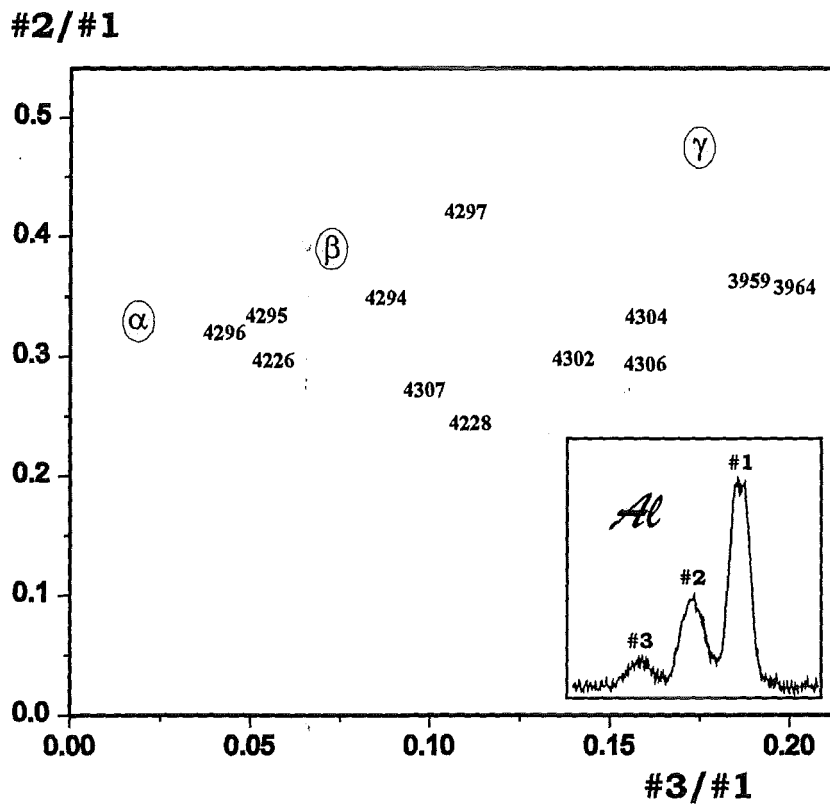

Figure 3: Plot of the intensity ratios #2/#1 versus #3/#1 for all shots on Al targets with the B_{appl} KALIF diode. The shot number is used as symbol in the plot. α, β, and γ mark intensity ratios as obtained from model spectra [3].

Accompanying calculations of model spectra [3] show that components #1 and #2 are from the early pulse, whereas #3 is emitted mainly during the later high temperature phase of the pulse. Thus the #3/#1 ratio is a measure for the peak temperature reached in an individual shot. This view is confirmed by the fact that in the "hottest" shots 3959 and 3964, a weak fourth component at about 8.14 Å was observed (cf. Fig. 2c.).

In contrast to the experimental results, calculations [3] predict 5 well visible components if the proton current in the focal plane were as one might infer from measurements with Faraday cups in the cathode plane (fc in Fig. 4) [5]. From the observation that the spectra always have considerably less components we concluded that the proton flux in the focal plane might terminate much earlier than the Faraday cup measurements suggest. Calculations for currents with various cutoff conditions are discussed in detail in [3]. Three sample current courses α, β, and γ were included in Fig. 4; the respective model spectra have intensity ratios as given in Fig. 3. For currents rising higher and lasting longer than γ, the #2/#1 and #3/#1 ratios converge to a point close to γ in Fig. 3; these currents can be excluded as unrealistic since they result in spectra with increasingly stronger short wavelength components that we did not observe. The calculated intensity ratios for model currents α, β, and γ are reasonably close to the observed ones, but the model input data obviously still need some modification to reproduce the observed intensity ratios.
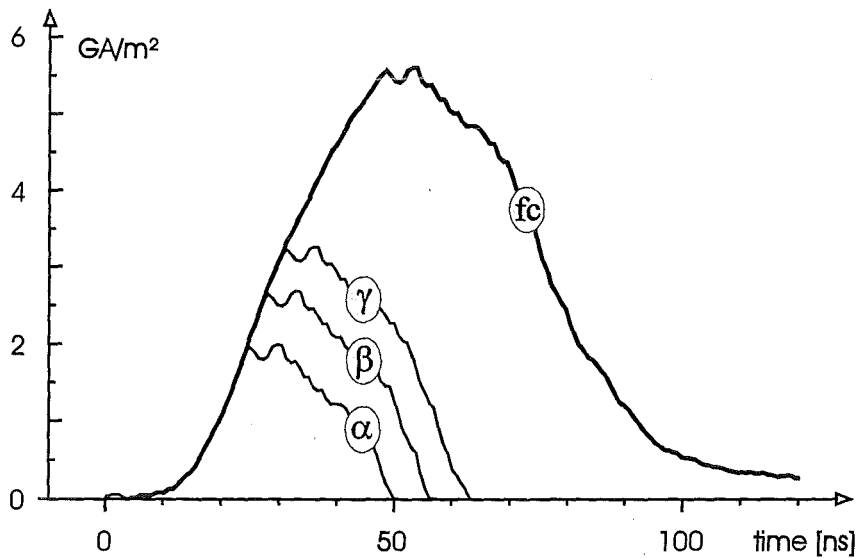

Figure 4: Different currents used in calculations [3] of K_α model spectra for the B_{appl} KALIF diode. fc is a current as derived from Faraday cup measurements [5].

The peak kT values calculated at the proton beam center are 13, 17, and 20 eV for currents α, β, and γ, respectively. If the current really were as indicated by fc (cf Fig. 4), the kT value would peak at 35 eV.

Single exploratory spectra were taken with Si and Mg targets (Fig. 5). For Si, the short wavelength component at about 7.14 Å has an electron configuration with two 2p electrons missing which means that altogether 6 outer electrons are removed, one more than for the corresponding Al component #3. Thus under comparable shot conditions, i. e. at similar temperatures, in Si higher ionization states are reached than in Al. The Mg signals were rather weak, and no third component could be identified. For Na the signals were even weaker so that no emission could be observed so far.
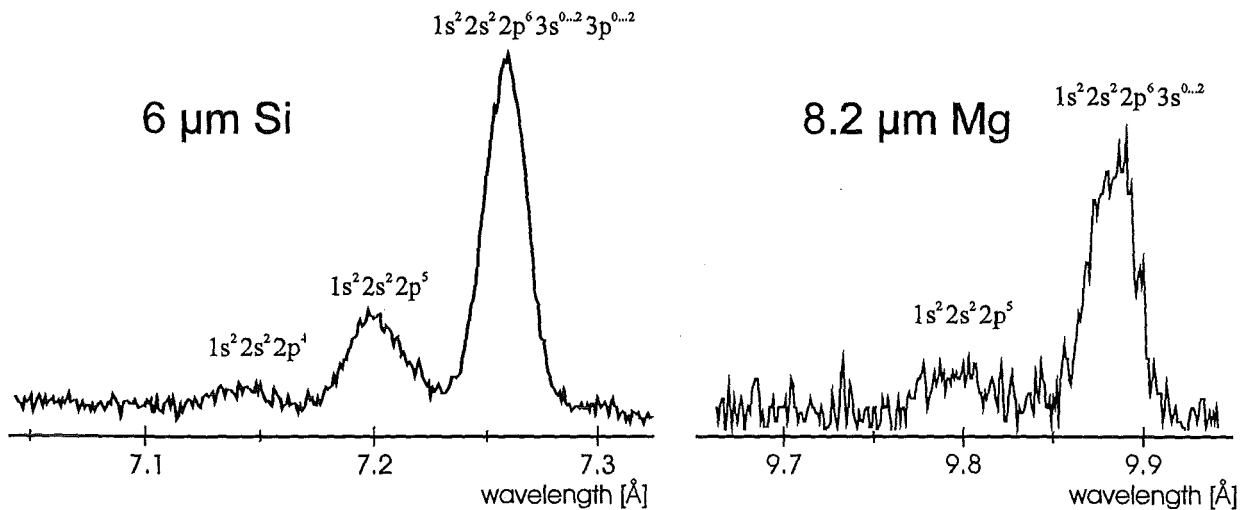
Figure 5: Si and Mg K_α emission spectra. The electron configurations given with the components apply to the atom which has not yet the 1s electron kicked out to allow for the K_α transition.

In preparation for absorption, different backlighter target materials were tested in a separate setup. It was found that the only elements that come close to the requirements are the rare earths that have broader emission in the required wavelength range due to their M transitions. Each element covers a band of about 10 % of the center wavelength which is sufficient for the absorption features expected. Fig. 6 gives a few sample backlighter spectra with the approximate positions of the absorption for several KALIF target elements of interest. The x-ray source diameter was determined by pinhole pictures to be approximately 150 μm which is sufficiently narrow in view of the desired resolution of 1000 or below. Backlighter spectra taken under realistic conditions during a KALIF shot showed that the backlighter source is too weak to compete successfully with the strong background signals.
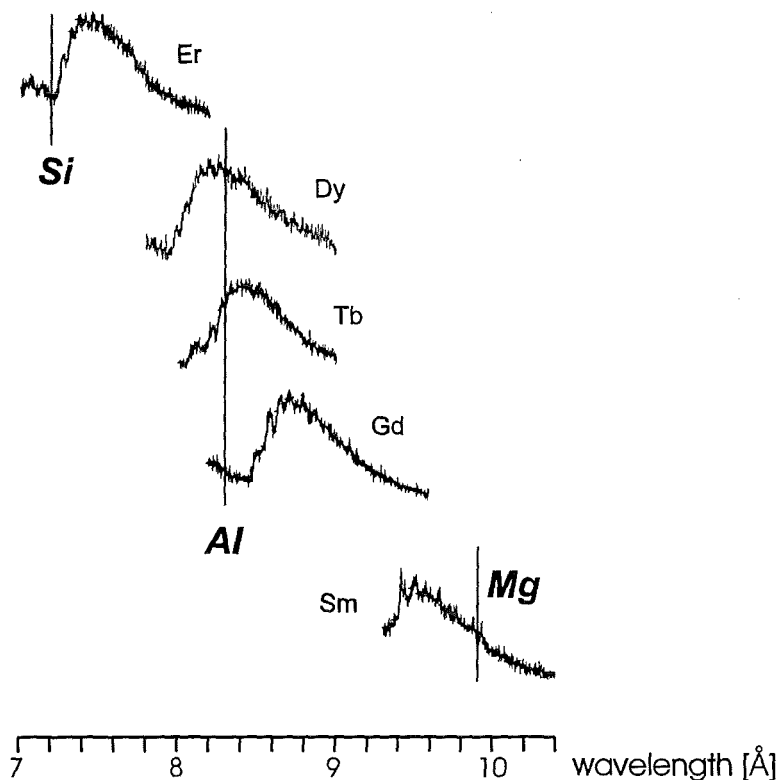

Figure 6: A selection of laser induced rare earths M spectra. The approximate positions of K_α absorption lines for Si, Al, and Mg are marked.

4. Discussion and Outlook

K_α emission spectra have proven to be a useful tool to study the beam target interaction. It was found that the proton flow arriving at the very target position is considerably different from that one extrapolated from other indirect measurements. The currents used in the modelling do not yet fully reproduce the observed variations of the spectra (cf Fig. 3); the range of #3/#1 needs to be slightly stretched but in such way that essentially no fourth component develops. At the same time the rise of #2/#1 with #3/#1 must be removed. In a next degree of refinement triangular current courses might be used in the models that are defined by three parameters as, e. g., the initial current rise, its duration, and the speed of the current decay.

The same calculations as for Al need to be performed for Si resulting in a plot corresponding to Fig. 3. Systematic measurements with Si targets will be a good test of the modelling. An even more stringent test is accomplished if information is gathered in a single shot that results in more than just two numbers. One additional number is obtained if the K absorption edge is determined in parallel with a 3-component K_α emission spectrum as is pointed out below. A total of 4 numbers could come from observations with a two-element target, e. g. Al with Si. Mg and Na are candidates that potentially have more satellite components at our conditions and thus give more simultaneous information per single shot. They require a collecting spectrometer to compensate for their reduced intensity.

K_α absorption spectra have two severe problems:

Absorption spectra in contrast to emmision present a snapshot only. The original concept was to put together a series of such snapshots taken for different delays during different KALIF pulses to obtain a time resolved development of the plasma during the pulse. This idea had to be dropped because of the poor shot-to-shot reproducibility of the spectra, cf Fig. 3.

The second problem arises from the structure of the backlighter spectra. Their smothness is rather poor; the ripple is due to the fact that the observed spectrum is a superposition of numerous single atomic emission lines. The observed intensity is the (weighted) sum of all lines that fall into the interval defined by the instrumental resolution. The absorption processes, though, occur at the "natural" resolution, i. e. at the actual atomic line width level. These are the Doppler line widths of the emitting and the absorbing atoms. Assuming Dy as backlighter material and $kT\approx200$ eV for the radiating laser induced plasma, the Doppler width is estimated to be about 0.0007 Å. Correspondingly, the Doppler width at $kT\approx20$ eV for an absorbing Al target is 0.0005 Å which is even narrower than for emission.

To predict the expected absorption to be compared with the observed result, would require to calculate both, the emission as well as the absorption spectra to a precision and with a resolution equal to the wider of the two linewidths, which is the backlighter width in this case. No such calculation is possible at present. One might consider to measure the true backlighter spectrum at the required 10^4 resolution level instead. This approach, however, does not solve the problem since it is still required to calculate the absorption with unrealistic accuracy.

To consider the spectra as sufficiently randomized due to the huge number of lines involved seems not a successful concept, since the line densities as well as the line strengths both are far from averaging to a smooth spectrum as is obvious from Fig. 6 where steep gradients are still present despite the fact that the instrumental resolution of 400 has the effect of averaging over 25 backlighter Doppler linewidths.

Two solutions to the problem complementary to one another might be envisioned. Both use continuum spectra, one method for the absorber, the other one for the backlighter: For bound-free transi-

tions the K-edge of the absorbing plasma has been calculated to shift with temperature ([6], Figs. 2.7 - 2.9). This only moderately structured feature can be adequately sampled with backlighter spectra structured as of Fig. 6. The other method is to use continuous bremsstrahlung from a laser induced plasma as backlighter. This approach requires a much stronger laser source with shorter pulses since the present laser system does not give bremsstrahlung spectra of noticeable intensity.

A completely different analytical approach is to measure the proton beam scattered by a high Z target with an array of fast diodes [7]. This method at least in principle also has the potential to identify a motion of the focal plane as source of the early proton flux decay.

References

[1] J. J. MacFarlane, P. Wang, and R. R. Peterson: "Theoretical Investigations of High Energy Density Plasmas in Support of KALIF Experiments". Fusion Power Associates, Report FPA-95-1 (January 1995).

[2] J. J. MacFarlane, P. Wang, J. E. Bailey, and T. A. Mehlhorn: "Diagnosing Plasma Conditions in Targets Irradiated by Intense Light Ion Beams Using K_α Satellite Line Intensity Ratios". Fusion Power Associates, Report FPA-97-1 (June 1997).

[3] H. Marten. K. Baumung, P. Hoppé, G. Meisel, J. J. MacFarlane, and P. Wang: "Simulation of KALIF Beam-Target Interaction Experiments", this report.

[4] J. H. Underwood: "Crystal and Multilayer Dispersive Elements" in: X-Ray Data Booklet, Lawrence Berkeley Laboratory, Center for X-Ray Optics, University of California, Berkeley, 2nd printing, PUB-49C Rev. (April 1986).

[5] P. Hoppé, M. P. Desjarlais, H. Bluhm, L. Buth, D. Rusch, O. Stoltz, and W. Väth: "Improvements of Beam Divergence by Emission Profiles with Better Homogeneity", in: Proc. 12th International Conference on High-power Particle Beams, Haifa (1998). In press.

[6] J. J. MacFarlane, P. Wang, H.-K. Chung, and J. F. Santarius: "Collisional-Radiative, Atomic Physics, and Radiation-Hydrodynamics Simulations of Aluminium and Silicon Targets Heated by the KALIF Proton Beam". Fusion Power Associates, Report FPA-96-9 (December 1996).

[7] H. Bluhm, P. Hoppé, H. Bachmann, W. Bauer, K. Baumung, L. Buth, H. Laqua, A. Ludmirski, D. Rusch, O. Stoltz, and S. Yoo: "Stability and Operating Characteristics of the Applied B Proton Extraction Diode on KALIF", in: Proc. 10th International Conference on High Power Particle Beams, San Diego (1994), p. 77-82.

5 Applications

OXIDE SCALE GROWTH ON MCrAlY COATINGS AFTER PULSED ELECTRON BEAM TREATMENT

G. Müller, G. Schumacher, D. Strauß, F. Zimmermann
Forschungszentrum Karlsruhe GmbH, Institut für Neutronenphysik und Reaktortechnik (INR)

Abstract

A new electron beam treatment method was applied to the surface of LPPS-MCrAlY coatings to improve the oxide scale behavior. The electron beam generated by the facility GESA has a diameter of about 10 cm and sufficient power density to melt a surface layer of about 20 μm of this area by just one electron beam pulse. Cooling rates are around 10^6 K/s and result in a nanometer grained single phase structure of the surface layer, that solidifies directionally. The high roughness of the as sprayed surface is reduced by the GESA process from $R_A = 5$ μm to 1.5 μm.

The oxidation behavior of treated coatings at 950 °C in air was examined. During oxidation a single phase α-alumina scale developed on the treated surface with a considerably lower growth rate as compared to the untreated coatings. Therefore, it is expected that electron beam treatment improves the oxidation resistance of MCrAlY coatings and their suitability as a bond coat for EBPVD thermal barrier coatings.

1. Introduction

In advanced stationary and aero gas turbines, inlet temperature have been dramatically increased in the past decade. Therefore the main corrosion mechanism limiting the blade life time is due to oxidation.

Structure and adherence of the thermally grown oxide (TGO) scale on MCrAlY coatings are the key issues for their oxidation resistance and bonding properties for electron beam deposited thermal barrier coatings (EBPVD-TBC). The TGO should consist of dense α-alumina to act as an effective barrier against migrating oxygen and to avoid stresses that could be initiated by development of transient alumina phases or chromium oxide and spinels [1,2] with different physical properties.

Low diffusivity of oxygen will lead to slow oxide scale growth. This is desirable because the scale failure due to cracking and spallation depends strongly on oxide thickness [3, 4]. Experiments with FeCrAl-based ODS alloys indicated that an increased scale growth rate leads to an earlier onset of the enhanced oxidation and scale cracking [5].

The surface treatment was conducted with the new pulsed electron beam facility GESA developed for the surface treatment of materials and the optimization of large area electron beam properties e.g. the homogeneity. A schematic of the pulsed electron beam facility GESA at FZK is shown in Fig. 1.

It consists of a high voltage generator with a pulse duration control unit, a multipoint explosive emission cathode, a controlling grid and an anode, forming a triode system.

The high voltage generator has a Marx-like configuration. The multipoint explosive emission cathode is built up from 700 graphite fiber bundles, each one connected through a resistor to the high voltage generator. Presently the emissive area amounts to 700 cm^2. A magnetic focusing system, consisting of 6 coils, guides the electron beam through a 50 cm long transport channel to the target and allows variation of the beam diameter in the range of 6 - 10 cm. A pulse duration control unit (PDCU) allows adjustment of the pulse duration between 5 and 40 μs.
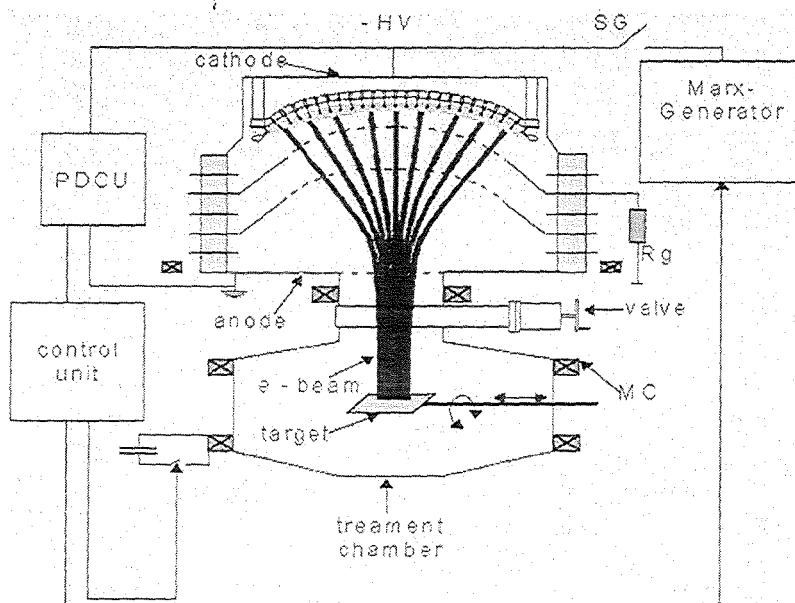
Fig. 1: Schematic of the pulsed electron beam facility GESA

The electron kinetic energy can be varied in the range of 50 - 150 keV with a power density of up to 2 MW/cm^2 and an energy density up to 50 J/cm^2 at the target. This is sufficient to melt any metallic material adiabatically up to a depth of 10 - 50 μm. For treatment of larger areas, experiments showed that overlapping of irradiated regions does not disturb the homogeneous melt layer structure.

The special feature of the GESA process [6,7] used for surface treatment, compared to other methods, is the large surface area that is covered by the electron beam. It allows the melting of an area up to 6 - 10 cm diameter by just one single pulse of 10 - 50 μs duration. As compared to the glazing methods using scanning electron or laser beams this procedure generates a homogeneous surface structure and allows very high cooling rates on the order of 10^6 K/s. Quick melting and rapid solidification due to heat conduction into the bulk produces nanocrystalline structures within the treated surface area. The nanocrystalline structure should lead to modified oxide nucleation and growth especially at the beginning of the oxidation process before substantial grain growth in the restructured alloy occurs.

2. Experimental

The specimens, consisting of Inconel 738 rods and plates, were coated by low pressure plasma sprayed (LPPS) commercial MCrAlY AMDRY 995, with Co-32Ni-21Cr-8Al-0,5Y in wt.% by Plasmatechnik AG, Switzerland. The coating thickness was 200 μm, which is one order of magnitude larger than the electron penetration depth applied in the experiments. Therefore, only the MCrAlY-coating is affected in the pulsed heat treatment.

Oxidation of coated specimens was conducted in a tube furnace at a constant temperature of 950 °C in air. Samples of electron beam treated and just polished specimens were analyzed after 100, 200, 400, 600, 800 and 1400 hours heat treatment. The samples were examined using optical (OM) and scanning electron (SEM) microscopy of the surfaces as well as the cross-sections accompanied by X-ray diffractometry for phase determination of the oxides and the underlying alloy.

3. Results and discussion

After the large area pulsed electron beam treatment, the irradiated surface of the MCrAlY coating has a rapidly solidified surface layer of about 20 μm depth. Fig. 2 is the micrograph of the cross section of an irradiated specimen which shows the surface layer, in which no grains are visible (top) and the unaffected MCrAlY structure with an average grain size of about 2 - 10 μm (below). The modified layer was resistant to etching, while the multi-phase structure shows strong interaction of the etching agent with the β- and γ-phases. Furthermore, the surface roughness caused by the LPPS process is reduced significantly from $R_A = 5$ μm to $R_A = 1.5$ μm.
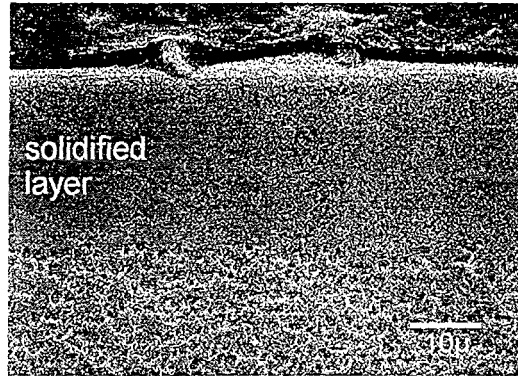

Fig. 2:   Metallographic cross-section of MCrAlY treated
by a single 40 μs electron pulse

To compare the oxide scale growth kinetics on polished coatings with and without pulsed electron beam treatment, a stationary oxidation at 950 °C in air was carried out. The XRD analysis (Fig. 3b) of the treated samples shows a directionally solidified $\gamma_{(200)}$- phase that remains stable during the oxide scale growth. The polished, not treated sample (Fig. 3a) exhibits the expected ratio between the γ and the β-peaks of the original two phase alloy structure. Already after 200 h the x-rays do not penetrate the β-depletion zone and no diffraction peaks of the β-phase are detected. A quick growing alumina-layer forms from which only α-Al_2O_3 x-ray patterns reach a noticeable intensity. The development of the α-Al_2O_3 peaks hints at a much slower growth rate of the oxide scale of the treated specimen (Fig. 3b) in comparison to the oxide on the specimen that was not treated (Fig. 3a).
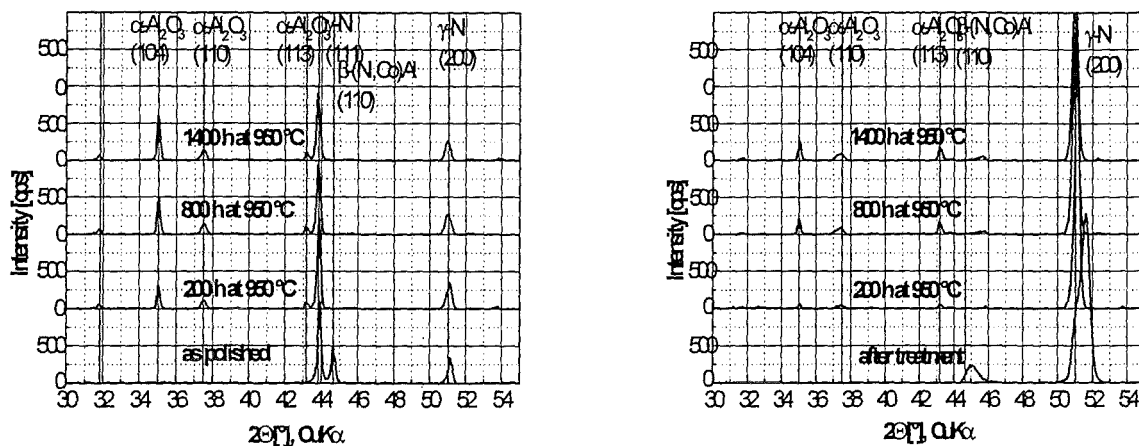

Fig. 3:   XRD after isothermal oxidation at 950 °C in air, comparison of polished (a) and treated (b) samples

Integration of all the α-Al_2O_3-peak counts shows the remarkable difference between treated and untreated specimens in (Fig. 4).
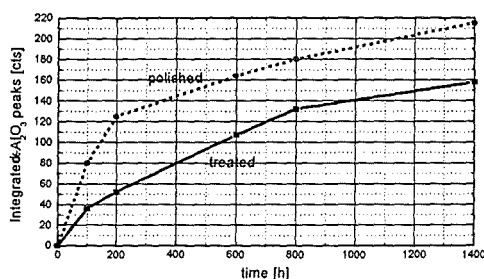
Fig. 4:   XRD counts as a measure of the α-alumina scale growth on a polished and an electron beam treated sample as a function of exposure to air at 950°C

The samples treated by the pulsed electron beam obviously form an oxide layer with better oxygen barrier properties and thus slower oxide scale growth. This is illustrated in Fig. 5 that shows a much smaller oxide scale thickness and β-depleted zone width in case of the electron beam treated than the one in the untreated specimen coating after 200 h at 950 °C in air.

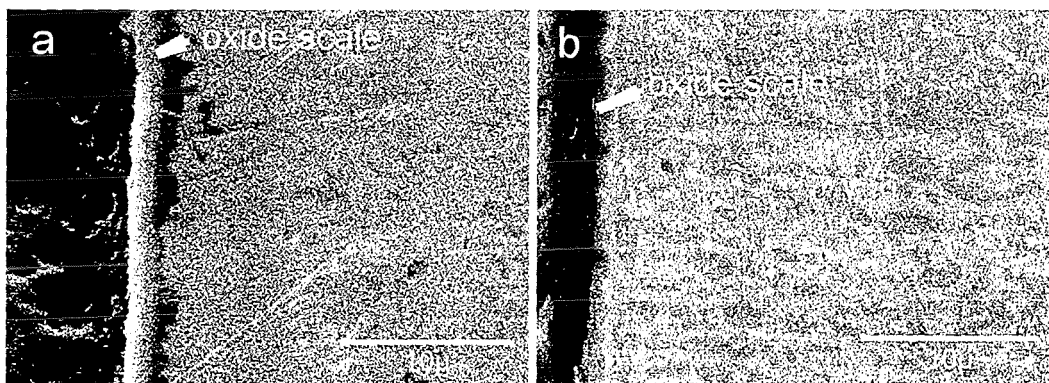Fig. 5:   Comparison of oxide thickness and β-depletion after 200h oxidation at 950 °C in air of a polished (a) and an electron beam treated sample (b)

The oxide surface of the coating, which was polished, shows after 200 h oxidation at 950 °C in air a very different morphology compared to the electron beam treated coating. Blade structures typical for Θ-Al_2O_3 appear on the polished surface although the XRD indicates only an α-alumina crystal structure (Fig. 6a – c). The oxide scale of the treated surface, (Fig. 6d – f) appears to be composed of typical α-alumina crystals. It seems to be obvious that the oxide scale on that surface forms a much better oxidation barrier. Moreover, the blade like structure on the untreated surface tends to spallation, the onset of which can be seen in Fig. 6a. After 1400 h extended spallation areas were observed that did not appear on the treated surface.
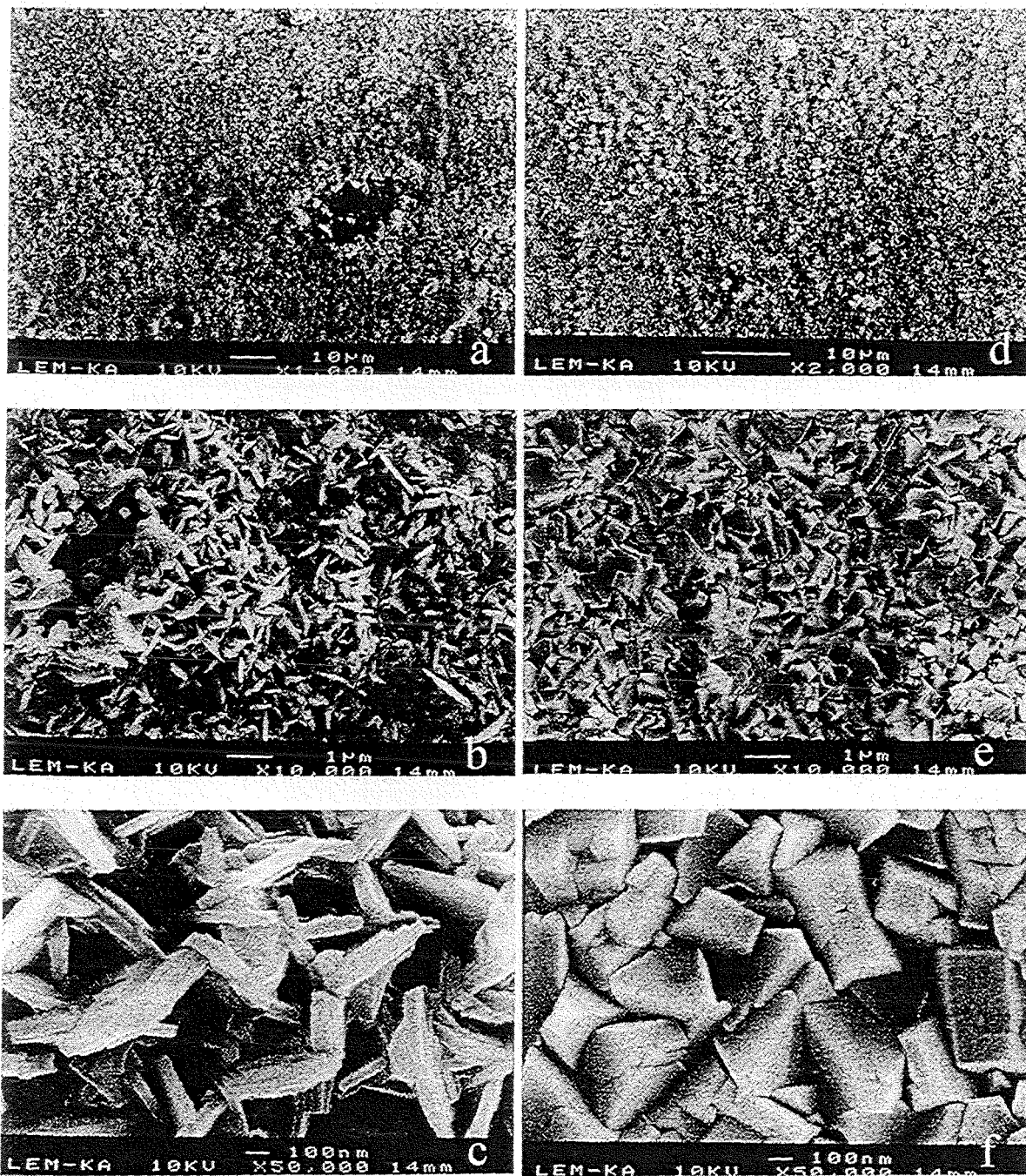
Fig. 6: Surface morphology after 200h oxidation at 950 °C in air of polished (a - c) and electron beam treated (d - f) samples

The blades are supposed to grow by grain boundary diffusion to the surface in the polished non treated coating, in which the grains are in the 2 - 10 μm size range, and by outward diffusion of aluminum [1,8].

Similar structures were observed in experiments with FeCrAl based ODS-[3] and with Ni-Cr-Al-Ti-Si-alloys [9] at 900 °C that did not appear at 1100 °C. The scale morphology at 900 °C was explained by possible Θ-Al_2O_3 formation that can occur at the lower temperatures. Since we could avoid the blade like structure by restructuring of the surface layer to very fine grains, one could assume that grain boundary diffusion within the coating alloy, that is dominant at lower temperatures contributes to the blade formation.

121

Grains are not visible in the solidified melt region after electron beam treatment (Fig. 2). Nevertheless, a small broad β-peak appears in Fig. 3b that may indicate the onset of β-precipitation with very small grains. These conditions do not favor blade like structures. It can be expected that the oxide scale that grows on an electron beam treated, instead of a polished, surface makes up a better basis for EBPVD-TBC's for three reasons: lower oxide growth rate, better surface morphology and less tendency for scale spallation.

4. Conclusions

The GESA installation is a powerful tool for surface annealing and melting. It allows treatment of surfaces with a pulsed electron beam of up to 10 cm diameter. Restructuring of the surface layer of an MCrAlY coating by the pulsed electron beam resulted in positive effects on the oxide scale growth during exposure to air at 950 °C. These effects include a smaller scale growth rate and formation of regular α-alumina grains as opposed to the higher growth rate, and blade like grains on the surface not treated by the electron beam.

It is expected that the electron beam treatment provides much better conditions for formation of oxide scales as an oxygen diffusion barrier and as a basis for deposition of EBPVD-TBC's. Experiments with TBC's on electron beam treated coatings are presently being carried out.

5. Acknowledgement

6. References

1. P.T. Moseley, K.R. Heyde, B.A. Bellamy and G. Tappin, Corr. Sci., 24, 1984, 547
2. N. Czech, V. Kolarik, W.J. Quadakkers, W. Stamm, Surf. Eng., 13(3), 1977, 384
3. F. Starr, Mat. at High Temp., 13(4) ,1995, 185
4. H.E. Evans, M.P. Taylor, Surf. Coat. Technol., 94-95, 1997, 27
5. W. J. Quadakkers, K. Schmitz, H. Grübner and E.Wallura, Mat. at High Temp., 10 (1), 1992, 23
6. G. Müller, G. Schumacher, D. Strauß, V. Engelko, A. Andreev, O. Kamarov, K. Shigalichin, Proc.11th Int. Conf. High Power Part. Beams, Prague, 1996, 267
7. G. Müller, G. Schumacher, D. Strauß, V. Engelko, A. Andreev, and V. Kavaljov, Proc.11th Int. Conf. High Power Part. Beams, Prague, 1996, 809
8. G.C. Rybicki, J.L. Smialek, Oxid. of Met., 31(3/4), 1989, 275
9. C. Leyens, K. Fritscher, M. Peters, W.A. Kaysser, Surf. Coat. Technol., 94-95, 1997, 155

APPLICATION OF GESA FOR IMPROVEMENT OF CORROSION RESISTANCE OF STEEL IN LIQUID LEAD

R. Huber, G. Müller, G. Schumacher
Institut für Neutronenphysik und Reaktortechnik, FZK

Abstract

One of the problems with the recently discussed accelerator driven subcritical actinide burners or nuclear reactors cooled by Pb or Pb/Bi is the corrosion of the structural metals by the liquid metal coolant. Research was started to find out if the surface of the materials that were treated by high energy pulsed electron beams (GESA) would be more resistant against liquid lead than the untreated surface. For this purpose a corrosion test stand was constructed that exposes treated and untreated specimens to liquid lead under oxygen control at 550°C. Examination after 200 hours exposure did not yet show differences in corrosion of 316 stainless steel but the oxide scale at surface parts under the controlled atmosphere was more advanced on treated specimens. Investigations of other steels and longer exposure time is under way

1. Introduction

Recently promising proposals were discussed on accelerator driven subcritical systems for energy production and as actinide burners. Those concepts include safety liquid metal cooling systems on the basis of Pb-Bi or Pb. However, corrosion problems with steel arise in using such coolants. With these problems the question came up, if treatment of the steel surface by GESA could enhance the corrosion resistance against liquid Pb-Bi and Pb. After such treatment improved corrosion resistance was observed with metallic materials also including stainless steel e.g. in contact with sulfuric acid.

Steel and liquid lead are not compatible. For Ni-Pb an eutectic is reported by Hansen /1/ at 324 °C that contains 0.46 at% Ni. At 550 °C about twice as much Ni is dissolved in Pb than at 324 °C. The solubility of iron in liquid Pb was given to be as low as $2\text{-}3 \times 10^{-4}$ wt% /1/, at about 1000 °C and that one of Cr to be 0.03 wt%. Since all the solubilities vary with temperatures, transport processes will take place which live from the high solubility at high temperatures and precipitation at low temperatures. A temperature difference of 150 °C is about typical for lead cooling loops and with high flow velocities, in the range of m/s, and long in pile times already small solubilities can lead to heavy corrosion effects.

One way to slow down corrosion of metals in liquid Pb would be to use metals with no or very low solubility in lead. Those metals could be Mo and W which are reported with solubilities of < 0.005 wt% at 1200 °C. Another way is to protect the metal surface by an oxide layer that has the ability to slow down the dissolution of the protected metal components to tolerable low values. The latter was worked out by Russian Scientists in Obninsk and St. Petersburg /2, 3/.

Oxygen is added to the liquid Pb in a concentration at which an protective oxide layer is formed on the surface of the metal, but no PbO is precipitated in the liquid lead. The most important result of the relevant studies and experiments is given in Fig. 1. It shows a steep increase of the corrosion effects at oxygen concentrations below 10^{-8} wt% because of strongly decreasing protection properties of the surface layer on the metal. The transition zone is characterized by an intact protecting oxide scale that allows only very low corrosion attack. At higher oxygen concentration (> 10^{-5} wt%) the corrosion effects increase slowly only by the reaction of PbO with the oxide scale but a more important disadvantage in this region is the

precipitation of solid PbO at the lower temperatures in the coolant loop. It is also shown in Fig. 1 that the transition zone shifts slightly as a function of the material used.
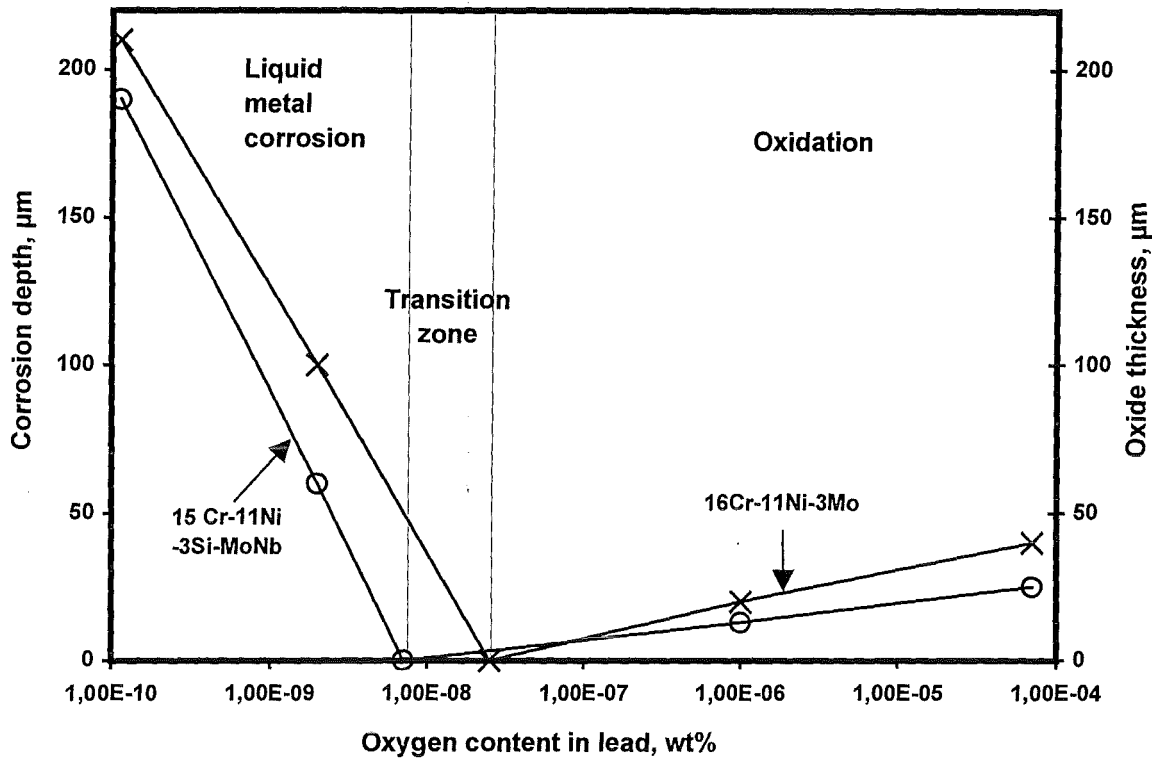

Fig. 1:   Corrosion behavior of steels in flowing lead after 3000 h at 550 °C

Now it is necessary to measure and control the oxygen concentration to keep the safe conditions of the liquid lead. After a certain time periode oxygen will be depleted by oxide formation on the metal surface and thus the conditions will shift to the region with low oxygen concentration and hence strong corrosion effects, if there would be no oxygen control.

2. Determination of the conditions for test loops

In large loops the concentration of oxygen is controlled by solid electrolyte cells that measure and feed oxygen into the liquid lead or lead bismuth. Such cells are sophisticated and require a special know how to build them. Small loops or little lead baths like we will use here can be controlled by an atmosphere with a definite oxygen partial pressure that determines the chemical potential μ_{O_2} of oxygen within the liquid metal bath. To prevent PbO precipitation and to support Fe_2O_3 formation the following conditions must be established:

$$2\Delta G^0_{PbO} > \mu_{O_2} = RT \ln P_{O_2} > 1.5\Delta G^0_{Fe_2O_3}$$

The standard values ΔG^0 of the free reaction enthalpy are known for the oxides in question and with these values the equilibrium partial pressure region of oxygen that retains the stable conditions for the transition zone in Fig. 1 can be determined. The easiest way to do this is to draw an Ellingham-diagram that contains the relevant oxides PbO, NiO, Fe_2O_3 and Cr_2O_3 and the oxygen partial pressures by the above equation and also the H_2/H_2O ratios as a function of chemical potential and temperature. The latter will be used to control the oxygen potential as follows.

$$P_{O_2} = \frac{P_{H_2O}^2}{P_{O_2}^2} \exp \frac{2\Delta G_{H_2O}^0}{RT}$$

The Ellingham-diagram in Fig. 2 demonstrates in which region the stable conditions exist and how they can be established. The ordinate shows the chemical potential of oxygen, the abscissa the temperature. Dashed lines in the diagram represent the isobars of the oxygen partial pressure and the lines of constant H_2/H_2O ratios in the gas atmosphere above the oxidizing species or the liquid lead that dissolved oxygen, respectively. The important region in the diagram is the one between the lines of the oxygen potential for PbO and Fe_2O_3 in the temperature regime of 400 - 550 °C.

For safe working conditions we have to select a field of oxygen partial pressures that would not cross the PbO- and Fe_2O_3-lines within the temperature regime of 400-550°C. Lines of constant H_2/H_2O ratios within the boarders of this field show the ratios that must be established to maintain the appropriate oxygen partial pressures.
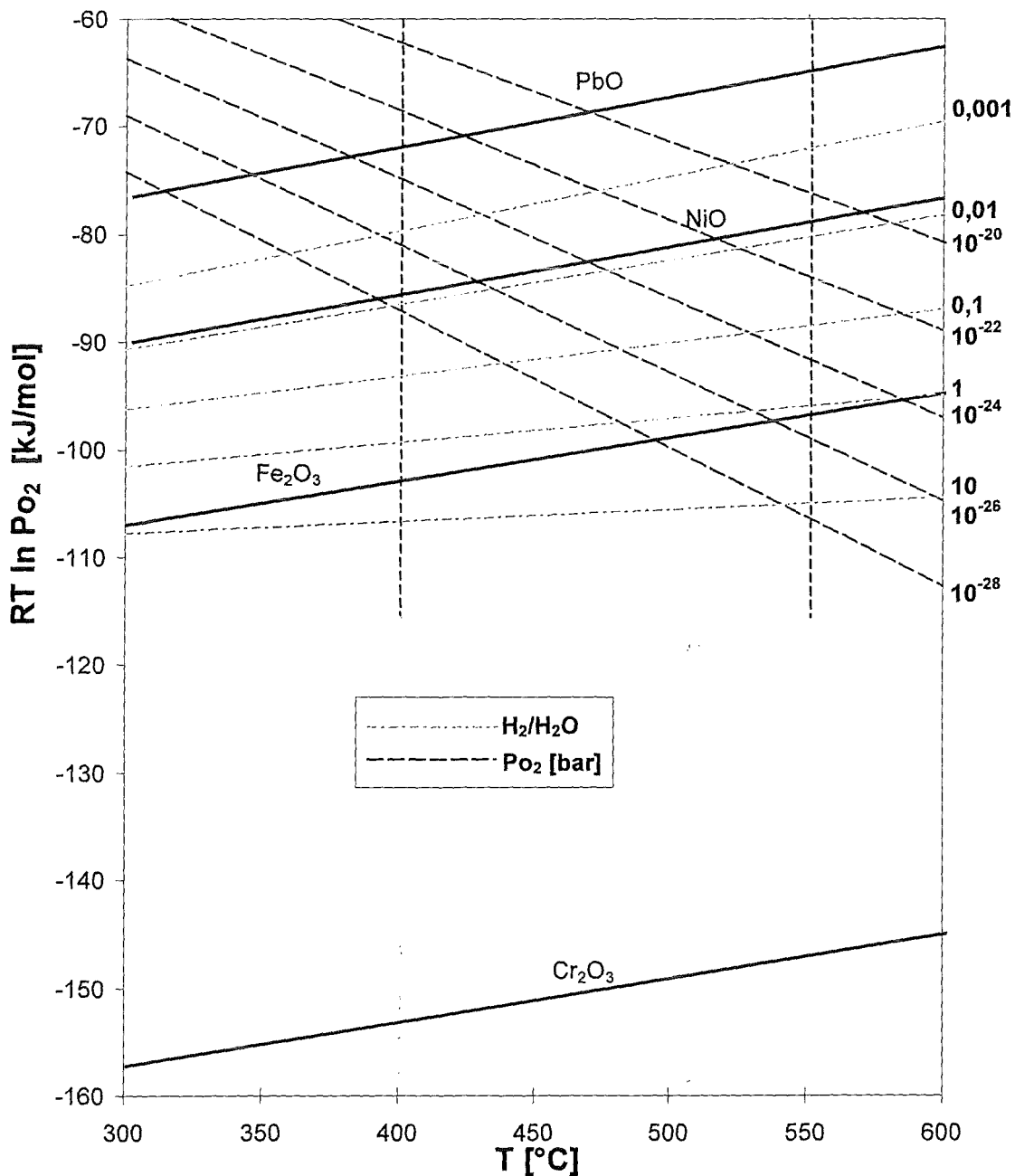

Fig. 2:   Ellingham-diagram of Pb-, Ni-, Fe- and Cr-oxides

If we chose a H_2/H_2O ratio of 0.4 we will attain $Po_2 = 10^{-24}$ at 550 °C and $Po_2 = 10^{-31}$ at 400 °C. At both temperatures we still form iron oxide and thus we are far away from formation of PbO, in the case of stagnant Pb. If we consider a liquid metal loop, there will be no equilibration across the temperature region via the H_2/H_2O ratio but through the oxygen dissolved in Pb (Pb/Bi). In this case we have to follow the P_{O_2} isobar. That means if we have H_2/H_2O = 0.4 at 550°C, we will have there $P_{O_2} = 10^{-24}$. At 400°C this isobar comes close to the PbO-line and thus ΔT must be not larger than 150°C, otherwise PbO will be formed.

The diagram in Fig. 2 also shows the advantage of controlling the oxygen partial pressure by the H_2/H_2O ratio. It would not be possible with an oxygen partial pressure of $10^{-24} - 10^{-31}$ to replace oxygen that was used for oxidation of the metal surface. However with a H_2/H_2O ratio of $0.3 - 3 \times 10^{-3}$ it is easy to replace the oxygen. With a gas flow of 200 cm³/min it is possible to provide easily up to 50 cm³ O_2/min which corresponds to about 400 cm² Cr_2O_3-oxide layer of 1µ thickness. With this gasflow solution of 10^{-8} wt% oxygen in 1000 cm³ Pb will take less than 1 second and may thus the controlling step may only be the uptake of oxygen from the gas phase. Thus, not only small and medium loops could be managed by controlling them via the H_2/H_2O ratio in the gas phase if one can deliver the available. oxygen to the lead, e.g. by bubbling.

3. Liquid lead corrosion test stand and experiments

Materials of interest for comparison of the compatibility to lead conditioned in the above described manner are:

Optifer, Manet, 1.4790, SS 316

Of further interest is the question, if treatment of the material surface by the GESA process could improve the corrosion resistance or could lower the required precision of the oxygen control or even avoid it. For this purpose specimens of 15 x 15 x 2 mm were prepared from the materials of interest treated by GESA on one side and just polished on the other side for easy comparison of the corrosion behavior.

A corrosion test stand was build up with control of the oxygen potential via the H_2/H_2O ratio in the gas phase as described above. Fig. 3 shows this equipment. The reactor is a quartz tube inside an oven that is controlled at 550 °C. A mixture of Ar and Ar5%H_2 allows to adjust the hydrogen concentration in the gas. The water vapor is added by passing the gas through water of a definite temperature. The maximum hydrogen concentration that can be introduced is 5 %, which is high enough and well below the lower explosion limit. In the actual experiments the ratio of Ar and Ar5%H_2 is 200 cm³min⁻¹ / 33 cm³min⁻¹ which gives a H_2/H_2O ratio of 0.4 at a water temperature of 18 °C. The lead in the oven is not moved but stagnant and contained in 5 crucibles together with 5 metal specimens. Each crucible contains 40 g of high purity lead.

The ratio of gas flows are measured and controlled and the partial pressure of water vapor is measured before the gas enters the oven and after it left it. There the gas passes also through an oxygen partial pressure measuring system.

The test so far run 165 h. The samples immerged about 1 cm deep into the liquid lead. Up to now a 316 steel specimen was examined by cutting it perpendicular to the surface and looking at the cross section by SEM (Scanning Electron Microscopy). After this short time there was no attack of Pb visible, which was expected. But the surface that was not covered by lead showed marked differences in the oxide scale between the untreated and the GESA treated surface. The oxide scale on the treated surface was of a continuous thickness of 1 µm, whilst the one on the nontreated surface was so small that it was not visible, probably in a dimension below 100 nm.
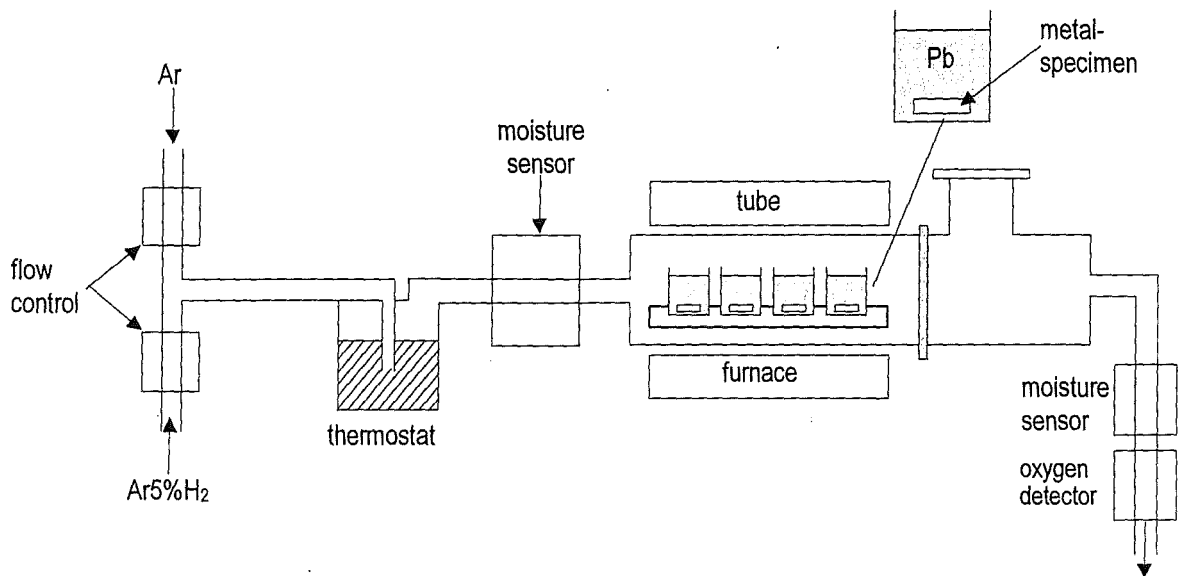
Fig. 3:   Corrosion test stand with stagnant liquid lead

That means, treatment by GESA favors solid oxide scale formation on stainless steel 316 as already observed with superalloys.

4. Conclusion for further work

It was shown that the oxygen potential in small and medium loops and test stands with stagnant liquid lead or lead-bismuth can be controlled by the H_2/H_2O ratio in the gas phase above the liquid metal. The exposure of a SS 316 steel specimen to liquid lead at 550 °C in a small test stand with stagnant Pb was to short to detect corrosion-effects. Therefore, we are not yet able to confirm a positive effect of GESA treatment on corrosion resistance of SS 316. However, the formation of a continuous solid oxide scale of 1 μm thickness on the treated surface indicates that GESA treatment will improve the oxide diffusion barrier and therefore also the corrosion resistance. The non-treated surface had only a very small, in the cross section not visible, oxide scale (< 100 nm). These experiments will be continued until corrosion effects appear that allow to draw conclusions about the influence of GESA treatment on the corrosion resistance.

The GESA process offers possibilities that exceed the surface restructuring by melting and rapid solidification. Metals or alloys precipitated before treatment develop during surface melting an alloy layer and thus change the surface properties entirely without changing the material properties. Therewith stable oxide formers may be introduced into the surface layer to stabilize the oxide scale or stable metals may be alloyed that are practically insoluble in liquid lead like Mo or W. Such surface alloying would decrease the influence of oxygen control or even reduce it to just inert gas conditions. Upcoming experiments and studies in this direction should show the potential of this promising techniques.

5. References

[1]   M. Hansen, Constellation of Binary Alloys, Metallurgy and Metallurgical Engineering Series, 2nd Edition, McGraw-Hill Book Company, 1958, p. 1065

[2]   V. Markov, et. al., Seminar on the Concept of Lead-Cooled Fast Reactor, Cadarache September 22-23, 1997 (unpublished)

[3]   Y. Orlov, et. al., Seminar on the Concept of Lead-Cooled Fast Reactor, Cadarache September 22-23, 1997 (unpublished)

Concrete recycling and scraping by electrodynamic fragmentation

C. Schultheiss, R. Straessner, H. Bluhm, P. Stemmermann

Forschungszentrum Karlsruhe GmbH, Hermann-von-Helmholtz-Platz 1,
76344 Eggenstein-Leopoldshafen

Abstract

Fragmentation of concrete rubble from demolished buildings can be achieved by high voltage discharges through the material. To induce the discharge channel in the solid it must be embedded in water. During this treatment concrete breaks selectively into its aggregates, i.e. into gravel, sand, and a cement suspension. Gravel and sand can immediately be reused to produce recycled concrete of mechanical strength equivalent to concrete prepared from primary raw materials. It has been proven, that the hydrated cement fraction can be recycled too for the production of new cement. This process helps to save energy as well as to reduce the CO_2 emission. The investigations described in this paper have demonstrated that recycling of concrete is technically and economically feasible.

Electrical discharges were also used to remove concrete from building structures. Possible applications are to remove concrete from pillar heads or contaminated walls. Several schemes have been investigated to scrape off concrete from surfaces. Good results were obtained with a multi electrode configuration and a *mechanically switched commutator*. A scrape off rate, of up to 13 cm^3/pulse has been achieved. Thus with a HV- pulse repetition frequency of 5 Hz a scrape off rate of 0.234 m^3/h could be realised. Compared to conventional mechanical methods the speed of removal was doubled.

1.   Introduction

Until today recycling of concrete means crushing the material in multistage jaw breakers and/or impact mills. However conventional breakers change the structure of the basic aggregates and produce a large fraction of useless dust and small particles. Therefore, until now broken concrete can only be used for road construction and as loose material for raising dams. Only in special cases it is allowed to use broken concrete for the construction of buildings. Actually in Germany half of the concrete rubble becomes finally dumped on a deposition site because of the disadvantageous size-distribution of the broken material. Another obstacle to recycling on a high quality level is the mixing of various kinds of concrete with different water-cement ratios.

Nevertheless, reusing concrete debris on a high quality level becomes more and more desirable, since the opening of new natural sources for gravel and sand becomes increasingly difficult.

Recycling of concrete rubble by means of under-water electrodynamic fragmentation is under investigation at the FRANKA-0 facility since two years. FRANKA-0 is a high voltage pulse generator producing pulses with a rise time of less than 200 ns and a pulse amplitude of 250 kV at a repetition rate of 5 Hz. Details can be found in a previous annual report /1/. The main goal of this investigation is to determine the optimum process parameters for separating concrete into its constituents i.e.: into gravel, sand and hydrated cement. A criterion for good separation is the production of gravel free from cement adhesions. A second goal is to demonstrate that concrete created from recycled aggregates has comparable strength as concrete from the primary raw materials.

During the destruction of chemical factories or nuclear power plants it may occur that concrete walls are contaminated. In many cases the contaminants will be concentrated in a thin surface layer only and especially in the cement matrix. If this surface layer can be scraped off a much smaller volume has to be deposited on special deposition sites and in addition the noncontaminated fraction can be recycled. Therefore we have also investigated a

scraping technique based on sub-surface discharges. This technique can also be used to remove concrete from large area deep holes.

In this paper we describe the progress made in both application areas and discuss some aspects of an industrial scale fragmentation device

2. Electrodynamic fragmentation

Electrodynamic fragmentation takes place, if a pulsed high voltage discharge is initiated in a solid dielectric material. During this high voltage breakdown, a specific energy of 10-100 J/cm is deposited in an initially 10 μm wide channel and heats it in a few μs to temperatures above 10^4 °K, thus creating a pressure of between 10^9 and 10^{10} Pa /2/. Comparable to the evolution in a chemical explosion the outward propagating acoustic wave exceeds the material strength in the vicinity of the discharge channel and fractures the solid compound (Fig. 1).

To induce the discharge inside the body to be fragmented, the high voltage breakdown strength in the surrounding medium must be larger than that of the solid material. This can be achieved if the solid is embedded in a dielectric liquid that has a higher dynamic breakdown strength. Since the breakdown strength of most liquid dielectrics increases faster than that of solid materials, if the high voltage pulse rise time is reduced, an operation regime can be found, where most of the breakdown discharges appear in the solid. For water and concrete this regime is achieved for pulse rise times of less than 500 ns.
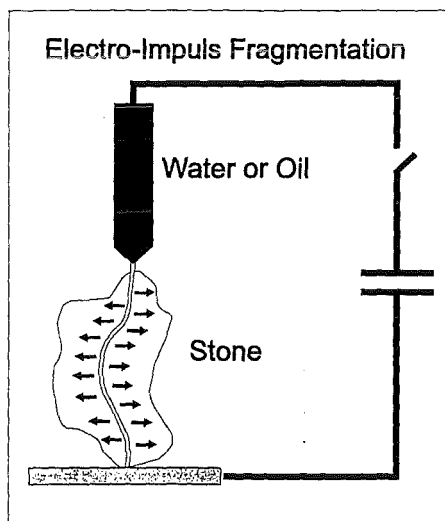

Fig. 1: For fast rising high voltage pulses the electric breakdown strength of some dielectric liquids becomes larger than that of solids. In this case the discharge runs through the solid, if it is embedded in such a liquid. For concrete and water this regime is achieved if the pulse rise time becomes less than 500 ns.

3.   Selectivity of fragmentation

The essential advantage of electrodynamic fragmentation in comparison with mechanical methods is its high degree of selectivity. The destruction of a compound material like concrete occurs mainly at the component boundaries. Thus for the recycling of composites a quality can be achieved that allows recycling at a high quality level.

The degree of selectivity is determined by acoustic inhomogeneities inside the material. The reason for this is the concentration of stress at the boundary between the inclusion and the compound matrix through the superposition of incoming and reflected pressure waves. Main cracks originating in a zone surrounding the discharge channel are fed by deformation energy, which has been stored previously in the material during the propagation of compression

waves. The main cracks move in a direction, where a maximum inflow of energy is to be expected. Secondary waves emitted from inhomogeneities and inclusions due to relaxation processes could transport this information to the moving crack.

4. Fragmentation of concrete

Concrete is a composite material of gravel, sand (together about 85 %) and cement-stone (about 15 %) and therefore a suitable object for selective destruction and complete separation. Sand and gravel (fraction > 0.5 mm) can be reused directly in the same way as the natural aggregates. The fraction with grain sizes < 0.5 mm mainly consists of cement including 10 % silt (mainly quartz, resulting from the fines in the concrete aggregates). It can be reused as a raw material for the production of Portland cement.
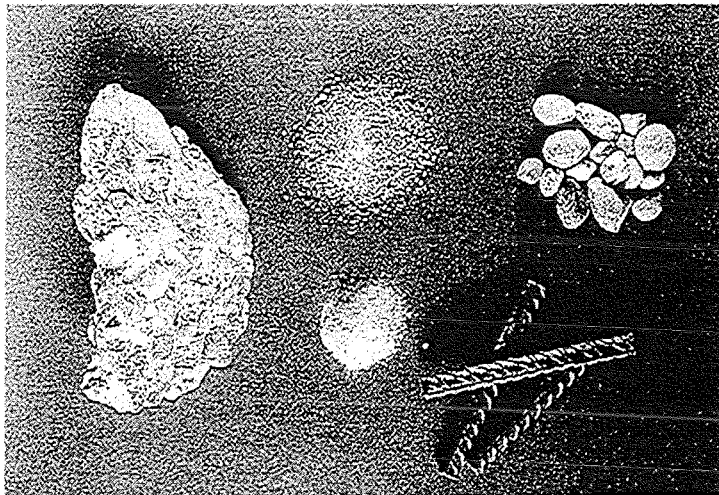

Fig. 2: The figure presents an example for the selective destruction of a piece of concrete into its aggregates gravel, sand, and hydrated cement including silt. Steel armament is recovered without significant adhesions.

The wear of the process vessel and of the electrodes (both built from normal steel) is of the order of 10 μg per shot, which is acceptably low for an industrial device. The steel armament of concrete can easily be recovered without significant adhesions at its surface. Since the fragmentation is done underwater, no dust will be released.

In table 1 the electric data and the corresponding productivity of fragmentation are listed. The values relate to an experiment, where 2 kg of concrete were destroyed within 45 s of operation at a repetition rate of 4-5 Hz.

Table 1: Productivity of fragmentation at FRANKA-0 for concrete recycling

Productivity [kg/h]	160
Average electric power [kW]	3
Specific energy consumption [kWh/t]	19

Fig. 3. shows the achieved grading curves after different times of treatment together with the initial grading curve of the natural aggregates for the specific concrete (according to DIN). It is striking, that no coarse fragments appear in the grading curve of the separated concrete aggregates. Nearly all particles are mono-mineral. Under a light microscope the gravel fraction (> 2mm) is apparently free from contaminants and baked particles. Spherical particles

are dominant in the sand fraction (< 2 mm, > 0.5 mm) and seldom with cement adhesions. The total fraction of cement in the aggregate part (gravel, sand) is about 1 %.
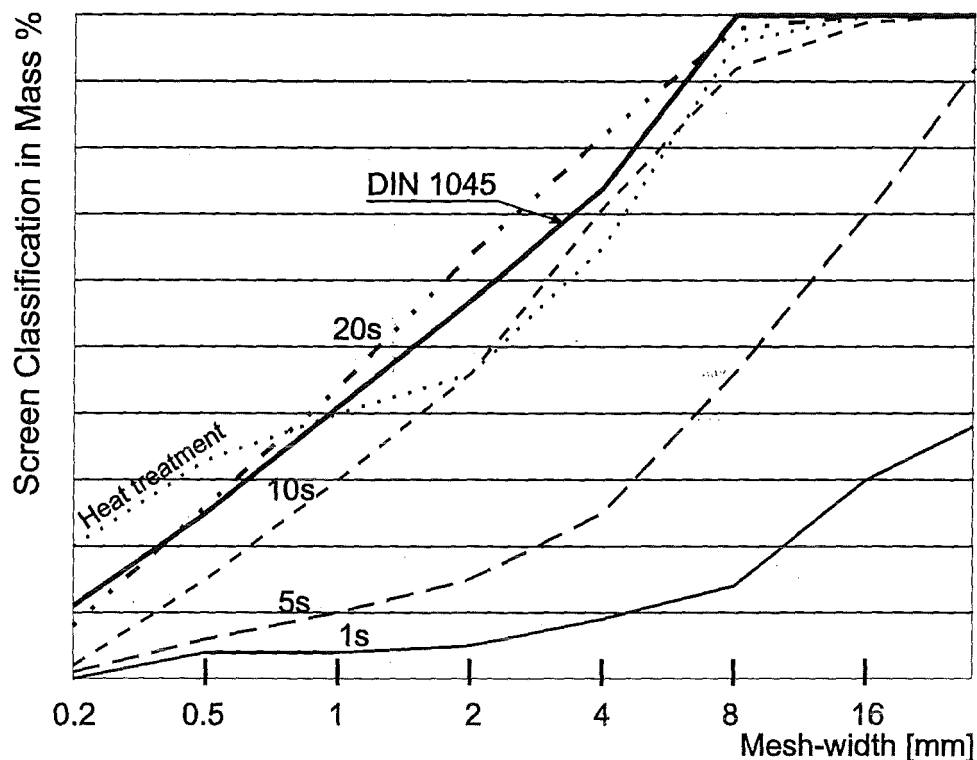

Fig. 3: Grading curves obtained after different times of concrete treatment in the fragmentation device FRANKA-0. In addition grading curves, following the German Industry Standard DIN together with those resulting from a heat treatment are presented.

The recycled aggregates are not mechanically predamaged and fulfil the increased demands of the frost-dew resistance according to DIN 52104. As already mentioned concrete made from recycled aggregates has an unchanged material strength.

The radiography of the silt fraction (< 0,063 mm) is free of quartz. It consists of calcium-silicate-hydrate, ettringit, calcium-aluminium-carbonate-hydrate and calcite.

From a chemical point of view the cement fraction is very similar to cement. On a laboratory scale cement clinker has been produced by baking it at high temperatures. Recycling the cement fraction has the following attractive advantages:

1. It saves raw material (clay, lime).
2. Milling of the raw materials becomes unnecessary.
3. No de-carbonisation of the milled raw material is required. (The baking process consumes 80 % of the energy investment.)
4. Reduction of the CO_2-emission is possible. (7 % of the world wide anthropo-generic CO_2 release is due to cement production (2).)
5. No waste disposal of the cement fraction is required.

Of course energy is necessary to dehydrate the cement fraction. If 50 % of the raw materials used for the cement production are replaced by the recycled cement fraction, a 10 % saving of the energy costs for the burn process can be expected.

5. Scrape-off schemes

The basic concept of electrodynamic drilling and scraping is to force the electrical discharge between two electrodes touching the probe surface to penetrate into the material a certain depth below the surface level in order to blow off pieces from it (Fig. 4). Different electrode configurations have been tried for drilling into concrete and for removing layers from its surface. The main objective required by an industrial project was to remove 0.5-1 m of concrete from the head of pillars.
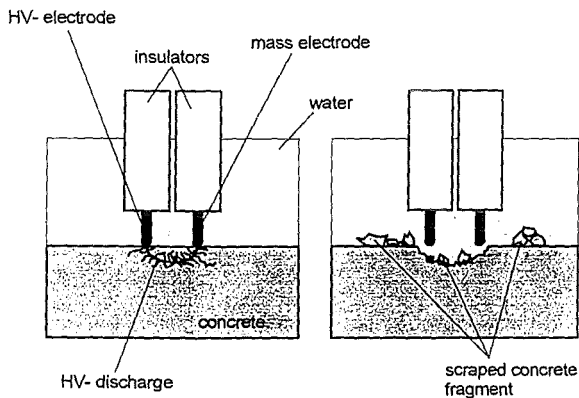
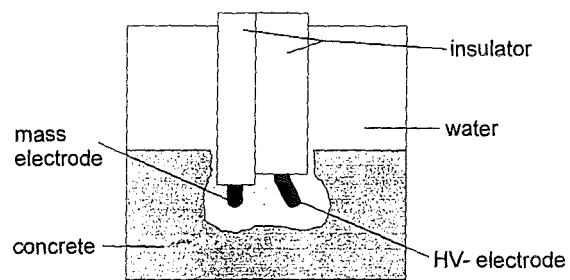Fig. 4: Basic scheme of electrodynamic scrape off

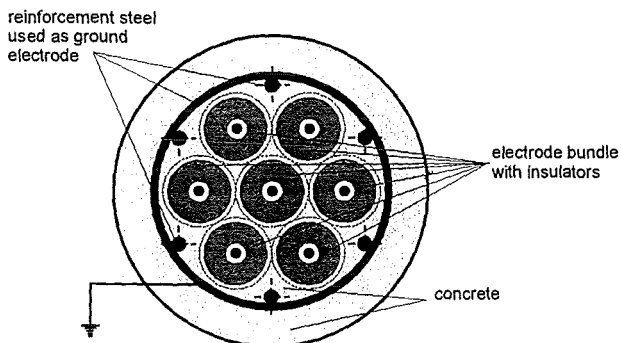Fig. 5: Electrodynamic drilling with a two-electrode system

Fig. 6: Electrodynamic drilling using an electrode bundle.

For that purpose electrode pairs (Fig. 5) as well as electrode bundles (Fig. 6) were tried to drill holes into the concrete. To completely remove the material, adjacent holes must be placed in such a way, that the remaining thin concrete walls between them collapse.

In a second approach we tried to remove thinner layers from the concrete surface by moving a pair of electrodes step by step across the concrete surface (Fig.7, left). Alternatively a configuration of 6 electrodes, which could be rotated in angular steps around the pillar axis has been used (Fig. 7, right). Either a separate ground electrode was added or the steel armament of the pillar was used as the counter electrode.

6. Multi-electrode systems with commutator

In both schemes it becomes necessary to supply more than one electrode with HV- pulses. Therefore the generator pulses have to be distributed with the help of a high voltage

commutator. Two different designs for the commutator, an *E-field- sensitive selfbreaking switch* and a *mechanical switch*, have been investigated. The first design was based on the assumption that the arc itself would always select that electrode with the most favourable
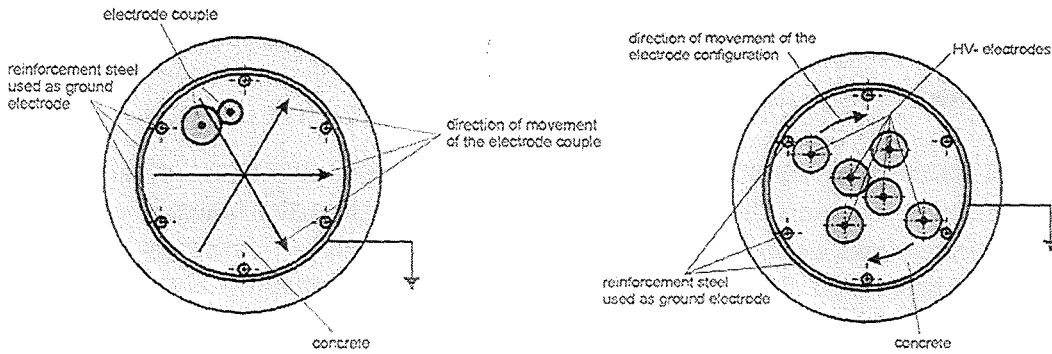

Fig. 7: Linearly moving electrode pair (left) and multi electrode configuration rotating by steps (right).
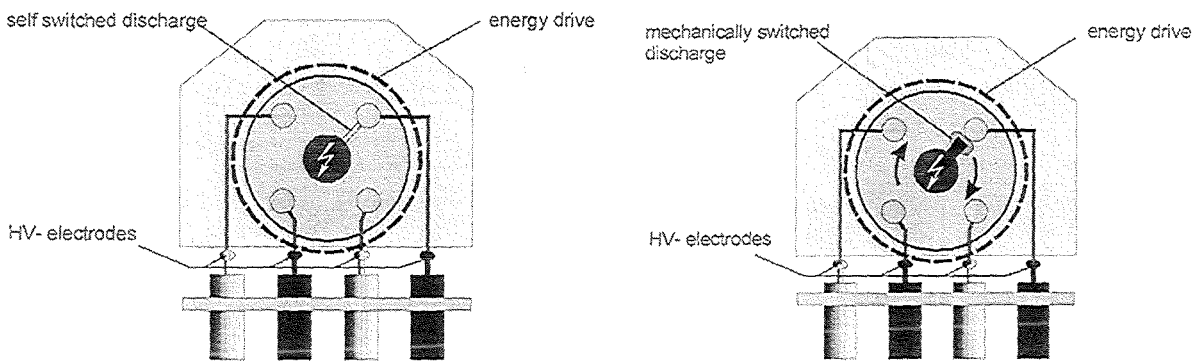

Fig. 8: Selfbreaking E-field- sensitive commutator (left) and mechanically switched commutator (right).

discharge condition (Fig. 8). It was supposed that this would favour the position with the lowest breakdown strength, i.e. a position where the largest part of the spark channel passes through the concrete. Thus it seemed guaranteed that an optimum advance would occur.

In the second design the high voltage pulses were distributed sequentially to all electrodes with the help of a mechanical switch (Fig. 8). Either one or two electrodes were supplied at a time.

7. Results and discussion

In case of the two electrode basic *electrodynamic drilling* scheme (Fig.5), a maximum interelectrode distance of 80 mm could be realised at 250 kV pulse voltage. In test runs where this interelectrode distance was exceeded, surface discharges were observed on the concrete, showing practically no scraping effect. With such a two-electrode system holes of 160 mm depth could be drilled into the concrete. Because soluble Ca,- Na- and K- salts accumulated in the water it was necessary to continuously refresh the water in the reaction zone. The dissolving salts caused a steady increase of the electrical conductivity in the process water. At a conductivity beyond 1500 μS/cm, discharges at 250 kV ceased to penetrate into the concrete. At a pulse amplitude of 350 kV it became possible to operate until 2400 μS/cm were reached in the process water.

The highest productivity in the scrape-off of concrete pillars was obtained with the electrode system rotating by steps, as shown in Fig. 7. To determine the efficiency of such a system, we simulated it by manually placing the electrodes at their foreseen positions. 540 high voltage pulses were applied to the specimen surface, scraping off 13 cm³/pulse on the average (Fig. 9). With a pulse repetition frequency of 5 Hz in a continuous operation mode a scraping rate

of $\Delta V/\Delta t$ = 234 l/h was calculated. The specific energy requirement was 70 J/cm^3 of scraped concrete. Fig. 10 shows a completely excavated head of a pillar.
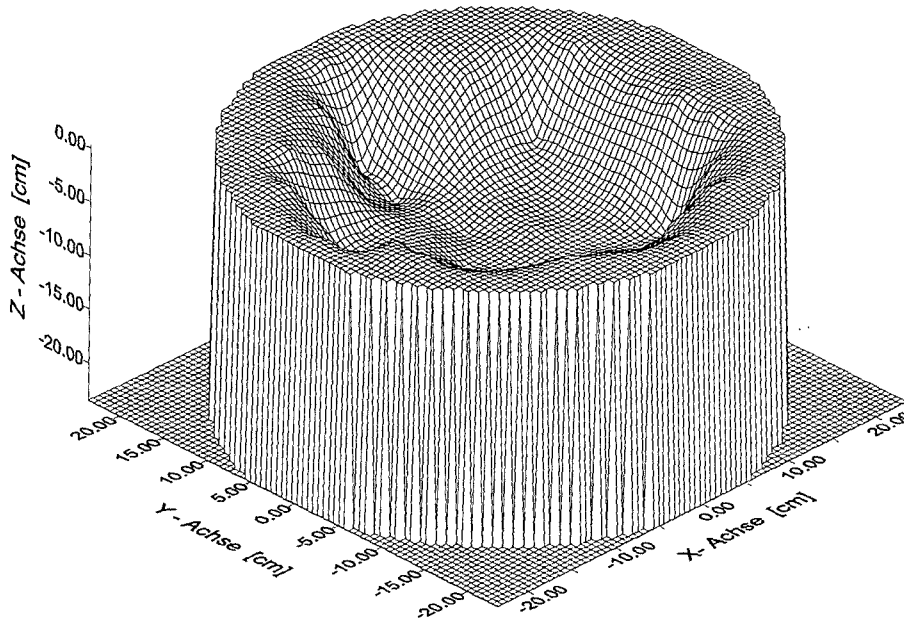

Fig. 9: Concrete pillar treated with a multi-electrode configuration rotating by steps.

The *E-field- sensitive commutator* was not successful. One reason for this may be the resistive losses in the water which simultaneously appear at all HV- electrodes. Also the selective breakdown at only one electrode did not occur. Because of the very heterogeneous electrical field distributions in the operation zone the electrical energy was dissipated in a large number of small partial discharges starting at several HV- electrodes at the same time.
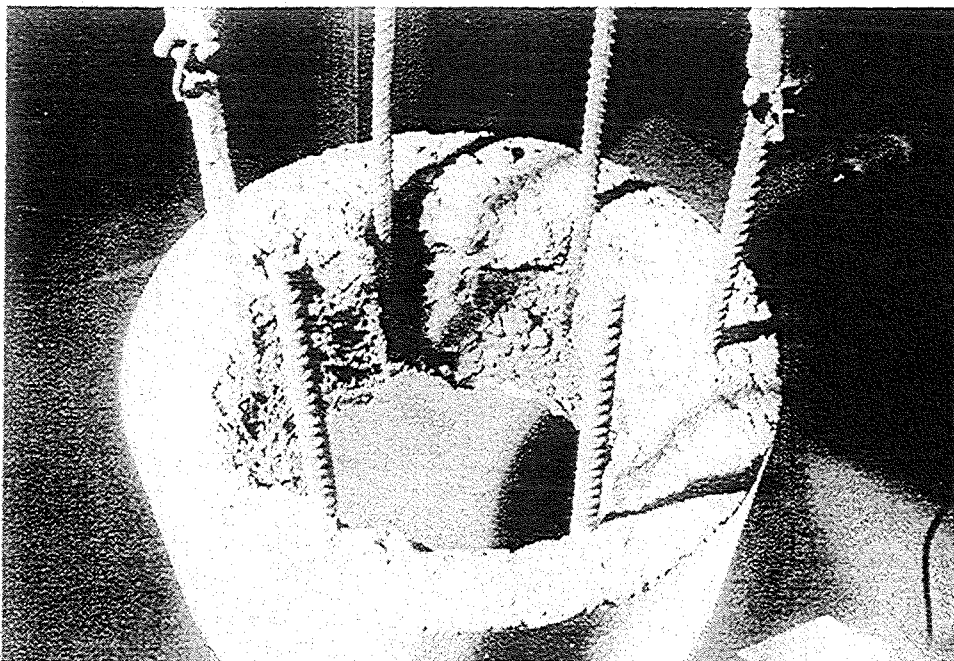

Fig. 10 Electrodynamically excavated pillar head.

The *mechanically switched commutator*, dividing the pulse energy between two electrodes was also not successful. The resistive losses in water were doubled and the split energy led to inefficient discharges.

The best results were achieved with the *mechanically switched commutator*, distributing the HV- pulses externally controlled to single electrodes. Each HV- electrode could be selected individually and supplied with a definite number of pulses. The resistive losses in water are minimised and the whole pulse energy is fed into one discharge channel. If a signal is measured from which the discharge conditions at the operating electrode can be derived, it seems feasible to automatically control the number of pulses at a certain position and to optimise the efficiency. Our measurements suggest that the shape of the discharge voltage pulse could be a good criterion for the breakdown conditions at a specific electrode.

References

/1/   W. Edinger, V. Neubert, C. Schultheiß, R. Sträßner, H. Wieczorek:
       Process and Device for Electrodynamic Fragmentation of Solids - FRANKA, in
       Physics of Intense Light Ion Beams, Production of High Energy Density in Matter, and
       Pulsed Power Applications, Annual Report 1995, H.-J. Bluhm (Editor),FZK 5840,
       (1996)

/2/   B.W. Sjomkin, A. F. Ussow and W. I. Kurez
       Grundlagen der elektrischen Impulszerstörung von Materialien, (in Russian), Kola
       Science Centre, 1995

FRANKA 1, status, results and perspectives

V. Neubert, C. Schultheiss, R. Straessner, Forschungszentrum Karlsruhe GmbH, Postfach 3640, 76021-Karlsruhe, FRG

The subject of this paper is the underwater electrodynamic fragmentation device, FRANKA-1. FRANKA-1 has been designed in tight cooperation with an industrial partner. Several parts, as for example the 350 kV- Marx-pulse generator, have been manufactured and tested. The goal of FRANKA-1 is to realize a prototype device, that can already be installed at an industrial site for routine processing. Since the design should allow changes and upgrading in power, a low degree of specialization has been chosen.

1. Introduction

In comparison with mechanical fragmentation systems like mills, breakers etc. underwater electrodynamic fragmentation, applied in the electro-impulse mode (1), has comparable energy consumption, benefits in material wear and in many cases has process typical advantages (2). A laboratory prototype device called FRANKA-0, which stands for „Fragmentierungs-Anlage-Karlsruhe", is in operation since 1995. On the basis of experiences, gained with FRANKA-0 the concept of FRANKA-1 for industrial applications was developed. FRANKA-1 is an advanced development of FRANKA-0 with an increase of pulse output voltage from 250 kV up to 350 kV and an average power doubled from 5 to 10 kW. In comparison with FRANKA-0 the discharge repetition rate has been increased from 5 to 7 Hz.

Actually the first application of FRANKA-1 will be the preparation of slag from refuse incinerators for use as concrete aggregates. Thereby the fragmentation goal for these cinder is a screen classification in the millimeter range. The benefit of electrodynamic fragmentation is the separation of metallic contents as well as washing effects, which reduce the obligatory four-month relaxing time of ashes and help to reduce costs for storing. To determine the optimum parameters and lowest costs for this process, investigations in this field are still subject of actual experiments on FRANKA-0.

For the case that slag fragmentation turns out to be economically not attractive, alternatively the electrodynamic recycling of electric- and electronic devices will be investigated too.

2. Concept of FRANKA-1

On the one hand the concept of FRANKA-1 is the development of a sufficiently powerful device, which can be used in a first industrial installation. On the other hand the concept should allow easy changes to the material feed or outlet, to the design of the processing vessel as well as to the pulse power unit.

Figure 1 shows an artist view of the device, which demonstrates the flow of material through the plant. The high voltage pulse generator (Marx generator) is positioned on a staging. Fig. 1 exhibits a feature, which will be subject of the next upgrade of FRANKA-1: By means of a mechanically driven switch at the end of the pulse generator the high voltage pulse can be distributed to more than one electrode. The unit comprising the switch and the electrodes is called multi-electrode-system MESYS and can be applied either for areal fragmentation tasks or to switch the energy flow from one electrode to an electrode array in order to distribute thermal- and high voltage stress.

To adapt the spark length between the high voltage- and the opposite ground electrode through the fragmentation material, the electrode system can be moved vertically. Marx generator and electrode system are mounted in a screened housing, which serves as a Faraday cage to suppress EMP radiation. A second purpose of the housing is noise-reduction, since discharges in the open process vessel together with the spark-gap switches of the Marx generator produce a noise level in the range of 110 dB. A third purpose of the screened housing is man-protection against electrical shock by means of an interlock system.
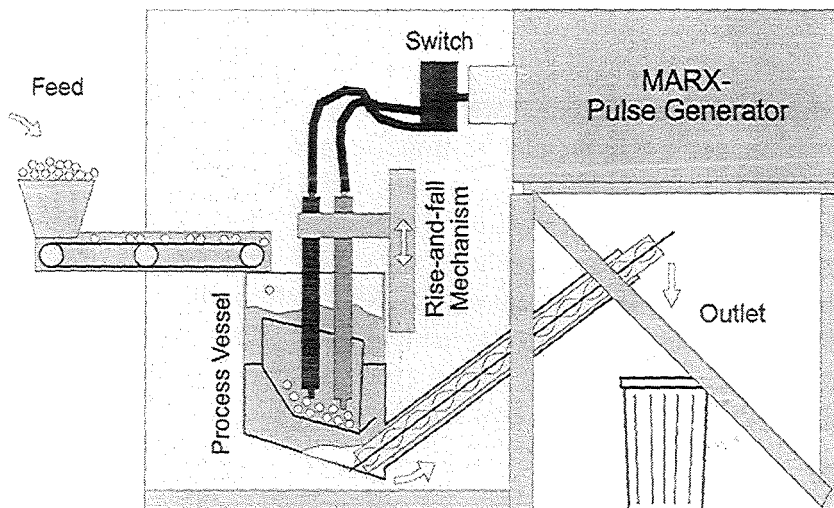

Fig.1: Concept of FRANKA-1 consisting of a material-flow-line through the fragmentation vessel and an electrical part, which consists of a Marx-pulse-generator with an output voltage of 350 kV and a pulse duration of 200 ns, a switch and a multi-electrode-system in the fragmentation vessel. Marx-generator as well as fragmentation vessel are mounted in a Faraday cage to inhibit EMP radiation. In addition the cage serves for noise reduction and man protection by means of an interlock system.

3. Marx- high voltage pulse generator

The principle of a Marx generator is to charge the capacitors parallel and to switch them into a series configuration. The main feature of the FRANKA-0 Marx is the use of 200 kV- high voltage capacitors, which are charged to only 50 kV as well as the use of simple air spark-gaps. Due to the relatively low voltage rating of the capacitors we expect an exponentially increased life-time of the order of 10^8 to 10^9 charge-cycles. Spark-gaps in air are low in cost and reliable for long term operation.

However high voltage strength of humid air at normal pressure is worse compared with dry nitrogen or electronegative gases like SF_6. The consequence of using air spark-gaps is a large

discharge path combined with correspondingly large energy losses by plasma production (see ref. 3).

Further disadvantages of the FRANKA-0 concept are the high inductance of the Marx, resulting from an interior conductor length of more then 10 m in the generator and the relatively high intrinsic capacitor inductance of 200 nH. Low mechanical stability of the spark-gap array is another weakness.

The aim in the new Marx generator design is to increase the number of capacitor stages from 5 to 7 in order to raise the output voltage up to 350 kV and to reduce the inductance level. Therefore the topology of the Marx construction was changed:
To benefit from single inductive load-lines at the ground- and high voltage side respectively, the discharge current path in the FRANKA-0 Marx is helix-like and therefore long and highly inductive, which is disadvantageous. Although the number of stages is increased from 5 to 7, the current path length of the FRANKA-1-Marx is comparable to that of FRANKA-0, because the spark-gap switches are mounted directly above the capacitors (see fig.2 „switch level"). If the Marx ignites, the current runs in a zigzag the shortest possible way though the Marx.

Because of shock waves from the sparks, which reach the switch electrodes either through the switch atmosphere or through the case material the gap distances tend to shift, especially because they are arranged on a mounting platform of rather soft polyethylene. By special means the mechanical stability is improved. Spherical electrodes were replaced by electrodes with Borda-profiles (4), where discharges can occur everywhere on the electrode surface, thus reducing the wear of the electrodes significantly. In addition, copper-tungsten alloy has been chosen as the electrode material, which is known to be highly resistant against thermal wear.
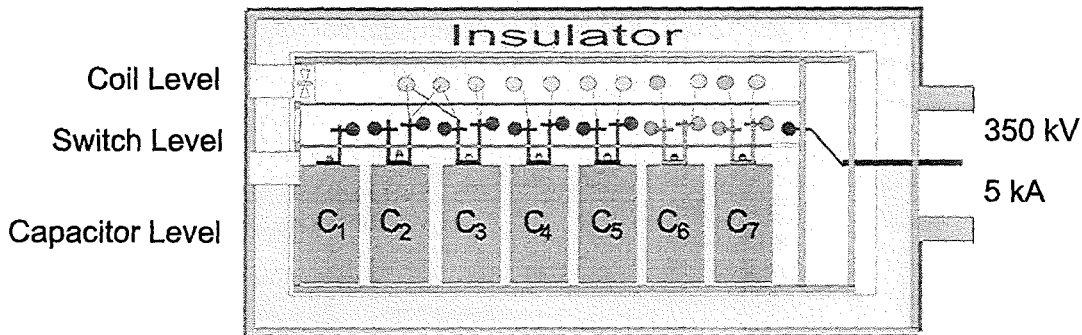

Fig.2: Scheme of the FRANKA-1 Marx-pulse generator. In contrast to the FRANKA-0 Marx the spark-gaps in the switch level are mounted directly upon the capacitors in order to minimize the current path in the Marx. The load inductance has been positioned on a level above the switches leading to a relatively complex connection topology.

First operation tests with the Marx demonstrate, that before ignition of the output switch (at maximum voltage) the switching- and erection time of the pulse generator is of the order of some 10th of nanoseconds. The diagnostic to measure the pulse voltage is a compensated voltage divider and to measure the pulse current a Rogowski coil. The upper signal in fig. 3 is the output voltage on a 100 kV/scale, which shows no pre-signal before the main signal appears. The signal below is the current with a sensitivity of 4.2 kA/scale. During switching the current signal is noisy. The fast erection of the Marx is obviously a consequence of the

„open" spark-gap arrangement, which assures, that UV-light production of the first switch helps to trigger the subsequent switches.

The Marx output switch is tuned to ignite at maximum voltage. The rise time of the pulse is 100 to 150 ns. The example of fig.3 shows a situation during tests, where the load in the discharge-current-circuit is an electrode system in water with concrete lumps between the electrodes. Because of the electrolytic conductivity of water (from public network) the initial current is carried by electrolytic discharges. Then, after about 400 ns, a flash occurs and the current increases to 11 kA.

A measure of the inductivity of the pulse generator is the ringing frequency $T_{2\pi}$. For FRANKA-1 $T_{2\pi}$ is 1.8 µs or 550 kHz and for FRANKA-0 it is 2.1µs or 480 kHz. The intrinsic inductance of FRANKA-1 is 840 nH, which is smaller than the1150 nH of FRANKA-0.

In short circuit cases or if the gap-length of the Marx output switch is untuned as well as at irregular flashover situations in the Marx generator, parts of the voltage pulse become reflected and travel back through the load line to the high voltage supply. This is an undesirable situation, because it disturbs the electronic control system, can lead to high voltage breakdowns and even destruct the HV-source. Separation of the Marx generator from the HV-source by means of large inductance air-cored coils significantly avoids disturbances during operation. However the separation is necessary at both: the high voltage side as well as the ground side.

The current signal can be used for controlling the rise and fall mechanism of the electrodes in the process vessel. In case of a too big electrode gap the discharge in the underwater arrangement is solely electrolytic. From fig.3 it can be easily seen during the first 400 ns after ignition that the current in this case is about 3 kA. In an adapted discharge, where the energy deposited in the discharge is maximum, the current is around 10 kA. In a short-circuit case the current increases to 20 kA.
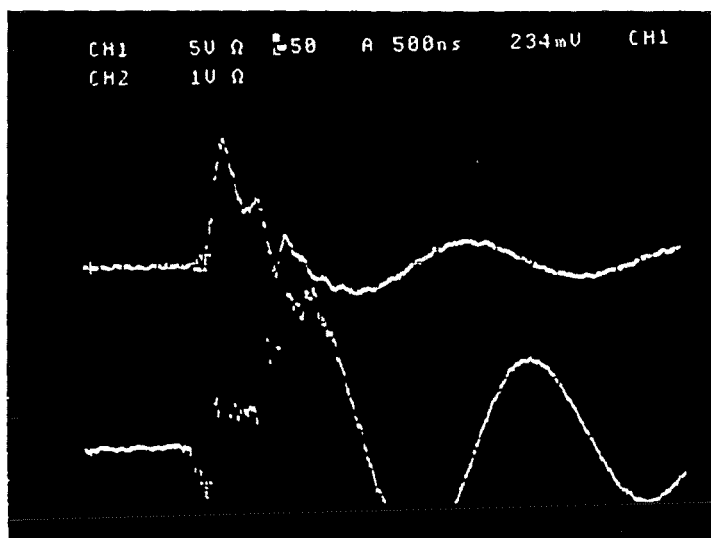

Fig.3. Voltage and current signal (below) of the FRANKA-1 Marx with a load, which is a standard electrode system consisting of a grounded half-sphere from steel and a rod-like high voltage electrode with concrete lumps in between. The electrode arrangement is underwater. In the beginning a strong electrolytic discharge can be observed followed by a flash-discharge 400 ns after the voltage has been applied. The ramp-time of the voltage

140

pulse is about 100 ns. The ringing frequency is 1.8 μs. The peak values of voltage and current are 210 kV and 10 kA respectively.

4. First results with the FRANKA-1 Marx

1. First operation of the Marx generator demonstrated, that the device can operate at a repetition rate of 7 Hz. In these tests the generator is connected with a load, which consists of a double electrode system under water with a 20 mm separation. The high voltage source used delivers 10 kW at 60 kV. The number of shots during the test phase was about $2 \cdot 10^5$.

2. Following ref.5 the spark-length L in the fragmentation material increases with the output voltage and therefore the mass of fragmented material scales like L^3. A 23 mm long stable discharge path in water can be achieved. For comparison on FRANKA-0 only 14 mm were possible. From ref. 5 it can be concluded that the reaction volume with FRANKA-1 discharges has been increased by a factor of about 4.

3. The specific energy during scrape-off experiments on concrete was 70 J/g.

4. Scraping and drilling of pillar heads was subject of a number of experiments with the FRANKA-1 pulse generator and is published under ref.6.

5. In comparison with FRANKA-0 the electrolytic conductivity limit, where electrolytic discharge overcome spark-like discharges totally, is increased from 1400 μS to 2400 μS.

5. Status of the project

The project goal is to finish the hardware in the second half of 1998 and to start the test phase at the Forschungszentrum first, before the final installation at a refuse incinerator plant. In the actual phase the construction of the whole fragmentation device is the main subject. Without a reduction of functionality, different possibilities have been checked to reduce investment costs for the construction of the housing or Faraday cage significantly.

6. References

[1] W. Edinger, V. Neubert, C. Schultheiss, R. Straessner, H. Wieczorek, „Process and Device for Electrodynamic Fragmentation of Solids - FRANKA, Interner Bericht 50U070.0P02A Forschungszentrum Karlsruhe, 1996
[2] H. Bluhm et al, invited plenetary talk presented at the 11th IEEE International Pulsed Power Conference, Baltimore, June 29- July 2, 1997
[3]D. Rusch, H. Giese, Interner Bericht 21.02.01 Forschungszentrum Karlsruhe, in German 1996
[4] Private communication W. Frey, INR, Forschungszentrum Karlsruhe
[5] B. W. Sjomkin, A. F. Ussow, W. J. Kurez, „Grundlagen der elektrische Impulszerstörung von Materialien" , from N. P. Tusow, Edition: Russische Akademie der Wissenschaften, Forschungszentrum Kola, Forschungsinstitut für physikalisch-technische Probleme der

Elektroenergiewirtschaft des Nordens, Polytechnische Universität Tomsk, translated from Russian in German, 1995, p. 218

[6] V. Neubert, C. Schultheiss, R. Straessner, to be published as Interner Bericht Forschungszentrum Karlsruhe, in German 1998

FRANKA-Stein:
A Semi-Industrial Prototype for the Fragmentation of Concrete

P. Hoppé, W. Frey, H. Giese, H. Lotz, J. Marek, M. Söhner, W. Väth

Abstract

FRANKA-Stein was designed as a semi-industrial prototype machine that allows the fragmentation of a continuous stream of concrete of 1t/h to its original constituents gravel, sand and cement. These components could then be used for e.g. the fabrication of 'new' concrete. Its design was based on FRANKA-0, a laboratory scale machine that operates in the 'batch' mode. The extrapolation to FRANKA-Stein operation conditions concern mainly the reaction chamber and the continuous concrete feed through, the design of the HV components and the safety and licensing issues to be considered for the envisaged industrial use of this recycling technology. In this contribution these aspects are described in detail together with the first results from the start-up experiments performed on FRANKA-Stein.

I. Introduction

The fragmentation of concrete into its original constituents gravel, sand and cement is of high interest mainly due to environmental considerations. If the original constituents of 'old' concrete could be used for the production of 'new' concrete, this would mitigate the deposition problem of the 'old' concrete, would greatly reduce the amount of CO_2 release required for the production of 'new' cement and finally would also help to reduce the exploitation and use of natural resources [1]. By mechanical means, the separation of concrete into its constituents cannot be achieved. The method of electrodynamic fragmentation seems to be well suited for the separation of a composite material like concrete because the electrical breakdown mechanism takes place at the boundary limits of inhomogeneities and therefore is very selective. The principles of the electrodynamic fragmentation are summarized in [2]. Based on these principles a small scale pilot plant called FRANKA-0 (Fraktionierungsanlage Karlsruhe) was developed by the Tomsk University and operated at FZK/INR since 1995. Measurements of the high voltage (HV) pulse characteristics of this machine [3], the results from numerous experiments and a description of the FRANKA-0 machine itself is given in [4,5]. These experiments proved, that 'new' concrete fabricated from the components of 'old' concrete -treated by the FRANKA machine- showed the same or even better properties than the original 'old' concrete [1]. Thus it was demonstrated in laboratory scale experiments that in principle concrete can be recycled into new concrete, i.e. in contrast to other recycling methods a down-cycling of the material was avoided. The main purpose of FRANKA-Stein is to investigate whether this method can be used for the recycling of amounts of concrete which are significant for an industrial application.

II. Design criteria for the semi-industrial prototype FRANKA-Stein

The FRANKA-Stein prototype was designed on basis of the experience and knowledge gained on the FRANKA-0 machine. The main design modifications refer to the following items:

(a) the concrete fragmentation chamber and the concrete transport scheme,

(b) the redesign of the HV components for the generation of the discharge and

(c) the requirements related to licensing- and safety issues for an industrial use of this fragmentation machine.

A detailed description of these modifications is given in the following.

(a) FRANKA-0 (Fig. 1) allows the treatment of about 2kg of concrete lumps (with dimensions of several centimeters) in a 'batch' type operation mode: the concrete lumps are loaded to the discharge bucket which must be filled with water before starting the fragmentation process. After treatment, the water has to be drained and the concrete fractions must be unloaded and separated [4].
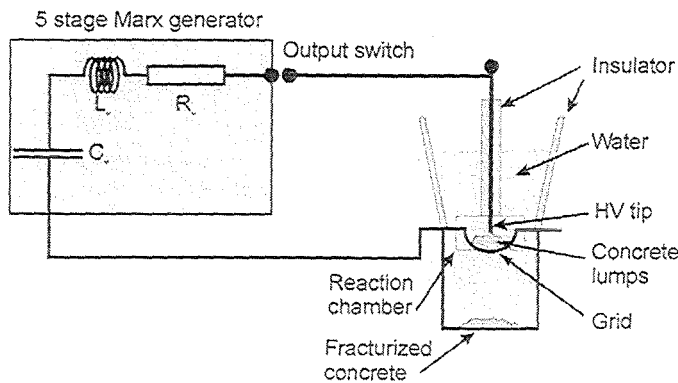

Fig. 1: Scheme of the FRANKA-0 machine

FRANKA-Stein -as a semi-industrial prototype- should be able to treat 1t of concrete per hour which is difficult to achieve in a batch operation mode. Thus a stream of concrete lumps (with dimensions of up to 10cm) must be fed continuously to the waterfilled HV fragmentation chamber. The necessary exposure time of the concrete in the active (i.e. destructive) HV region must be matched to the desired degree of fragmentation, the properties of the concrete itself, the time dependent insulating properties of the water in the reaction chamber, the performance of the HV pulse generator etc. Finally all fractions of the concrete must be transported out of the reaction chamber to the separation units. The water must be reprocessed and fed back into the system.

(b) On FRANKA-0 the required size distribution of the concrete is achieved after an exposure time of about 20s with a repetition rate of the HV pulses of 5Hz. The FRANKA-0 HV pulses are characterized by a voltage gradient of 1...2MV/μs to a peak voltage of 200 to 240kV (assuming a load of about 200Ω) and an energy of about 750J per pulse stored in the Marx generator. Hence the energy necessary for the fragmentation of 1kg of concrete suitable for recycling purposes is about 35kJ. The distance of 2 to 5cm between the tip of the HV discharge electrode and the ground grid limits the size of the concrete lumps on FRANKA-0 to dimensions of about 5cm [1,4].
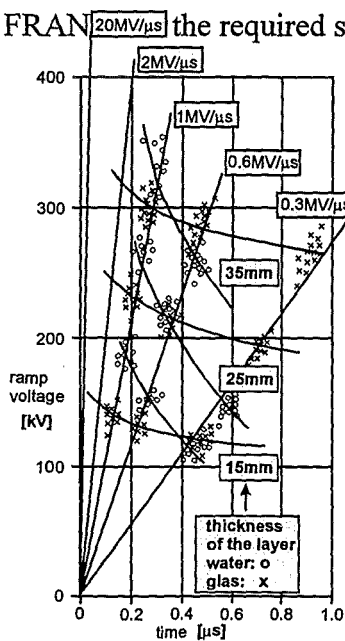

Fig. 2: Breakdown curves [6]for water (o) and concrete(x)

For FRANKA-Stein the fragmentation of concrete lumps with dimensions of up to 10cm is envisaged. This value roughly defines the cross section of the reaction chamber to about 10 by 10cm and also sets transport velocity of the concrete to 1cm/s to achieve the projected mass flow of 1t/h. These dimensions require -extrapolating linearly the FRANKA-0 data- a HV pulse which peaks around 400kV. With the mass flow envisaged the average

HV exposure time is reduced to 10s. An increase of the pulse frequency much above 5Hz seems not to be reasonable, hence a single discharge must be more energetic and also more efficient e.g. due to a voltage gradient above 1...2MV/µs: the shorter rise time of the pulse should enhance the probability for a breakdown through the concrete (Fig. 2) and hence the fragmentation efficiency [6]. This increase of efficiency can actually not be quantified and therefore the energy of a single pulse should reach up to 1.5kJ. Based on these rough estimates the fragmentation of 1t/h of concrete by FRANKA-Stein led to a required electrical power (ref. to the wall plug) around 10kW.

(c) Additional design criteria result from environmental and safety requirements like:

1. to avoid the possibility to come into contact with high voltage or high currents when operating the machine. All HV components must be grounded automatically when the machine is not in operation or when access to HV components is feasible.
2. to limit the 'noise' emission of the operating machine (acoustic and electro-magnetic) to levels which are in agreement with the standards.
3. to fulfill the standards with respect to gas emission from the machine (e.g. from the gas switches) and for the ground water pollution in case of an accident (e.g. oil losses from the Marx).

With respect to the envisaged separation of the concrete constituents these design considerations are obviously not complete: neither the separation- nor the water reprocessing systems were specified. These systems actually cannot be described due to a lack of experience: the establishment of a reliable data base for the design of both systems will be part of the experiments on FRANKA-Stein and will be performed in cooperation with the Institut für Technische Chemie -WGT of the FZK.

III. Description of FRANKA-Stein

FRANKA Stein consists of the following 3 main components: a **HV generator** that delivers the HV pulses to the concrete/water filled **reaction chamber** and a **transport system** for the concrete into and out of this reaction chamber (Fig. 3).
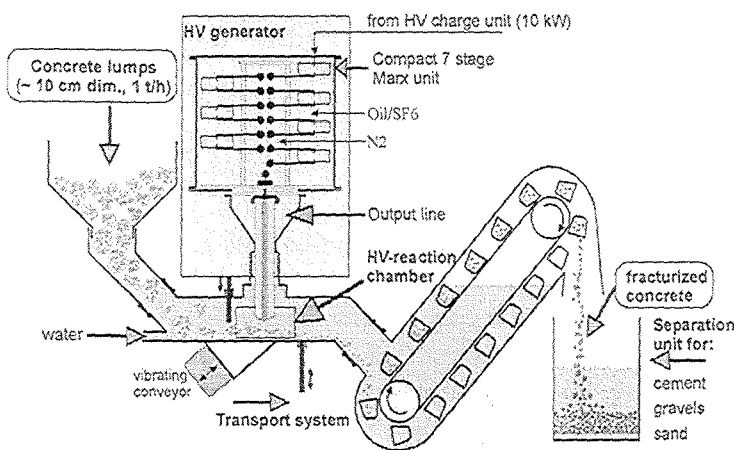

Fig. 3: Scheme of FRANKA-Stein

The required electrical energy for the HV pulses is stored first in a compact 7 stage Marx generator. For time intervals of about 200ms the 140nF capacitors of each stage are charged in parallel to a maximum voltage of 60kV and are discharged in very short time scales (about 1µs) by 7 self-breakdown gas switches to the reaction chamber. If the load in this reaction chamber (i.e. the mixture of water and concrete) is assumed to have a low resistivity the output pulse is approximately a (damped) sine wave

145

which -assuming a given capacitance- oscillates with a frequency that depends mainly on the Marx inductance. In order to achieve a fast risetime this inductance must be minimized. The parallel charge-up of the Marx capacitors is made by coils with inductivities sufficiently high (mH) to not influence the capacitor discharge. The 'charging towers' (see Fig. 4) are connected via a filter network and a 20m long cable to the HV charging unit. This unit is a constant current source that can deliver a maximum current of 1A for an adjustable voltage up 60kV. The Marx discharge gas switches are located in a common housing which can be pressurized with N_2 gas up to 3bar. This allows the adjustment of the level of the HV output pulse from 200 to 500kV. The Marx generator itself with its filter net work and the grounding circuits is confined in a vessel which can be filled with either SF6 or oil.

From the Marx output switch the HV pulse is transferred via a conical shaped coaxial output line to the reaction chamber. This output line can store just a fraction of the Marx energy and was designed such that voltages across the load even higher than the series discharge voltage of the Marx generator (7 times the charge voltage / capacitor stage) are achievable. The inner conductor of the output line is a metallic rod which is insulated by a thick PE cylinder against the ground tube. This ground tube is connected to the reaction chamber while the inner rod with the insulator penetrates into the waterfilled section of the reaction chamber.
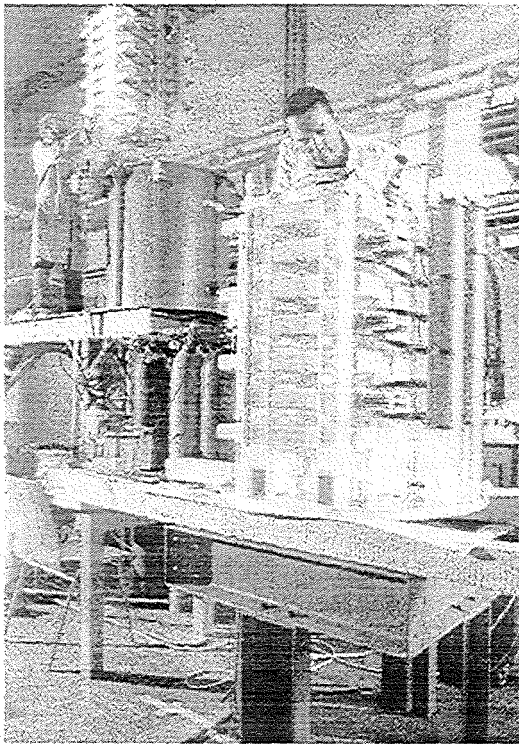

Fig. 4: Assembly of the Marx generator

The reaction chamber itself is formed by a robust, thick wall T-fitting normally used for the construction of oil pipe lines. The fitting has a flange on its upper side which is penetrated by the HV rod. The flange on the opposite side carries the ground electrode. The electrical energy supplied by the HV rod discharges through the concrete/water load. The current flows back to the generator via the ground electrode and the inner surface of the outer structure elements that completely confines the HV components. With the chosen thickness of the confining wall on ground level and the skin depth of the electrical waves, the outer surface of the machine will present no electrical hazard. Both side end flanges of the T-fitting can be partly blocked by an adjustable inlet and outlet gate respectively. These gates are part of the control mechanisms for the time the concrete is being treated in the reaction chamber. The vibrating conveyer -adjustable in its vibration amplitude- and the intensity of the water circulation will also serve to control the exposure time. The concrete loading is made via a funnel-type inlet head, down a 45° elbow to the reaction chamber. A second 45° elbow directs the concrete constituents to an elevator type exhaust unit. This transport scheme for the concrete fulfills both main requirements: to keep the HV reaction chamber always under water and to allow a continuous and controlled feed through of concrete. The mechanical support system of the reaction chamber tolerates the required amplitudes for the conveyer and avoids the transmission of mechanical shocks to the HV generator parts.

During the last 18 month the FRANKA Stein machine was designed, fabricated and mounted (Fig. 4) in the hall 2 of the building 630 of the INR. All supply-, control- and safety related

systems were established and are operational as well as the screen room and the data acquisition system. The results of first measurements are given in the following.

IV. First results from the FRANKA-Stein start-up experiments

The main objectives of the start-up measurements were the determination of the electrical parameters of the HV generator and the establishment of a reliable mathematical model that allows the calculation of e.g. the voltage at the HV tip or the energy deposition into the discharge on basis of the measured currents I_M and I_O at the positions M and O shown in Fig. 3. The monitor for the output current I_O is a self-integrating Rogowski coil which was calibrated by using a 4.166kA / 100ns pulse generator. In addition this monitor signal was cross checked with the signal I_M of a commercially available Rogowski coil placed one the ground side of the Marx.

In all experiments performed so far the output line was filled with demineralized water. The calculations were made by using different codes like PSpice, Leiter or -for simple cases- by just solving the differential equations.
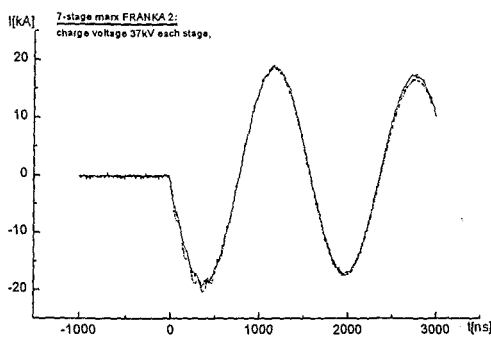
Measurements with a short load:

Fig. 5: Comparison of calculated (dashed) to measured current (solid) for a short load

In these measurements, the HV tip was directly connected to the ground electrode thus presenting a low inductance short load to the HV generator. With the given capacitance of the series Marx of 20nF the best agreement between the measured and calculated curves was achieved with a Marx inductance of $L_M=2.95\mu H$ and a Marx series resistance of just $R_M=0.35\Omega$ (Fig. 5).

The corresponding values given in [3] for the FRANKA-0 Marx are $C_M=22nF$, $L_M=5\mu H$ and a surprisingly high $R_M=6\Omega$. The lower inductance of the FRANKA-Stein Marx promises a faster pulse rise while its very low R_M value indicates that electrical energy can be transferred to the discharge until its resistivity becomes significantly smaller than 0.35Ω (which seems not very likely). The impedance's and the transit times of the different sections of the output line (see Fig. 3) used in the model are: $Z_1=3.5\Omega$ / 3.5ns, $Z_2=60\Omega$ / 7ns and $Z_3=80\Omega$ / 1ns.
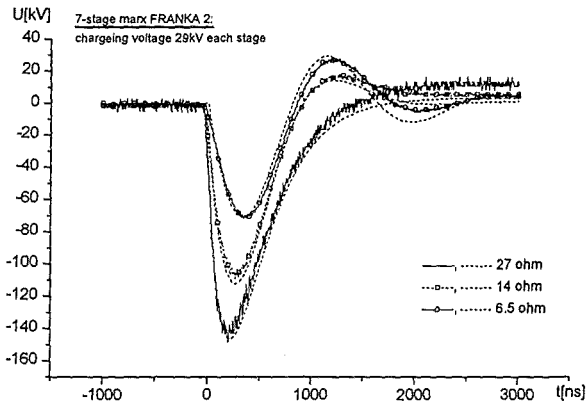
Measurements performed using resistive loads:

U[kV]

7-stage marx FRANKA 2:
chargeing voltage 29kV each stage

40
20
0
-20
-40
-60
-80
-100
-120
-140
-160

—, ······· 27 ohm
···□···, ······· 14 ohm
—○—, ······· 6.5 ohm

-1000   0   1000   2000   3000   t[ns]

Fig. 6: Comparison of calculated (dashed) to measured
voltage at the load (solid) for different ohmic
loads

The direct measurement of the load voltage V_L in an operating reaction chamber (filled with a water/concrete mixture) by e.g. a high voltage divider seems to be not practicable. Hence the most interesting discharge properties like energy delivered to the pulse and the breakdown sequence cannot be observed directly. In the following the question was investigated, whether the current I_O can be used to determine the load voltage. Therefore the HV generator with the parameters determined in the short load experiments was modeled with PSpice and the load voltage V_L was calculated for different ohmic loads and a charge voltage of 29kV per Marx stage (Fig. 6). These calculated voltages are to compare with the 'measured' load voltages determined as follows:

- the values of the ohmic loads connected between the HV tip and ground result from the measured decay time constant when discharging a 30kV/70nF capacitor into the resistor.
- the measured I_O current was multiplied with this resistor value.

The agreement between the measured and calculated load voltage demonstrates the possibility to determine the load voltage on basis of the measured I_O current if combined with a proper generator model. It be pointed out that the parameters of the model remained unchanged for the calculation of the load voltage for different ohmic loads.
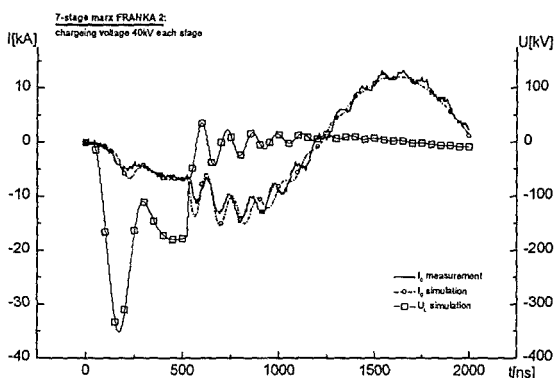
Breakdown characteristics of a 1cm water gap

7-stage marx FRANKA 2:
chargeing voltage 40kV each stage

I[kA]   U[kV]

10   100
0   0
-10   -100
-20   -200
                —I, measurement
-30   —○— I, simulation   -300
                —□— U, simulation
-40   -400

0   500   1000   1500   2000   t[ns]

Fig. 7: Voltage at the load V_L calculated from the
measured current I_O and the PSpice model
of the HV generator

The discharge characteristics of a 'water' break-down experiment were measured and compared to calculations performed with the HV generator Pspice model that uses the parameters determined before (Fig. 7). In this experiment just water -no concrete- was in the reaction chamber and the distance between the sharp edge HV tip and ground was only 1cm. The measured initial resistance of this arrangement was 246Ω. The load voltage V_L rises first with a gradient around 3.5MV/μs to its peak value of 350kV. This voltage is well above the 280kV which would be expected for a 7 stage

Marx charged to 40kV per stage. This voltage enhancement is due to 'resonant' loading: the Marx capacitance discharges through an inductance and loads up the smaller output line capacitance. It is interesting to note, that this field enhanced 1cm water gap does not break down until 520ns which is in contrast to the 100ns expected from Fig. 2. This result is not yet understood but might indicate that even a small water gap between the HV tip and the concrete could hinder the fragmentation of the concrete.

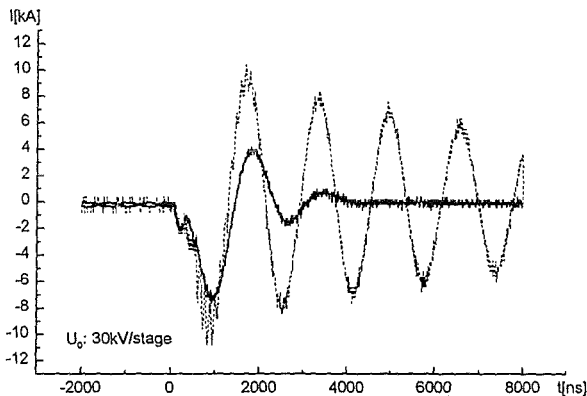## Resistivity of the discharge after break-down

Fig. 8: Damping of the discharge after break-down for a 1cm water gap (dashed) and a 4cm concrete/water gap (solid)

The output currents I_0 for a water discharge (1cm gap) and a discharge into a concrete/water mixture (4cm gap) showed quite important differences with respect to the damping characteristics of the current oscillations after breakdown (Fig. 8). From these oscillations the values of the 'spark resistance' were estimated using PSpice and the HV generator model. The spark resistance of the 1cm water gap was 0.3Ω and that of the 4cm concrete/water gap was 3.3Ω which is significantly higher than expected. This result confirms that -even after breakdown- the Marx with its 0.35Ω series resistance still delivers most of its energy to the discharge. This result would also indicate that internal heating of the Marx should not present a major problem.

V. Conclusions

Until today the Marx of FRANKA-Stein was charged up to its design value of 50kV/stage. Occasionally, arcing at several locations were observed in the Marx tank when filled with SF6 gas at 1bar. Numerous field calculations were performed to reduce the risk of electrical break-down thus extending the SF6 operation range. Safety related measures in order to use oil instead of SF6 in the Marx were initiated. The maximum continuous operation time achieved so far was 30min with a repetition rate of 2Hz and charging to 30kV/stage. Neither problems with the loading unit nor excessive heat-up in the Marx were noticed. After some hours of operation time arcing inside of the switch tower was observed which seems to be related to the deposition of corrosion products -presumably from the switches- on the inner insulator surfaces of the switch tower. In summary it can be stated that the HV design of FRANKA-Stein should meet the requirements for the fragmentation of 1t of concrete per hour. However, the main problem seems to be closely connected with the design of the reaction chamber and the presence of a water gap between the HV electrode and the concrete lumps. This water gap shifts the time the HV components are stressed from the expected 100 to 200ns to much longer times of typically from 500 to 1000ns. Similar observation were not made on FRANKA-0. This is possibly due to the bucket type discharge chamber which keeps most of the concrete -even after a discharge- close to the HV tip. On FRANKA-Stein the discharge itself can blow the concrete off the HV tip mainly in the transport direction. Therefore the confinement of the concrete near the HV tip for continuous operation conditions must be

improved and hence the design of the reaction chamber and the concrete transport system must be optimized.

With respect to the other design criteria formulated in sect. II the following results were achieved:
- the pulse rise may reach up to 4MV/μs, depending on the load resistance and the water resistivity. Due to the resonance loading as much as 500kV peak voltage may be achieved. This should allow the use of HV gaps of more than 4cm.
- the acoustic noise source is mainly concentrated on the reaction chamber, the noise from the Marx discharge is negligible. Hence a local acoustic shielding of the T-fitting seems to be feasible.
- electrical hazards for operational staff of the machine does not exist. The HV discharge is completely confined within coaxial components, i.e. by principle no voltage on the outer surface of the generator can occur. Consequently, no problems with electro-magnetic noise were observed when operating the machine.
- The discharge voltage for the load and hence the discharge energy can be remotely controlled by variation of the N_2 pressure in the switch tower. The use of N_2 avoids the release of dangerous gases to the environment.
In summary this means that licensing of the machine should not present a major problem. The modular design of the FRANKA-Stein HV generator allows extrapolation to larger units as well as its use for similar problems.

References

[1] C. Schultheiss et al.: Concrete recycling and scraping by electrodynamic fragmentation, p.?, this report
[2] B. W. Sjomkin et al.: Grundlagen der elektrischen Impulszerstörung von Materialien, (in russ.), Kola Science Center, (1995)
[3] D. Rusch et al.: Zur pulstechnischen Auslegung der zweiten FRANKA Generation, internal report no. INR1952, 11.1996, unpublished
[4] W. Edinger et al.: Process and device for electrodynamic fragmentation of solids, in Annual report 1995, H. Bluhm (Editor) FZK 5840 p. 151, 1996
[5] H. Bluhm et al.: Industrial applications of high voltage pulsed power techniques: Developments at Forschungszentrum Karlsruhe (FZK), IEEE Pulsed Power Conf. 1997
[6] A. A. Dulson et al.: Electrodaynamic high voltage pulse devices and technologies, IEEE Pulsed Power Conf. 1997

FRANKA-3, an Electro-Dynamic Fragmentation Facility, Operating at Liquid Nitrogen Temperature

H. Giese, D. Rusch

Abstract: Complementing the investigations currently performed at the facilities FRANKA-0 and FRANKA-2 (see related contributions in this report), work at FRANKA-3 (KRYO-FRANKA) is destined to extend the application of the high voltage pulse fragmentation method to elastic and tenacious compound materials at liquid nitrogen temperature. All components of the facility are available, and are presently being assembled. After assessment of the electric parameters of the facility, first scanning tests on candidate materials will be performed in co-operation with an industrial partner.

1.   Introduction

As discussed in earlier reports [1, 2], solid materials can be fragmented by inserting them between a pair of electrodes and applying high voltage pulses of sufficient amplitude, length and appropriate risetime, provided that the discharge path along the surface of this material is impeded in an appropriate way. In the existing FRANKA facilities this is accomplished by immersing the material in question into water. Using pulse amplitudes in the range of 250 kV and pulse rise-times of the order of 250 ns, the efficiency of the method has been tested in the pilot plant FRANKA-0 on a wide spectrum of materials, including glass, small electric and electronic appliances, silicon-monocristals, and concrete etc. While in many cases these exploratory tests yielded promising results, in particular in view of the breakdown of concrete into its basic components, gravel, sand and cement, and the re-use of these components for the production of new concrete without significant loss in rigidity, the method was found to work less favourably in the attempt to fragment elastic materials or tenacious material compounds. The reason for the unsatisfactory performance lies in the fact that the pressure wave initiated by the electrical discharge plasma channel is not able to disintegrate the material but is simply dissipated within the bulk material. In an attempt to improve the performance of the method in this field of application, investigations were launched at the Tomsk Polytechnical University [3], in which elastic materials (in particular rubber) were immersed into liquid nitrogen (LN_2) to increase their rigidity. The electro-dynamic fragmentation method then proved to be more efficient, but relatively little conclusive information is available about the results of these studies.

It was therefore decided to construct a corresponding facility at FZK, allowing the exposure of small material samples (max. diameter ~15 cm) immersed in a bath of liquid nitrogen to pulsed voltages of up to 350 kV with possible ramp rates of 2 MV/μs, or 20 MV/μs. Before describing the layout and components of this facility, the present report recalls some of the results of earlier studies of electrical discharge under liquid nitrogen.

2. Previous experience with electrical discharges in LN₂

2.1 General investigations of electric discharge under liquid nitrogen

Although a considerable amount of information is found in literature on investigations concerning the electrical characteristics of LN_2 [4-25], only a relatively small fraction of the experience gained so far is transferable to the complex field of the electro-dynamic fragmentation. While in earlier times, electric discharge experiments in LN_2 were made mainly to widen the basic knowledge on discharge phenomena in different media (LN_2 being a simple molecular liquid without internal dipole moment) [4,5,6,7], the discovery of high temperature superconduction (HTSC) has given these investigations a new impetus. One of the promising projected fields of application of HTSC materials is in high voltage coaxial power cables, by which the voltage drop along such cables could be dramatically reduced. In this application, LN_2 has to fulfil two tasks: (1)It has to reliably cool the HTSC conductors, and (2) it forms part of the high voltage insulation. Usually LN_2 impregnated paper is proposed to be used as a dielectric. Over the recent years, numerous investigations were therefore performed to elucidate in more detail the electrical behaviour of LN_2. The focus of these studies was on the following essential topics:

1. The 3 pre-breakdown phenomena: light emission, density change streamers and partial discharge current pulses [8,9,10].
2. The dynamics of N_2 gas bubbles, created e.g. by partial discharge currents or by superconductor quenching, under the influence of electric field gradient forces, buoyancy and viscosity [11,12,13,14].
3. The contribution of area and volume effects to electrical breakdown in LN_2 [15,16,17].
4. The influence of impurities like e.g. ice crystals on electrical breakdown in industrial grade LN_2 [18-23].

Since a detailed description of the results of these investigation would largely exceed the frame of the present report, only some points of particular importance in the context of the operation of the FRANKA-3 facility will be discussed hereafter.

Concerning topic 2 of the above list, it is well known that gas bubbles (i.e. gaseous enclosures) in dielectrics lead to local field distortion and thus weaken the electric strength of the materials. In the present context, this phenomenon is of particular interest since the temperature of liquid gases under atmospheric pressure stabilises close to the boiling point. In such liquids, even the minute heat production inferred by pre-breakdown currents can lead to the appearance of local inhomogeneities like N_2 gas bubbles and turbulences. These inhomogeneities enhance streamer formation [24] and thus reduce the breakdown threshold. In the practical case of FRANKA-3 this means that partial discharge paths, the formation of which takes place on a nanosecond timescale [25], can lead to the formation of bubble chains, along which premature breakdown occurs, before a discharge path through the material to be fragmented has been established.

Apart from these micro-effects, which have been discussed in literature in great detail, one should keep in mind that the situation in FRANKA-3 is further, and possibly much more seriously, aggravated by the fact that each shot evaporates a considerable quantity of LN_2. A rough estimation leads to the following results:

FRANKA-3 is estimated to deposit an energy of approx. 300 J per shot into the material that is being fragmented [26]. If one assumes that all this energy is finally converted into heat and

using an evaporation energy for LN_2 of 159.4 kJ/Litre, one finds that each FRANKA-3 shot evaporates 1.9 ml of LN_2. With a density change from 800 kg/m^3 for LN_2 to 1.25 kg/m^3 for N_2 gas this means, that each FRANKA shot produces approx. 1.9 ml x 800/1.25 = 1.2 Litres of N_2 gas. Assuming a shot frequency of 5 Hz, 6 Litres of LN_2 gas would have to be removed from the processing area within 1 second to avoid gas bubble breakdown. Although the viscosity of LN_2 is relatively small (2,1 mp[1] @ 77°K, as opposed to 1 cp[1] for water @ 20°C) which facilitates bubble movement to the surface under buoyancy force, it has to be doubted that this is feasible. Corresponding experiments [4,5] have shown that N_2 gas bubbles in LN_2 submitted to buoyancy force only, move upward with a speed of about 0.2 m/sec or 4 cm in the time period of 200 ms between two FRANKA-3 shots. Given a depth of the LN_2 bath of 20 cm, a substantial number of gas bubbles will not be able to reach the LN_2 surface before the next shot occurs. The consequence of this is probably that a considerable number of electric discharges will pass through the gas bubbles, rather than through the material to be fragmented. Only practical experience will show, however, to what extent this impedes the application of the electro-dynamic fragmentation technique in liquid gas.

Another important factor in the operation of FRANKA-3 could be the accumulation of impurities in the LN_2 bath [18-23]. Typical impurities in industrial grade LN_2 whose surface has been exposed to the atmosphere are e.g. ice crystals, originating from frozen-out air humidity. Other contaminants that appear in the course of machine operation are electrode and insulator wear. Such contaminants lead to local field distortions with the possible consequence of premature electrical breakdown. If the discharge paths are guided along the contaminants instead of passing through the material to be fragmented, this could degrade the operation efficiency of the facility. On the other hand, it is clear that due to the above-mentioned low viscosity of LN_2, heavy contaminants will sink significantly faster to the bottom of the processing vessel, than in other dielectric liquids like e.g. in water, and are therefore less likely to interfere with the electrical discharge process. Although this seems to indicate that in LN_2 the impact of the presence of such contaminants on the process efficiency could be less aggravating than in other dielectric liquids, a final judgement has to await the results of the FRANKA-3 investigations.

2.2 Electrical breakdown of rubber under liquid nitrogen

The only experiments that are of direct relevance for the FRANKA-3 project are those conducted over the recent years, at the Polytechnical University in Tomsk/Russia. The aim of these experiments was to investigate the applicability of the electro-dynamic fragmentation method to the mechanical breakdown of polymers, with particular attention given to the possibility of recycling rubber e.g. from scrap car tyres [3].

In the course of these experiments, various types of rubber samples of 3 to 40 mm thickness were immersed in a bath of liquid nitrogen and exposed to high voltage pulses. All experiments were carried out in 'pin-plate-geometry', i.e. the samples were placed on a conductive plate (the bottom of the cryo container) and a pointed rod electrode was installed on top of the sample. In order to compare the breakdown voltages of rubber and LN_2, and thus to assess the useful operation range of the method, two sets of experiments were made: One with the rubber sample in position, the other using the same electrode spacing, but with liquid nitrogen filling the inter-electrode-gap.

---

[1] mp = millipoise; cp = centipoise

An overview of the results obtained from the experiments conducted in Tomsk is shown in Figure 1. Depicted is the change of the breakdown voltage as a function of sample thickness in the case of LN_2 for three different pulse rise times: 200 ns, 1 µs and 5 ms sine wave, and for two different rubber samples: car tyre rubber and vacuum seal rubber. The rise times always refer to a pulse amplitude of 250 kV and can thus be expressed as ramp rates of 1.25 MV/µs, 250 kV/µs and 50 V/µs. One observes, that the breakdown behaviour of LN_2 differs significantly from other dielectric liquids, like transformer oil, glycerine, alcohol or water (at normal conditions).
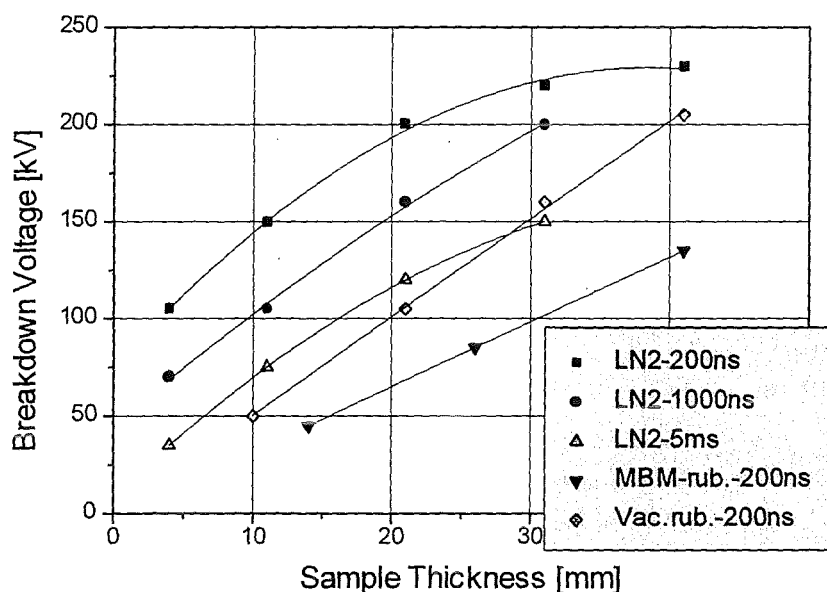
Fig. 1: Dependence of the breakdown voltage on sample thickness [3].
⇒ For LN_2, three different pulse rise times were used: 200 ns, 1000 ns, 5 ms
⇒ For rubber, 2 different compositions were tested, using a pulse rise time of 200 ns

Although in the parameter range of the experiments performed in [3], breakdown occurs at progressively higher voltages, when the sample thickness is increased and when pulses of shorter risetime are used, one finds a clear saturation tendency for sample thicknesses (gap-widths) above 20 mm, a phenomenon occurring at much greater gap widths in the other dielectric liquids mentioned above. This extraordinary behaviour is linked to pre-breakdown discharge processes. As was discussed in Sec. 2.1, these processes lead to the formation of local inhomogeneities like N_2 gas bubbles and turbulences. Such inhomogeneities enhance streamer formation and are apparently able to reduce the breakdown threshold of the liquid to such an extent that above a certain lower limit of the applied electrode voltage, it becomes largely independent of the electrode spacing. As was mentioned in Sec. 2.1, another reason for premature electrical breakdown in LN_2 with its surface exposed to normal atmospheric air, can be the accumulation of ice crystals within the liquid, originating from frozen out air humidity.

Although these problems could be significantly reduced by pressurising the LN_2 and by minimising the contact of its surface to atmospheric air, such steps had not yet been taken up to now.

Another anomaly is observed in the change of the breakdown voltage with pulse rise time: While in water, a change of a factor of 10 is observed when passing from a pulse rise time of 200 ns to 1 μs, the corresponding change in LN_2 is merely 25%.

The results of the measurements made using different rubber samples showed the normal characteristics of solid materials, i.e. a linear increase of the breakdown voltage with sample thickness. Vacuum rubber and three-layer car tyre rubber show higher breakdown voltages then mono-layer car tyre rubber.

From these results, the authors of [3] conclude that the useful operating range for a rubber fragmentation facility (i.e. the range in which the electrical discharge is more likely to pass through the rubber than through the LN_2) lies in the range:

- Pulsed voltage amplitude ~ 200 kV
- Pulse risetime 200 to 500 ns
- Sample thickness up to 30 mm

It remains to be seen whether these parameters are confirmed by the FRANKA-3 experiments, or whether its higher ramp rate of 2 MV/μs (20 MV/μs with intermediate storage) allows to extend the operating regime beyond the mentioned sample thicknesses of 30 mm.

In conclusion one might state that although the results presented in [3] give some useful hints concerning the fragmentation of rubber under LN_2 , they do not allow any reliable conclusions concerning the fragmentation efficiency that can be expected from such a process.

3. Set-up of the FRANKA-3 Facility

3.1 General layout

In order to minimise electromagnetic interference problems, to shorten the pulse rise time and to reduce the operating noise level, the new FRANKA facilities FRANKA-2 (FRANKA-Stein) and FRANKA-3 (KRYO-FRANKA) were designed as closed coaxial systems. A detailed description of the different components of the high voltage pulse supply unit was given in the contribution to this report on FRANKA-2. The present description therefore largely concentrates on the processing section of FRANKA-3 and only briefly recalls the characteristics of the pulse supply section.

The FRANKA-3 facility consists basically of the following components:

1. High voltage pulse generator (Marx-Generator)
2. Optional intermediate storage
3. A conical adapter section
4. The processing section
5. The LN_2 bath with pneumatic hoist

Components 1 to 4 are suspended from a gallery, such that the processing section and the LN_2 bath are easily accessible from all directions.

The high voltage pulse generator (1) is a 7 stage Marx generator using 14 MAXWELL pulse capacitors of 70 nF, two of which are connected in parallel in each stage. Inductive stage decoupling is employed using cylindrical monolayer chokes of 600 μH. The maximum erected voltage of the Marx is conceived as 350 kV with a ramp rate of 2 MV/μs. The energy

contents of the fully charged Marx is 1.2 kJ. All components of the Marx generator are accommodated in a cylindrical tank of 1m diameter and 1 m height.

The optional intermediate store (2) is a 50 cm long coaxial water capacitor with inner and outer conductor diameters of 30 cm and 50 cm respectively. Gas pressure adjustment in the outlet spark gap allows to control the voltage level at which the intermediate storage fires into the load.

The conical adapter section (3) gradually reduces the diameter of the coaxial intermediate store to a diameter of about 18 cm, suitable as a feedthrough for the electrode insulator. The bottom part of the adapter section accommodates a Rogowski coil, used to monitor the discharge current.

3.2   The processing section
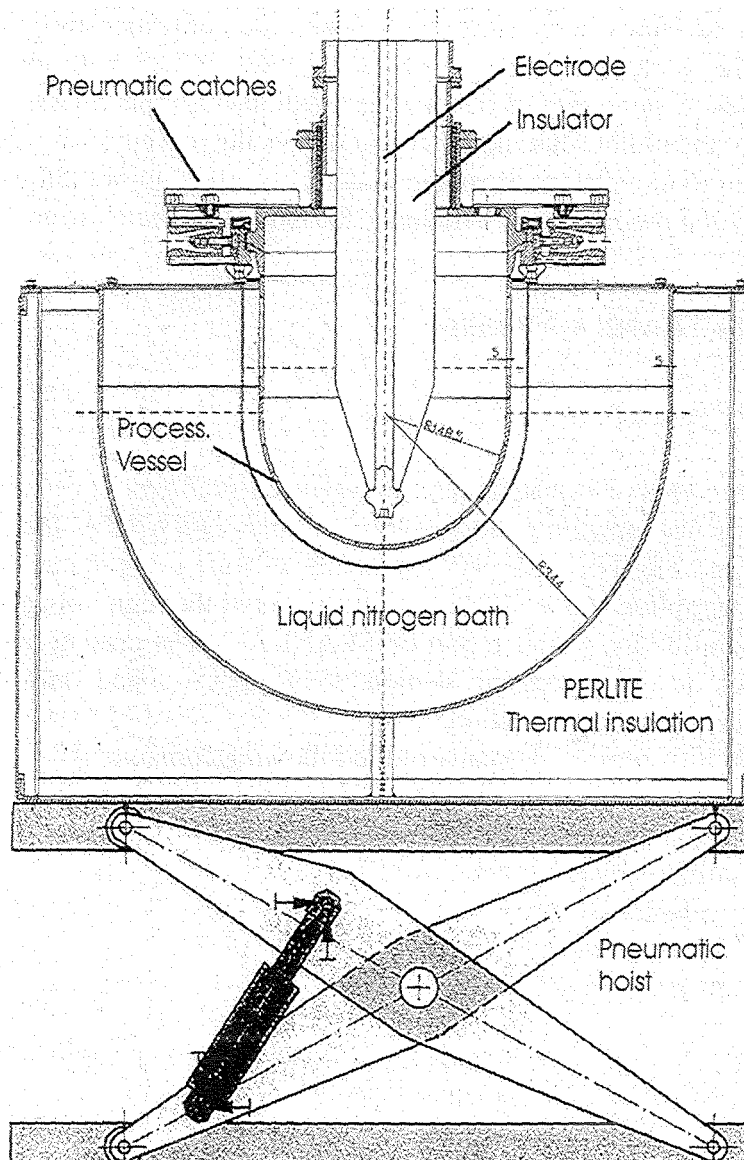
Fig. 2: The processing section of FRANKA-3

The layout of the processing section is shown in Fig. 2. The material that is to be fragmented is placed on the bottom of a cylindrical vessel with half-sphere bottom, made of low temperature ductile steel 1.4541. The upper end of this processing vessel has a conical profile, sitting centred in its counter profile in the upper, stationary part of the processing section. Eight pneumatic catches allow easy and safe attachment and detachment of the processing vessel.

The bottom of the processing vessel is perforated to allow LN_2 drainage when it is lifted out of the LN_2 bath. The hole diameter presently varies from 1 mm at the bottom to 3 mm on the side wall of the spherical part. These hole sizes represent a compromise in the effort to minimise the amount of fragmented material washed out through the holes and to maximise the drain velocity. The time span presently required for complete drainage of the processing vessel is about 5 minutes. In order to reduce this time span it is envisaged to enlarge the hole diameters and to catch escaping fragmented material by a fine mesh grid, positioned in the LN_2 bath directly underneath the vessel.

To allow fast ventilation of the processing vessel during operation and to achieve a certain degree of shock-wave decoupling between the vessel bottom and the upper stationary structures, the vessel side walls contains a great number of oblong holes.

Figure 2 also shows the approximate axial position of the high voltage electrode, protruding from the conical adapter section of the high voltage pulse supply unit. The electrode is made of low temperature ductile steel 1.4541 of 20 mm diameter and is surrounded by an insulator of 50 mm thickness. The material chosen for this insulator (UHM-PE = Ultra-High-Molecular Polyethylene) is expected to favourably combine low temperature ductility and high voltage insulation capability, but little experience has been accumulated in this domain up to now, and manufacturers are reluctant to guarantee long time stability for these operating conditions. The lower end of the insulator is pointed to reduce adhesion of gas bubbles. First tests at FRANKA-2 have shown that gas bubble adhesion to the insulator is a severe problem, since it encourages the formation of tree-like discharge paths along the insulator surface, degrading its insulation capability and destroying its structure. It remains to be seen, whether with the steeper pointing angle of the insulator used in FRANKA-3 this problem still prevails.

A threaded joint in the upper, stationary part of the processing section allows to move the processing vessel including its 8 pneumatic catches up and downwards by simple rotation, and thus to vary the distance between the lower end of the high voltage electrode and the vessel bottom. In the present design, this distance can be set to any value between 0 and 8 cm.

Following the recommendation given in [3], the LN_2 filling level will be adjusted in such a way that the material samples are positioned at about 15 cm below the LN_2 surface.

3.3 The LN_2 bath and supply

Flooding and draining of the processing section with LN_2 is accomplished be raising and lowering an LN_2 bath located underneath the recipient. The LN_2 bath is accommodated in a cylindrical container of 90 cm diameter and 60 cm in height, filled with Perlite (thermal insulation) granules. Embedded into these granules and centred within the outer container is a stainless steel (type 1.4541) half sphere of 70 cm diameter and 5 mm wall thickness with cylindrical upper end. During operation this inner container is filled with LN_2 from a reservoir up to a height of about 40 cm, resulting in a bath volume of approx. 0.1 m^3 = 100 litres. Using the above mentioned LN_2 consumption of FRANKA-3 with 5 Hz operation of 5 x 1.9 ml/sec, this volume would in principal suffice for an operation of almost 3 hours. It has to be taken into account, however, that the lower (non-insulated) end of the high voltage electrode has to be kept under a sufficiently thick layer of LN_2, to avoid parasitic electrical breakdown across

the LN_2 surface and the N_2 gas on top of it. To ensure continuous operation, the bath has therefore been equipped with an automatic topping-up system, consisting of an electrically operated LN_2 inlet valve, controlled by a dip PT100 sensor.

The top cover of the outer container has openings for visual inspection, for the insertion of the PT100 dip sensor, and for the connection of 2 high power N_2 gas exhaust pumps, each of which has a pumping capacity of 2.8 m^3/min.

The complete LN_2 bath assembly is mounted on an electrically driven pneumatic hoist. At a later stage of the investigations it is planned to control the lifting speed electronically in two steps: High speed lifting up to the point, where the processing section touches the LN_2 surface, and slow motion lifting above this point to avoid excessive LN_2 boiling

4. Economical Aspects

As already commented in [1], the electro-dynamic fragmentation method is a relatively costly procedure for the breakdown of materials. This arises, since apart from the investments to be made for (a) the construction of the powerful high voltage pulse generator, for (b) the protection of operating personal, and (c) for RF shielding, the electrical efficiency of the method is rather poor: ca. 10%.

Apart from these points, an additional cost factor has to be taken into account in the operation of FRANKA-3: the LN_2 consumption. Judging from the experience accumulated during the investigations at the Tomsk Polytechnical University, about 1 kg of LN_2 (1.25 litres) is needed for sufficient cooling of 1 kilogram of material to be fragmented. The price of 1 litre of LN_2 on the german market varies from about 0.35 to 0.90DM/litre, depending on the ordered amount. Although in an industrial application, this consumption can obviously be somewhat lowered, if follow-up material is pre-cooled by the N_2 gas, developing during the immersion of previous material, it is evident that in general, the electro-dynamic fragmentation method will have a possibility of market penetration only in special industry branches:

- in the field of relatively valuable materials, and
- in cases where standard grinding methods do not lead to satisfactory results.

These fields of application will have to be selected in co-operation with the industrial partner.

In the light of the relatively high costs of the method, it should be mentioned that at the present time the initially envisaged breakdown of car tyres into rubber granules and steel carcass seems rather unattractive. Furthermore, earlier tests have shown that it will be difficult to arrive at sufficiently small rubber grain sizes that allow re-use in the vulcanisation of new car tyres.

It is interesting to note that existing conventional facilities for the recycling of rubber from scrap car tyres also use cryogenic techniques: After increasing the rigidity of the rubber by bathing the tyres in an LN_2 bath, the frozen tyres are put into a mechanical crusher, that separates the rubber from the steel carcass. The rubber is finally ground into fine granules. In the most advanced of these recycling plants, the rubber granules are coated with a Latex film. This is done directly after grinding and avoids surface oxidation. The problematic issue of this method lies in the fact that the rubber powder contains steel particles originating from broken carcass wires. Since even with the use of modern magnetic separators these particles can not be removed with sufficient confidence, car tyre manufacturers are reluctant to use this product

for car tyre production. The powder is therefore used in other rubber industry branches, or as an additive in paints and in the bitumen industry.

5. Outlook

After completion of the functional tests of the high voltage pulse supply assembly, presently performed on the FRANKA-2 facility, the set-up of FRANKA-3 will be completed. Following a series of measurements in which the electrical parameters for different discharge regimes under LN$_2$ are assessed, first scanning tests on candidate materials, as selected by the industrial partner are envisaged.

6. References

[1]   B.W. Sjomkin, A.F. Ussow, V.I. Kurets, „ *The Principles of Electric Impulse Destruction of Materials* ", Russian Academy of Sciences, Kola Science Centre, Editor N.P.Tusow, 1995 (in Russian).

[2]   H.J. Bluhm (Editor), „Process and Device for Electrodynamic Fragmentation of Solids - FRANKA", in *Physics of Intense Light Ion Beams, Production of High Energy Density in Matter, and Pulsed Power Applications, Annual Report 1995,* FZK-Report FZKA-5840,1996, pp.151-157.

[3]   V.I. Kurets, E.N Tarakanovskii, G.P. Filatov, „Electric Pulse Resistance of Liquid Nitrogen and rubber," in *Russian Physics Journal*, Vol. 38, No. 5, 1995, pp.455-457.

[4]   Y. Takahashi and K. Ohtsuka, „Corona Discharges and Bubbling in Liquid Nitrogen," in *J. Phys. D: Phys.*, Vol. 8, 1975, pp.165-169.

[5]   Y. Takahashi, „Koronaentladungen in flüssigem Stickstoff," in *Bull. Facul. Sci. & Eng., Chuo University*, Vol. 20, 1977, pp.247-255.

[6]   Y. Takahashi, „Über Lichtenbergsche Figuren bei Kryo-Temperaturen," in *Scientia Electrica*, Vol. 23, Fasc. 2, 1977, pp.66-74.

[7]   Y. Takahashi, „Zur Alterung von Tieftemperaturisolierungen durch Teilentladungen," in *Elektrotechnische Zeitschrift*, Ausg. A, Bd. 99, 1978, H.2, pp.100-104.

[8]   K. Yamazawa *et al.*, „Observation of Prebreakdown Light Emission Phenomena in Liquid Nitrogen," in *Trans. of the Inst. of Electrical Engineers of Japan*, 1995, pp.193-196.

[9]   K. Yamazawa, K. Sugiura, H. Yamashita, „Prebreakdown Light Emission, Density Change Streamer and Current Pulses in Liquid Nitrogen," in *Proc. 12th Int. Conf. on Conduction and Breakdown in Dielectric Liquids*, Roma, Italy, July 15 - 19, 1996, pp.222-225.

[10]   M. Nur *et al.*, „Spectroscopic Investigation of Corona Discharges in Liquid and High Density Gaseous Nitrogen," in *Proc. 12th Int. Conf. on Conduction and Breakdown in Dielectric Liquids*, Roma, Italy, July 15 - 19, 1996, pp.238-242.

[11]   M. Hara *et al.*, "Impulse and AC Breakdowns of LN2 in the Presence of Thermally Induced Bubbles," in *Trans. of the Inst. of Electrical Engineers of Japan*, 1988, pp.83-89.

[12]   M. Hara, Z. Wang and H. Saito, „Thermal bubble breakdown in Liquid Nitrogen under Non-uniform Fields," in *IEEE Trans. on Dielectrics and Electrical Insulation*, Vol. 1, No. 4, 1994, pp.709-715.

[13]   M. Hara and Z. Wang, „An Analytical Study of Bubble Motion in Liquid Nitrogen under DC Non-uniform Electric Fields," in *Proc. 4th Int. Conf. on Properties and Applications of Dielectric Materials*, Vol. 2, 1994, pp.459-462.

[14]   Y. Suda *et al.*, „Bubble Motion in Liquid Nitrogen between Electrodes in a Microgravity Environment," in *Proc. 12th Int. Conf. on Conduction and Breakdown in Dielectric Liquids*, Roma, Italy, July 15 - 19, 1996, pp.144-146.

[15]   H. Okubo *et al.*, „Area and Volume Effects on Breakdown Strength in Liquid Helium and Liquid Nitrogen," in *Proc. 9th Int. Symp. on High Voltage Engineering*, Graz, Austria, 1995, pp.7052-1 - 7052-4.

[16]   H. Goshima *et al.*, „High Voltage Insulation Based on Area and Volume Effects of Cryogenic Liquids For Superconducting Power Apparatus," in *Trans. of the Inst. of Electrical Engineers of Japan*, Part B, Vol. B, No. 7, 1996, pp.812-818.

[17]   N. Hayakawa *et al.*, „Mutual Contribution of Area and Volume Effects on Breakdown Strength in Liquid Nitrogen," in *Proc. 12th Int. Conf. on Conduction and Breakdown in Dielectric Liquids*, Roma, Italy, July 15 - 19, 1996, pp.333-336.

[18]   K. N. Mathes, „Electrical Properties of Cryogenic Liquids and of Ice at Cryogenic Temperatures," in, *Ann. Rep. of Conf. Elec. Insul.*, 1965, pp.20-23.

[19]   M. Delucchi *et al.*, „A Statistical Analysis of the AC Dielectric Strength of Liquid Nitrogen with IEC Spherical Electrodes under Controlled Conditions," in *J. Electrostatics*, Vol. 12, 1982, pp.315-322.

[20]   H. Shimizu, M. Kosaki and K. Horii, „Ice as Capacitor Dielectric," in *Int. Conf. on Properties and Applications of Dielectric Materials - Conf. Record*, Vol. 2, 1985, pp.539-542.

[21]   A. Jaksts and B. Mazurek, „Particle Initiated Flashover in Liquid Nitrogen," in *Cryogenics*, Vol. 30, 1990, pp.68-71.

[22]   R.Hanaoka *et al.*, „Effect of Electrode Ice Layer on Prebreakdown Current in Liquid Nitrogen," in *IEEE Trans. on Dielectrics and Electrical Insulation*, Vol. 1, No. 4, 1994, pp.741-746.

[23]   M. B. Srinivas *et al.*, „On High Field Dielectric Loss Tangent of Commercial Liquid Nitrogen," in *Proc. 9th Int. Symp. on High Voltage Engineering*, Graz, Austria, 1995, pp.7886-1 - 7886-4.

[24]   A. Badent *et al.*, „Preliminary Report for the IEEE DEIS Liquid Dielectrics Committee - International Study Group on 'Streamer Propagation in Liquids'," in *Proc. 12th Int. Conf. on Conduction and Breakdown in Dielectric Liquids*, Roma, Italy, July 15 - 19, 1996, pp.375-378.

[25]   M. Kanegami, „Waveform Analysis of Partial Discharge Current in Liquid Nitrogen Immersed Insulation," in *IEEE 1996 Annual Report, Conf. on Electrical Insulation and Dielectric Phenomena*, Vol. 2, 1996, pp.529-532.

[26]   D. Rusch, H. Giese, „Zur pulstechnischen Auslegung der zweiten FRANKA-Generation," in *Forschungszentrum Karlsruhe, Interner Bericht 21.02.01, INR Bericht Nr.1952*, 1996.

Production and compaction of nano-crystalline materials
by pulsed power techniques

R. Böhme, D. Rusch, A. Weisenburger, INR, and G. Link, ITP

An exploding wire device was used for the production of fine-grained oxides of Al_2O_3 and ZrO_2. These oxides were compacted to greens of simple shape by a dynamic compaction process in a pulsed magnetic press and sintered to ceramics in a microwave oven. In another reaction vessel voltage and current during a wire explosion were measured. It was also used for the generation of small amounts of submicron particles of various metals and alloys.

1. Introduction

There is a trend in many industries towards smaller particle sizes, e.g. electronic components with micrometer dimensions require ultrafine electroconductive coatings, advanced catalysts have large specific surfaces and novel ceramics is expected to have grain sizes in the 100 nm range. Many submicron and nanometer scaled materials can be produced by the exploding wire technique. An exploding wire device installed at the Forschungszentrum Karlsruhe was described in the previous report about the application of pulsed power /1/. This apparatus, developed in co-operation with the Russian Institute of Electrophysics (IEP) in Ekaterinburg, was operated for the production of a stock of Al_2O_3- and ZrO_2-powders. These powders have the required average grain size of < 50 nm. They were used to form greens, which could be sintered to ceramics. The greens were produced from these ultrafine powders by compacting them in a pulsed magnetic device. This apparatus, which was also developed in co-operation with the Russian institute, was described in the last report /1/. In the last and final step nanostructured greens manufactured by dynamic compaction were sintered to fine grain ceramics in the mm-wave radiation of a gyrotron installed at the Forschungszentrum.

For a closer investigation of the potential of the exploding wire technique a new reaction vessel was installed. It permits a better diagnosis of the physical processes taking place during an explosion. In this vessel wires made of various metals and alloys were exploded. The reaction products obtained were collected and analysed.

2. Production of nano-crystalline materials by the exploding wire technique

The electric energy stored in a capacitor bank was used for the explosion of metal wires of 0.8 mm diameter and 227 mm length. The explosion frequency was about one per two seconds. Air was circulating through the reaction chamber. The coarse particles produced in the explosions were collected in two cyclones, the finest fraction of powder was trapped in an electric filter and a filter made of sintered metal. For various customers a stock of Al_2O_3- and ZrO_2-powder was collected from the electric filter. The productivity of the device was not satisfactory. Large amounts of the smallest particles adhere to larger particles and are sorted out as waste together with them. Thus, only approximately 9 % of the alumina and about 10 % of the zirconia were trapped by the electric filter. The powder collected in the electric filter still contained some large particles and may therefore be not well suited for the manufacturing of novel ceramics. For this reason, several attempts were made to separate particles with diameters > 80 nm from the finest fraction and to increase the yield of this fraction. The

separation in a gas centrifuge was found to become very expensive and dismissed. Separation from a liquid suspension of powder by an ultracentrifuge failed due to agglomeration. A separating device based on the principles of a mobility analyser is still under development. The first results were obtained using a recently developed cyclone shown in Figure 1[1]. It is designed for the separation of particles with a limiting diameter of about 100 nm, a value usually not reached by conventional cyclones. In first exploratory trials the fine powder fraction contained no particles > 200 nm, but its yield was low. A micrograph of a typical sample is shown in Figure 2. At present possible modifications of the separating unit are being investigated with the aim of increasing its output of fine powder.
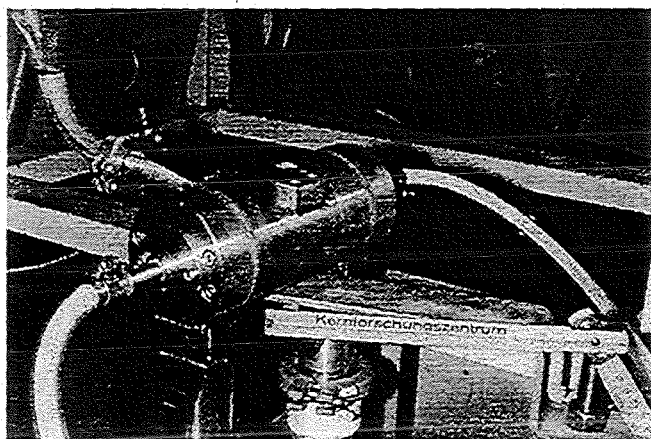
Fig. 1: Cyclone for the separation at 100 nm grain size

A new reaction vessel of ca. 180 l volume was built for the diagnosis of the processes taking place during the wire explosion. The vessel can be filled by various gases required for the production of oxide, nitride and submicron metal samples. The gases are circulated through the vessel and aerosols produced by the electric explosion of metal wires are collected in a filter made from sintered metal. Voltage and current during the explosion was recorded. By shortening the wire, varying the wire diameter and changing the voltage the specific energy inserted could be varied. The pressure of the atmosphere surrounding the wire was varied between $0.6 \cdot 10^5$ Pa and $1.5 \cdot 10^5$ Pa. Powder samples of Fe, Ni and Ti metal and of alloys like brass and TiAl6V4 were produced in an argon atmosphere. In nitrogen gas TiN and AlN was obtained and in air Al_2O_3, ZrO_2 and TiO_2 were generated.

Fig. 2: TEM micrograph of a sample of Al_2O_3 separated by the new cyclone

The investigation of the particle size distribution by electron microscopy revealed that by application of high pressure and energy input above the sublimation energy of the metal most of the particles have diameters in the range between 20 and 80 nm. Only a small amount of particles in the range below

---

[1] Prof. Dr.-Ing. J. Schneider, Fachhochschule Flensburg, Institut für Verfahrenstechnik, and LUT GmbH, Eckernförde

20 nm and above 100nm were found. Energy input below the sublimation energy and low pressures favour the generation of particles with sizes in the nanometer and also in the submicrometer range. Typical examples are shown in Figure 3.
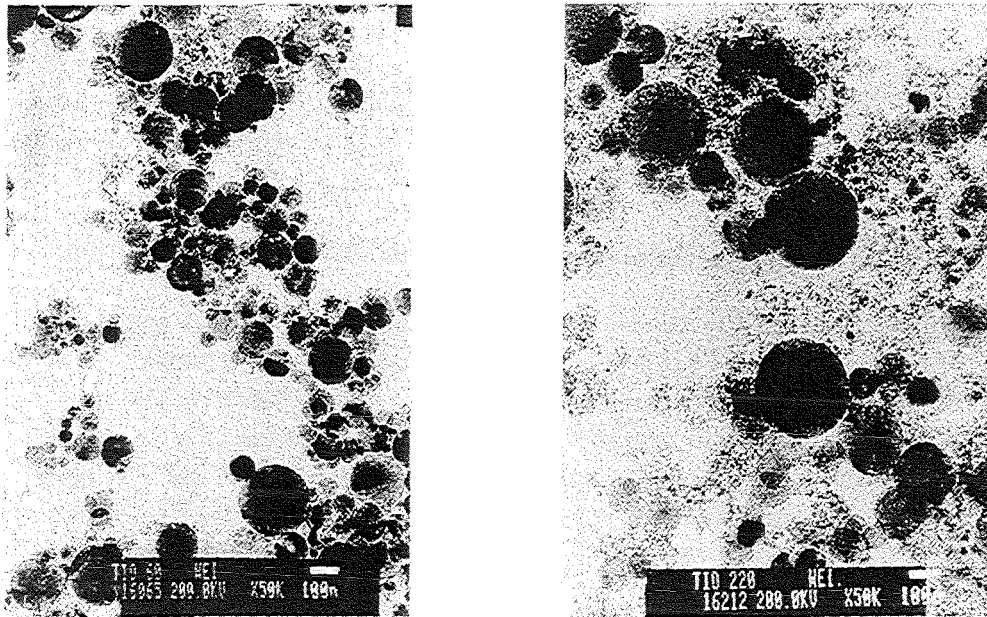
Fig 3: TEM micrographs of Ti-oxide particles produced by electrical explosion of wires. Energy input > sublimation energy (left) and < sublimation energy (right)

3. Compaction of nano-crystalline powders by a pulsed magnetic field

Nanoscaled powders were compacted to sinterable greens in a device described previously /1/. A magnet pulsed for about 300 μs forces a piston to compress powder contained in a mould with a pressure up to 2.8 GPa. This pulsed magnetic press was equipped with new instrumentation in order to measure the compaction pressure as a function of time. A typical example of the pressure applied for the uniaxial compaction of Al_2O_3 samples of 15 mm diameter and 2 mm height is shown in Figure 4. The initial density of the nanoscaled alumina powder was < 3 % and the density of the compacted greens was up to 76 % of the theoretical density. Greens made of TiO_2 reached 86 % of the theoretical density. Uniaxial compaction was also applied to microcrystalline Fe powder and magnetic alloys produced by melt spinning. In all cases solid compacts could be produced, reaching 99 % of the theoretical density in the case of Fe.

The production rate of the apparatus used for dynamic compaction is still very low and unacceptable for industrial applications. Based on experience gained during nuclear fuel production the design of a compaction device with higher output has been initiated in a co-operating institute.

The nanostructured greens manufactured by dynamic compaction from oxides of Al, Ti and Zr were sintered in a microwave oven connected to a gy-
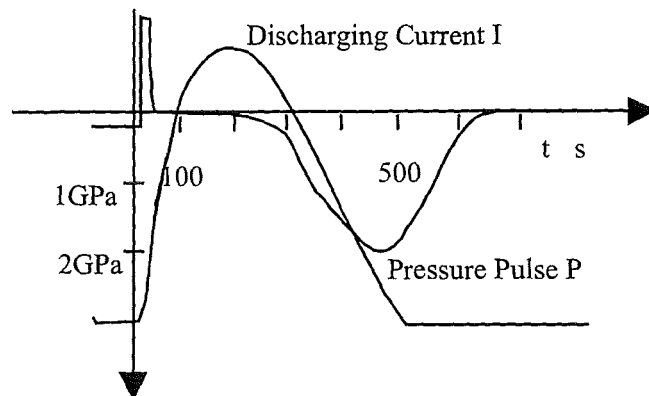
Fig. 4: Pressure pulse P and discharging current I

163

rotron installed at the Forschungszentrum. This 30 GHz gyrotron radiates mm-waves which easily heat these oxides even at low temperatures. In order to prevent excessive grain growth high heating rates between 30 and 100 K/s and no dwelling times were applied. A detailed study was made about the dependence of the density after sintering from the density of the greens and the sintering parameters /2/. Maximum densities reached after sintering at temperatures considerably lower than applied to standard ceramics were 93 %, 94.5 % and 93 % of the theoretical density for TiO_2, ZrO_2 and Al_2O_3, respectively. The grain size of these samples was in the range of 100 nm, a value being considered a prerequisite for novel nanoscaled ceramics.

4. Pulses of the nanopowder generator: measurements and numerical simulation

The pulse generator, see Fig. 5, consists of a capacitor bank of 3 µF which is charged to 40 kV. The stored energy is 2.4 kJ. A spark switch connects the pulse source and the load, i.e. the wire to be exploded, in the new reaction vessel of ≈ 0.8 m diameter. The total inductance of the circuit, as determined with a solid short circuit in place of the wire, is ≈ 1 µH. The normal load is a wire of up to ≈ 220 mm length and up to ≈ 1 mm diameter. To insert the wire before the pulse it is pushed from the top through a guiding hole towards contact electrodes. Contact is assured by short sparks which develop with the beginning of the pulse.
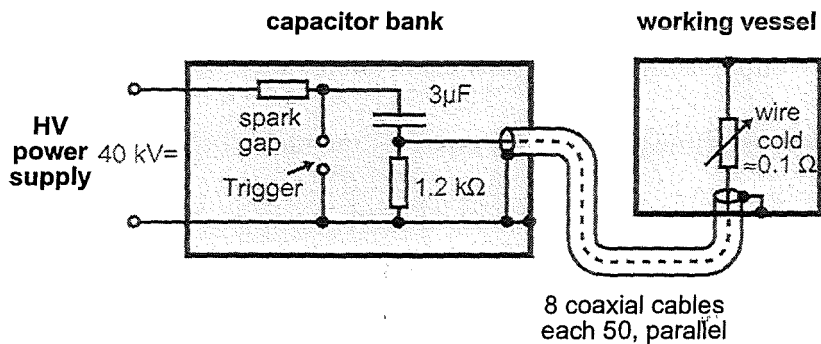
Fig. 5: Scheme of the pulse generator for nanopowder production

The determination of voltage and current at the load is characterized by the same difficulties as with intense ion or electron beam generation: access to the most important measuring locations - here at the ends of the wire - is difficult, if not impossible. Therefore we use a numerical simulation of the network to determine voltages and currents in inaccessible locations by modifying the calculation to approximate voltage and current at accessible locations. The numerical simulation is done with the code LEITER /3/, a transmission line calculation. A new type of "junction" describes the wire as a resistor, which changes its material phase and electrical resistance according to the pulse applied to it. Fig. 6 presents the result of the calculation for a fundamental case.

When the spark gap is closed the pulse generator is an L-C-R-circuit with an initially low series R. Therefore the start of the pulse current is an approximately sinusoidal half-wave of ≈ 5 µs duration, during which most of the available energy of 2.4 kJ is deposited in the wire. As the wire is heated up to the boiling temperature its resistance increases by an order of magnitude and increases further with the evaporation. The oscillation of the L-C-R-circuit changes to aperiodic behaviour. Such an aperiodic ending of the pulse is indeed observed.
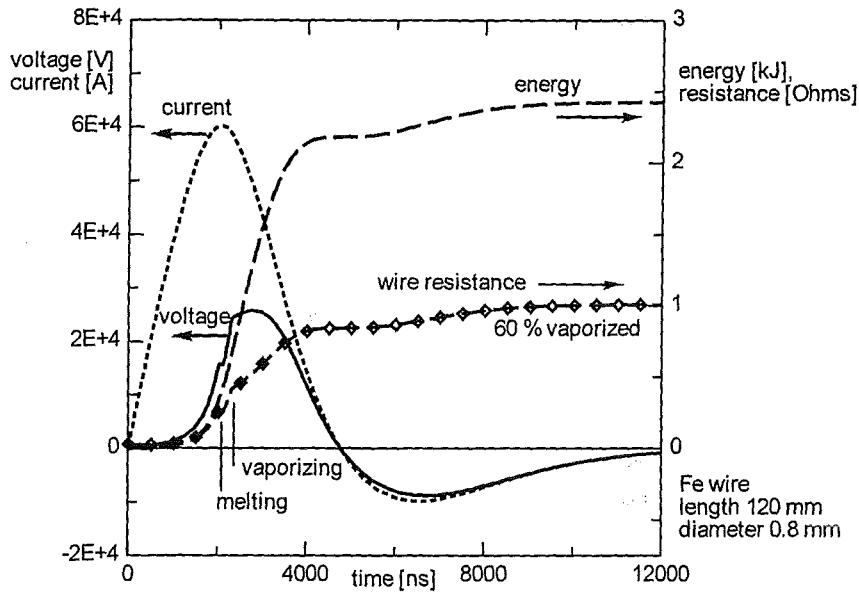
Fig. 6: Result of the numerical simulation for the fundamental case

Another, longer lasting oscillatory characteristic can also be observed, which is due to a low total load resistance. Only a spark in place of the wire or parallel to the wire can lead to this low total load resistance. The environment of the wire explosion enables the formation of such a spark. The wire is surrounded by a gas at approximately atmospheric pressure. From the sparks at the ends of the wire and supported by the thermal electrons emitted by the wire a spark may form parallel to the wire. Such a spark would within several tens of nanoseconds divert the current from the wire and cut off the voltage across the wire. Fig. 7 shows the result of a numerical simulation for such a case.

Such a spark should ignite as late as possible, if at all. However, the increase of the wire resistance with the reduction of its cross section by evaporation favours the occurrence of high voltages at the wire, as known from opening switches.
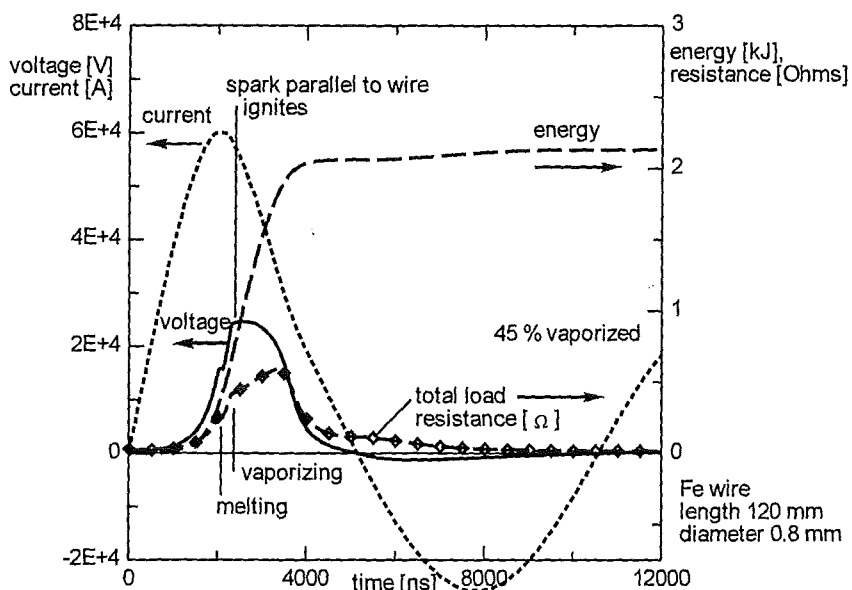
Fig. 7: Numerical simulation: a spark parallel to the wire diverts heating from the wire and leads to an oscillating end of the pulse

As a third scenario, when the wire is opening to a gap somewhere, a spark may also develop across the gaseous gap. In a third type of calculation, for which no graphical results are shown here, it was found that this type of spark has very low resistance and can therefore not transfer much energy to the solid or liquid parts of the wire. It behaves in the same way as the initial contact producing sparks at the ends of the wire.

According to the calculations in which the evaporation is modelled as the slow boiling from the surface of the wire only a part of the wire would be transformed into vapour, but in reality even longer wires than the 120 mm used in the calculations are completely transformed into powder. This indicates that the powder formation passes through lower energetic states, e.g. the disintegration into clusters. Since for a maximum of powder output the pulse energy should not be reduced the wire dimensions are the most important parameters to change the grain size distributions. The gas pressure in the discharge vessel may be another important parameter, but actually it cannot be raised enough to influence the spark formation remarkably.

5. Summary

Several attempts to separate the nanoscaled oxide powders produced by the exploding wire technique were not successful. However, a new type of cyclone shows promising results, but its yield of nanopowder has to be increased. Exploding wires were also used for the production of metal and alloy samples with grain sizes in the submicron and nanometer range.

Greens were made from Al_2O_3, ZrO_2 and TiO_2 by uniaxial dynamic compaction. The piston was driven by a pulsed magnetic field. Green densities up to 86 % of the theoretical density were obtained. These greens could be sintered by mm-waves of a gyrotron to ceramics with densities above 93 % of the theoretical density. The grain size of the sintered bulk material was in the range of 100 nm, which is of the order needed for a novel type of ceramics.

For diagnostics of the physical process causing the wire explosion a new reaction vessel was installed. Voltage and current during an explosion were measured and compared with results of numerical simulations.

6. References

/1/ H.-J. Bluhm (Ed.): "Physics of Intense Light Ion Beams, Production of High Energy Density in Matter, and Pulsed Power Applications - Annual Report 1995", report FZKA 5840, November 1996

/2/ G. Link, A. Weisenburger, R. Böhme, M. Thumm: "Millimeter wave sintering of nano-crystalline oxide ceramics", CIMTEC '98, Florence, Italy, June 14th -19th, 1998

/3/ D.Rusch: "Das Programm LEITER als Version 1.0 für PC", Int. Report 51.03.01/07B (=INR-1898), (1994), and "Neuerungen im Programm LEITER mit Version 1.1 für PC", Int. Report INR-1908, (1995); LEITER Version 1.2 with new junction type "wire" to be documented.

„Deposition of thin Glass Layers on Plastic Foils"

W. Frey, G. Schmitt, C. Schultheiß, M. Söhner, H. Wieczorek

Technology-Transfer-Project: Cooperation partner: Forschungszentrum Karlsruhe (Germany) - Stamp Foil (Italy)

Abstract: The deposition of thin glass layers on plastic foils by means of the ELBA technology was tested in an industrial rollcoater prototype plant located at our industrial partner in Italy. The subject of this project was to evaluate the efficiency of the ELBA technology especially for this application and in general to test the channel spark (CS-) systems under industrial conditions.

Introduction

By the deposition of thin glass layers (thickness 30-60nm) on plastic foils (thickness in general 12-50μm) the permeability of oxygen and water vapor can be reduced. These glass coated foils can be used for the packaging of materials which must be protected against oxidation, drying or contact with water vapor (examples: food, electronic components, implants, container filled with liquids).
Up to now there are several products on the market for flexible packaging.
1. aluminum coated foils (production in Europe 1997: about 70.000t)
Example: polyester (thickness 12μm) coated with aluminum (thickness 60nm)
permeation of oxygen: film without coating   100-150 cm³/m²24h 25°C
                            coated film   < 1 cm³/m²24h 25°C
2. compound foils
3. foils for special use coated with SiO_x, AlO_x

Compared with other foils available on the market the advantages of glass coated foils are:

- Transparent foils: packed materials are visible.
- Transparency for microwaves: without opening the packaging it is possible to heat food in a microwave-oven.
- Recycling: in contrast to aluminum coated or compound foils it is possible to recycle the glass coated foils.
- Saving of resources: up to 50% of the foil material can be saved.
- The glass coating material is cheaper then SiO_2 or Al_2O_3.
- The color of SiO_x coated foils is yellow, which is undesirable for some applications (food packaging).
- AlO_x coated foils have a higher barrier only against water vapor but not against oxygen.

The KARLA-plant

The paragon of the KARLA-plant was an aluminum evaporation plant which had been used by our industrial partner (fig. 1). This plant includes a controlled vacuum pump system and a foil transport system (rollcoater) with a cooled main cylinder (fig. 2). The regular foil speed of this plant was up to 6 m/s, for our tests it had to be reduced down to 1mm/s. Our contribution to the construction was the implementation of several ELBA systems instead of the aluminum evaporator. We implemented two arrays [1] in the vacuum camber (each of them with 13 CS-systems in a serial configuration) below the main foil transport roll (fig. 2/3). The arrangement allows the coating of foils up to a width of 70 cm.
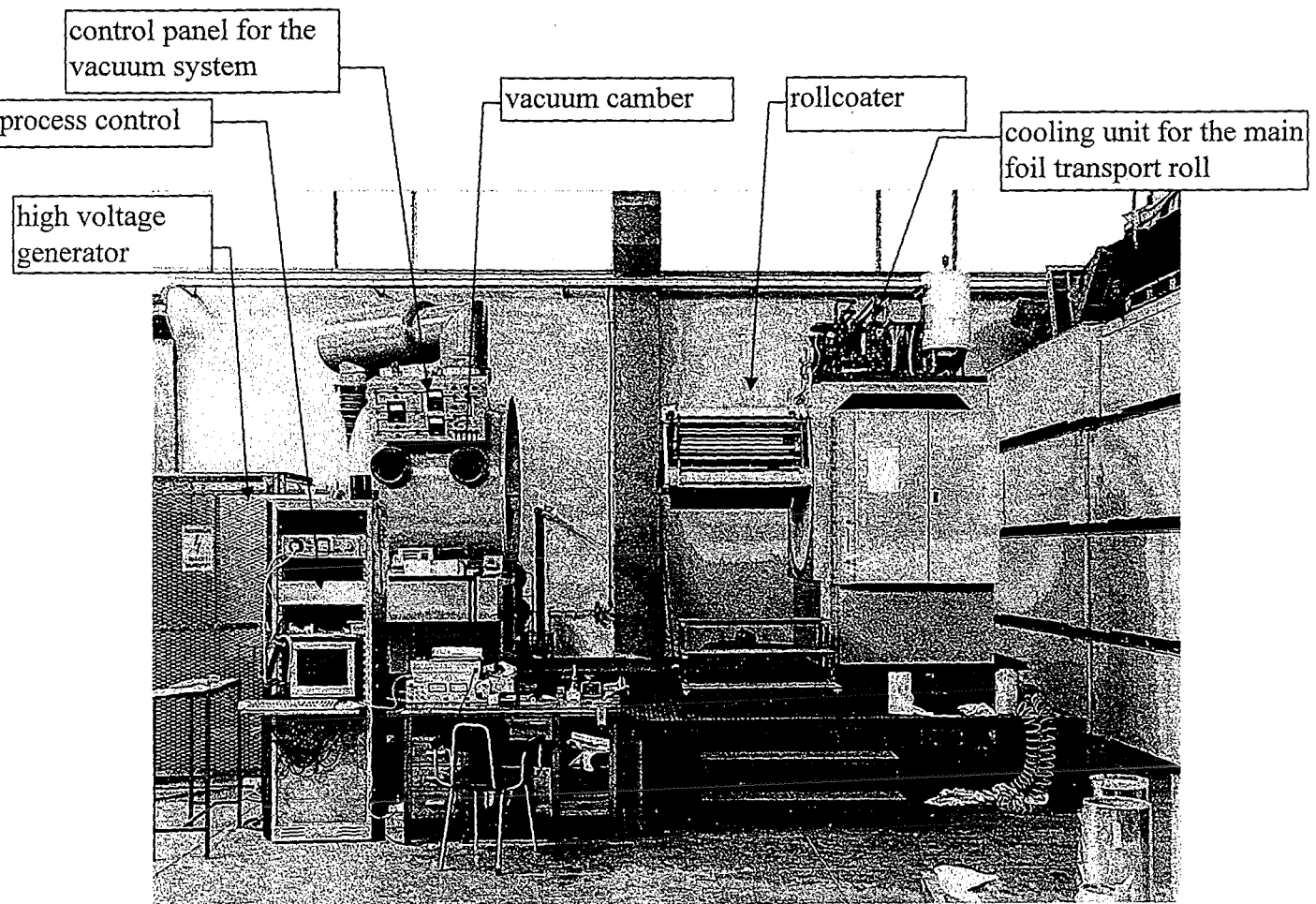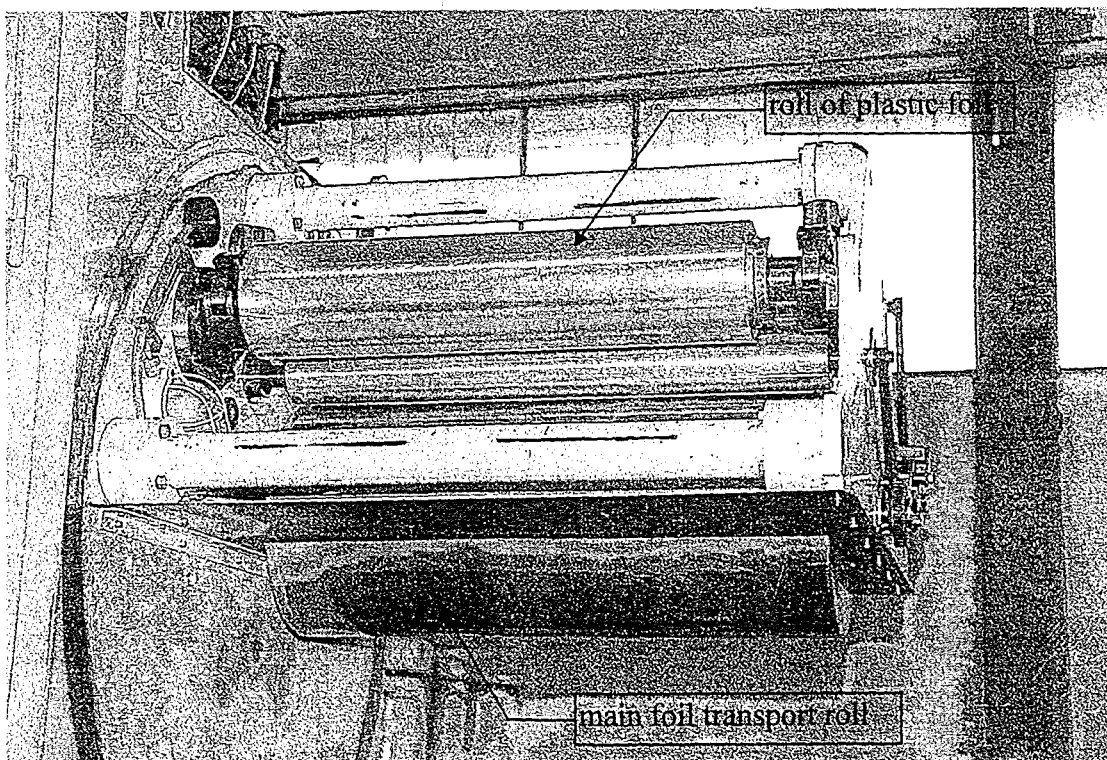
Fig. 1: evaporation plant KARLA

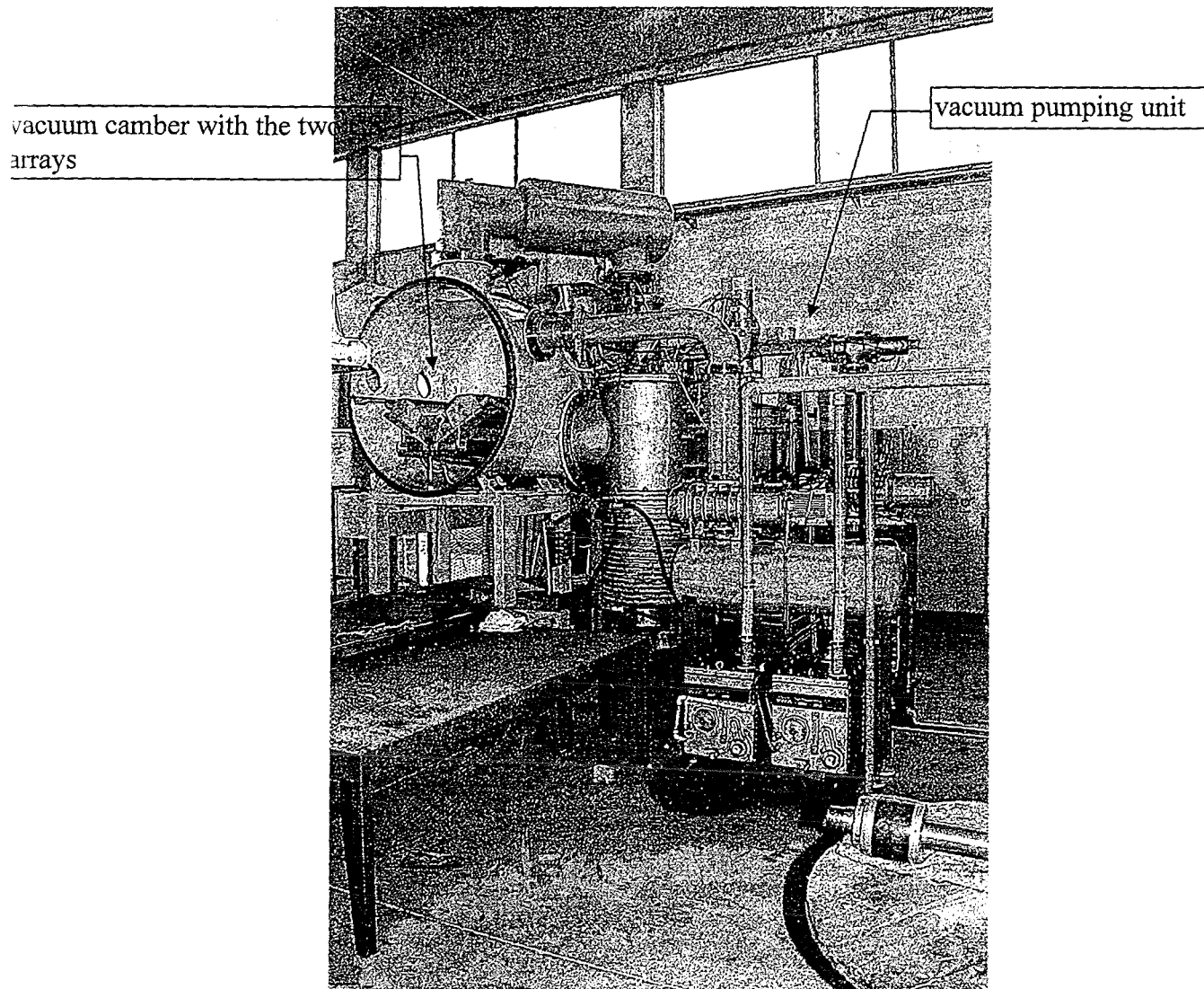Fig. 2: Close up of the rollcoater

vacuum camber with the two arrays

vacuum pumping unit

Fig. 3: Vacuum chamber with the evaporation unit (two channel spark arrays for the glass evaporation)

Results

All measurements on the permeation of oxygen were made in the laboratory of our industrial partner with an industrial standard unit (ASTM D 1434). The time dependent effect of coated foils described in [1] could not be confirmed by these measurements. It is suggested that this effect was produced by the previously used measurement system: During the measurement with different pressures on both sides of the test foil a continuous flow of air and dust through the foil was produced. Thereby the surface was coated with different materials and the foil behaved like a filter. The reason for the apparently observed time dependent effect was an increased stopping of the „filter". This method had therefore to be discharged.

One of the important prerequisites to get high-quality glass coated foils was the right choice of the glass type. Due to delivery problems from industry only two types of different glasses could be tested: DURAN-Glass (borosilicate glass) and AR-Glass (lime-soda glass). The main differences between these types of glasses are their viscosity's: they had the same viscosity of 10^4 dPa s at different temperatures: DURAN-Glass at 1270°C and AR-Glass at 1040°C (source: SCHOTT- technical glasses).

Coated foils with DURAN-Glass showed only a marginal effect on the reduction of permeation (up to a factor of 4). By coating foils under the same conditions with AR-Glass, the permeation of oxygen was reduced up to a factor of 40. It seems that the viscosity is a main criterion for the choice of glasses for this application. To verify this assumption it is necessary to test further glass types of different viscosity's in a laboratory facility.

Another criterion of the coating quality is the choice of an adequate substrate foil (with regard to microstructure, surface roughness). For industrial applications the coating of polyethylene- (PE) and polypropylene- (PP) foils are most important because both foils can be welded. Because of their better mechanical characteristics and lower oxygen permeation polyester- (PET) foils were used too. A disadvantage is that the PET-foils cannot be welded together, for the use in flexible packaging they must be combined with PE- or PP- foils. Several foils used by the industrial partner for aluminum coating were also tested in the KARLA plant. Fig. 4 shows the SEM - photograph of the surface of a 12μm PET-foil coated with glass. The surface of the PET-foil is quite smooth (even with an enlargement of 100.000 it is not possible to see any surface structure). This surface smoothness becomes also apparent on the back of the glass layer (for the photograph the glass layer was broken in a bath of liquid nitrogen). The permeation of oxygen could be reduced by a factor of 40 (permeation of oxygen of a 12μm PET-foil: without glass layer: 108 cm³/m²24h 25°C, with glass layer: <3 m³/m²24h 25°C). Fig. 5 shows the SEM- photograph of the surface of a PE-foil coated with glass. Compared to the PET-foil surface it is quite rough. Also the back of the glass layer shows this roughness. This sample (it was coated under the same conditions as the PET-foil) exhibits a reduction of oxygen permeation only by a factor of 8.
This indicates that the roughness of the foil surface is another important criterion influencing the quality of the glass coatings. Further tests with other types of foils need to be done to get more information in this area.

surface of the foil

downside of the glass layer

LEM-KA 10KV X30.000 15mm
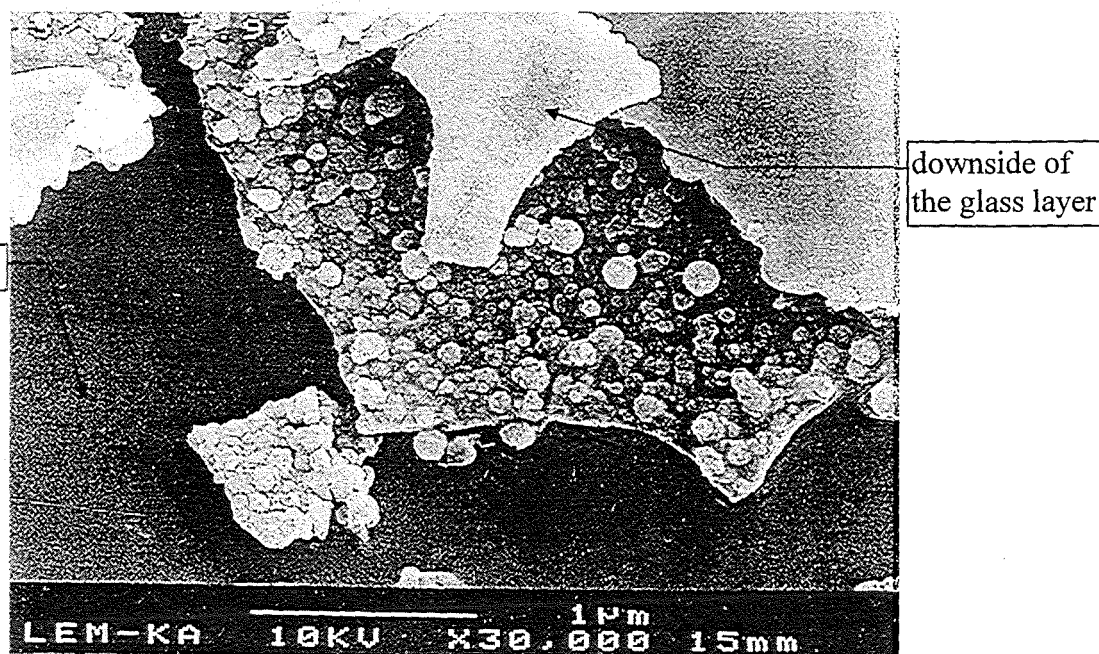
Fig. 4: SEM-photograph of the surface of a AR-Glass coated PET-foil

surface of the foil

downside of
the glass layer
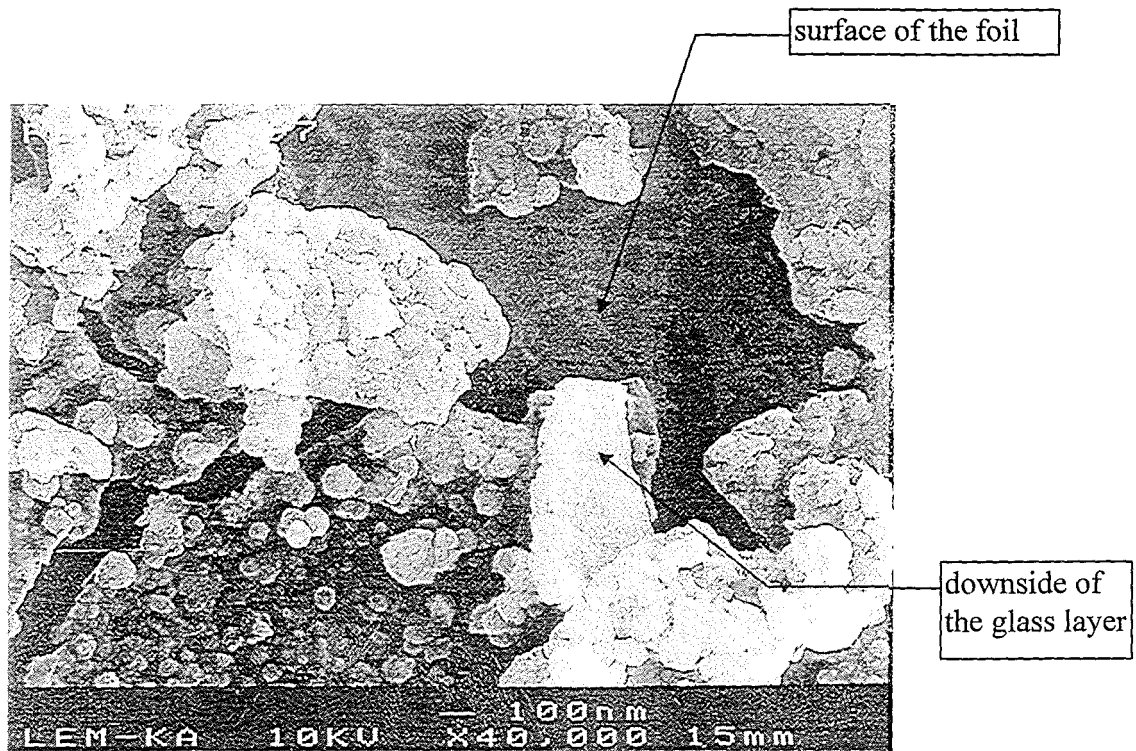
Fig. 5: SEM-photograph of the surface of a AR-Glass coated PE-foil

Problems with the channel spark (CS-) systems

The first tests of the CS-systems under industrial conditions were done at the KALRA-plant in
Italy. Fig. 6 shows a schematic of the CS-system (with surface discharge trigger) used in the
KARLA-plant. Several effects limited our efficiency and the life time of the system
components. Due to the electronbeam-wall interaction the dielectric tube was heated up to
1200°C and it was not possible to use the system at repetition rates above 80 Hz. The electron
beam deposits most of its energy inside the tube, ablating tube material. After two hours under
coating conditions (80Hz) the tubes were destroyed. In this case the ablation took place at the
inner side of the tube and not at the target. Therefore a reproducible ablation at the target and
a reproducible deposition of glass on plastic foils were impossible. Because of the back of
reproducibility and the very low foil transport speed (several mm/s) in comparison to an
aluminum evaporation plant (several m/s) the CS-systems, at this state of the development,
are not yet qualified for this industrial application.
To reduce the effect of energy loss in the dielectric tubes, tubes with a larger diameter were
tested in the laboratory at FZK [2]. The electronbeam-wall interaction was much smaller, so
most of the energy was deposited in the target. Results: With this new dielectric tube the
quantity of ablated glass was 4 times higher, the reproducibility of the ablation was higher and
the life time of the dielectric tubes was improved by more than 20 times [2]. Up to now these
results have only been tested in a one channel laboratory unit and not under industrial coating
conditions.

171
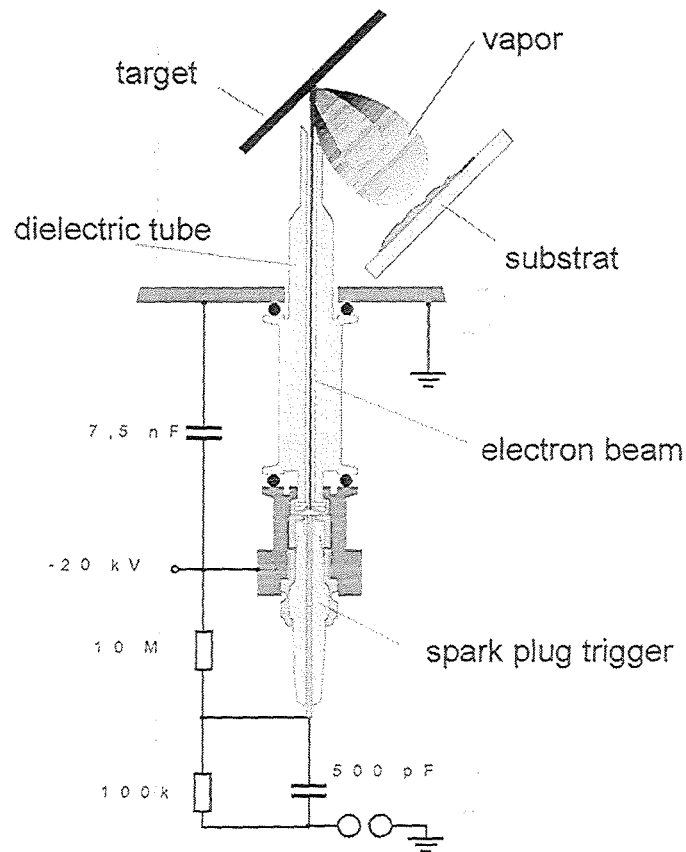
Fig. 6: Schematic of one CS-system used at the KARLA plant

Outlook

The main hindrance in the use of the ELBA technology in industrial applications is the insufficient lifetime of the system components (under working conditions with a frequency of 80 Hz it is presently only 6 hours). New ELBA systems with higher efficiency and reliability are under development [2].

References:

[1] M. Konijnenberg, G. Krafft, G. Schmitt, C. Schultheiß, M. Söhner: „ELBA Deposition of Glass Layers on Hydrocarbon Foils" Wissenschaftliche Berichte Nov. 1996 FZKA 5840 ISSN 0947-8620

[2] W. Frey, M. Söhner, C. Schultheiß: „New Trigger Devices for Channelspark Systems" this report

New Trigger Devices For Channelspark Systems

W. Frey, M. Söhner, Ch. Schultheiß

Forschungszentrum Karlsruhe, Institut für Neutronenphysik und Reaktortechnik
P. O. Box 3640, D-76021 Karlsruhe, Germany

Abstract

The ablation efficiency of a channelspark system is mainly influenced by its trigger plasma source. Compared to the application of a surface-discharge trigger plasma source a channelspark system triggered by a Penning-discharge exhibits high rates of ablated bulk material per shot, a high reproducibility and lifetime.

Introduction

Air filled channelspark (CS) systems are high efficiency and low cost electron beam sources used for thin film production by means of pulsed electron beam ablation. An electron beam (15 keV, 10^5 A·cm^{-2}, pulse duration: 100 ··· 200 ns) is directed onto a target, consisting of the desired film material. The beam penetrates a few micrometers into the target material, ablating bulk material, which finally deposits on the substrate, e.g. a 12 µm PET foil [1].
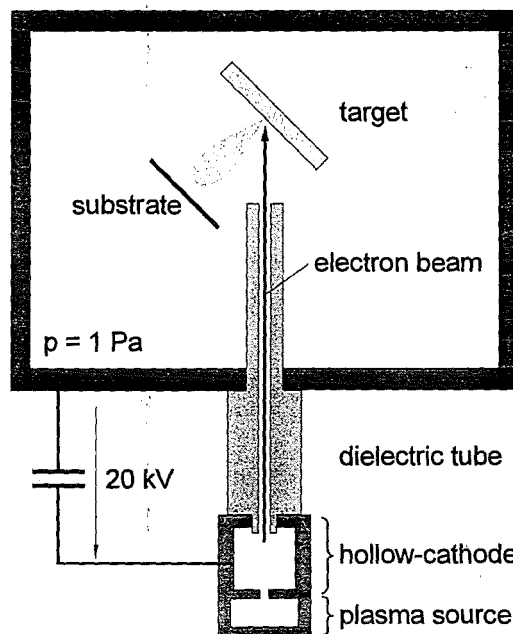
Figure 1: Components of a channelspark system for thin film production.

The merits of this method of thin film production are its simplicity, the low heat stress for substate materials, low costs and the conservation of stoichiometry. Contrary to UV-laser ablation, the pulsed electron beam ablation is not restricted to non-transparent materials.

The electron beam is generated by injecting a plasma into the hollow cathode. While the trigger source delivers plasma to the hollow cathode, the electrons escape through the dielectric channel and are accellerated towards the target. The electron beam propagates confined by its own magnetic field (z-pinch). The beam current density is about 10^5 $A \cdot cm^{-2}$. Thus, the neutral gas density at a working pressure of 1 Pa is sufficient to achieve space charge neutralisation [2].

Surface-Discharge Trigger Plasma Source

For the industrial prototype plant KARLA [1] a plasma source based on a surface discharge was used, Fig. 2. To ignite the electron beam the energy storage capacitor C_E = 7.5 nF is charged. When the charging voltage amounts to U_0 = 19.5 kV the spark gap closes. This causes a voltage drop along the ceramic tube located between the electrodes of a conventional spark plug, Fig. 2, resulting in a discharge along the ceramic surface, generating the plasma for electron beam ignition. After beam generation the current rises up to 1.5 kA discharging the storage capacity C_E.
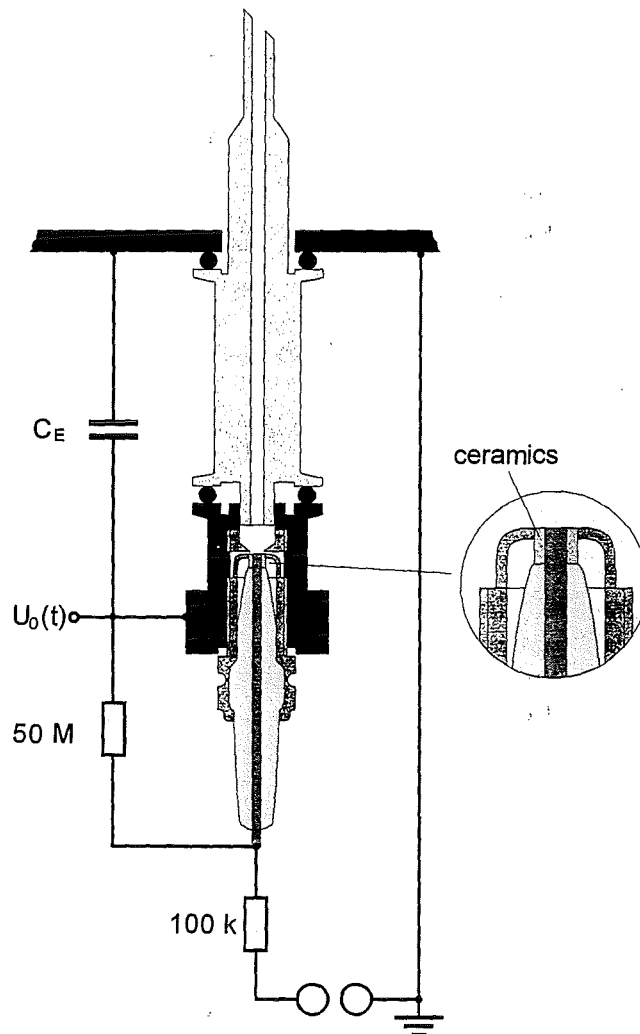
Figure 2: Channelspark system with surface-discharge trigger plasma source.

The plasma produced by the surface discharge mainly consists of ceramic material. Due to the erosive nature of this process of plasma generation, the lifetime of the

plasma source is limited to a maximum of $1.5 \cdot 10^7$ shot. The trigger lifetime is sufficient for a 46 hour continuous operation at a repetition frequency of 60 Hz. The trigger plasma source is cheap and easy to replace.

Penning-Discharge Trigger Plasma Source

In order to increase lifetime and to improve ablation performance a new trigger plasma source based on a non-erosive process was developed. A reflex discharge, also known as penning-discharge, is used for trigger plasma generation. The source consists of the anode cylinder two cathodes and a Helmholtz coil to provide a magnetic field directed parallel to the electron beam axis, Fig. 3.

For trigger plasma generation and subsequent electron beam ignition the energy storage capacity C_E and the auxillary capacity C_A are charged to $U_0 = 19.5$ kV providing positive potential at the anode cylinder and negative potential at the cathodes.
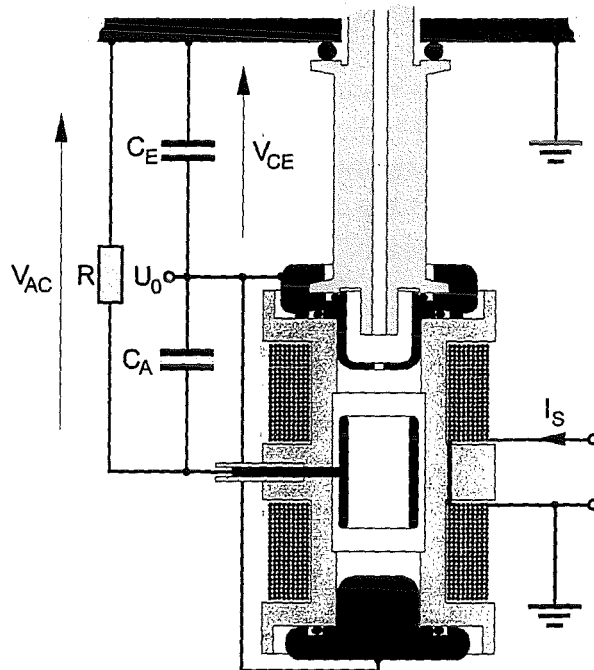
Figure 3: Channelspark system with Penning trigger plasma source.

The trigger plasma generation is started by by the application of a pulsed magnetic field to the Penning tube. The pulse duration is 240 µs, Fig. 4. The magnetic field amplitude amounts to B = 0.2 T.

Due to the axial magnetic field seed electrons are forced to move azimuthally. They are confined in the penning discharge tube and multiplied by electron impact ionisation. Ions colliding with the cathodes's surfaces further produce electrons and increase the plasma density. At a pressure of p = 1 Pa the mean free path length of electrons for impact ionisation is aproximately 4 cm. Due to the dimensions of the

Penning tube (diameter: 20 mm, length: 44 mm) charge carrier multiplication by impact ionisation without magnetic field is not possible.
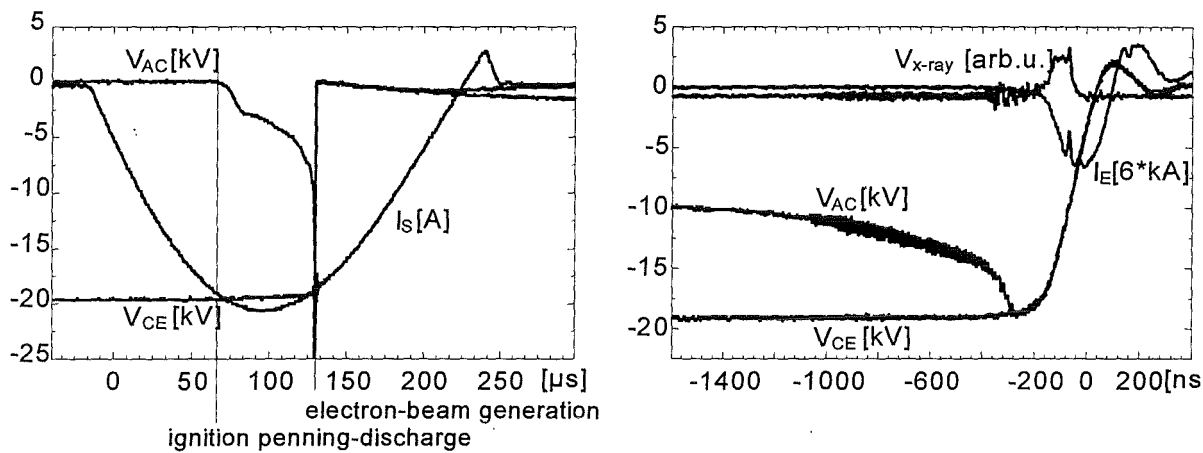
Figure 4: Ignition of the penning-discharge and generation of the electron beam during the transient magnetic field pulse. The diagramm at right shows the electron beam generation with a higher time resolution.

Due to the increasing conductivity of the penning discharge plasma, the potential at the anode cylinder V_{AC} approaches the hollow cathode potential V_{CE} within 45 µs, Fig. 4. At a sufficient high density, provided by discharging the auxillary capacity, the plasma passes through the bore hole in the upper cathode into the hollow cathode volume and finally ignites the electron beam. The beam duration is 160 ns indicated by Bremsstrahlung mesurements, Fig. 4. The current through the dielectric tube amounts to 1,2 kA.

Results

In order to quantify the ablation efficiency of the channelspark system applying different trigger plasma sources, ablation tests with float glass targets (AR-glass) were done. Depending on the distance a from the end of the dielectric tube to the target the average values of ablated material vary from 1.5 µg per shot to less than 0.25 µg per shot when the surface discharge trigger and an inner tube diameter of 3 mm are used, Fig. 5, left. Applying the surface discharge trigger the reduction of ablation efficiency with increasing tube to target distance a is suspected to be caused by a insufficient space charge neutralisation of the electron beam outside the dielectric tube. Thus, the electron beam diverges, resulting in a lower current density on the target surface.

For both inner tube diameters the CS system with penning trigger plasma source exihibits larger ablation values and an improved beam transmission. The plasma generation in the penning tube starts several 10 µs before electron beam ignition. Compared to the delaytime of the CS system with surface discharge trigger of about $T_D = 1$ µs, the time for plasma expansion into the dielectric tube is 50 times longer, causing a higher partial gas and plasma densitiy in the dielectric tube which results in a better space charge neutralisation of the electron beam.

Especially at larger tube to target distances a, the rate of ablated mass increases if the inner tube diameter is choosen to be 5 mm. Tube erosion patterns observed with tubes having an inner diameter of 3 mm clearly indicate a loss of beam energy by beam/wall interactions resulting in lower rates of ablated material. The lifetime of a 3 mm channel is about 10^6 shot. A 5 mm channel still works after $30 \cdot 10^6$ shot.
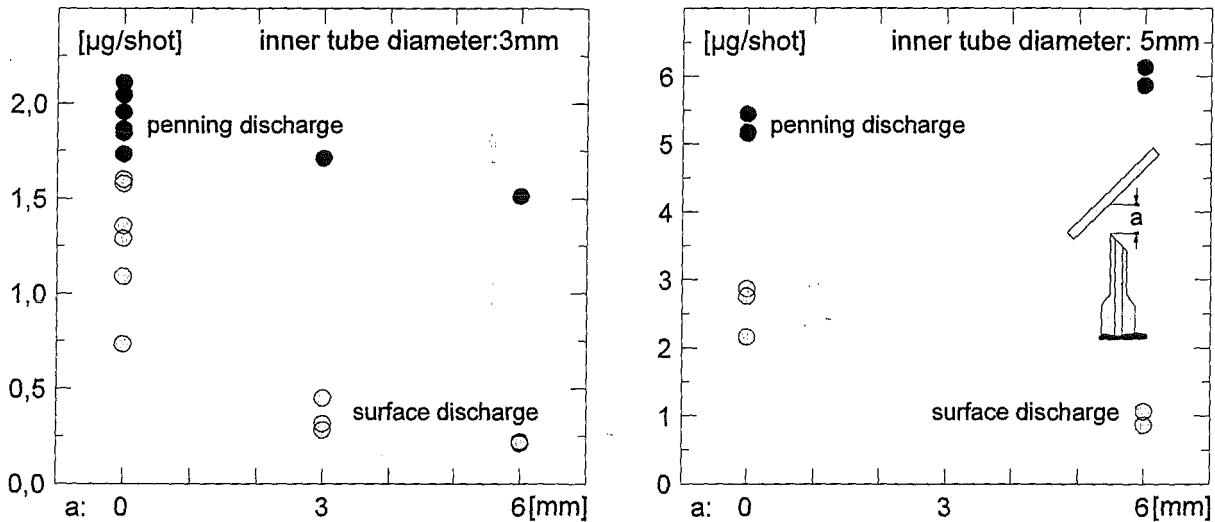

Figure 5: Rates of ablated bulk material per shot from float glass targets depending on the distance a from the end of the dielectric tube to the target, the inner tube diameter and the trigger plasma source.

The CS system with penning discharge trigger further exhibits a better reproducibility of ablated bulk material proved by the low scattering of successive ablation rate measurements at a = 0 mm, Fig. 5, left. Up to now the system has run at a repetition frequency of 60 Hz for $30 \cdot 10^6$ shot without failure. The developed system promises to be a high-efficiency and long-lifetime electron beam source for industrial applications.

[1]   Söhner, M.: Deposition of thin glass layers on plastic foils,
       Annual Report 1996/97, INR, Forschungszentrum Karlsruhe GmbH, 1998.

[2]   Mattacotta, F.C.; Ottaviani, G.: Science and Technology of Thin Films,
       World Scientific Publishing Co., Singapore, 1995, p.: 89-119.

A 2 dim modelling of magnetized plasma target interaction and quantification of erosion of the ITER tokamak slot divertor[*]

H. Würz[1], S. Pestchanyi[2], F. Kappler[1]

1. Forschungszentrum Karlsruhe,INR, Postfach 3640, D-76021 Karlsruhe, Germany

2. Troitsk Institute for Innovation and Fusion Research, 142092 Troitsk, Russia

Abstract

As is well known a plasma shield from vaporized target material formed in front of the divertor during plasma disruptions reduces the target heat load because it converts the energy of the hot plasma into hydrodynamic motion, ionization and radiation of the plasma shield. However the plasma shield doesn't reduce the melt layer thickness of metallic targets. A realistic quantification of erosion by vaporization of the ITER slot divertor needs a 2 dim analysis because of the finite width of the disruptive hot SOL plasma, the asymmetrical distribution of power density across the SOL plasma, because of the tilting of the target in the ploidal plane and the subsequent 2 dim MHD motion of the plasma shield and because of quantification of possible damages of the divertor wings by radiation emitted from the intensely radiating plasma shield in front of the in- and outboard targets. Therefore the 2 dim radiation magnetohydrodynamics (R-MHD) code FOREV-2 was developed. In this paper results of a 2 dim analysis of MHD motion of carbon plasma shields and of erosion of the ITER slot divertor made from graphite and tungsten are presented for horizontal (target perpendicular to the poloidal magnetic field) and vertical (target inclined to it) graphite targets.

1. Introduction

During not normal operation of a tokamak the divertor plates can be hit by the rather hot central tokamak plasma. For ITER the power density of the impacting hot plasma can achieve values up to 100 MW/cm^2 along the inclined magnetic field lines [1]. If the target remains unshielded such power densities result in large target erosion by vaporization. A plasma shield formed in front of the target from vaporized material reduces the target heat load because it converts the energy of the hot plasma into hydrodynamic motion, ionization and into radiation of the plasma shield. Thus wall erosion quite sensitively depends on the shielding efficiency of the plasma shield

---

which in turn depends on the physical properties and the long term stability of the plasma shield.

Recently the physical properties of essentially one-dimensional non-LTE carbon plasma shields formed in disruption simulation experiments were studied experimentally and theoretically [2]. The calculated plasma shield parameters such as time dpendent plasma temperature and electron density distributions, conversion efficiency of deposited energy into radiation in the plasma shield, total and soft x-ray (SXR) radiation leakage fluxes from and energy balance in the plasma shield were in quite good agreement with the experimental values [3, 4] thus demonstrating that a realistic modelling of ITER disruptive plasma wall interactions at power density levels of MW/cm^2 is possible.

In this report the R-MHD code FOREV-2 for a 2 dim modelling of magnetized hot plasma wall interaction, and its validation are described and results of a 2 dim analysis of MHD motion and erosion of the ITER slot divertor are presented for power densities of the impacting hot plasma in the range 3 to 100 MW/cm^2.

2. The simplified ITER slot divertor

The outboard wing of the slot divertor is shown schematically in Fig. 1a in the poloidal plane. The distance from the x point to the dump plate is about 2.0 m. The upper part of the side walls and the dump plate (vertical target) are inclined. The coordinate system used in the 2 dim plasma target calculations is also indicated. The x coordinate is parallel to the separatrix, the y coordinate is across the SOL and the z coordinate is the toroidal direction. The asymmetrical (realistic) power density profile of the impacting hot plasma across the scrape off layer (SOL) is indicated in Fig. 1b. At the vertical target the separatrix strike point (SSP) always is downstream. During disruptions and ELMs a shift of the separatrix can't be excluded [5]. Therefore the smaller dump plate and the tungsten dome could be hit during such an event too. In this case the following two different situations might arise: horizontal target and separatrix upstream. Figure 1b shows the geometry as used in the 2 dim calculations with FOREV-2. For the vertical target the target inclination angle is assumed to be 20°. In x direction the computational region extended up to 2.5 m. The unperturbed magnetic field lines $\vec{B}_0$ are assumed to have components in x- and z-direction according to $\vec{B}_0$ = (B_x, B_y, B_z) = (0.5 T, 0, 5 T). Thus the impact angle of the hot SOL plasma in toroidal direction is 5°. The disruptive hot SOL plasma is assumed to consist from 10 keV ions and 10 keV Maxwellian electrons with equal energy carried by ions and electrons. FOREV-2 calculations were performed for realistic power density profiles across the SOL. The half width was 4 cm. Peak power densities along the magnetic field lines ranging from 3 MW/cm^2 up to 100 MW/cm^2 were used up to now. (All power density values given are along the field lines.) In this 2 dim analysis of the ITER slot divertor only graphite targets (horizontal and vertical) were considered. For vertical targets the cases separatrix up- and downstream (this always is with reference to the x-point) were modelled. Calculations were performed for the two slot widths 20 and 60 cm.
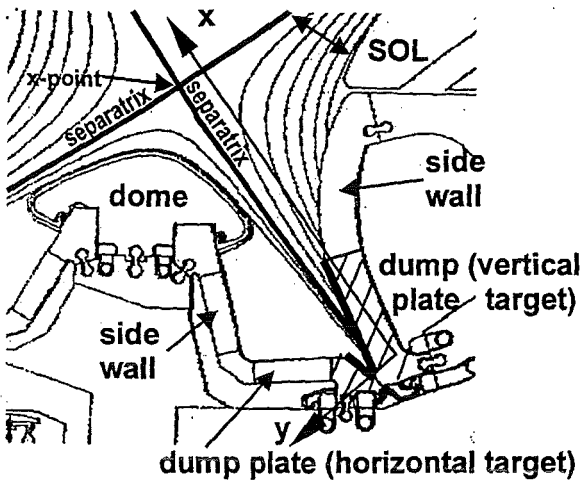
Fig.1a. Poloidal cross section of the outboard wing of the ITER slot divertor and coordinate system for the 2dim calculation.
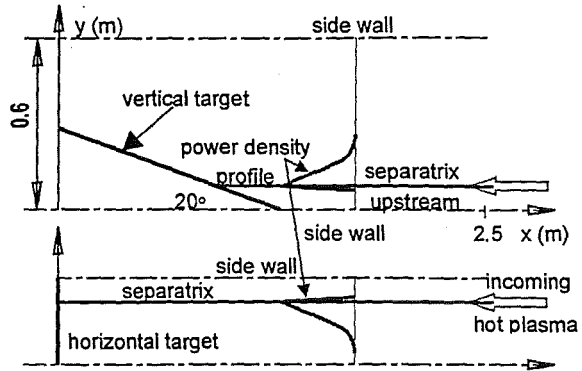
Fig.1b. Simplified geometry for 2 dim calculation for the slot divertor with vertical and horizontal target (dump plate) in poloidal plane. Incoming hot plasma along magnetic field lines $\vec{B}_0 = (B_x, B_y, B_z) = (0.5T, 0, 5T)$.
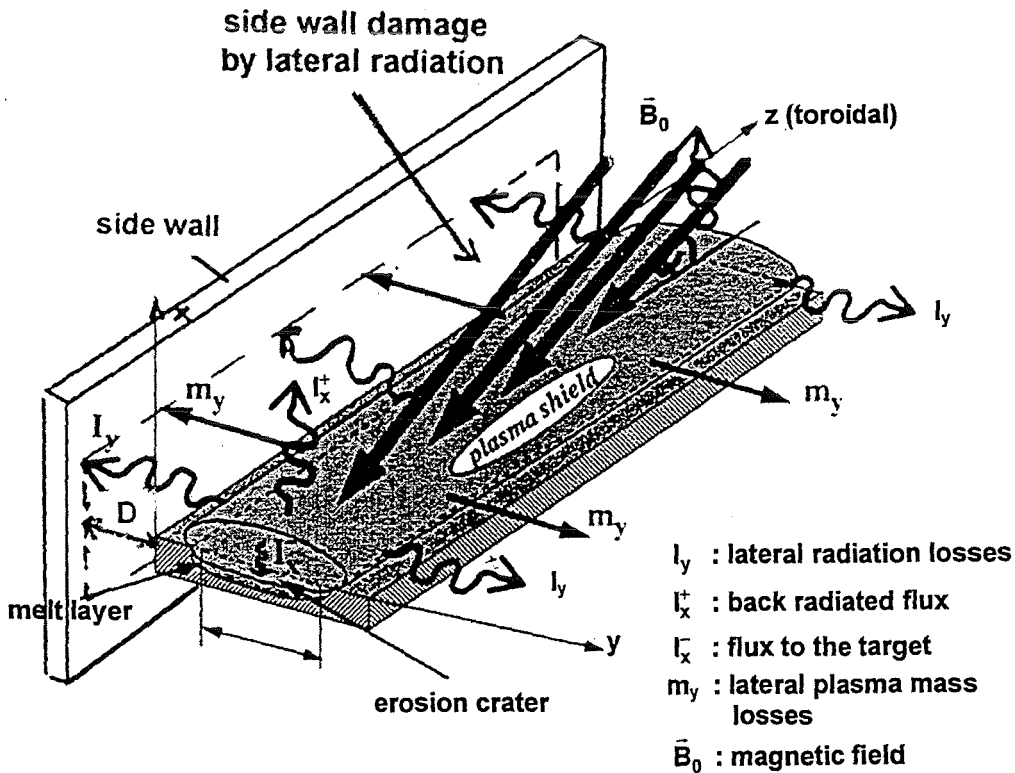
I_y : lateral radiation losses
I_x^+ : back radiated flux
I_x^- : flux to the target
m_y : lateral plasma mass losses
$\vec{B}_0$: magnetic field

Fig.1c. Horizontal divertor target with side wall and plasma shield schematically

181

Fig. 1c shows a horizontal target together with the evolving plasma shield, the inclined guiding magnetic field lines and because of the limited width D_{SOL} of the impacting plasma lateral radiation fluxes which hit the side walls and may cause damage there. Moreover MHD motion of cold target plasma across magnetic field lines may result in plasma mass losses (indicated as m_y in Fig. 1c) which could decrease the shielding efficiency of the plasma shield at the SSP.

3. The 2 dim R-MHD code FOREV-2

FOREV-2 allows a 2 dim modelling of the hot plasma target interaction in presence of an external magnetic field $\overline{B}$. FOREV-2 uses a 2½ dim MHD model which takes into account all 3 components of $\overline{B} = (B_x, B_y, B_z)$ but uses the fact that the main component B_z is constant along z (toroidal direction). The system of equations which has to be solved consists of the 5 balance equations (mass, energy and 3 components of momentum), 3 magnetic field diffusion equations and the 2 dim radiation transport equation. The equations and their solution are described in [6]. Therefore here only some general remarks will be given.

The method of "Large Particles" is used [7] for solution of the system of equations In this method the calculation for a full time step is splitted into several substeps following each other. The substeps are defined according to the different physical processes used to describe the whole problem, such as MHD motion of target plasma, magnetic field diffusion, radiation transport, heating and momentum transfer from the incoming hot plasma, heat conductivity inside the solid target. FOREV-2 uses an Eulerian mesh.

3.1 The splitting procedure for the MHD movement

— Eulerian mesh
--- shifted and expanded mesh
—▶ boundary velocity
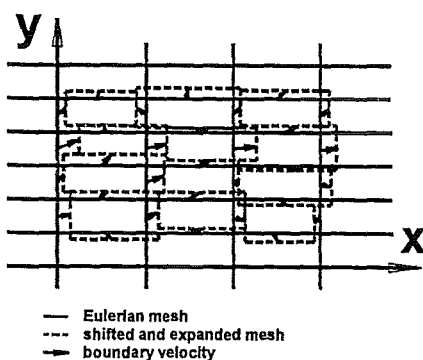
Fig.2. Mesh transformation in each time step according to the mesh boundary velocities schematically.

The calculation of the 2½ dim MHD movement of target plasma is splitted into two substeps, a Lagrangian and an Eulerian one. The first substep is Lagrangian. It is followed by the Eulerian substep. In the Lagrangian substep of the splitting procedure mesh boundary velocities are calculated using the subsystem of equations with force terms only. In the next substep the mesh boundary velocities then are used to perform a transformation of the expanded mesh back to the Eulerian as is schematically indicated in Fig. 2. The system of equations remaining from the first substep contains convective terms. It is automatically solved by this redistribution of all physical quantities from the expanded mesh back to the Eulerian mesh

3.2   2 dim radiation transport

Originally in FOREV-2 a 2 dim forward reverse method (MFR) based on the assumption of isotropy of the radiation flux was used for calculation of the 2 dim radiation fluxes. However from comparisons with results from 2 dim S_N calculations [8] it became evident that the radiation flux in the plasma shield is angular dependent. Moreover for side wall erosion angular dependent leakage radiation fluxes have to be calculated. The 2 dim S_N method though principally most suited can't be used because of excessive computational times and because of intrinsic difficulties in exact calculation of the divergence of the radiation flux in the mesh center. Such an inaccuracy could result in overheating of low dense plasma regions and this reduces drastically the size of the time steps of the MHD calculation.

To circumvent these problems and to account for the anisotropy of the radiation flux an improved forward reverse method (IFRM) was developed adopting and generalizing a method developed for 1 dim radiation transport [9]. This method uses averaged cosines of the radiation fluxes outgoing from the mesh as obtained from 2 dim S_N calculations. For each mesh boundary the ratio of the radiation fluxes obtained from the 2 dim S_N method and from the IFRM method is determined. A mean factor $\overline{\eta} = F_{out}(S_N)/F_{out}(IFRM)$ averaged over all η values of the meshes is calculated and applied for correction of the IFRM fluxes. As angular integrated quantities are changing much more slowly 2 dim S_N updating of average cosines and renormalization is sufficient once per 500 time steps. Once per 20 time steps new IFRM radiation fluxes are calculated.

The term quartz plasma is used below. The plasma actually consists of silizium and oxygen ions. 40 group Rosseland opacities for quartz were used for the radiation transport calculations. The opacities were obtained from CRE optical data calculated by use of the code TOPATOM [10]. Frequency group optimized 24 group Rosseland and 69 group Planck opacities were used for carbon. The CRE optical data of carbon too were calculated with TOPATOM.

4.   Validation of FOREV-2 using results from simulation experiments

At TRINITI Troitsk magnetized plasma target experiments were performed at the plasma gun facilities 2MK-200 CUSP [11] and MK-200 CUSP [12]. The plasma β value was below 0.3, the plasma ion temperature was around 500 eV, the Maxwellian distributed electrons had temperatures of around 300 eV. Experiments were performed with perpendicular targets. In this case the magnetic field lines are perpendicular to the target, thus simulating a horizontal target in the poloidal plane but neglecting the toroidal component of the magnetic field. In the calculations the power density profile of the impacting magnetized plasma was assumed to be Gaußian with full width at half maximum (FWHW) of 0.8 cm and its time evolution to have a half width of 10 µs. Peak power density is reached after 3 µs, remains constant for 5 µs and then decays exponentially. The target size in y direction was 3 cm. The full width of the calculational region was 5 cm. Side walls were assumed to be fully transparent. Calculated and measured electron temperature profiles along the separatrix (in x direction) at 10 µs are shown in Fig. 3 for an energy density of the

magnetized plasma of 200 J/cm². At a distance of 1 cm from the target the temperature is up to 50 eV whereas in the tokamak plasma shield it is only 1 eV. Due to this steep temperature gradient close to the target electron heat conduction
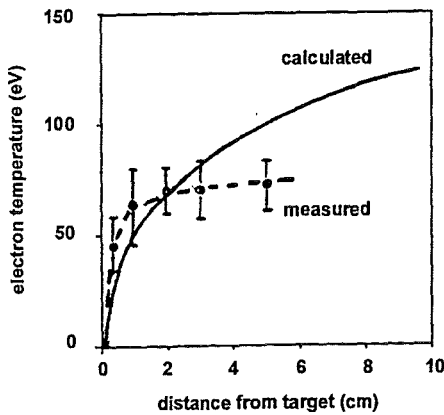

Fig.3. Comparison of measured and calculated electron temperature profiles in a carbon plasma shield. Peak power density is 18 MW/cm².

becomes the dominating target heat source in these simulation experiments. Direct energy deposition of the magnetized plasma to the target is negligible, because of the low impact energy the magnetized plasma after 0.8 μs is fully stopped in the evolving plasma shield.

Calculated and measured electron density profiles in a carbon plasma shield at different distances from a graphite target and for different times are shown in Figs. 4 for a peak power density of the magnetized plasma of 42 MW/cm². The calculated profiles and density values are in rather good agreement with the measured values. Lateral plasma jets
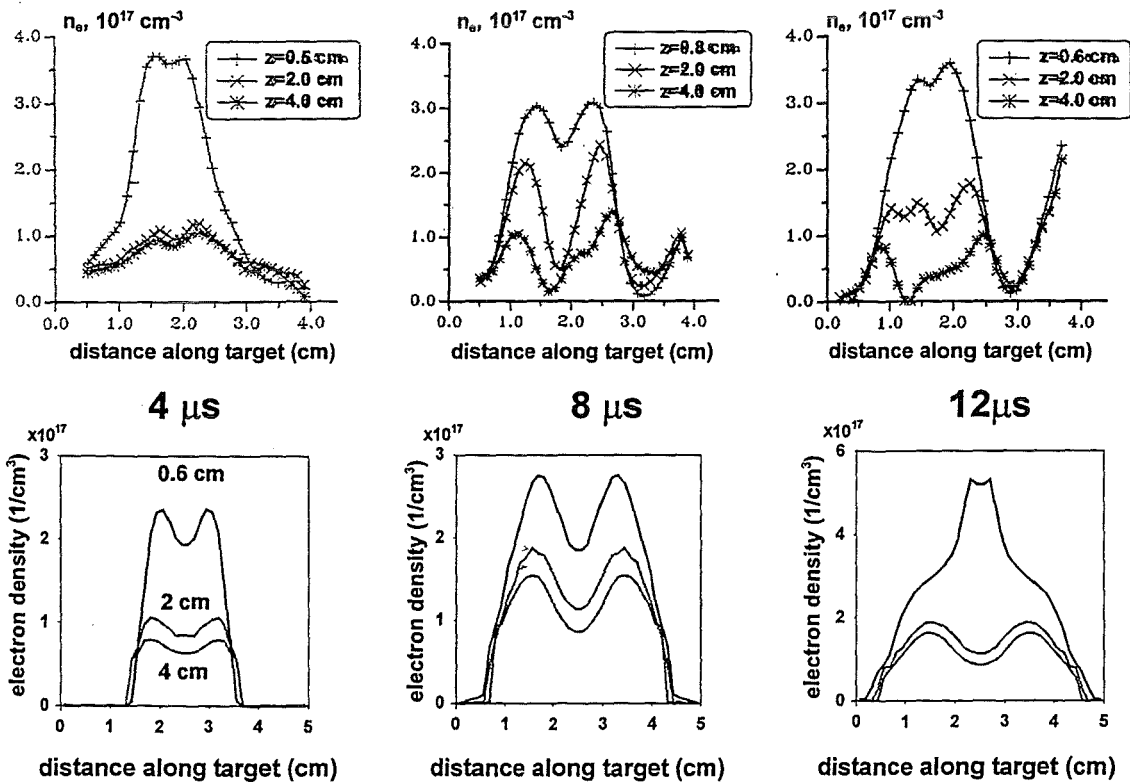
Fig.4. Comparison of measured (above) and calculated (below) electron density in a carbon plasma shield at different times and distances from target. For the calculation a Gaussian power density profile with peak power density of 42 MW/cm² was used.

are observed at larger distances. The reason for the lateral jets is momentum transfer from the hot plasma ions. Lateral jets are not occurring at peak power densities of 20 MW/cm². Calculated 2 dim electron density contours and the plasma flow $\Gamma = nv$ (arrows)are shown in Fig. 5 in a carbon plasma shield at two different times for a peak power density of the magnetized plasma of 20 MW/cm². The carbon density range for the contour plot is 1.4 x 10^{16} up to 10^{17} cm^{-3}. The density decreases with increasing distance from the target. In the region closer to the target where the plasma flow is indicated the carbon density increases up to 5 x 10^{18} cm^{-3}. At early times (t ≤ 14 μs) the plasma flows across the magnetic field lines to the separatrix (inward flow) and then along the separatrix upstream. The thickness of the layer in which this inward flow occurs is about 1.5 mm. The reason for the inward flow is pushing away of the guiding magnetic field component B_x from the region

Fig.5. Contour plot of plasma density and plasma flow (Γ=nv, arrows) in a carbon plasma shield. Perpendicular graphite target, Gaussian power density profile with peak value of 20 MW/cm².

of maximum power density (separatrix) to the sides resulting in depletion of B_x in the center as seen from Fig. 6. Due to its high electric conductivity the magnetic field lines are frozen in at the graphite target. Thus the magnetic field lines are bent near the target. Then a y component of magnetic field arises as shown in Fig. 7 for lateral (y direction) positions below the separatrix. Above the separatrix B_y changes its direction.

According to the y component of the motion equation (see [6]) which writes as

$$\frac{\partial \rho u_y}{\partial t} + \vec{\nabla} \rho u_y \, \vec{u} + \frac{\partial}{\partial y}\left(P + \frac{B^2}{2\mu_0}\right) = \frac{1}{\mu_0}\left(\vec{B}\vec{\nabla}\right)B_y$$

the x and y dependence of B_y causes plasma movement to the center according to

$$\frac{\partial \rho u_y}{\partial t} \approx \frac{1}{\mu_0}\left(\vec{B}\vec{\nabla}\right)B_y$$
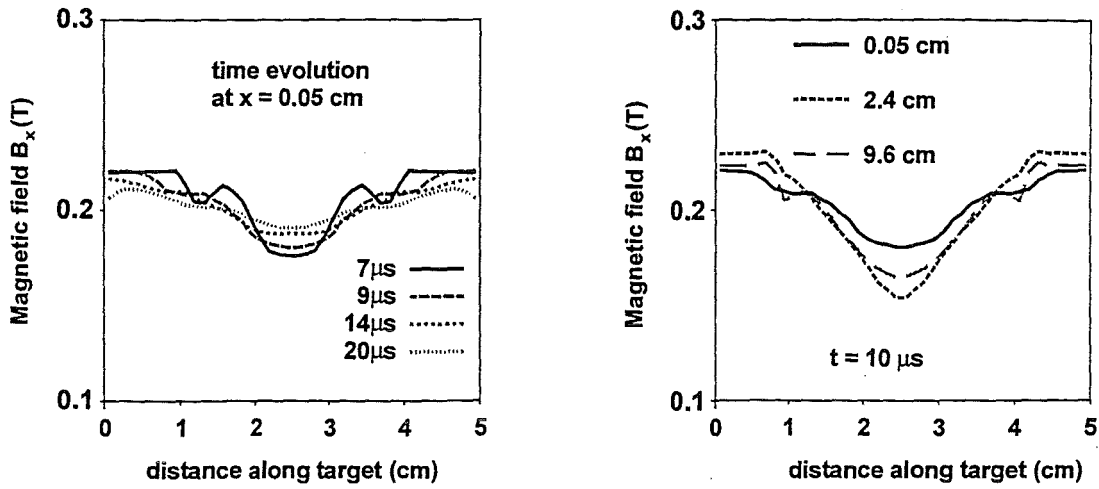
Fig.6. Time and space dependent change of B_x by the evolving plasma shield for different distances from the target.

Later in time ($t \geq 20$ µs) B_x diffuses back into the cold dense part of the plasma shield and B_y disappears as is seen from Fig. 7. Momentum transfer by the hot ions continues. As a consequence the plasma flow close to the target changes its direction and flows outward as shown in Fig. 5 at t = 20 µs. Profiles of carbon density and plasma temperature along the separatrix are shown in Fig. 8 for the time moments 14 µs and 20 µs. At 14 µs the dense plasma extends over
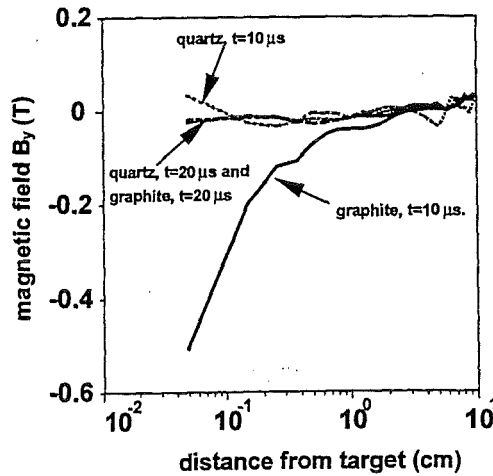
Fig.7. B_y component of magnetic field below the separatrix in carbon and quartz plasma shield at two different times.
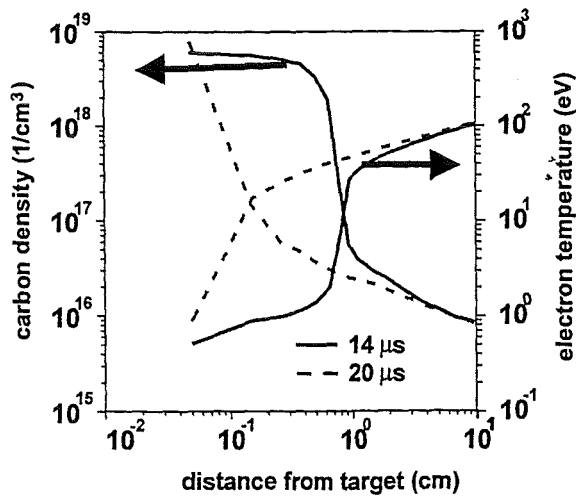
Fig.8. Plasma density and electron temperature profile in a carbon plasma shield along the separatrix.

a layer of thickness of 7 mm, at 20 µs only over 1 mm. Due to the reduced plasma mass at 20 µs the plasma temperature in the first mesh adjacent to the target increases from 0.5 eV to 0.9 eV. The target heat flux by electron heat conduction is shown in Fig. 9. During the period of plasma flow to the separatrix with high plasma density and

186

low plasma temperature the target heat flux by electron heat conduction is small. After plasma flow reversal (t > 20 μs) the plasma density close to the target decreases but the plasma temperature increases and thus the electron heat conduction flux to the target increases again. The calculated erosion value is 0.25 μm. It is fully determined by electron heat conduction. The measured value is 0.2 μm.

Time dependent erosion rates during one single shot were measured for quartz under the same experimental conditions. Erosion values of 0.8 μm were obtained [3]. This experiment was also analysed with FOREV-2. Quartz has a smaller electric conductivity than graphite and therefore B_x is not frozen in at the target. Pushing out of B_x by the vaporized material now occurs also at the target. Consequently there is no magnetic field component B_y as seen from Fig. 7 and thus the plasma shield is experiencing no lateral magnetic force and momentum transfer from the hot plasma ions is dominating the movement. The plasma close to the target all the time flows along the target in outward direction away from the separatrix as shown in Fig. 10 for two different times. This outward flow just from the beginning reduces the plasma shield density at the center, and increases the plasma temperature in comparison with

Fig.9. Comparison of electron heat conduction fluxes at position of separatrix strike point for graphite and quartz target. Gaussian power density profile with peak value 20 MW/cm². FWHM=0.8cm.

carbon and thus results for at least 10 μs in a higher electron heat conduction flux to the target in comparison with graphite as shown in Fig. 9. Typically this target heat flux amounts up to 1 MW/cm² whereas the radiative heat flux is around 0.02 MW/cm². Fig. 11 shows a comparison of measured and calculated time dependencies of erosion of quartz at two different positions. The calculated erosion values are in good agreement with the measured ones. In the experiment the time dependent erosion left and right from the center differs because of the asymmetric power density profile of the magnetized plasma [3]. In the calculation a Gaußian profile was used.

The electron heat conduction flux q_{el} along the magnetic field lines to the target is calculated according to

$$q_{el} = \alpha \, n_e \, \kappa_{\parallel} \, \Delta T/\Delta x$$

with n_e the plasma electron density, $\kappa_{\parallel}$ the Spitzer conductivity [13] α an accommodation coefficient and $\Delta T/\Delta x$ the temperature difference between the target surface (at boiling temperature) and the plasma temperature in the first mesh. n_e is given as
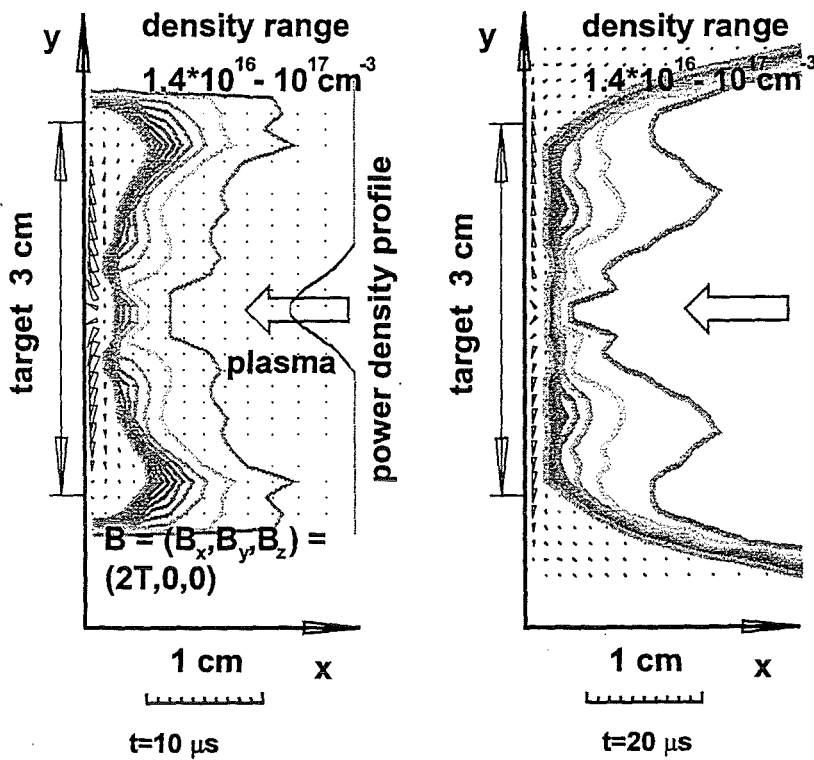
$$n_e = Z_{eff} \, n_c$$

Fig.10. Contour plot of plasma density and plasma flow ($\Gamma=nv$, arrows) in an quartz plasma shield for perpendicular quartz target. Gaussian power density profile with peak value of 20 MW/cm².

with Z_{eff} the average charge and n_e the carbon density. At temperatures around 0.5 eV Z_{eff} is small and if changes within an energy interval of 0.1 eV by one order of magnitude. Despite of limited accuracy of q_{el} in these cases its influence on erosion is small because of a self regulating process which reduces q_{el} at larger erosion rates. This mechanism also is responsible for the negligible influence of the accommodation coefficient α on erosion.
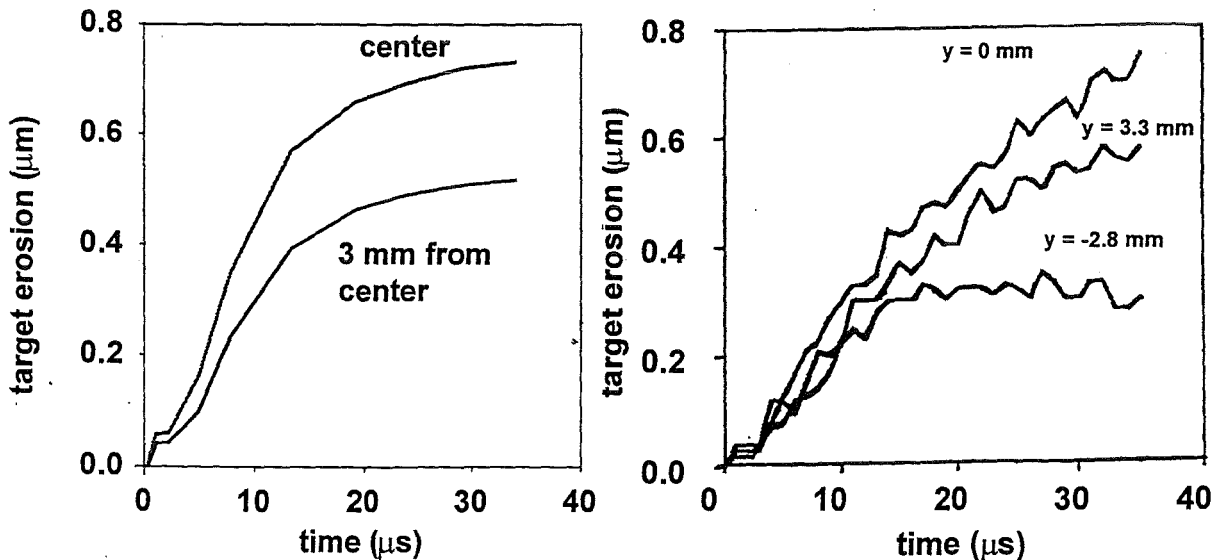
Fig.11. Comparison of measured and calculated time dependent erosion at different target positions.

The quite different MHD motion of carbon and quartz plasma shields can also be seen from a plasma mass balance as shown in Figs. 12 and 13. For carbon (Fig. 12)
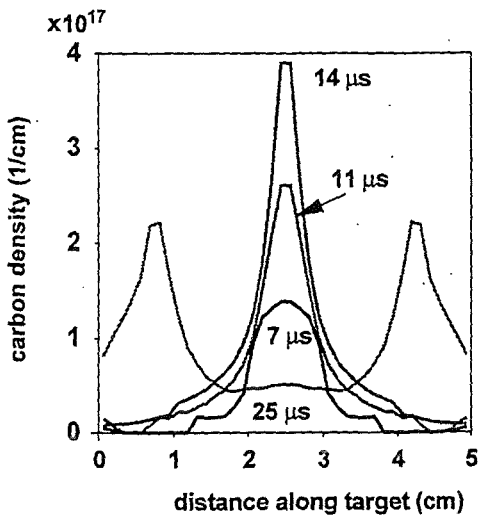
Fig.12. Distribution of graphite mass density in the plasma shield. Transparent boundary conditions at the side walls.
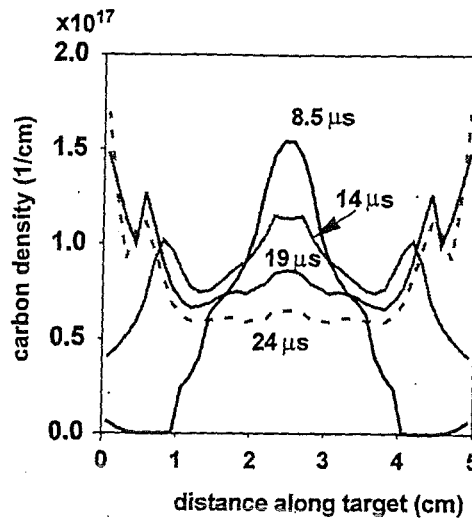
Fig.13. Distribution of quartz mass density in the plasma shield. Transparent boundary conditions at the side walls.

at times below 15 μs most plasma mass is accumulated in the center (at the position of the separatrix) indicating flow of plasma to the center. At later times the plasma mass in the center decreases because of plasma outflow for the center. For quartz the plasma mass in the center during all times remains rather small but due to permanent plasma outflow from the center the lateral width of the plasma shield increases. The total plasma mass in the center is larger for carbon than for quartz despite a factor of 3 larger erosion for quartz.

5. Energy balance for ITER targets and slot divertor side wall damage

5.1 Horizontal graphite target

The time evolution of calculated target heat fluxes during a hot plasma target interaction is shown in Fig. 14 at the position of the separatrix strike point (SSP) for a realistic power density profile with peak power density of 10 MW/cm². Heat deposition by the impacting hot plasma electrons dominates the target heat load at all times. The hot plasma ions after a few μs are fully stopped in the evolving plasma shield. The contribution of radiation to the target heat load is negligible everywhere. The erosion profile is determined by direct energy deposition. The rather weak decrease of this heat load with ongoing time (Fig. 14) reflects MHD motion of the carbon plasma shield away from the strike point resulting in a depletion of the shielding efficiency at this position. The energy laterally radiated away from the plasma shield amounts up to 85 % of the input energy. Radiation fluxes to the side walls are shown in Fig. 15 at different times. The deposition width increases with time because of expansion of the plasma shield and reaches typically 1.5 m after 500 μs. Maximum heat flux values typically are 4.0 kW/cm² at early times and around 2 kW/cm² at later times for a slot width of 20 cm.
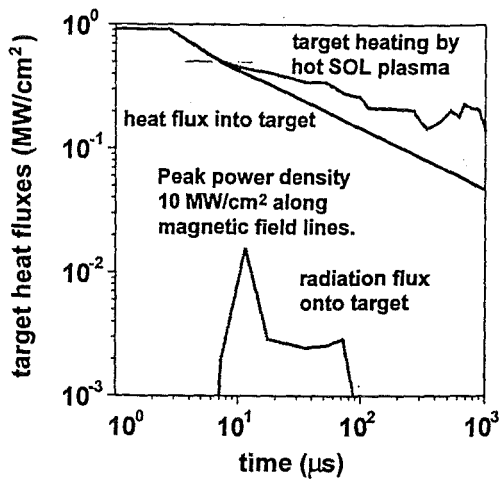
Fig.14. Time evolution of target heat fluxes at the separatrix strike point (SSP) for horizontal graphite target and realistic power density profile with peak power density of 10 MW/cm².
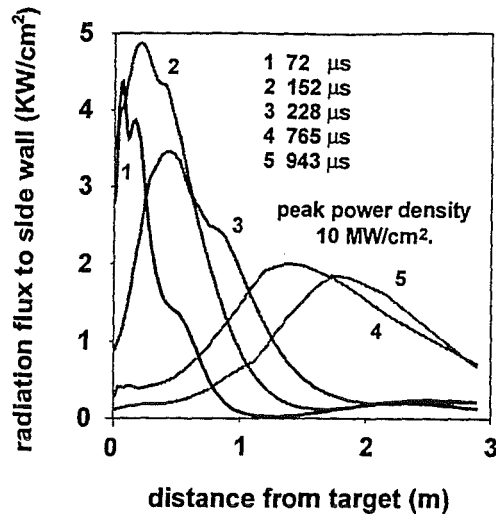

Fig.15. Radiation flux from carbon plasma shield to the side wall. Horizontal graphite target, side wall distance 20 cm and realistic power density profile.

5.2 Vertical graphite target

For a vertical target with poloidal inclination angle of 20° the time evolution of calculated target heat fluxes are shown in Fig. 16 for the two cases separatrix up- and downstream at different target positions. For upstream separatrix this position is the SSP, for downstream separatrix the position is at maximum erosion which is not identical with the SSP. Realistic power density profiles with peak power density of 10 MW/cm² were used. Again direct heating by the hot SOL plasma electrons dominates the target heat load. The radiation flux is the same for both cases. It contributes with about 30 % to the target heat load. The reason for this is that the highly radiating volume
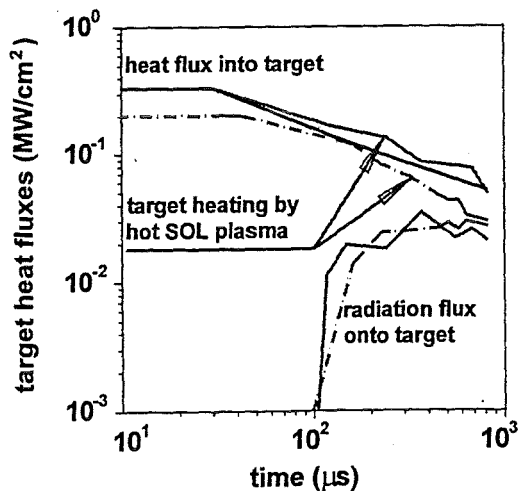

Fig.16. Comparison of the time evolution of target heat fluxes for vertical graphite target for upstream (solid line) and downstream (dashed line) separatrix. Peak power density is 10 MW/cm² along magnetic field lines.

always remains rather close to the target as is seen from Fig. 17 which shows the 2 dim radiation field (arrows, change of size indicates the radiating region) and 2 dim plasma density profiles. Radiation fluxes to the side wall are shown in Fig. 18 at different times. Typical heat flux values are 25 kW/cm² and thus are a factor of 10 larger than for a horizontal target. The deposition width remains below 1 m. The

radiative heat load to the side wall scales linearly with the peak power density of the impacting hot plasma.
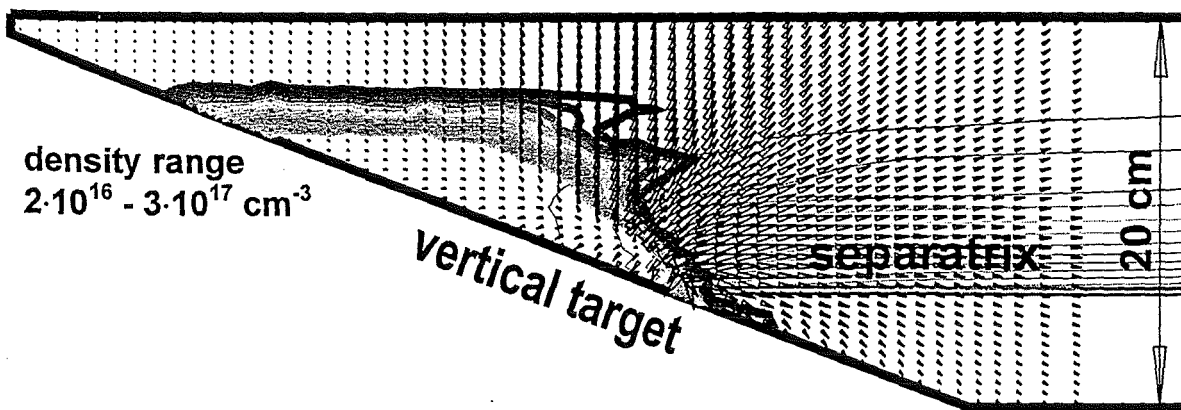

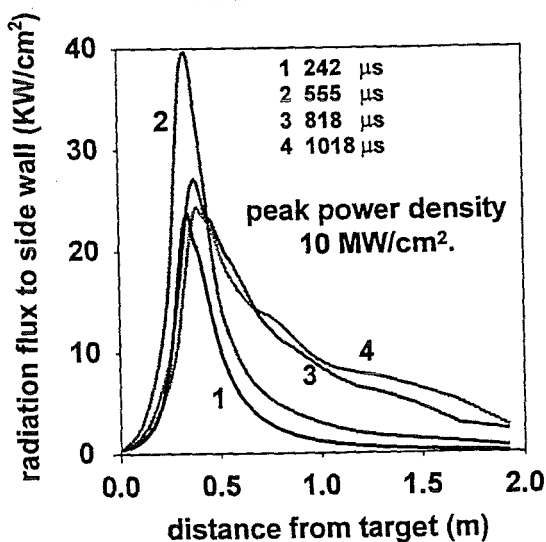**Fig.17. 2 dim radiation field (arrows) and plasma density for vertical target at 367 μs.**

Fig.18. Radiation flux from carbon plasma shield to side wall. Vertical graphite target, side wall distance 20 cm, realistic power density profile.

5.3 Side wall damage

The slot width of the ITER divertor is 60 cm. The radiative heat load to the upper side wall in this case is reduced by a factor of 2.5 in comparison to a slot width of 20 cm. Thus side wall heat loads for vertical graphite targets and downstream separatrix typically are 10 kW/cm² for peak power densities of 10 MW/cm². A first estimation on damage of side walls was performed for a vertical graphite target. For peak power density of 10 MW/cm² and times up to 100 ms the surface temperature of tungsten side walls remains below 3000 K. Below 10 MW/cm² melting of tungsten side walls does not occur within 1 sec. For a peak power density of 100 MW/cm² melting and vaporization of tungsten side walls occurs. After 2 ms tungsten side walls start to melt over a length of about 1 m. Tungsten evaporation starts after about 10 ms

6. MHD motion of plasma shields and target erosion for ITER conditions

6.1 Horizontal targets

6.1.1 Gaußian power density profile

Fig. 19 shows a contour plot of plasma density and plasma flow $\Gamma = nv$ (arrows) in the carbon plasma shield 150 µs after start of the target heating. The power density profile of the incoming hot plasma is Gaußian in y direction with a peak power density of 100 MW/cm² at the separatrix and a half width of 5 cm. The carbon density range for the contour is $7 \cdot 10^{16}$ to $8.5 \cdot 10^{17}$ cm^{-3} with decreasing density at increasing distance. Close to the target the carbon density increases up to 10^{19} cm^{-3} at the SSP. A plasma flow to the separatrix (inward flow) is clearly to be seen. The reason for this flow regime again is depletion of B_x and built up of a B_y component as discussed in chapter 4. The inward plasma flow along the target surface towards the center (maximum
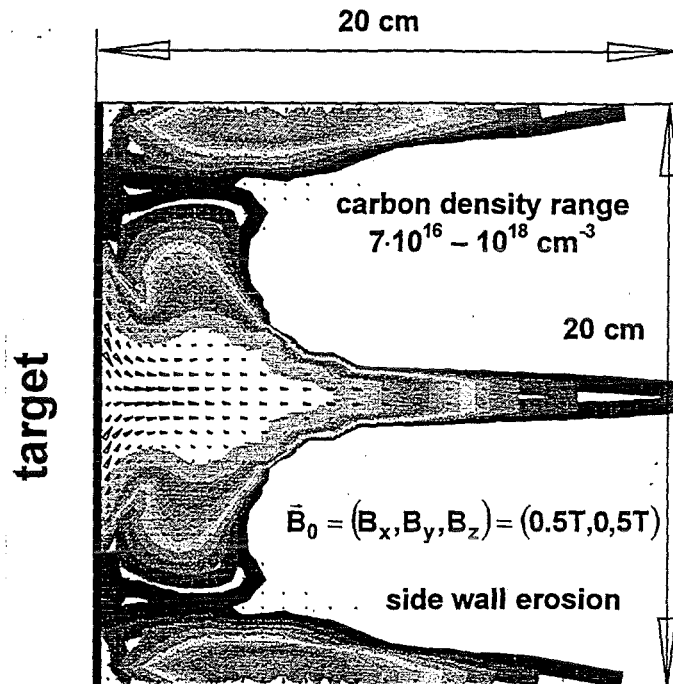
Fig.19. Contour plot of plasma density and plasma flow (Γ=nv, arrows) at 150 µs for horizontal target. Incoming hot plasma 10keV. Gaussian power density profile with halfwidth of 5 cm, peak power density is 100 MW/cm².
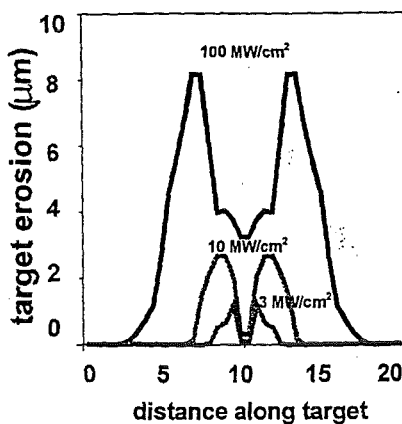
Fig.20. Comparison of erosion profiles at 1 ms for different peak power densities.

heat load) improves the shielding in this region and erosion at the SSP becomes less than at the wings of the power density profile as is seen from Fig. 20 showing a comparison of erosion profiles for different peak power densities at 1 ms. The increase in erosion width with increasing power density is due to erosion by radiative energy transfer from the plasma shield to the target.

6.1.2 Realistic power density profile

The realistic power density profile across the SOL has a steep gradient at one side and shows a less pronounced decrease at the other side (see Fig. 1b). In this case the plasma forced by the steep gradient flows along the target to the
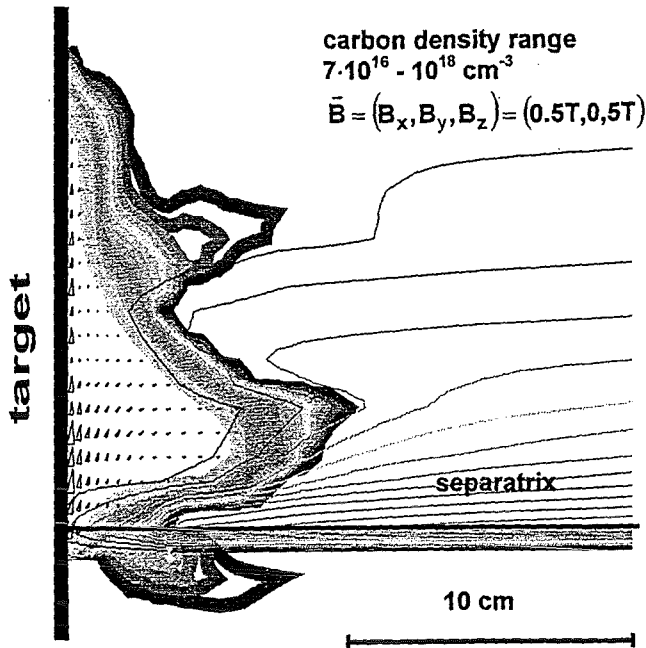
carbon density range
$7 \cdot 10^{16} - 10^{18}$ cm^{-3}

$\bar{B} = (B_x, B_y, B_z) = (0.5T, 0, 5T)$

separatrix

10 cm

Fig.21. 2 dim plasma density and plasma flow (arrows) at 62 µs. Incoming hot plasma 10 keV, realistic power density profile, halfwidth 5 cm, peak power density is 100 MW/cm^2.

side of the gradual decrease. From Fig. 21 it is seen that the shielding layer at the position of the peak power density continuously is depleted by this plasma flow. Fig. 22 shows target erosion profiles at 0.5 ms for different peak power densities. The depletion of the plasma shield at the location of the peak power density (separatrix strike point) results in rather strong erosion. As long as the peak power density is above 10 MW/cm^2 erosion outside of this peak mainly is caused by radiation resulting in the rather broad erosion profile shown in Fig. 22. For 10 MW/cm^2 erosion during at least 0.5 ms is occurring practically only in the region of the separatrix strike point. Radiation is insufficient for broadening of the erosion profile.
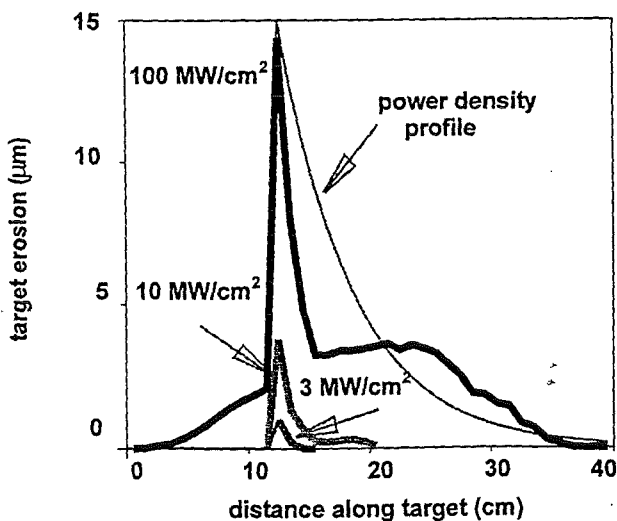

Fig.22. Target erosion for horizontal graphite target at 0.5 ms. Realistic power density profile with different peak power densities.

6.2 Vertical target

2 dim plasma density profiles and the plasma flow pattern (arrows) in the plasma shield are shown in Fig. 23 for a vertical target and downstream separatrix strike point at 740 µs for 10 MW/cm^2. The density lines correspond to carbon densities in the range of 7 x 10^{15} to 10^{17} cm^{-3}. Close to the target the plasma flows along the target surface downwards then changes its flow direction, forms a plasma bubble and moves outside of the hot plasma impact region towards the upper side wall and upwards (in x direction). The upward velocity typically is 10^5 cm/s. The plasma bubble with central plasma density of 3 · 10^{17} cm^{-3} has plasma temperatures below 2 eV and is weakly heated by lateral radiation fluxes of up to 5 kW/cm^2 from the target plasma shield. In case of upstream separatrix strike point, the downward flow results in a depletion of shielding

density range
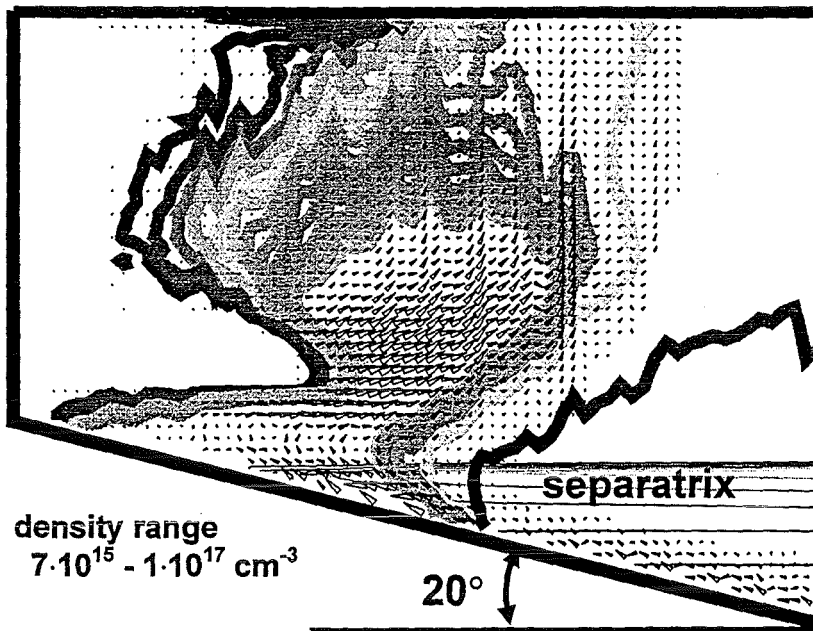$7 \cdot 10^{15} - 1 \cdot 10^{17}$ cm^{-3}

20°

separatrix

Fig.23. 2dim plasma density contours and plasma flow pattern (arrows) in the plasma shield at 740 μs for vertical target with downstream separatrix. Slot width 60 cm, Peak power density 10 MW/cm^2.

at the position of the strike point, whereas in case of downstream separatrix strike point the downward flow of the plasma shield results in an improved shielding at the strike point position and thus in a reduction of the target heat load by the hot SOL plasma as seen from Fig. 16. The erosion is markedly different for both cases. For the downstream separatrix strike point peak erosion is about a factor of 10 less than for the case with upstream separatrix strike point. In Fig. 24 calculated peak target erosion values are shown for the horizontal and the vertical graphite target with separatrix upstream for a peak power density of 10 MW/cm^2 and for a vertical target for 100 MW/cm^2. Erosion of the horizontal and vertical target at 10 MW/cm^2 are comparable despite a factor of 3 lower heat load of the impacting hot plasma at the vertical target. Erosion of vertical targets and upstream separatrix is smaller at 100 MW/cm^2 than at 10 MW/cm^2. The reason is upstream target erosion by radiation in the 100 MW/cm^2 case and subsequent downward movement of the plasma shield providing increased shielding at the strike point of the separatrix. In the 10 MW/cm^2 case the plasma shield at the separatrix strike point permanently is depleted by downwards flow of the target plasma.
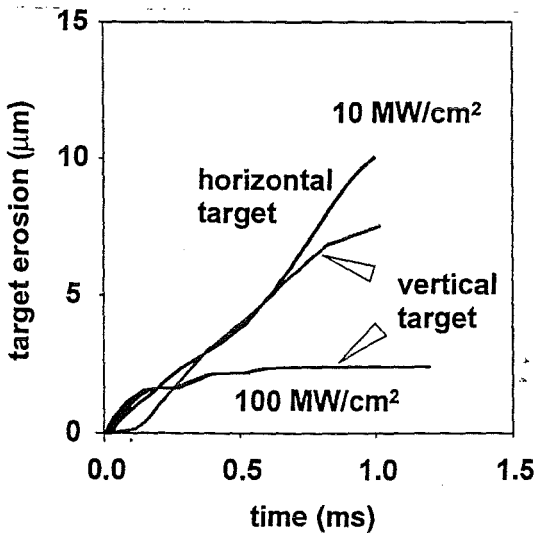

Fig.24. Comparison of target erosion for horizontal graphite target at 10 MW/cm^2 and vertical graphite targets with upstream separatrix at 10 MW/cm^2 and 100 MW/cm^2.

7. Impurity transport in the slot divertor

The plasma shield ions are moving upward in the ITER slot divertor towards the x-point. The MHD motion of these impurities was studied with FOREV-2 for a horizontal graphite target. For the incoming hot plasma a Gaussian distributed power density profile with peak power density of 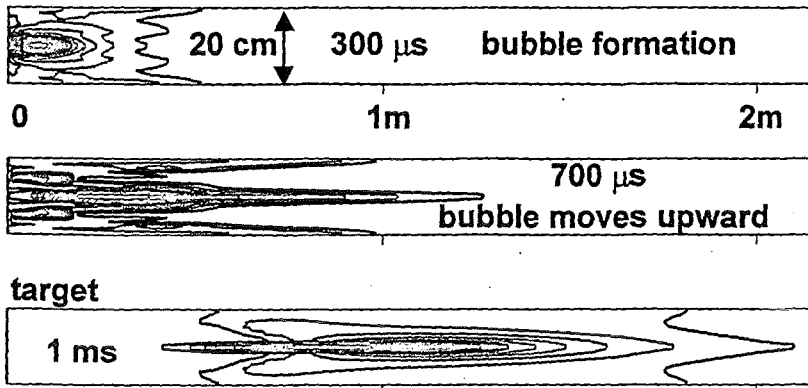10 MW/cm^2 and a half width of 5 cm was assumed. The time duration of the heat load was 40 μs. These conditions simulate a powerful ELM. Interactions of the impurity ions with the neutrals from the gaseous divertor and with the stationary SOL plasma were not taken into account in these first calculations.

Fig.25. Impurity transport in the slot divertor. Gaussian power density profile with FWHM = 5cm and peak power density of 10 MW/cm^2. Time duration of the heat load is 40μs. Plasma density ranges are $6 \cdot 10^{15} - 7.2 \cdot 10^{16}$ cm^{-3}, $3.2 \cdot 10^{15} - 3.9 \cdot 10^{16}$ cm^{-3} and $2.0 \cdot 10^{15} - 2.3 \cdot 10^{16}$ cm^{-3} for upper, middle and lower plot correspondingly.

The movement of the plasma shield in the (x,y) plane along and across the magnetic field lines with $B_x = 0.5$ T and $B_z = 5$ T is shown in Fig. 25 for a perpendicular target at x = 0. Early in time there is an effective MHD motion of cold plasma close to the target across B_z which stops the impurity expansion. After about 400 μs formation of an impurity plasma bubble of temperature below 1 eV is completed. This bubble driven by pressure gradients moves upward in the slot at velocities of about 5×10^5 cm/s as is seen from Fig. 26. About 1.1 ms after switching off heating the density of the mainly singly ionized impurities reaches a value of 4×10^{15} cm^{-3} at a distance of 2 m from the target. During a time period of 0.5 ms the impurity flux at the x point remains at a level of 2×10^{21} ions/cm^{2}s. Such a high impurity flux could trigger a current quench disruption.
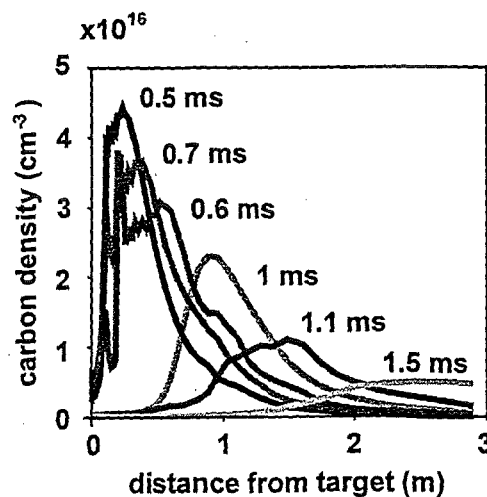

Fig.26. Time evolution of carbon density profiles in the slot center.

8.   Conclusions

The 2 dim results obtained demonstrate that a realistic analysis of disruptive erosion of the divertor target and the ITER slot divertor has to be performed with a 2 dim code. Vertical targets in comparison with horizontal ones favourably reduce the upward directed movement of the plasma shield in the slot and the target erosion for downstream separatrix, but result in comparable erosion in case of upstream separatrix and penalize with drastically increased radiation fluxes to the side walls resulting in larger damage by melt layer erosion. The reduced upward directed movement means improved retention of impurities in the divertor slot. Now the tools for a consistent damage analysis of the rather complicated ITER slot divertor are available.

9.   Acknowledgement

10.   References

[1]   G. Janeschitz et al., J. Nucl. Mater. 220 - 222 (1995) 73.

[2]   H. Würz et al., J. Nucl. Mater. 220 - 222, 1995, p. 1066.

[3]   H. Würz et al., Fusion Technology Vol. 32, No. 1, 1997, p. 45.

[4]   H. Würz et al., ANS Topical Meeting on Technology of Fusion Energy June 16 - 22, 1996, Reno.

[5]   J. Lingertat et al., J. Nucl. Mater, 241 - 243, 1997, p. 402.

[6]   S. Pestchanyi, H. Würz, "The 2 dim radiation magnetohydrodynamics code FOREV-2", to be published as FZKA report.

[7]   O.M. Belozerkovsky, Y.M. Davidov, "The method of large particles in gas dynamics", M. Nauka 1981 (in russian).

[8]   B. Bazylev, "The 2 dim S_N code TWORAD", private communication.

[9]   I.V. Nemchinov Appl. Math. and Mech. Vol. 34, No. 4, 1970, p. 706.

[10]   B. Bazylev et al., Phys. Eng. J. 58, 6, 1012 (1990) (in Russian).

[11]   N.I. Arkhipov et al., Fusion Technology 1994, Vol. 1, p. 463, 1995.

[12]   N.I. Arkhipov et al., J. Nucl. Mater 233 - 237, 1996, p. 767.

[13]   L.Jr. Spitzer, "Physics of fully ionized gases", J. Wiley NY, 1962.

STATIONARY PARTICLE-IN-CELL SIMULATIONS ON ELECTRON AND ION DIODES

W. Bauer[1], M. Baus[2], E. Stein[1], B. Schrempp[2], T. Westermann[2]

1) Forschungszentrum Karlsruhe GmbH, Postfach 3640, D - 76021 Karlsruhe, Germany
2) Fachhochschule, Moltkestraße 4, D - 76133 Karlsruhe, Germany

ABSTRACT

The stationary Particle-in-Cell - program system „BFCPIC" [1] has been modified to run on unix workstations. A new mesh generator „InGrid" producing the boundary fitted grid was incorporated in „AutoCad" and applied to diode meshing. The mesh generated by InGrid can be exported to both the stationary PIC-code „BFCPIC" and the time resolving PIC-code „KADI2D"[2]. For calculating the applied magnetic fields the commercial FEM code „ANSYS" is used. As input for the calculation of the magnetic field the current in the coils is computed using the equivalent circuit option of ANSYS. To test the whole program system simulations on a simple electron diode for KALIF-HELIA [3] have been performed. As a second step the simulation of the present applied-B diode [4] was repeated and identical results compared to the old program system. were found. Finally, the simulations on a new design of the selfmagnetically B_Θ-insulated ion diode [5] are summarized.

I. INTRODUCTION

Our stationary Particle-in Cell -Code „BFCPIC" based on boundary fitted grids is used since 1988 in two versions: BFCPIC2D is two-dimensional and serves mainly to simulate the self-magnetically insulated $B_\Box$-diode [5]. The 2.5-dimensional BFCPIC2H allows for externally applied magnetic fields and is used to model applied-B diodes [4] and recently, as is shown below, for electron diodes. Although these codes are time independent we have gained quite a lot of physical insight from these simulations. First simulations using the new time-dependent PIC-code „KADI2D" are described in ref. [2]. This code is also based on boundary-fitted grids and some of the features of the stationary codes could be adopted for it. To validate this program tests were made using the same models as for the stationary codes, and a comparison under equal conditions has given equal results [2]. One purpose of the simulations shown below was, to supply material for this comparison. Another was to assist the design of an electron diode for KALIF-HELIA.

Since 1988 great changes in the computer world have taken place, and the codes have been gradually adopted to new computer systems. The main change was the step from large main-frame MVS computers to small UNIX workstations. While in early days the knowledge of FORTRAN and some job control language was sufficient to run the codes, today a great variety of partly commercial codes, partly own developments are in use. This paper describes in its first part the work with this combination of programs and summarizes in its second part some results obtained for several versions of the KALIF-HELIA electron diode, for the applied-B diode and for the B_Θ-diode.

II. STEPS OF A SIMULATION

The generation of the grid starts from an AutoCAD-drawing of the diode. By copying the lines relevant for the simulation on a new layer the grid boundary is fixed. Using the program „InGrid" [6] that is incorporated into AutoCAD the grid is constructed interactively. This requires some experience: Although by far not all features of AutoCAD are used for the grid generation, user's mistakes in AutoCAD result in rather strange effects at the generated grid or, more often, to a failure of the whole program. The final grid is then exported either into the format needed for the PIC-codes or into the ANSYS-format. Thereby both files have to be modified slightly to meet the requirements of the different systems: For ANSYS the correct element type (plane53) and the corresponding material constants have to be added, to the PIC-file a „head" has to be added that contains informations about electrodes, boundaries and direction of current flow.

ANSYS [7] is used to calculate the magnetic field excited by external coils. These coils are in general situated outside of the PIC-model, so that an ANSYS-model has to be constructed around the PIC-model and combined with it for the calculation of the magnetic field. Recently the current in the coils is calculated by the equivalent circuit option of ANSYS. Two difficulties had to be overcome in combining the PIC-code with ANSYS:

a) The ANSYS-grid is unstructured, while the PIC-code grid is structured. This is the reason for starting with the grid for the PIC-code and constructing the ANSYS-grid only for the outer regions. The combination of both grids was a difficult programming task.

b) Since in ANSYS the rotation axis has to be perpendicular, while in the PIC-code it is horizontal, the InGrid-grid has to be rotated and mirrored for ANSYS. The ANSYS results then again have to be rotated and mirrored to be used as an input for the PIC-code.

The results of the PIC-code are transformed into a format readable by the postprocessor Techplot [8] by using a program „Visart" [9]. Finally the results are plotted by Techplot as is shown in the examples below.

III. ELECTRON DIODES FOR KALIF-HELIA

Our new 6-MV generator KALIF-HELIA [3] will be run first in negative polarity using an electron diode. The program system described above has been checked and practiced first on two versions of an electron diode: Figures 1a and 1b show the electrical potential distribution in two preliminary variations and in a final shape 1c that will be used experimentally. Both diodes need a pair of Helmholtz-coils as shown in Fig. 3, situated outside of the area indicated in the figures 1a-1c producing a magnetic field that counteracts the pinching of the electrons down to the axis due to their self-field. Figs. 2a and 2b illustrate the electron current density obtained for different coil currents. Table I. gives a summary of the simulation results obtained so far for several geometrical parameters and different amplitudes of the applied external magnetic field. Fig.3 also shows the lines of constant vector potential A_z computed by ANSYS.

The general behavior is as expected. A shorter gap gives higher electron current. The numbers, however, differ slightly from results one would obtain using the simple Child-Langmuir-Law, since the rounding at the electrodes and the effect of more or less pinching is not considered in the formula. A higher external field reduces the pinching. A longer part of the transmission line adds more electrons and increases the current. Figs. 4a and 4b show an interesting difference for different electron currents: At low current the transmission line is not
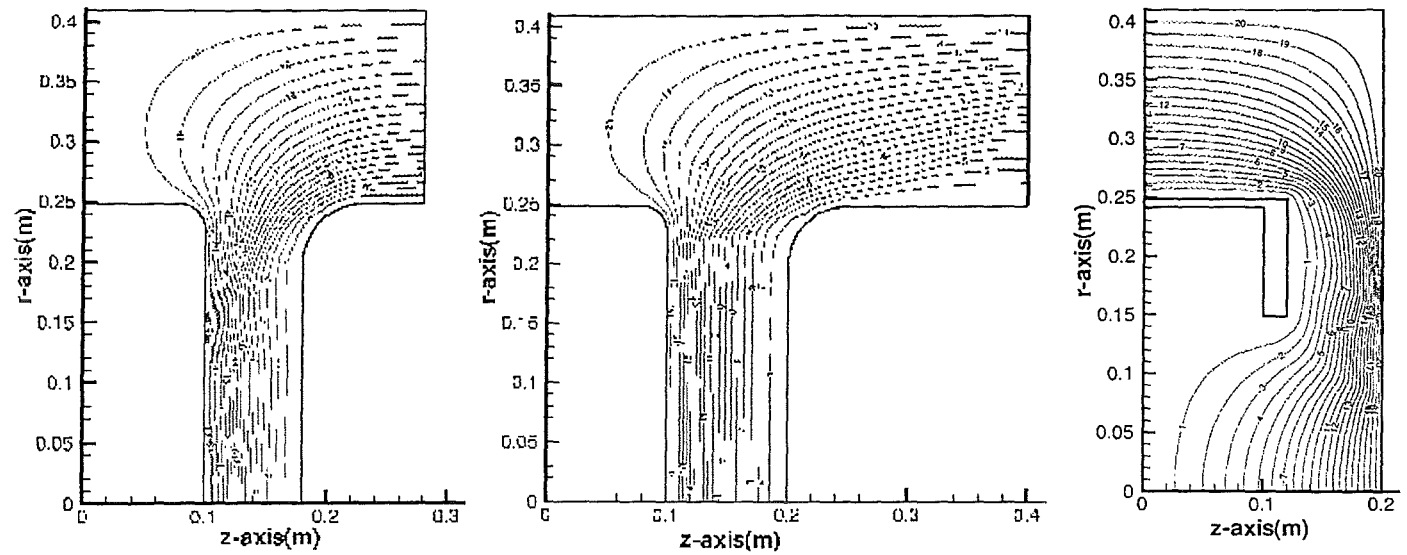
Fig. 1a, b, c: Equipotential lines in differently shaped electron diodes for KALIF-HELIA
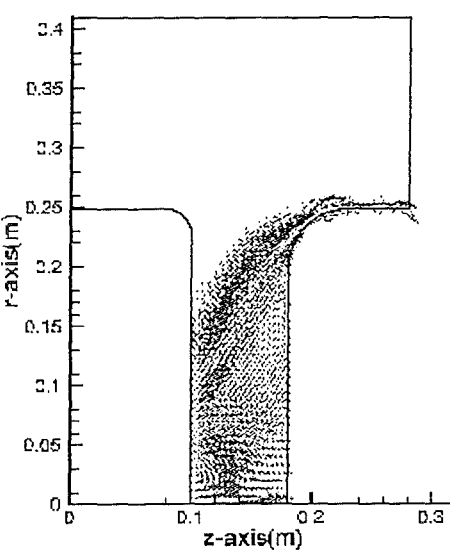

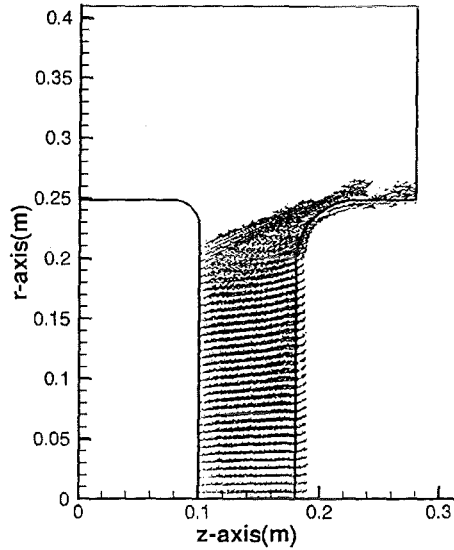Fig. 2a: Electron current density, showing pinching of the electrons.

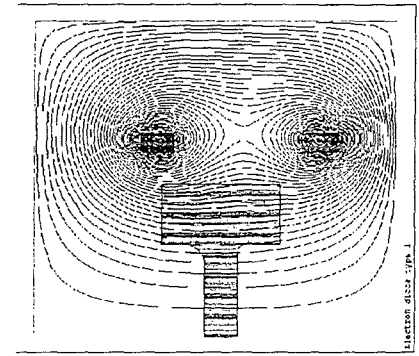Fig. 2b: High coil current counteracts the pinching.

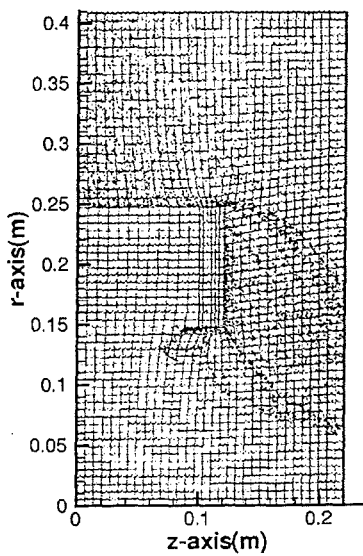Fig. 3: ANSYS-result , rAz-lines and position of the coils

Fig. 4a: Small electron current is not sufficient to insulate the coaxial line
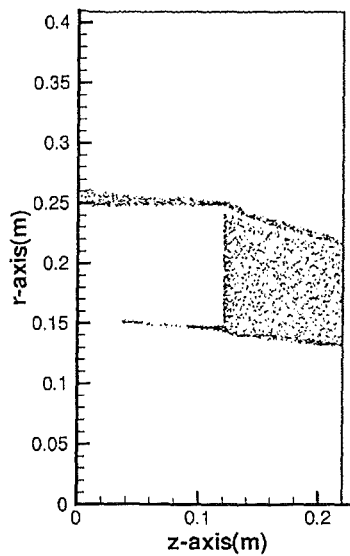
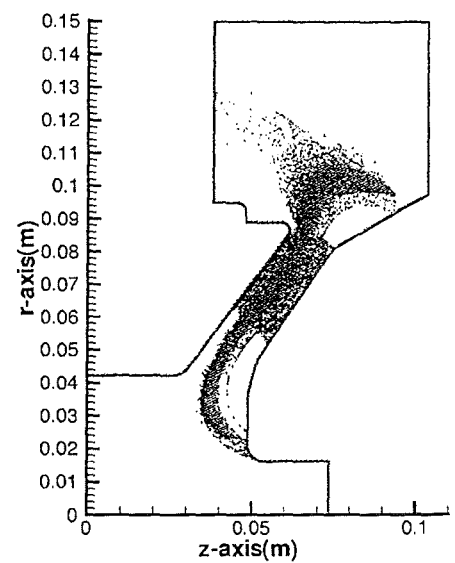Fig. 4b: At high electron current the coaxial line is insulated

Fig. 5. Electrons and Ions in the applied-B-Field-Ion Diode

well insulated and electrons spread out all over the space between inner and outer conductor, whereas at higher current the magnetic insulation keeps this space free of electrons. In Table I the cases, where the magnetic insulation breaks down are marked. Between I=327 kA and I=335 kA is a rather sharp transition between poor and good magnetic insulation.

Table I. Electron Current I_E and Impedance $\square$ in Electron diodes of shapes A, B, C as function of gap distance G and coil current I_C

Shape	I_C [kA]	80 [mm]		100 [mm]		120 [mm]	
		I_E [kA]	Ω	I_E [kA]	Ω	I_E [kA]	Ω
A	40	457.6	13.1	368.3	16.3		
A	80	458.3	13.1	427.9	14.0		
A	160	523.7	11.5	421.0	14.3		
A	240	606.1	9.9	493.0	12.1		
B	40	552.6	10.9	419.9	14.3		
B	80	479.1	12.5	346.6	17.3		
B	160	574.3	104	468.8	12.8		
B	240	700.9	8.6	539.8	11.1		
C	40	655.3	9.2	322.0	18.6	277.7	21.6
C	80	821.3	7.3	312.2	19.2	270.3	22.2
C	120	676.2	8.9	326.9	18.4	244.3	24.6
C	160	642.2	9.3	395.7	15.2	335.3	17.9
C	240	653.1	9.2	451.6	13.3	375.0	16.0

[marked cases refer to poor magnetic insulation due to low electron current]

IV. APPLIED-B ION DIODE

The simulation results on the applied-B diode Fig. 5 are identical to the results obtained with the old program system. Whereas the general picture of electrons emerging from the cathode tip and forming an electron sheath are obtained as expected, the numbers for the ion current are by more than a factor 10 lower than in the experiments. This is due to the fact, that in the 2.5-dimensional code without time dependency the effect of instabilities and movement of the electron sheath cannot be modeled. So the result shown in Fig. 5 is only a confirmation that the transition in the program system from MVS to UNIX is completed without apparent errors.

As is described in more detail in [10] recently a new feature of ANSYS has been used to calculate the current in the coils of the applied-B diode using an equivalent circuit model incorporated in ANSYS (since version 5.3). Here the constituents of the circuit shown in Fig. 6 - capacitors, coils, resistances are modeled as elements, and applied voltages as boundary conditions. The resulting time resolved current is then used as input for the calculation of the magnetic field. Fig. 7 shows the current versus time obtained. The curve reproduces very well the experimentally
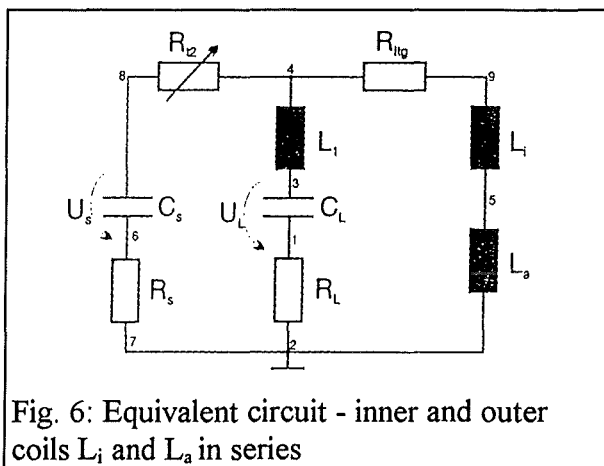

Fig. 6: Equivalent circuit - inner and outer coils L_i and L_a in series
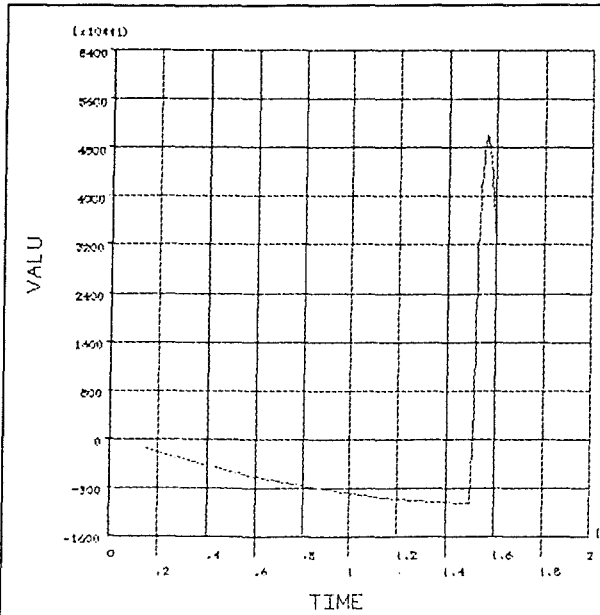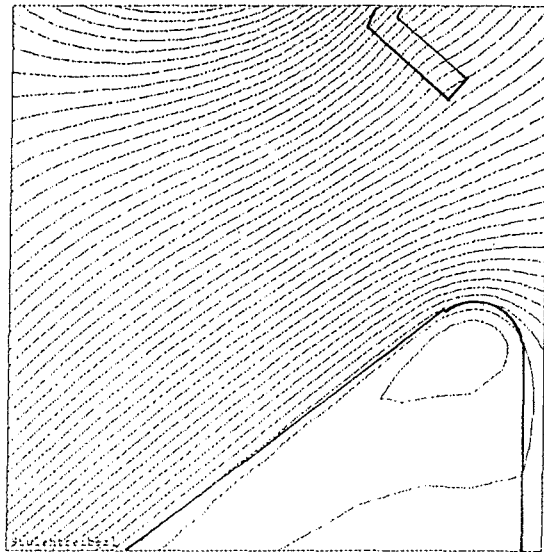
Fig. 7: Current calculated by ANSYS

Fig. 8: rA_Θ -lines parallel to anode surface

measured current. Fig. 8 shows the lines of equal vectorpotential (rA_Θ) in the vicinity of the anode. Since electrons emerging from the cathode tip expand along these lines, it is essential, that they are parallel to the anode surface. In addition to fulfill the request of zero angular momentum of the ions coming from the anode little penetration of the magnetic field into the anode at the time instant of the beginning high voltage pulse is necessary, which can also be seen in the figure.

Following experiments [11] a new set of simulations was carried out, where the inner and outer coils were driven by separate power supplies. Fig. 9 shows the
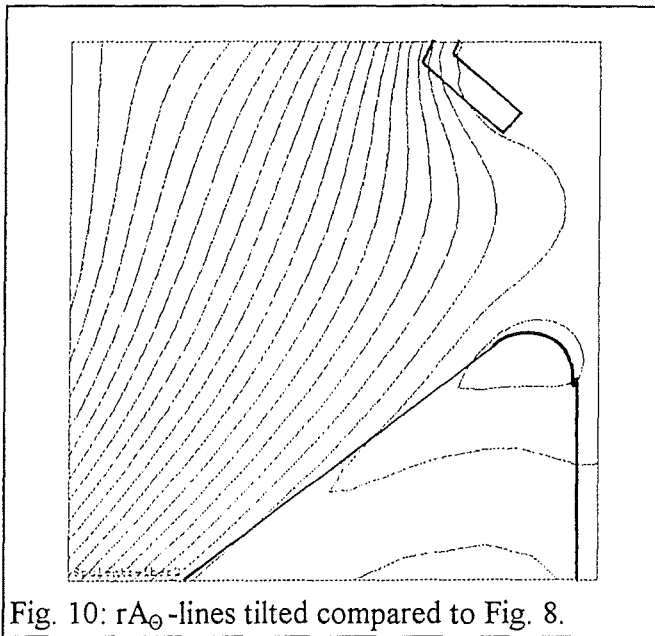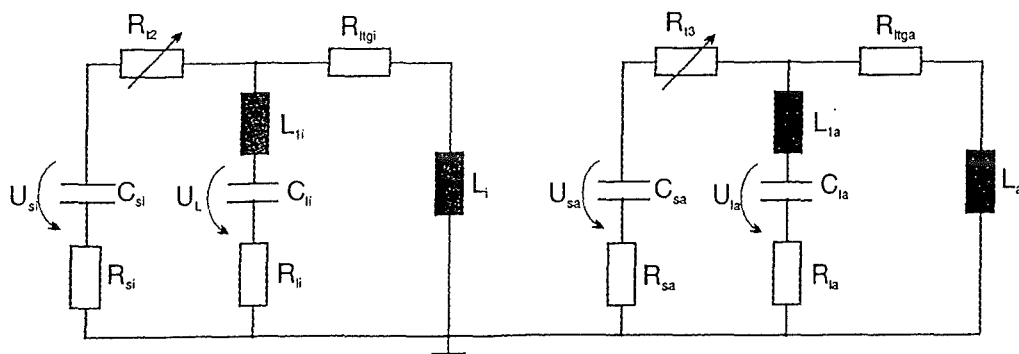

Fig. 10: rA_Θ -lines tilted compared to Fig. 8.

Fig. 9: circuit diagram with separate power supplies for inner and outer coils L_i and L_a

separate power supplies. Fig. 9 shows the corresponding circuit and in Fig. 10 it can be seen, that for an experimentally given power supply setting the vector potential lines are tilted as compared to Fig. 8. To obtain a magnetic field that is optimized for the focusing of the ion beam the self-field of the beam has to be taken into account [11], which is not included in the ANSYS-calculation.

V. SELFMAGNETICALLY B$_\Theta$-INSULATED ION DIODE

Following the arguments summarized in [5] a modified B$_\Theta$-Diode as shown in Fig. 11 was simulated. As can be seen in the figure there is an anomaly of the potential distribution that probably is due to numerical effects in the program: Circles of negative equipotential lines certainly do not have a physical meaning in this geometry. Reducing the convergence criterion at the potential calculation, improving the calculation accuracy and increasing the relation between electron and ion time steps helped to improve the situation slightly, but did not remove the anomaly completely. Since all these steps dramatically increase the necessary cpu-time the program was run on the fasted available computer. Further attempts are in preparation.
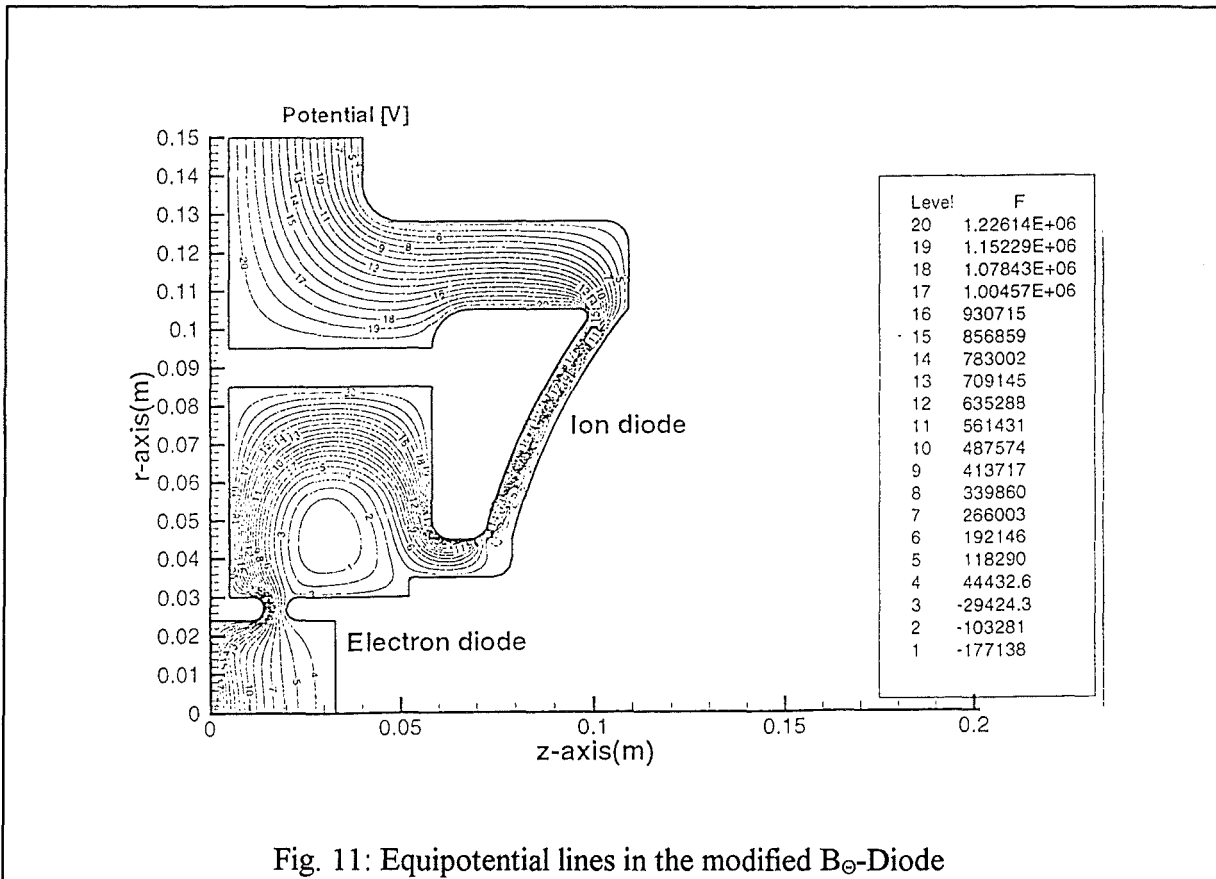

Level	F
20	1.22614E+06
19	1.15229E+06
18	1.07843E+06
17	1.00457E+06
16	930715
15	856859
14	783002
13	709145
12	635288
11	561431
10	487574
9	413717
8	339860
7	266003
6	192146
5	118290
4	44432.6
3	-29424.3
2	-103281
1	-177138

Fig. 11: Equipotential lines in the modified B$_\Theta$-Diode

Assuming that this error does not essentially change the simulation results obtained so far, the following general rules can be stated:

Keeping the gap width at the electron diode constant, the total electron and ion currents are controlled by the gap width of the ion diode gap as usual. The maximum B$_\Theta$-field occurs at the lower end of the ion emitting anode and is approximately proportional to the total current. This is in contradiction to the considerations that were the basis of this design: The B$_\Theta$-field is

supposed to be governed mostly by the electron diode. This is not the case. On the other hand, if the ion diode is switched off completely (no electron and no ion emission), then the electron diode follows roughly the Child-Langmuir-Law.

Keeping the gap at the ion diode constant the total current is not influenced much by changing the gap of the electron diode. It has to be concluded that the electron diode does not play the expected role in the combined operation of both diodes. The reason can be seen from the simulations: Increasing the current in the electron diode (by decreasing the gap width) increases B_D, thus improving the insulation in the ion gap. This keeps the electron sheath farer away from the anode and consequently decreases the ion current. The future task is, to find an optimum, where the ion current is maximized and the electron current is minimized. This was postponed until the anomaly described above will be understood.

CONCLUSIONS

The step between the old and the new computer systems is completed successfully. After some practicing a sufficient variety of models is available to compare stationary results to time dependent simulations. First simulations on the electron diode are performed. The effect of electron inflow from the KALIF-HELIA transmission line has been shown principally; it was found that at 330 kA a sharp transition between poor and good magnetic insulation takes place. Simulations on the applied B-diode confirm the correct transition from the old to the new computer systems. A new way of calculating the magnetic coils in the applied-B diode using the equivalent circuit feature of ANSYS has been successfully employed. First attempts to overcome a numerical anomaly in the BFCPIC2D - code and preliminary conclusions on a redesigned B_Θ-Diode were reported.

REFERENCES

[1]   T. Westermann, „A Particle-in-Cell Method as a Tool for Diode simulations",
        Nuclear Instr. Meth. A 263 (1988), p. 271
[2]   C.-D. Munz, P. Omnes, R. Schneider, E. Sonnendrücker, E. Stein, U. Voss,
        T. Westermann, „KADI2D-A Particle-in-Cell Code based on Finite-Volume Methods",
        Proc. 12th Int. Conf. High Power Part. Beams, Haifa, 1998
[3]   P. Hoppé, W. Bauer, H. Bluhm, V. Carboni, J. Fockler, G. Keßler, K. Leber, K. Nielsen, K. Prestwick,
        W. Ratajczak, D. Rusch, J. Singer, I. Smith, P. Spence, „The KALIF-HELIA Accelerator:
        Description, Program and Status", Proc. 12th Int. Conf. High Power Part. Beams, Haifa, 1998
[4]   W. Bauer, W. Höbel, A. Ludmirsky, E. Stein, T. Westermann, „A Contribution to the
        Magnetic Focusing in an Applied-B-Extractor Ion Diode by a Laser Pulse driven
        Solenoid" Proc. 10th Int. Conf. High Power Part. Beams, San Diego, 1994, p. 83
[5]   W. Bauer, P. Hoppé, H. Bachmann, H. Bluhm, L. Buth, H. Messier, D. Rusch,
        E. Stein, O. Stoltz, W. Väth, T. Westermann, „Recent Results from Experimental and
        Numerical Investigations of the Selfmagnetically B_Θ-Insulated Ion Diode",
        Proc. 11th Int. Conf. High Power Part. Beams, Prague, 1996, p. 1123
[6]   E. Halter, B, Schrempp, Fachhochschule Karlsruhe, private communication
[7]   ANSYS® ANSYS, Inc. 201 Johnson Road,, Houston, PA, 15342-1300
[8]   Tecplot® Amtec Engineering, Inc. Bellevue, Washington
[9]   S. Kleinheinz, „Das VISART-Konzept einer standardisierten Schnittstelle zwischen
        Codes und Auswerteprogrammen", FZK-Reports 5995 and 5596, 1997,
        Forschungszentrum Karlsruhe
[10]   M. Baus, „Zeitabhängige Analyse von Magnetfeldstrukturen in Hochstrom-Ionendioden mit Hilfe der
        Finite-Element-Methode", Diploma work Fachhochschule Karlsruhe 1998
[11]   P. Hoppé, H. Bluhm, D. Rusch, O. Stoltz, W. Väth, M.P. Desjarlais, „Improvement of Beam
        Divergence by Emission Profiles with better Homogeneity",
        Proc. 12th Int. Conf. High Power Part. Beams, Haifa, 1998